GENIORS

Research and Innovation Action (RIA)

This project has received funding from the European Union's Horizon 2020 research and innovation programme under grant agreement No 755171.

Start date : 2017-06-01 Duration : 48 Months
http://geniors.eu/

Assessment of the corrosion vulnerability of common plant materials in thepresence of key process streams

Authors : Pr. Colin BOXALL (ULANC), Richard Wilbraham (ULANC), Ghebrehiwot Berhane (ULANC), Jessica Higgins (ULANC), Mick Bromley (ULANC)

GENIORS - Contract Number: 755171

Project officer: Roger Garbil

Document title	Assessment of the corrosion vulnerability of common plant materials in thepresence of key process streams
Author(s)	Pr. Colin BOXALL, Richard Wilbraham (ULANC), Ghebrehiwot Berhane (ULANC), Jessica Higgins (ULANC), Mick Bromley (ULANC)
Number of pages	151
Document type	Deliverable
Work Package	WP9
Document number	D9.6
Issued by	ULANC
Date of completion	2021-04-30 18:43:06
Dissemination level	Error (13) !

Summary

Corrosion assessment work detailed in this report has had two primary objectives: 1) To perform corrosion assessments for process plant steels in the presence of as many of the GANEX inventory permutations as resource permits. 2) To carry out long term corrosion studies in relevant inventory permutations of high risk. With regards to the former, corrosion assessments of the following key compounds: TODGA, DEHiBA, AHA, SO3-Ph-BTP, SO3-Ph-BTBP, SO3-Ph-BTPhen, hydrazine and CDTA have been carried out. Compounds have been tested in predominantly aqueous solutions, where corrosion is found to be more rapid than organic solutions and at concentrations equivalent to both normal and maloperation conditions. Of the target inventory permutations, AHA and SO3-Ph-BTP have been shown to be corrosion accelerators, increasing recorded currents in the transpassive dissolution region, i.e. under high redox stresses associated with maloperation conditions. In the case of the latter, SO3-Ph-BTPhen has been shown to have similar corrosion accelerating properties whilst SO3-Ph-BTBP has been shown to be a suitable replacement ligand with no corrosion acceleration effect. Complementary evidence on the corrosion protection properties of DEHiBA, CDTA and hydrazine and confidence in their long-term corrosion protection behaviour with stainless steel process pipework is also provided here, with corrosion protection maintaining even at high nitric concentrations. This also allows for other partner groups within the consortium to focus attention on diminishing the risks associated with the implementation of AHA and SO3-Ph-BTP within the GANEX flowsheet Finally, preliminary investigations into the corrosion behaviour of inventory permutations under a realistic energy gamma radiation field have been conducted . The first of these irradiation experiments has focused on the stability of CDTA. The evidence presented in here reports indicates that CDTA exhibits relatively high radiation tolerance and retains its corrosion inhibition qualities even at total absorbed doses in the Mega Gray region.

Approval

Date	By
2021-05-18 16:06:21	Mr. David GRAHAM (NNL)
2021-05-28 15:39:32	Mr. Chris RHODES (NNL)
2021-05-31 11:28:25	Mr. Stéphane BOURG (CEA)

GENIORS

GEN IV integrated oxide fuels recycling strategies

Deliverable D9.6: Assessment of the corrosion vulnerability of common plant materials in the presence of key process streams

Author(s): Richard Wilbraham, Colin Boxall, Ghebrehiwot Berhane, Mick Bromley, Jessica Higgins 26/4/2021

Reporting Period: **01/05/2017 – 30/04/2021**

ULANC

COLIN BOXALL

Contributors
Richard Wilbraham, Colin Boxall, Ghebrehiwot Berhane, Mick Bromley, Jessica Higgins

Due date of Deliverable: **30/04/2021**
Submission date of Deliverable Report: **30/04/2021**

Writer	Reviewed by Domain Coordinator	Approved by Coordinator
Scientific Contact Colin Boxall	**DM Coord. Name** David Graham	**S. BOURG**

Dissemination Level		
PU	Public	
RE	Restricted to a group specified by the partners of the ACSEPT	
CO	Confidential, only for partners of the ACSEPT project	**X**

This project has received funding from the EURATOM research and training programme 2014-2018 under grant agreement No 755171. The content of this deliverable reflects only the author's view. The European Commission is not responsible for any use that may be made of the information it contains.

CONTENTS

This project has received funding from the EURATOM research and training programme 2014-2018 under grant agreement No 755171. The content of this deliverable reflects only the author's view. The European Commission is not responsible for any use that may be made of the information it contains.

INTRODUCTION TO DELIVERABLE D9.6

ASSESSMENT OF THE CORROSION VULNERABILITY OF COMMON PLANT MATERIALS IN THE PRESENCE OF KEY PROCESS STREAMS

The aim of this preamble is to provide some preliminary information about the five experimental programs reported on in this deliverable.

This report represents the first comprehensive collation of the work delivered by ULANC on the corrosion vulnerability of common plant materials in the presence of key process streams in the European Grouped ActiNide EXtraction (EURO-GANEX) process. The work was begun during the previous SACSESS program (funded by the Lloyd's Register Foundation as matching support to SACSESS's EURATOM funding) and continued throughout the current GENIORS program (Deliverable 9.6, funded by the GENIORS core grant from EURATOM).

A simplistic overview of the EURO-GANEX flowsheet is shown in Figure 1:

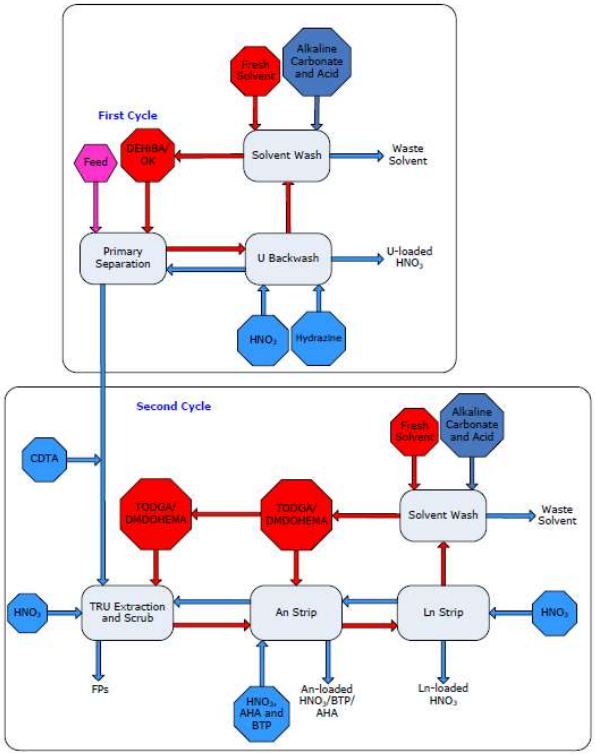

Figure 1: Block flow diagram of the EURO-GANEX flowsheet [1].

The EURO-GANEX flowsheet is a two cycle process that does not extract pure plutonium but rather a mix of Pu, Am, and Np, providing a non-proliferation advantage over the traditional UK PUREX process [2-5].

This project has received funding from the EURATOM research and training programme 2014-2018 under grant agreement No 755171. The content of this deliverable reflects only the author's view. The European Commission is not responsible for any use that may be made of the information it contains.

In the EURO-GANEX first cycle extraction Di(2-ethyl hexyl) isobutyramide (DEHiBA) and odourless kerosene (OK) are used to selectively extract uranium, technetium and neptunium, the latter two species subsequently scrubbed back into the aqueous phase using hydrazine, leaving a pure uranium product in the OK/DEHiBA organic phase.

The aqueous phase then passes to the second cycle, where *trans*-1,2-diaminocyclohexane-*N*,*N*,*N'*,*N'*-tetraacetic acid (CDTA) is initially added to prevent extraction of fission products (in particular Zr and Pd), before contact with *N*,*N*,*N'*,*N'*-tetraoctyldiglycolamide (TODGA) and *N*,*N'*-dimethyl-*N*,*N'*-dioctylhexylethoxymalonamide (DMDOHEMA) in an OK organic phase. DMDOHEMA selectively extracts Pu(IV) and Np(IV) from the aqueous phase while TODGA extracts remaining An(III) and Ln(III) ions in their entirety.

This loaded An(III/IV)/Ln(III) organic stream is then fed to the TRU back-extraction stage, where the loaded organic stream is contacted with an acteohydroxamic acid (AHA) aqueous phase supplemented by a hydrophilic, aqueous phase, actinide (III) selective stripping ligand. The result is extraction of Pu(IV) and Np(IV) by AHA and An(III) ions by the An(III) extraction ligand into the aqueous phase, producing a proliferation resistant grouped actinide product while Ln(III) species remain complexed with TODGA in the organic phase. In the EURO-GANEX process 2,6-bis(5,6-di(sulfophenyl)-1,2,4-triazin-3-yl)-pyridine (SO_3-Ph-BTP) has been tested as a suitable An(III) extraction agent and been shown to have good selectivity, kinetics and solubility for actinide (III) extraction [6-8]. However, due to the degradation of BTP ligands under radiolysis [7;9], radiologically stable sulfonated bistriazinylbipyridine (SO_3-Ph-BTBP) [6] and 1,10-phenanthroline ligands (SO_3-Ph-BTPhen) [10-12] are also currently under investigation by other project partners as possible replacements for SO_3-Ph-BTP.

Within the SACSESS program ULANC, using funding from the Lloyd's Register Foundation (LRF) identified potential corrosion vulnerabilities in this latter TRU back-extraction step, in particular that AHA and SO_3-Ph-BTP may act as corrosion accelerators under oxidative maloperation conditions on common plant process stainless steels [13,14]. In response, a description of these potential consequences were highlighted in the final SACSESS report (summary of WP1.1 [15]) and it was recommended that for each of the possible inventory permutations detailed in Table 1 and Table 2 (normal operations and mal-operations), the behaviour in storage tanks be studied with regards to any safety-critical potential corrosion reactions that could occur. Green boxes indicate those species/tank combinations that are foreseen to occur, whilst red boxes indicate those that are combinations that are foreseen as being highly unlikely .

This project has received funding from the EURATOM research and training programme 2014-2018 under grant agreement No 755171. The content of this deliverable reflects only the author's view. The European Commission is not responsible for any use that may be made of the information it contains.

Table 1: EURO-GANEX – Inventory combinations during normal operations.

(a)

		Species						
		U	*FP*	*An*	*Ln*	*DEHiBA*	*DEHiBA Degradation Products*	*HNO_3*
Tank	*U Product*	✓	×	×	×	×	×	✓
	CDTA Mixing	×	✓	✓	✓	×	×	✓
	FP	×	✓	×	×	×	×	✓
	An/Ln Buffer	×	×	✓	✓	×	×	×
	Ln Product	×	×	×	✓	×	×	✓
	An Product	×	×	✓	×	×	×	×

(b)

		Species				
		Hydrazine/ Hydrazoic Acid	*CDTA*	*DMODOHEMA/ TODGA*	*DMODOHEMA/TODGA Degradation Products*	*HNO_3/ AHA/BTP*
Tank	*U Product*	×	×	×	×	×
	CDTA Mixing	✓	✓	×	×	×
	FP	✓	✓	×	×	×
	An/Ln Buffer	×	×	✓	✓	×
	Ln Product	×	×	×	×	×
	An Product	×	×	×	×	✓

Table 2: EURO-GANEX – Inventory combinations during maloperation.

(a)

		Species						
		U	*FP*	*An*	*Ln*	*DEHiBA*	*DEHiBA Degradation Products*	*HNO_3*
Tank	*U Product*	✓	✓	✓	✓	✓	✓	✓
	CDTA Mixing	✓	✓	✓	✓	✓	✓	✓
	FP	✓	✓	✓	✓	✓	✓	✓
	An/Ln Buffer	✓	✓	✓	✓	✓	✓	✓
	Ln Product	✓	✓	✓	✓	✓	✓	✓
	An Product	✓	✓	✓	✓	✓	✓	✓

(b)

		Species				
		Hydrazine/ Hydrazoic Acid	*CDTA*	*DMODOHEMA/ TODGA*	*DMODOHEMA/TODGA Degradation Products*	*HNO_3/ AHA/BTP*
Tank	*U Product*	✓	×	×	×	×
	CDTA Mixing	✓	✓	✓	✓	×
	FP	✓	✓	✓	✓	×
	*An/Ln Buffer**	✓	✓	✓	✓	✓
	Ln Product	✓	✓	✓	✓	✓
	An Product	✓	✓	✓	✓	✓

Consequently, within the GENIORS program ULANC has had two primary objectives:

1) To perform corrosion assessments for process plant steels in the presence of as many of the GANEX inventory permutations as resource permits.
2) To carry out long term corrosion studies in relevant inventory permutations of high risk.

This deliverable report describes four programmes of experimental work that

This project has received funding from the EURATOM research and training programme 2014-2018 under grant agreement No 755171. The content of this deliverable reflects only the author's view. The European Commission is not responsible for any use that may be made of the information it contains.

predominantly detail work carried out with regards to objective 1), specifically corrosion assessments of the following key compounds:

1. The organic phase extraction ligands TODGA, DEHiBA and TBP;
2. The aqueous phase extraction ligands AHA, SO_3-Ph-BTP, SO_3-Ph-BTBP, and SO_3-Ph-BTPhen;
3. The reductant hydrazine; and
4. The fission product masking/hold-back ligand, CDTA.

Compounds are tested in both aqueous and organic conditions and at concentrations / conditions found under both normal and maloperation conditions. Measurements are made using a range of classical electrochemical and corrosion measurement / characterisation techniques.

This report also describes work conducted during a fifth experimental programme addressing objective 2), specifically long-term corrosion studies carried out within a gamma field. Preliminary results and their analysis are presented.

All work was conducted at ULANC in the UTGARD (Uranium / Thorium beta-Gamma Active R&D) Laboratory. UTGARD Lab is a UK Government-funded facility established for the study of spent nuclear fuel recycle and waste management as part of the EPSRC (Engineering and Physical Sciences Research Council) supported NNUF (National Nuclear Users Facility) initiative.

REFERENCES

[1] Process Description of the EURO-GANEX Process, NNL 13172, R3.1.1, 05/06/2014
[2] R. Taylor, M. Carrott, H. Galan, A. Geist, X. Hères, C. Maher, C. Mason, R. Malmbeck, M. Miguirditchian, G. Modolo, C. Rhodes, M. Sarsfield, and A. Wilden, The EURO-GANEX process: Current status of flowsheet development and process safety studies, Proc. Chem., 21 (2016) 524-529.
[3] C.G. Bathke, B.B. Ebbinghaus, B.A. Collins, B.W. Sleaford, K.R. Hase, M. Robel, R.K. Wallace, K.S. Bradley, J.R. Ireland, G.D. Jarvinen, M.W. Johnson, A.W. Prichard, and B.W. Smith, The attractiveness of materials in advanced nuclear fuel cycles for various proliferation and theft scenarios, Nucl. Technol., 179 (2012) 5-30.
[4] K. Bell, C. Carpentier, M.J. Carrott, A. Geist, C. Gregson, X. Heres, D. Magnusson, R. Malmbeck, F. McLachlan, G. Modolo, U. Mullich, M. Sypula, R.J. Taylor, and A. Wilden, Progress towards the development of a new GANEX process, Proc. Chem., 7 (2012) 392-397
[5] M.J. Carrott, K. Bell, J. Brown, A. Geist, C. Gregson, X. Heres, C. Maher, R. Malmbeck, C. Mason, G. Modolo, U. Mullich, M. Sarsfield, A. Wilden, and R.J. Taylor, Development of a new flowsheet for co-separating the transuranic actinides: The "EURO-GANEX" process, Solvent Extr.

This project has received funding from the EURATOM research and training programme 2014-2018 under grant agreement No 755171. The content of this deliverable reflects only the author's view. The European Commission is not responsible for any use that may be made of the information it contains.

Ion Exch., 32 (2014) 447-467.
[6] A. Geist, U. Mullich, G. Modolo, and A. Wilden, Selective aqueous complexation of actinides with hydrophilic BTP and BTBP: Towards improved i-SANEX processes, Organisation for Economic Co-operation and Development - Nuclear Energy Agency, San Francisco, USA, 2012, pp. 1-9.
[7] P.J. Panak and A. Geist, Complexation and Extraction of Trivalent Actinides and Lanthanides by Triazinylpyridine N-Donor Ligands, Chem. Rev., 113 (2013) 1199-1236.
[8] A. Geist, U. Mullich, D. Magnusson, P. Kaden, G. Modolo, A. Wilden, and T. Zevaco, Actinide(III)/Lanthanide(III) Separation Via Selective Aqueous Complexation of Actinides(III) using a Hydrophilic 2,6-Bis(1,2,4-Triazin-3-Yl)-Pyridine in Nitric Acid, Solvent Extr. Ion Exch., 30 (2012) 433-444.
[9] M.J. Hudson, C.E. Boucher, D. Braekers, J.F. Desreux, M.G.B. Drew, M.R.S. Foreman, L.M. Harwood, C. Hill, C. Madic, F. Marken, and T.G.A. Youngs, New bis(triazinyl) pyridines for selective extraction of americium(III), New J. Chem., 30 (2006) 1171-1183.
[10] F.W. Lewis, L.M. Harwood, M.J. Hudson, M.G.B. Drew, A. Wilden, M. Sypula, G. Modolo, T. Vu, J. Simonin, G. Vidick, N. Bouslimani, and J.F. Desreux, From BTBPs to BTPhens: The effect of ligand pre-organisation on the extraction properties of quadridentate bis-triazine ligands, Proc. Chem., 7 (2012) 231-238.
[11] F.W. Lewis, L.M. Harwood, M.J. Hudson, M.G.B. Drew, V. Hubscher-Bruder, V. Videva, F. Arnaud-Neu, K. Stamberg, and S. Vyas, BTBPs versus BTPhens: Some reasons for their differences in properties concerning the partitioning of minor actinides and the advantages of BTPhens, Inorg. Chem., 52 (2013) 4993-5005.
[12] G. Benay, R. Schurhammer, and G. Wipff, Basicity, complexation ability and interfacial behavior of BTBPs: a simulation study, Phys. Chem. Chem. Phys., 13 (2011) 2922-2934.
[13] R.J. Wilbraham, C. Boxall, Electrochemistry Communications, 62 (2016), pp52-55.
[14] C. Boxall, R. Wilbraham, SACSESS 6th Half Yearly Beneficiary Activity Report (2016).
[15] S. Bourg, P. Guilbaud, E. Mendes, C. Ekberg, M. Gibilaro, P. Soucek, G. Modolo, A. Geist, E. Boo, B. Duplantier, C. Rhodes, R. Taylor, M. Harrison, L. Flint, K. Bell, C. Sharrad, B. Hanson, Final Report Summary - SACSESS (Safety of ACtinide Separation proceSSes), CEA, (2016) 1-35.

This project has received funding from the EURATOM research and training programme 2014-2018 under grant agreement No 755171. The content of this deliverable reflects only the author's view. The European Commission is not responsible for any use that may be made of the information it contains.

STUDY OF PROCESS STEEL CORROSION IN THE PRESENCE OF THE NON-AQUEOUS PHASE EXTRACTION LIGANDS TODGA, TBP AND DEHiBA

1. INTRODUCTION

In the EURO-GANEX first cycle extraction Di(2-ethyl hexyl) isobutyramide (DEHiBA), Figure 1, and odourless kerosene (OK) are used to selectively extract uranium, technetium and neptunium, the latter two species subsequently scrubbed back into the aqueous phase using hydrazine, leaving a pure uranium product in the OK/DEHiBA organic phase.

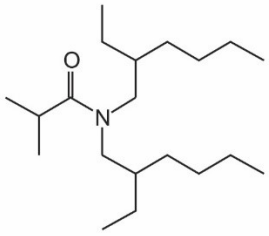

Figure 1: Chemical Structure of DEHiBA

The aqueous phase then passes to the second cycle, where *trans*-1,2-diaminocyclohexane-*N*,*N*,*N'*,*N'*-tetraacetic acid (CDTA) is initially added to prevent extraction of fission products (in particular Zr and Pd), before contact with *N*,*N*,*N'*,*N'*-tetraoctyldiglycolamide (TODGA), Figure 2, and *N*,*N'*-dimethyl-*N*,*N'*-dioctylhexylethoxymalonamide (DMDOHEMA) in an OK organic phase. DMDOHEMA selectively extracts Pu(IV) and Np(IV) from the aqueous phase while TODGA extracts remaining An(III) and Ln(III) ions in their entirety.

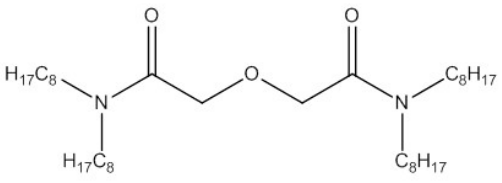

Figure 2: Chemical Structure of TODGA.

Thus, both ligands are critical to the functionality of both the 1st and 2nd extraction cycles.

This project has received funding from the EURATOM research and training programme 2014-2018 under grant agreement No 755171. The content of this deliverable reflects only the author's view. The European Commission is not responsible for any use that may be made of the information it contains.

Importantly, neither material has hitherto been studied with regards to their corrosion behaviour. However, previous studies of simpler malonic acids with shorter hydrocarbon side chains to TODGA, suggest that complexation and dissolution of iron precipitates could be possible under process conditions [1], processes that may have implications for the corrosion resistance of ferritic materials such as used in process steels. Consequently, this section presents the results of studies of the effect of DEHiBA and TODGA on the corrosion behaviour of common process steels, the first time these ligands have been studied in this context.

Additionally, whilst not utilized within the EURO-GANEX flowsheet, studies are also described with regards to the corrosion behaviour of tributyl phosphate (TBP), Figure 3.

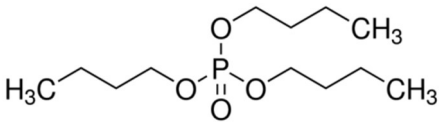

Figure 3: Chemical Structure of TBP.

Such a material is heavily used in the current UK PUREX flowsheet for the extraction of Pu and U from the heavier actinides and is also utilized in combination with TODGA in the *i*-SANEX solvent phase and thus may be of general interest to the GENIORS consortium.

This project has received funding from the EURATOM research and training programme 2014-2018 under grant agreement No 755171. The content of this deliverable reflects only the author's view. The European Commission is not responsible for any use that may be made of the information it contains.

2. EXPERIMENTAL

All electrochemical experiments have been conducted in a small volume electrochemical cell (200 µl) in order to allow high ligand concentrations to be achieved with the synthesized TODGA (Technocomm Ltd., Scotland, UK). Working electrodes were constructed using 1 mm diameter SS316L and SS304L wire (both commonly used process steels) or 250 µm Au wire in glass Pasteur pipettes, backfilled with epoxy resin and polished using decreasing SiC paper grades and 6, 3 and 1 µm diamond polishing pastes. To complete the three electrode cell, a $Ag/AgNO_3$ tetrafluoroborate (TFB)/Octanol reference electrode (see below) and coiled platinum wire counter electrode were inserted via simple PTFE manifold. An image of the completed cell is shown in Figure 4:

Figure 4: Low volume electrochemical cell.

Linear sweep voltammetry (LSV) was used as the predominant experimental technique to assess *in situ* corrosion behaviour.

Initially both odorless kerosene and dodecane were used as the solvent medium. However, due to their extreme non-polarity both long chain alkanes would not allow traditional non-aqueous electrolytes (ammonium tetrafluoroborate or perchlorate) to dissolve in them.

While also highly non-polar, and therefore suffering from similar electrolyte solubility issues, 1-octanol, while usually substituted for 1,2-dichloroethane in electrochemistry experiments [2], does contain a slightly polar OH group. Through vigorous ultrasonic mixing we were able to dissolve up to 50 mmol dm^{-3} tetrafluoroborate electrolyte, which in conjunction with the use of working electrodes < 1mm in diameter is sufficient to allow electrochemical experiments to be performed with limited polarisation resistance using either a Ag/AgCl aqueous reference electrode or more accurate $Ag/AgNO_3$ Octanol/TFB reference electrode, Figure 5.

This project has received funding from the EURATOM research and training programme 2014-2018 under grant agreement No 755171. The content of this deliverable reflects only the author's view. The European Commission is not responsible for any use that may be made of the information it contains.

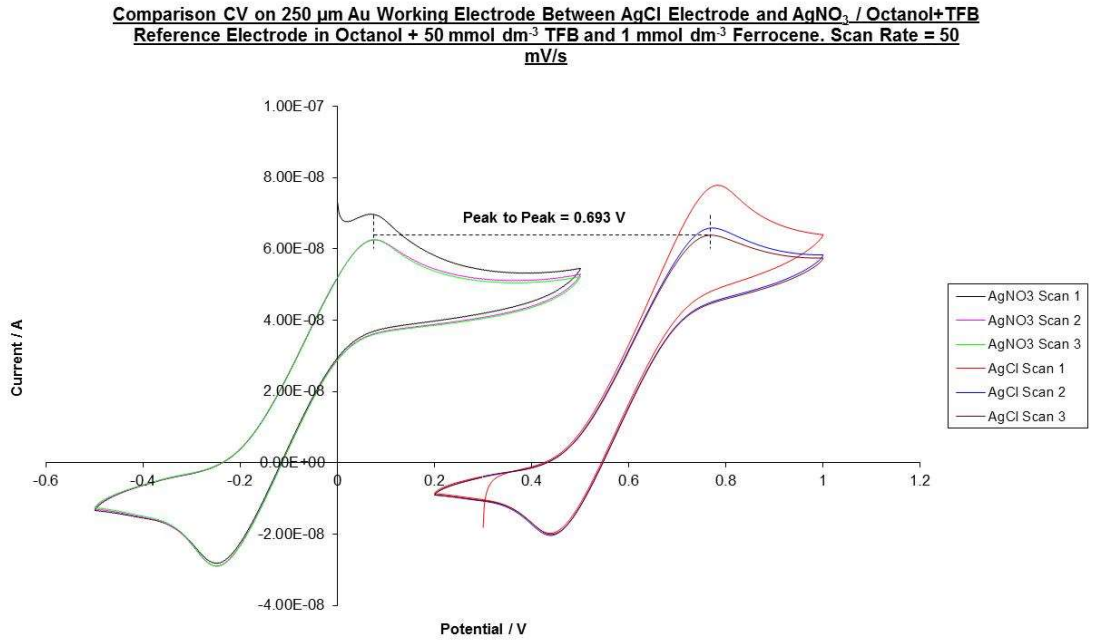

Figure 5: Cyclic Voltammograms (CV) of a 250 µm Au working electrode in 1 mmol dm^{-3} ferrocene in octanol with 50 mmol dm^{-3} TFB electrolyte. Plots are vs. either a Ag/AgCl reference electrode or a Ag/$AgNO_3$ octanol/TFB reference electrode. Scan rate = 50 mV/s.

The latter Ag/$AgNO_3$ Octanol/TFB reference electrode was constructed as follows:

A 250 µm Ag wire was polished with 600 grit SiC paper and then cleaned with deionised water and acetone. A fill solution of 50 mmol dm^{-3} TFB in 1-octanol was then created through sonication in an ultrasonic bath for ~ 20 minutes. To this was added 10 mmol dm^{-3} $AgNO_3$ and the solution further sonicated for 15 mins (N.B. only a small portion of the $AgNO_3$ actually dissolves in octanol). ~150 µl of this solution was then pipetted into a glass, Vycor® fritted tube. The Ag wire was then left in 20% wt. HNO_3 for one minute to allow a thin layer of $AgNO_3$ to form and dried gently on a tissue before being inserted into the tube and the whole assembly capped. Typically with regular 5 minute sonication periods between experiments this electrode was suitable for up to one days use while stored in the dark in 50 mmol dm^{-3} TFB in octanol. After a day or cease in sonication the electrolyte and $AgNO_3$ tended to precipitate in the electrode frit, requiring cleaning and re-assembly using the above method.

Importantly, the recent work of Dilasari *et al.* suggests that TFB should not affect the corrosion behaviour of process steels in octanol [3] and therefore corrosion results presented here can be said to be unaffected by the presence of the electrolyte.

In order to explore the electrochemical/corrosion behaviour of non-specific An/Ln extractants, TBP and TODGA were used at concentrations in line with *i*-SANEX/1c-SANEX processes (up to 0.5 mol dm^{-3} TBP and up to 0.5 mol dm^{-3} TODGA) in the above

This project has received funding from the EURATOM research and training programme 2014-2018 under grant agreement No 755171. The content of this deliverable reflects only the author's view. The European Commission is not responsible for any use that may be made of the information it contains.

octanol organic phase

DEHiBA it is present as 0.1 mol dm^{-3} DEHiBA in odourless kerosene in contact with 5 mol dm^{-3} HNO_3 aqueous phase in the 1st cycle uranium extraction step. Thus, DEHiBA was explored at concentrations up to 1 mol dm^{-3} (assumed upper maloperation concentration) in octanol as the organic phase.

Studies were also performed in the aqueous phase via contact with a DEHiBA loaded organic phase. In these studies Exxsol D80 was used as the organic phase, with and without 0.1 mol dm^{-3} DEHiBA. 750 µl was contacted with 750 µl of a 5 mol dm^{-3} HNO_3 aqueous phase by shaking for 1 minute, before mixing using a thermomixer (Eppendorf, thermomixer C) for 15 minutes. The mixed phases were then microfuged at 3000 rpm for 1 minute and the aqueous phase was gently micropipetted to a separate tube for corrosion testing using steel wire electrodes as detailed above.

3. RESULTS

3.1. STUDIES OF THE CORROSION BEHAVIOUR OF TODGA IN NON-AQUEOUS SOLVENTS

Linear Sweep Voltammetry (LSV) experiments were initially performed using a 250 µm Au disk electrode in order to understand the background electrochemical behaviour of both octanol and TODGA. Accordingly, voltammograms and polarization curve results for Au electrodes with TODGA concentrations up to 0.5 mol dm^{-3} are shown in Figure 6.

Considering first the LSV of Figure 6, the solvent window for octanol appears to be from ~-0.6 V to +0.5 V vs. the Ag/AgNO3 TFB/Octanol reference. Within the window of octanol stability there is no observed electrochemical oxidation or reduction of TODGA at all concentrations tested. At potentials anodic of +0.5 V, within the window of solvent oxidation/breakdown, while the current varies greatly between TODGA concentrations there is no correlation between TODGA concentration and the observed current increases, suggesting current variations are more to do with solvent breakdown than any TODGA oxidation behaviour. Turning to the polarization plot of Figure 6, it can be seen that again while there are small variations between conditions there is little change in either E_{corr} or i_{corr} with increasing TODGA concentration. A second LSV scan (not shown) was also run directly after the first scan shown in Figure 6 in order to see what effect the products of solvent breakdown may have on further electrochemical scans. However, with the exception of a slight positive shift in E_{corr} (~80 mV) no significant differences to the initial scans of Figure 6 were observed.

This project has received funding from the EURATOM research and training programme 2014-2018 under grant agreement No 755171. The content of this deliverable reflects only the author's view. The European Commission is not responsible for any use that may be made of the information it contains.

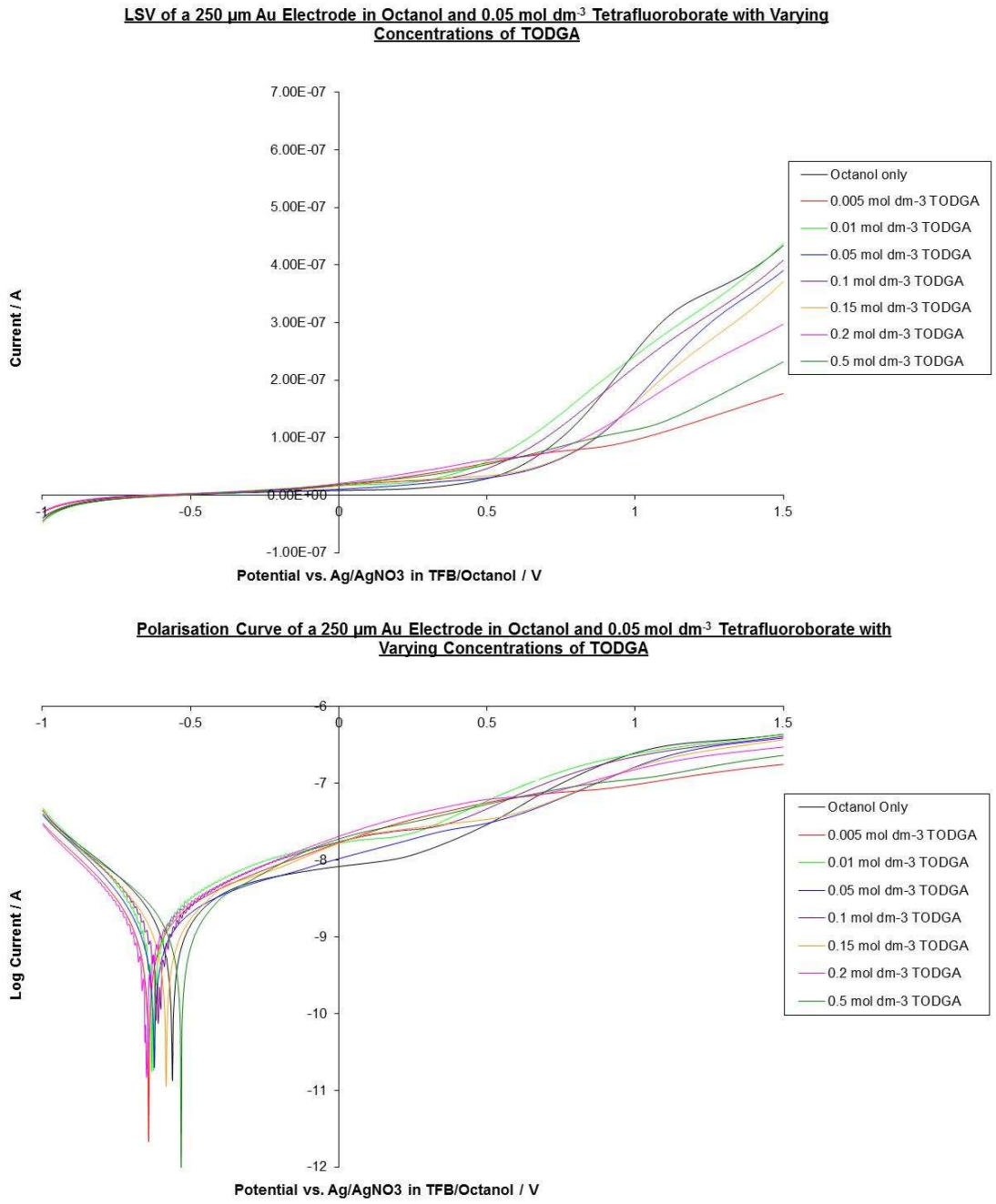

Figure 6: Linear sweep voltammograms (top) and polarisation curves (bottom) for Au microelectrodes in 1-octanol with increasing concentrations of TODGA. Scan speed = 10 mV/s.

Voltammograms and polarization curves for electrodes made from the common process steel, SS304L, in octanol with TODGA concentrations up to 0.5 mol dm^{-3} are shown in Figure 7.

This project has received funding from the EURATOM research and training programme 2014-2018 under grant agreement No 755171. The content of this deliverable reflects only the author's view. The European Commission is not responsible for any use that may be made of the information it contains.

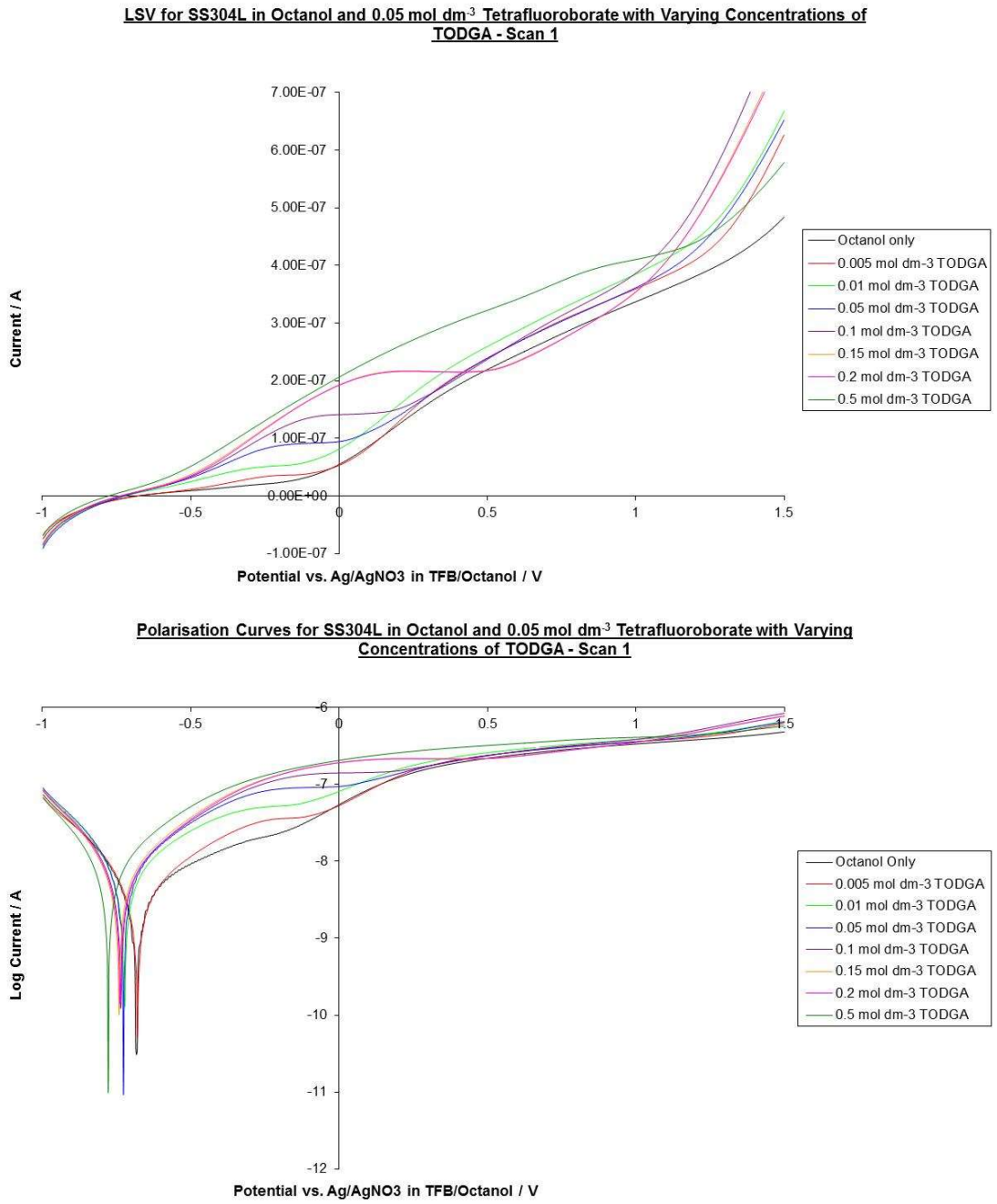

Figure 7: Linear sweep voltammograms (top) and polarisation curves (bottom) for SS304L electrodes in 1-octanol with increasing concentrations of TODGA. Scan speed = 10 mV/s.

In the first instance, it can be seen from Figure 7 that **in the absence of TODGA** the voltammogram recorded on SS304L is quite different to that recorded on Au microelectrodes, Figure 6. To aid the reader, a direct comparison between the two electrode voltammograms is shown in Figure 8.

This project has received funding from the EURATOM research and training programme 2014-2018 under grant agreement No 755171. The content of this deliverable reflects only the author's view. The European Commission is not responsible for any use that may be made of the information it contains.

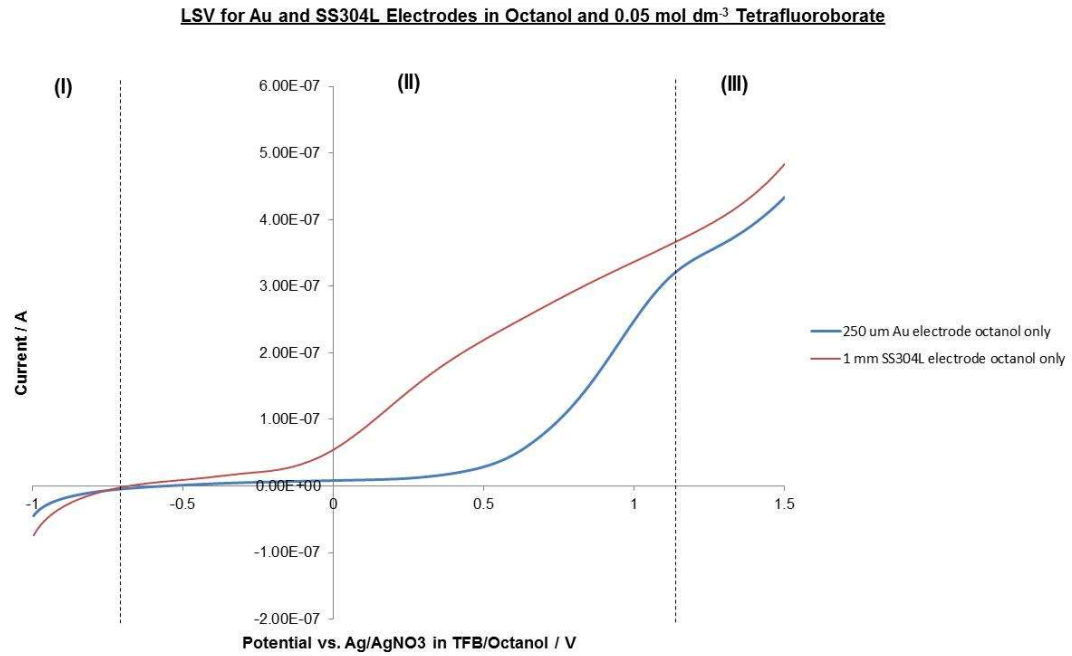

Figure 8: Linear sweep voltammograms of a 1mm SS304L electrode and 250 µm Au electrode in 1-octanol. Scan speed = 10 mV/s.

The LSV of each electrode can be split in to 3 common regions: (I) Solvent reduction, (II) solvent stability/oxidation and (III) secondary oxidation, all indicated on Figure 8. In region (I) it can be seen that the reduction current of the solvent at SS304L electrodes is slightly greater than that recorded on Au electrodes. As the change in current is small, this is most likely due to the difference in size between the two electrodes, 1 mm diameter SS304L vs. 250 µm diameter Au, allowing increased reduction of octanol and greater observed currents. Region (II) contains both the window of solvent stability and primary oxidation of the solvent. Considering the former first, it can be seen that the larger size of the SS304L electrode, while increasing the observed current in region (I), also results in an increase in polarization resistance, resulting in the slight increase in current in the region of solvent stability. Turning now to the latter region of solvent oxidation, it can be seen that despite the extra resistance at the larger electrode, onset of solvent oxidation on SS304L occurs at a potential almost 600 mV more negative than that measured on a Au electrode. Such a large shift in the onset of oxidation would suggest that on SS304L electrodes at potentials < 0.5 V the current, instead of being derived from solvent oxidation, is actually associated with oxidation of the electrode, specifically the steel passive oxide layer.

Thus, in order to test whether oxidation of the steel passive layer is responsible for the current increase observed at -0.2 V in Figure 8, a second scan of the SS304L electrode was carried out straight after the scan shown in Figures 7 and 8 in order to evaluate the surface after the oxide layer had been potentially oxidized/damaged as suggested above. The results of this scan overlaid onto Figure 8 are shown in Figure 9.

This project has received funding from the EURATOM research and training programme 2014-2018 under grant agreement No 755171. The content of this deliverable reflects only the author's view. The European Commission is not responsible for any use that may be made of the information it contains.

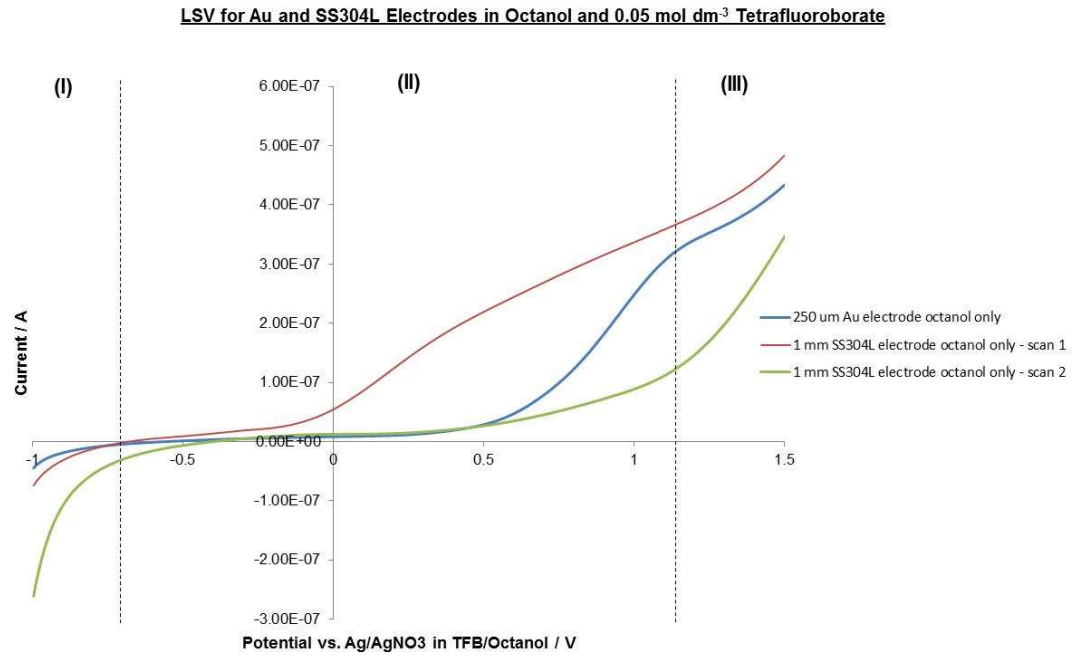

Figure 9: Linear sweep voltammograms of a 250 µm Au electrode scanned once and a 1mm SS304L electrode scanned twice in 1-octanol. Scan speed = 10 mV/s.

Figure 9 shows that scanning a second time has a drastic effect on the voltammogram of SS304L. First the oxidation peak at -0.2 V is gone and instead only a small oxidation peak at +0.5 V, in line with that observed on the Au microelectrode, is apparent. Therefore, as suggested above, it appears that the large oxidation current in the first scan of SS304L is associated with a passivating oxide layer that is stripped during this scan and thus not observed in the subsequent scan. This is further evidenced by an increase in the reduction current of region (I), presumably derived from either (1) reduction of the solution phase oxidation products Fe (III), Ni (II/III) and/or Cr (VI) generated in the first LSV scan or (2) from more effective reduction of the solvent at the steel surface now that the passivating oxide layer has been in part dissolved during the first scan.

Returning to Figure 7, the effect of increasing [TODGA] is an increasing oxidation current in the window of SS304L passivity (-0.7 V to 0V) with the current peak at ~-0.3 V. This suggests that TODGA is actively complexing with one or more components of the steel passive layer (Fe, Ni, Cr), driving its dissolution. Visibly such dissolution has little effect on the electrode surface – as might be expected as the TODGA is in effect electropolishing the surface through passive layer removal.

It is interesting to note that the measured open circuit potential (OCP) of SS304L before scanning in the experiments of Figure 7 is ~-0.68 V, with little variation in OCP with increasing TODGA concentration, putting the OCP on the edge of the TODGA derived

This project has received funding from the EURATOM research and training programme 2014-2018 under grant agreement No 755171. The content of this deliverable reflects only the author's view. The European Commission is not responsible for any use that may be made of the information it contains.

surface dissolution wave of the first scan. However, in the presence of potential oxidisers, such as HNO_3, Pu(IV) or Cr(VI), this potential could rise, pushing the OCP into a region of steel corrosion vulnerability.

Voltammograms and polarization curves for SS316L electrodes in octanol with TODGA concentrations up to 0.5 mol dm^{-3} are shown in Figure 10.

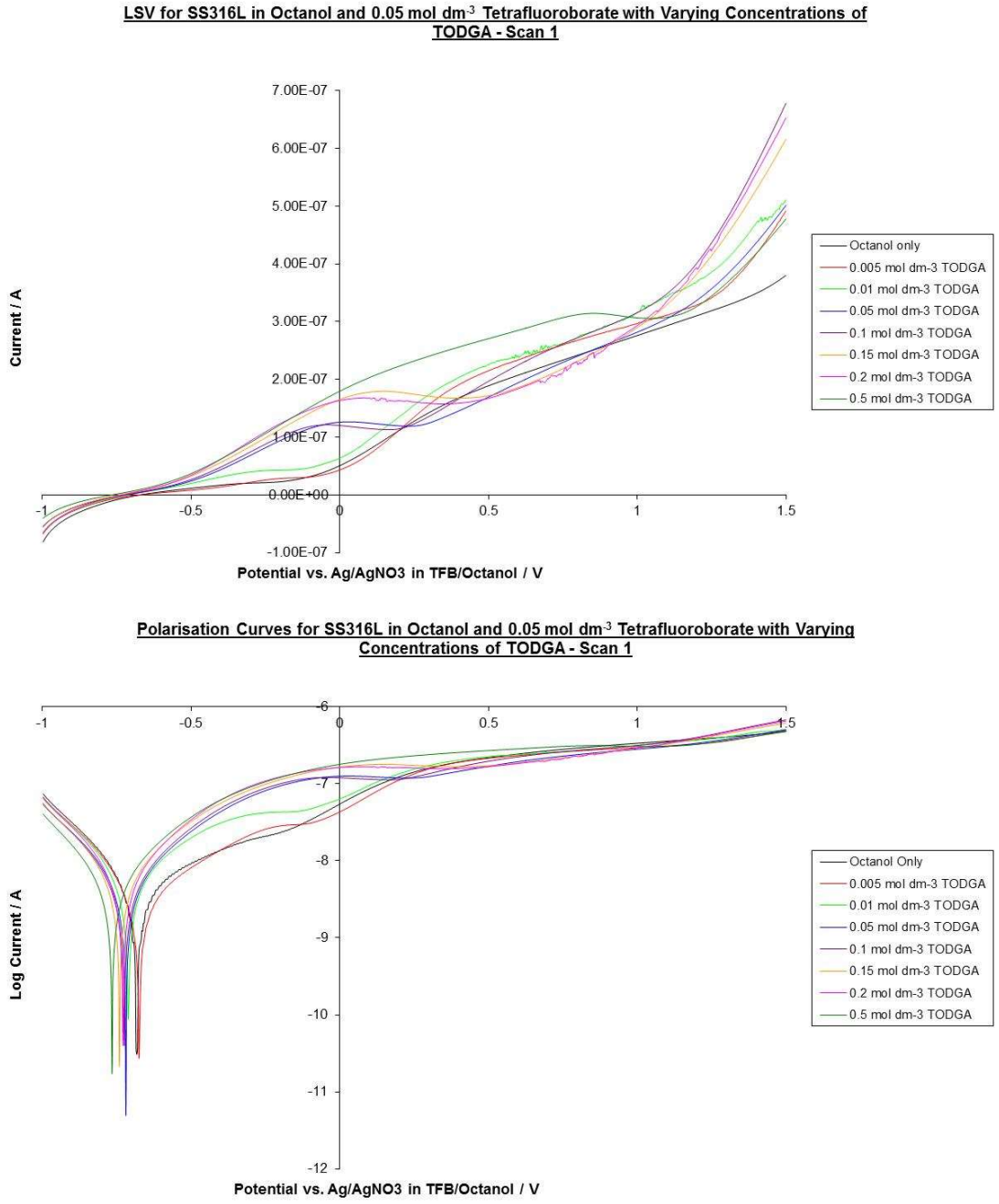

Figure 10: Linear sweep voltammograms (top) and polarisation curves (bottom) for SS304L electrodes in 1-octanol with increasing concentrations of TODGA. Scan speed = 10 mV/s.

This project has received funding from the EURATOM research and training programme 2014-2018 under grant agreement No 755171. The content of this deliverable reflects only the author's view. The European Commission is not responsible for any use that may be made of the information it contains.

From Figure 10 it can be seen that, unlike widely reported literature studies of transpassive corrosion under aqueous conditions, there is very little difference in current and electrode response between SS304L and SS316L. This suggests that the mechanism of steel dissolution by TODGA is not intergranular in nature, as found under aqueous transpassive dissolution conditions, as the silica content difference between the steels has little effect on corrosion current density [4,5].

Due to it being possessed of four octyl side chains, the concentration of TODGA in the aqueous phase is very low, of the order of 40 µmol dm^{-3}. Accordingly, no tests were conducted to determine the effect of TODGA on the corrosion behaviour of either stees in nitric acid after the nitric had been contacted with TODGA.

3.2. STUDIES OF THE CORROSION BEHAVIOUR OF DEHiBA IN NON-AQUEOUS SOLVENTS

Cyclic voltammograms for Au microelectrodes in octanol with DEHiBA concentrations up to 1 mol dm^{-3} are shown in Figure 11.

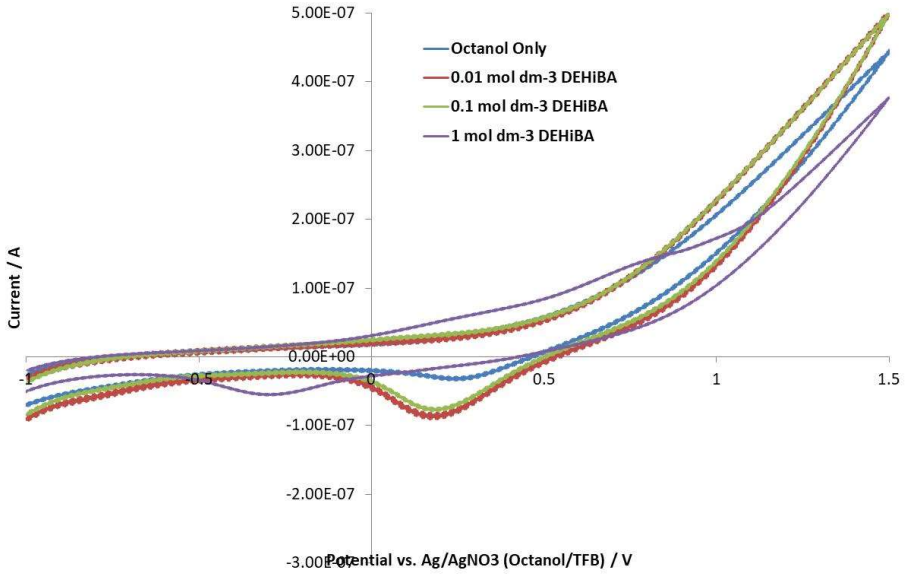

Figure 11: Cyclic voltammograms of a 250 µm Au Electrode in octanol with 0.03 mol dm^{-3} TFB electrolyte and increasing concentrations of DEHiBA. Scan speed = 50 mV/s.

Across all conditions in Figure 10 currents are low, being in the µA range. Considering the TFB loaded octanol electrolyte first, solvent breakdown appears to occur at > 0.5V vs. $Ag/AgNO_3$ reference electrode, with subsequent reduction of some of the oxidized products apparent in the observed reduction wave at ~0.2V. Up to 0.1 mol dm^{-3} DEHiBA voltammograms are almost identical to those in the absence of DEHiBA, suggesting DEHiBA has very little electrochemical effect on the voltammetry of gold. However, at a

This project has received funding from the EURATOM research and training programme 2014-2018 under grant agreement No 755171. The content of this deliverable reflects only the author's view. The European Commission is not responsible for any use that may be made of the information it contains.

possible maloperation concentration of 1 mol dm^{-3} DEHiBA, solvent breakdown currents are lowered at >0.5V and the reduction wave shifts to ~-0.25V, suggesting DEHiBA is in part buffering the solvent against breakdown.

Voltammograms and polarization curves for SS316L wire electrodes in octanol with DEHiBA concentrations up to 1 mol dm^{-3} are shown in Figure 12 and Figure 13.

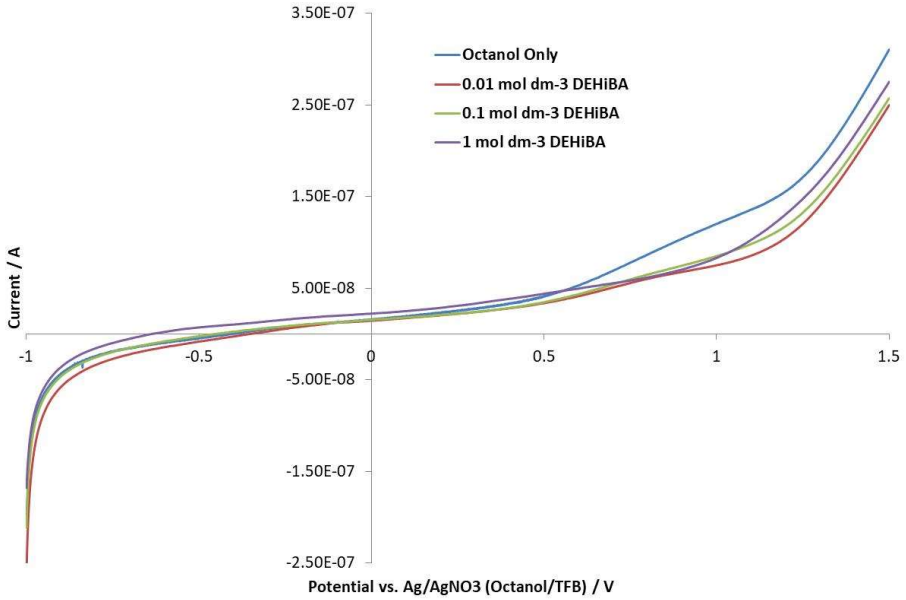

Figure 12: Linear sweep voltammogram of a 1 mm SS316L electrode in octanol with 0.03 mol dm^{-3} TFB electrolyte and increasing concentrations of DEHiBA. Scan speed = 1 mV/s.

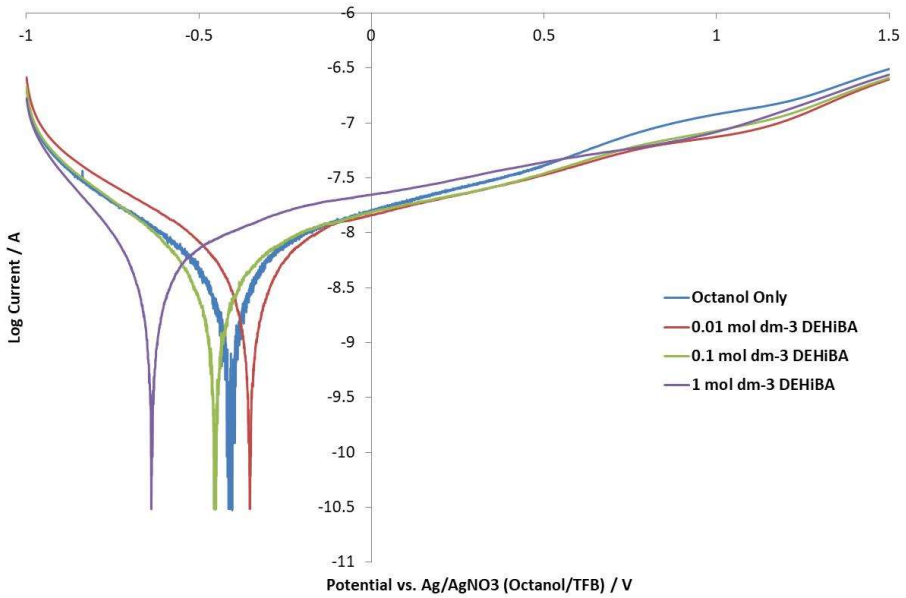

Figure 13: Tafel plot of a 1 mm SS316L electrode in octanol with 0.03 mol dm^{-3} TFB electrolyte and increasing concentrations of DEHiBA. Scan speed = 1 mV/s.

Again currents in Figure 12 and Figure 13 are low, suggesting that generally corrosion

This project has received funding from the EURATOM research and training programme 2014-2018 under grant agreement No 755171. The content of this deliverable reflects only the author's view. The European Commission is not responsible for any use that may be made of the information it contains.

under organic conditions is very low compared to that found in aqueous nitric acid solutions. Indeed no visible signs of corrosion were observed on the electrodes/in the electrolytes after scanning across all conditions tested.

Considering Figure 12 first, DEHiBA has little effect on the measured current vs. that measured in octanol alone at potentials < 0.5V (point of solvent breakdown). However, above 0.5V DEHiBA appears to reduce the measured currents, suggesting a stabilization effect of the octanol electrolyte towards solvent breakdown.

Turning now to the calculated Tafel plot (log(i) vs E) in Figure 13, addition of up to 1 mol dm^{-3} DEHiBA reveals that current measurements are indistinguishable from those observed in the absence of DEHiBA, suggesting neither a corrosion acceleration or corrosion inhibition of the SS316L steel occurs. In the presence of 1 mol dm^{-3} DEHiBA, there is a slight cathodic shift in E_{corr}, indicating a possible extension in the range of steel passivity, i.e. some corrosion surface inhibition effect at this concentration.

In order to determine if there is any significant difference between conditions, a linear polarisation resistance (LPR) corrosion rate calculation using the data of Figure 13 was carried out. Full details of this method and how the corrosion rate is derived may be found in the ASTM standards G59 – 97 and G102 - 89 [6,7]. Briefly, the corrosion current (i_{corr}) is calculated using the polarisation resistance (R_p) determined from a linear regression around the corrosion potential and measurement of anodic (b_a) and cathodic (b_c) transfer coefficients from the corresponding arms of the tafel plot. i_{corr}, the sample equivalent weight, surface area and density are then used to determine the corrosion rate, expressed in µm/yr or nm/yr.

The results of this analysis (not shown) reveal that corrosion rates across all conditions are very low, being 10's of nm a year and that no significant differences exist in the corrosion rate regardless of the presence absence of DEHiBA.

3.3. STUDIES OF THE CORROSION BEHAVIOUR OF DEHiBA IN AQUEOUS SOLVENTS

DEHiBA has a structure similar to that of TBP which is known to have a solubility as high as 0.5 mmol dm-3 in 5 mol dm^{-3}. Thus, in contrast to our work on TODGA, voltammograms and polarization curves for SS304L wire electrodes in 5 mol dm^{-3} HNO_3 contacted with either Exxsol D80 or Exxsol D80 with 0.1 mol dm^{-3} DEHiBA were recorded and are shown in Figure 14 and Figure 15. These reveal that while currents above 1V, the region of transpassive dissolution, are considerably greater in aqueous HNO_3 than those recorded in organic octanol solutions, very little change occurs in the

This project has received funding from the EURATOM research and training programme 2014-2018 under grant agreement No 755171. The content of this deliverable reflects only the author's view. The European Commission is not responsible for any use that may be made of the information it contains.

electrochemical corrosion behavior of SS304L in the presence of either Exxsol or Exxsol D80 and DEHiBA. In particular, figure 15 suggests that only one small difference is apparent between conditions. In the steel passive range between 0.65 and 0.9V it seems that contact with Exxsol D80, regardless of the presence of DEHiBA, slightly reduces the recorded current in this region.

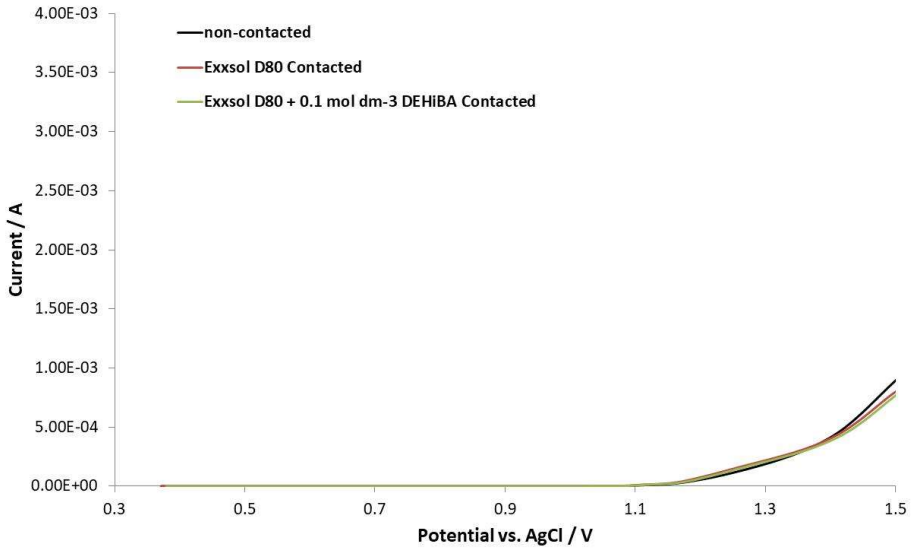

Figure 14: Linear sweep voltammogram of a 1 mm SS304L electrode in 5 mol dm^{-3} HNO_3 and contacted with either Exxsol D80 or Exxsol D80 and 0.1 mol dm^{-3} DEHiBA. Scan speed = 1 mV/s.

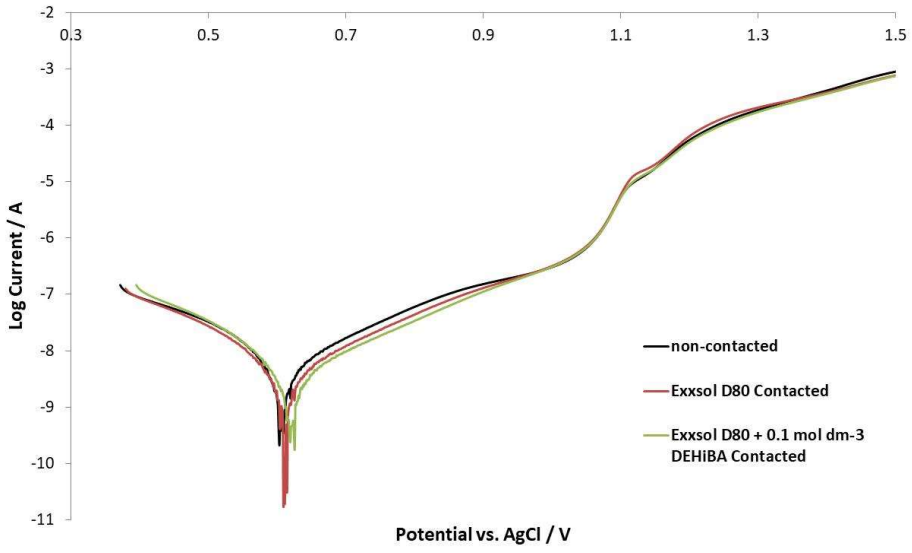

Figure 15: Tafel plot of a 1 mm SS304L electrode in 5 mol dm^{-3} HNO_3 and contacted with either Exxsol D80 or Exxsol D80 and 0.1 mol dm^{-3} DEHiBA. Scan speed = 1 mV/s.

This could indicate some inhibition of the slow Cr(III) to Cr(VI) oxidation that is known to occur in this region. However, as this occurs in both the presence and absence of DEHiBA we suspect it is most likely just due to a thin layer of Exxsol D80, or one of its

This project has received funding from the EURATOM research and training programme 2014-2018 under grant agreement No 755171. The content of this deliverable reflects only the author's view. The European Commission is not responsible for any use that may be made of the information it contains.

components, coating the steel surface, acting as a corrosion inhibitor by blocking aqueous phase access to steel itself. Carry over of some Exxsol D80, or one of its components, in the aqueous phase cannot be ruled out as the complete disentrainment of the organic phase from the aqueous phase after microfuging is difficult – as is the removal of the organic phase from over the aqueous phase by micropipetting.

Voltammograms and polarization curves for SS316L wire electrodes in 5 mol dm^{-3} HNO_3 contacted with either Exxsol D80 or Exxsol D80 with 0.1 mol dm^{-3} DEHiBA are shown in Figure 16 and Figure 17.

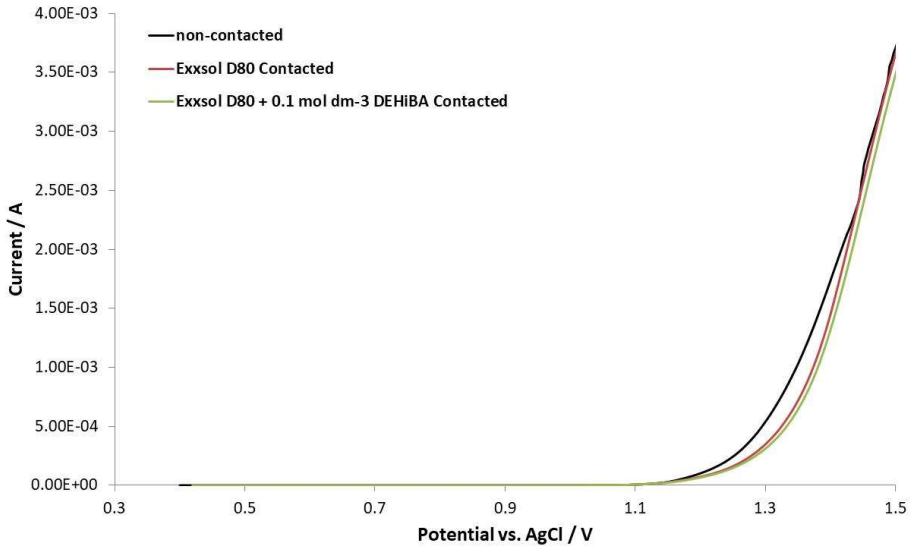

Figure 16: Linear sweep voltammogram of a 1 mm SS316L electrode in 5 mol dm^{-3} HNO_3 and contacted with either Exxsol D80 or Exxsol D80 and 0.1 mol dm^{-3} DEHiBA. Scan speed = 1 mV/s.

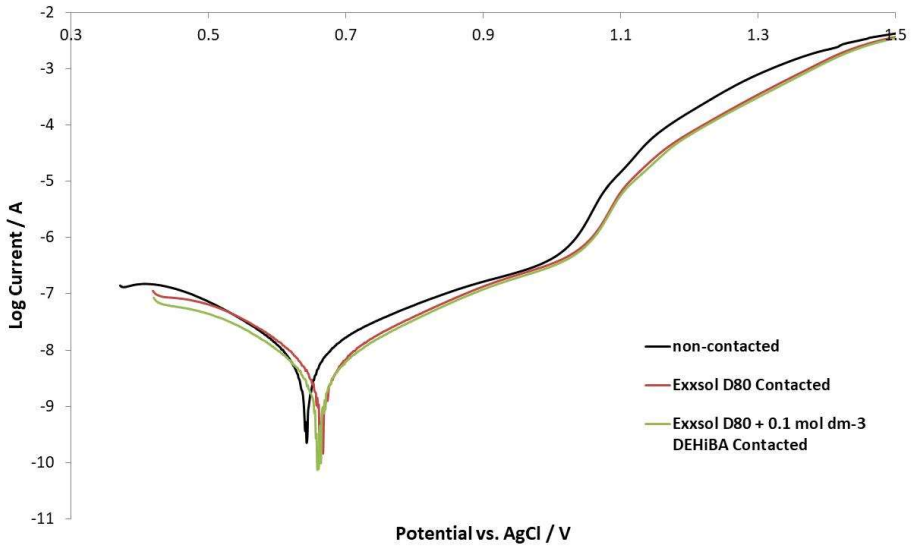

Figure 17: Tafel plot of a 1 mm SS316L electrode in 5 mol dm^{-3} HNO_3 and contacted with either Exxsol D80 or Exxsol D80 and 0.1 mol dm^{-3} DEHiBA. Scan speed = 1 mV/s.

This project has received funding from the EURATOM research and training programme 2014-2018 under grant agreement No 755171. The content of this deliverable reflects only the author's view. The European Commission is not responsible for any use that may be made of the information it contains.

Comparison between Figure 14 and Figure 16 reveals that a larger transpassive current at >1V is observed for SS316L wire compared to SS304L wire; as well, a visible discolouration of the electrolyte occurs after scanning, presumably due to some oxidative leaching of Cr and Fe from the SS316L steel wire. Such an observation is suggested to be due to the decreased silica content in SS316L which protects against intergranular corrosion in oxidative acidic environments [4,5].

Interestingly, contact with Exxsol D80, regardless of the presence of DEHiBA, again reduces the recorded current in the passive region. However, for the SS316L wire of Figures 16 and 17, the current reduction is more pronounced and extends also to the transpassive region at > 1V. Again we suspect this effect is most likely due to a thin layer of Exxsol D80, or one of its components, coating the steel surface, acting as a corrosion inhibitor by blocking aqueous phase access to steel itself.

3.4. STUDIES OF THE CORROSION BEHAVIOUR OF TBP IN NON-AQUEOUS SOLVENTS

Voltammograms and polarization curves for SS304L electrodes in octanol with TBP concentrations up to 0.5 mol dm^{-3} are shown in Figure 18.

It can be seen from Figure 18 that TBP has very little effect on the corrosion behaviour of SS304L in octanol. This is also the same for SS316L electrodes (not shown). This suggests that TBP does not readily complex with the main metal constituents of stainless steel (Fe, Ni, Cr). As such and as shown above, the primary corrosion species in an *i*-SANEX process is likely to be TODGA. In order to test this, concentrations of TODGA and TBP were added at 0.2 mol dm^{-3} and 0.5 mol dm^{-3} respectively in order to create a pseudo-*i*-SANEX solvent phase. Voltammograms and polarization curves of an SS304L electrode in this *i*-SANEX mixture are shown in Figure 19.

The addition of 0.5 mol dm^{-3} TBP to TODGA does appear to slightly increase the TODGA driven steel dissolution current at +0.3 V. This effect may be explained as follows; as the steel passive layer is breached through TODGA complexation of Fe/Ni/Cr, there is some leach of uncomplexed steel corrosion products which may become complexed with the excess of TBP in solution, further increasing the rate of TODGA derived steel dissolution. Thus, our earlier assumption that TBP does not complex with the main constituents of stainless steel may be an oversimplification and instead TBP, while not complexing with the base metal/oxide layer, can complex with corrosion product solution ions such as Fe(III) or Cr(III) in a similar mechanism to that described previously for the aqueous complexation of transpassively generated Fe(III) by AHA.

This project has received funding from the EURATOM research and training programme 2014-2018 under grant agreement No 755171. The content of this deliverable reflects only the author's view. The European Commission is not responsible for any use that may be made of the information it contains.

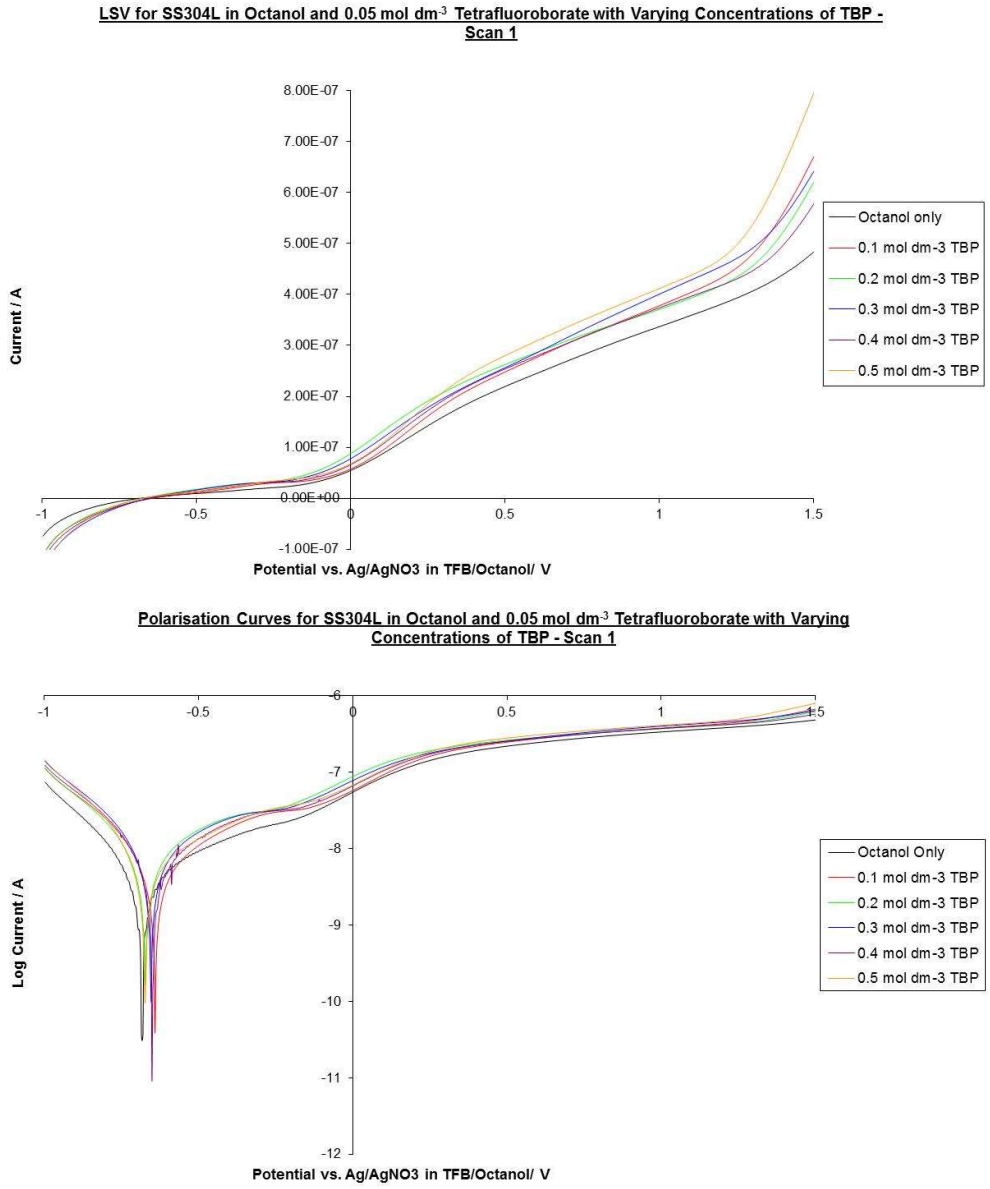

Figure 18: Linear sweep voltammograms (top) and polarisation curves (bottom) for SS304L electrodes in 1-octanol with increasing concentrations of TBP.

This project has received funding from the EURATOM research and training programme 2014-2018 under grant agreement No 755171. The content of this deliverable reflects only the author's view. The European Commission is not responsible for any use that may be made of the information it contains.

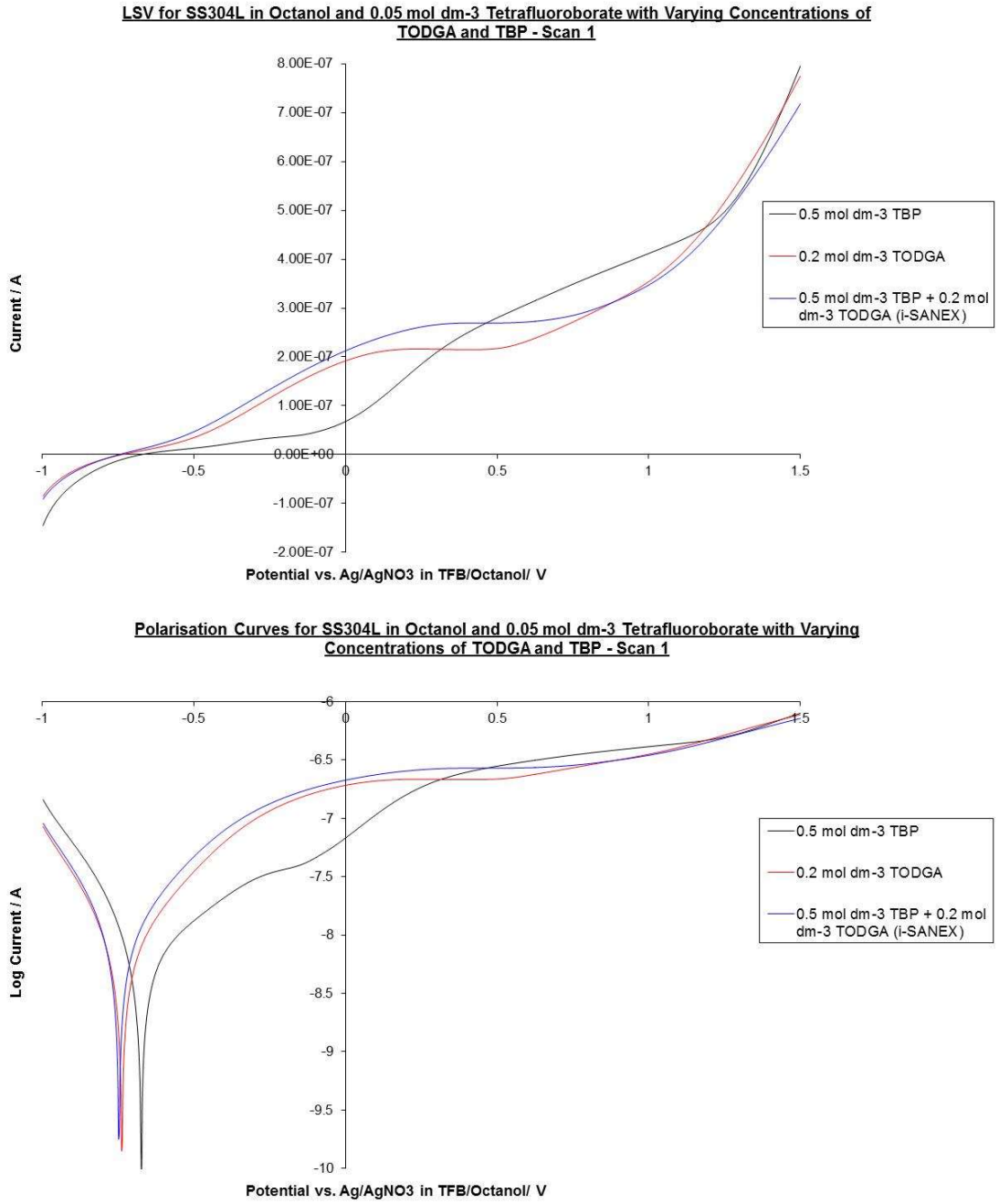

Figure 19: Linear sweep voltammograms (top) and polarisation curves (bottom) for SS304L electrodes in 1-octanol with either 0.5 mol dm^{-3} TBP alone, 0.2 mol dm^{-3} TODGA alone or TBP and TODGA together (pseudo i-SANEX).

This project has received funding from the EURATOM research and training programme 2014-2018 under grant agreement No 755171. The content of this deliverable reflects only the author's view. The European Commission is not responsible for any use that may be made of the information it contains.

4. CONCLUSIONS AND FURTHER WORK

The following conclusions can be made, based on the data presented above:

For organic phase experiments, LSV measurements on 304L and 316L steels in the organic phase confirm that corrosion in the solvent (Octan-1-ol or Exxsol D80) is insignificant compared to aqueous phase (HNO_3) corrosion.

Organic phase corrosion experiments on 304L and 316L steels in the presence of TODGA reveal a small increase in oxidation current at ~-0.1 V with increasing TODGA concentration in the region of steel passivity. There is little difference in current between SS304L and SS316L steels, suggesting any corrosion process is not intergranular in nature. Furthermore, currents remain in the µA range, suggesting any increase in corrosion rate is minimal.

Comparisons between first and second scans on 304L suggest that the main mode of action of TODGA on the steel is to at-least dissolve its passive layer – an observation in keeping with the fact that previous studies of simpler malonic acids with shorter hydrocarbon side chains to TODGA, suggest that complexation and dissolution of iron precipitates may be possible under process conditions [1].

DEHiBA appears to have little effect on corrosion of SS316L in the organic phase, if anything acting as a slight corrosion inhibitor. Furthermore, contact of organic phase with a 5 mol dm^{-3} HNO_3 aqueous phase produces no significant increase in corrosion in the presence or absence of DEHiBA.

In the organic phase, it has been demonstrated that TBP alone has little effect on the corrosion behaviour of both SS304L and SS316L steels. However, in combination with TODGA in a pseudo *i*-SANEX process, TBP appears to slightly increase the previously described small TODGA corrosion current.

For aqueous phase experiments, LSV measurements show that SS304L and SS316L are significantly corroded in 5 mol dm^{-3} HNO_3 over the potential range studied (0.3 to 1.2 V vs saturated silver chloride reference electrode). SS316L is significantly more susceptible to transpassive dissolution than SS304L.

Contact with the organic phase (Exxsol D80), inhibits transpassive corrosion of SS316L at potentials > 1V. The presence of DEHiBA in the contacting organic phase has little effect on SS304L corrosion, but reduces corrosion of SS316L over Exxsol contact alone.

This project has received funding from the EURATOM research and training programme 2014-2018 under grant agreement No 755171. The content of this deliverable reflects only the author's view. The European Commission is not responsible for any use that may be made of the information it contains.

Aqueous phase experiments on TODGA-contacted HNO_3 were not attempted due to TODGA having a substantially lower aqueous solubility than that expected for DEHiBA.

Recommendations for further work: Electrochemical impedance spectroscopy (EIS) measurements on SS304L and SS316L in 5 mol dm^{-3} HNO_3 contacted with Exxol-D80 and DEHiBA may help to determine if the formation of an adsorbed hydrophobic layer of DEHiBA and / or a layer of Exxol-D80 or one of its components at the steel surface is the cause of surface corrosion inhibition.

TODGA may be removing the passive film from the surface of the both steels in the organic phase. Thus, experiments should be conducted on both steels in the presence of both the TODGA loaded organic phase and the baseline 5 mol dm^{-3} HNO_3 simultaneously in order to see if this putative TODGA-driven passive layer removal results in greater vulnerability of the steels to nitric acid attack and thus corrosive dissolution.

The studies reported above should be repeated on DMDOHEMA. However, as alternative ligands are currently being assessed for use in GANEX-2, these too should be subject to corrosion vulnerability assessments. Thus, it is recommended that the studies described above are repeated in the presence of the new organic phase extractant, mTDDGA.

REFERENCES

[1] E.B. Borghi, S.P. Ali, P.J. Morando, M.A. Blesa, Cleaning of stainless steel surfaces and oxide dissolution by malonic and oxalic acids, J. Nucl. Mat. 229 (1996) 115-123
[2] K. Kontturi and L. Murtomaki, Electrochemical determination of partition coefficients of drugs, J. Pharm. Sci., 81 (1992) 970-975.
[3] B. Dilasari, J. Park, P. Kusumah, K. Kwon, and K.C. Lee, Corrosion behavior of stainless steel 304, titanium, nickel and aluminium in non-aqueous electrolytes, Journal of the Korean Electrochemical Society, 17 (2014) 26-29.
[4] P. Fauvet, F. Balbaud, R. Robin, Q.T. Tran, A. Mugnier, and D. Espinoux, J. Nucl. Mater., 375 (2008) 52-64.
[5] J.S. Armijo, Corrosion, 24 (1968) 24-30.
[6] ASTM International. Standard Test Method for Conducting Potentiodynamic Polarization Resistance Measurements. G59 - 97, 1-4. 2014.
[7] ASTM International. Standard Practice for Calculation of Corrosion Rates and Related Information from Electrochemical Measurements. G102 - 89, 1-8. 2015.

This project has received funding from the EURATOM research and training programme 2014-2018 under grant agreement No 755171. The content of this deliverable reflects only the author's view. The European Commission is not responsible for any use that may be made of the information it contains.

STUDY OF PROCESS STEEL CORROSION IN THE PRESENCE OF THE ACTINIDE (III/IV) EXTRACTION LIGANDS AHA, SO_3-Ph-BTP, SO_3-Ph-BTPhen AND SO_3-Ph-BTBP

1. INTRODUCTION

In the EURO-GANEX process, after DMDOHEMA selectively extracts Pu(IV) and Np(IV) from the aqueous phase and TODGA extracts the remaining An(III) and Ln(III) ions in their entirety, the loaded An(III/IV)/Ln(III) organic stream is then fed to the TRU back-extraction stage, where the loaded organic stream is contacted with an AHA aqueous phase supplemented by a hydrophilic actinide (III) selective stripping ligand. The result is stripping of Pu(IV) and Np(IV) by AHA and An(III) ions by the An(III) extraction ligand into the aqueous phase, producing a proliferation resistant grouped actinide product while Ln(III) species remain complexed with TODGA in the organic phase.

In the EURO-GANEX process 2,6-bis(5,6-di(sulfophenyl)-1,2,4-triazin-3-yl)-pyridine (SO_3-Ph-BTP) has been tested as a suitable An(III) extraction agent and been shown to have good selectivity, kinetics and solubility for actinide (III) extraction [1-3]. However, due to the degradation of BTP ligands under radiolysis [2,4], radiologically stable sulfonated bistriazinylbipyridine (SO_3-Ph-BTBP) [1] and 1,10-phenanthroline ligands (SO_3-Ph-BTPhen) [5-7] are also currently under investigation as possible replacements for SO_3-Ph-BTP in the EURO-GANEX process, Figure 1.

Importantly, little is known about the influence of the above ligands and AHA on the corrosion behaviour of steels that typically make up plant such as tanks, pipework and reactors/contactors employed in each extraction step/unit operation of a reprocessing facility. Given the ability of said ligands to complex with actinide(III) and lanthanide(III) species [3,8], the potential stripping via complexation of either Fe^{3+} or Cr^{3+} from the steel and subsequent destabilization of the protective oxide film may be a concern.

Here we present electrochemical corrosion studies performed on the nuclear process steels, 304L and 316L stainless (SS), in the presence of all three ligands for use as An(III) extraction agents: SO_3-Ph-BTP, SO_3-Ph-BTBP and SO_3-Ph-BTPhen. In order to provide conditions typical of those expected in the aqueous phase of a EURO-GANEX process experiments have also been performed in the presence and absence of AHA concentrations up to 0.5 mol dm^{-3} in 5% wt. (1.13 mol dm^{-3}) HNO_3.

This project has received funding from the EURATOM research and training programme 2014-2018 under grant agreement No 755171. The content of this deliverable reflects only the author's view. The European Commission is not responsible for any use that may be made of the information it contains.

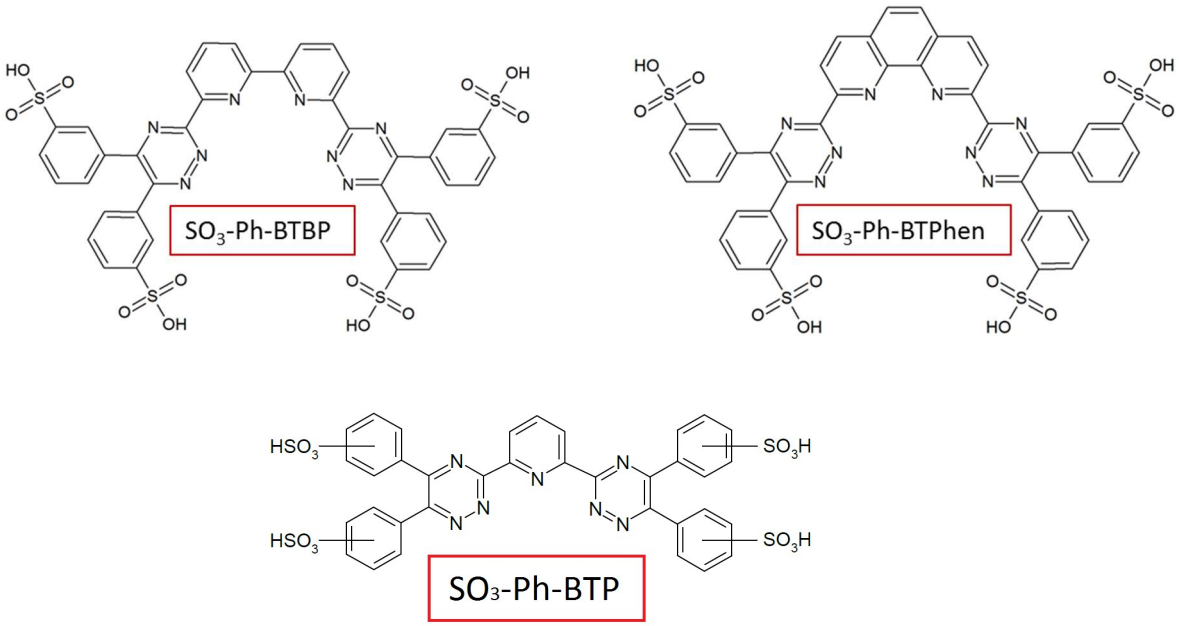

Figure 1: Chemical Structures of SO_3-Ph-BTBP, SO_3-Ph-BTPhen and SO_3-Ph-BTP.

2. EXPERIMENTAL

2.1. MATERIALS

SO_3-Ph-BTPhen AND SO_3-Ph-BTBP were synthesised by the University of Reading (UK) and SO_3-Ph-BTP was supplied by Technocomm Ltd. (Falkland, UK). All other chemicals were of AnalaR grade or better and supplied by Sigma Aldrich (Gillingham, Dorset, UK). All H_2O used was Ultrapure from a Direct-Q 3 UV Millipore water purification system (Millipore, Watford, UK) to a resistivity of 18.2 MΩ.cm.

A 20 ml stock solution of 0.54 mol dm^{-3} AHA was prepared in deionised H_2O and used for EQCM studies of ligand and AHA behaviour. The stock solution was kept refrigerated up to a maximum of five days and colourmetrically checked daily for AHA degradation using UV-vis spectrophotometry [9].

2.2. LINEAR SWEEP VOLTAMMETRY STUDIES

All LSV experiments were conducted in a small volume (200 µl) electrochemical cell in order to achieve high ligand loadings with what limited synthesised material was available. LSV measurements were performed using a PGSTAT120N potentiostat (Metrohm Autolab B.V., Utrecht). Working electrodes were constructed using 1 mm diameter SS316L (wt.%: C-0.015%, Si-0.38%, Mn-1.5%, P-0.035%, S-0.002%, Cr-17.0%, Mo-2.5%, Ni-10.0% and the remainder Fe) and SS304L (wt.%: C-0.03%, Si-0.75%, Mn-2.0%, P-0.04%, S-0.015%, Cr-18.0%, Ni-10.0% and the remainder Fe) wire (Advent,

This project has received funding from the EURATOM research and training programme 2014-2018 under grant agreement No 755171. The content of this deliverable reflects only the author's view. The European Commission is not responsible for any use that may be made of the information it contains.

Oxford, UK) in glass Pasteur pipettes, backfilled with epoxy resin and polished using decreasing SiC paper grades and 6, 3 and 1 µm diamond polishing pastes. To complete the three electrode cell a Ag/AgCl reference (RE-5B, Bioanalytical Systems Inc., USA) and coiled platinum wire counter electrode were inserted via a simple PTFE manifold. Current measurements were then recorded from 0.5 to 1.5V at a scan rate of 10 mV s^{-1}.

2.3. ELECTROCHEMICAL QUARTZ CRYSTAL MICROBALANCE (EQCM) STUDIES OF SS2343

EQCM experiments were conducted using a RQCM frequency counter (Inficon Ltd, Blackburn UK) and Q-sense open module (Biolin Scientific, Cheshire, UK) connected to a PGSTAT128N potentiostat (Metrohm Autolab B.V.). QCM piezoelectrodes were comprised of polished SS2343 (wt.%: C-0.020%, Si-0.38%, Mn-1.5%, P-0.041%, S-0.025%, Cr-16.5%, Mo-2.5%, Ni-10.5% and the remainder Fe) and were supplied from Biolin Scientific. SS2343 is a compositional analogue of SS316L with almost identical electrochemical/potentiodynamic properties as SS316L [10].

QCM crystal substrates were AT-cut quartz with a nominal resonant frequency of 5 MHz. Piezoelectrodes were created using physical vapour deposition (PVD) of SS2343 onto a thin Ti/Au adhesion layer (front and rear). The thickness of the steel layer is 100 nm with a surface roughness of 1.4 nm (± 0.2 nm) with little reduction in the fundamental frequency of 5 MHz. Frequency change to mass conversion was conducted assuming the applicability of the Sauerbrey equation [11] and a conversion factor of 0.0557 Hz/ng/cm^2. This conversion factor was determined by the standard Cu deposition and stripping method [12,13].

Experimentally, 2 ml aliquots of each ligand were prepared. For studies in the presence of additional 0.5 mol dm^{-3} AHA, aliquots of the AHA stock were taken and diluted to the desired concentration before being acidified using concentrated HNO_3 to a concentration of 1.13 mol dm^{-3} (5% wt.) and the relevant ligand added. Simultaneous LSVs and voltamassograms were then recorded from 0.5 to 1.5 V at a scan rate of 10 mV s^{-1} using a platinum wire counter and Ag/AgCl reference electrode. *Ex situ* SEM images and roughness measurements using a Phenom desktop SEM (Phenom-world, Eindhoven) were taken before and after each electrochemical microgravimetry experiments to assess any associated changes in surface morphology.

The unusually high sweep rate of 10 mV/s for both the QCM and disk electrode studies was selected for two reasons: 1) To avoid uncertainty in AHA concentration during AHA with ligand experiments, due to the acid catalysed hydrolysis of AHA in the low pH environment. As AHA is added as a ‘spike’ and not continuously renewed (for safety reasons – AHA is teratogenic) then, at a more typically used LSV scan rate of 0.1 mV/s,

This project has received funding from the EURATOM research and training programme 2014-2018 under grant agreement No 755171. The content of this deliverable reflects only the author’s view. The European Commission is not responsible for any use that may be made of the information it contains.

there would be a 40% loss of AHA during the LSVs of Figs. 8 and 9 due to acid catalysed hydrolysis of the hydroxamate group. Even at 1 mV/s, a loss of up to 7% of the AHA concentration will occur during the LSVs of Figure 2 and 3 over the voltage window used (both values calculated using the rate constants for AHA degradation in 1.13 mol dm^{-3} HNO_3 reported by Andrieux *et al.* [9,14]). Therefore, we ran the LSVs of Figure 2 and under conditions where AHA loss and thus uncertainty in [AHA] was no more than 1%, i.e. 10 mV/s. For comparisons sake, disk electrode studies in the absence of AHA were also run at this scan rate. 2) Thickness of the SS2343 layer on the QCM crystals. The SS2343 layer on the QCM crystals is very thin (100 nm) and therefore LSVs recorded at 0.1 mV/s over the potential range employed in Figs. 2 and 3 would result in the complete stripping of SS2343 during the first scan (and have been observed to do so in experiments conducted in these laboratories), rendering study of corrosion behaviour in the secondary passivation region (one of the main foci of this study) impossible. By using faster scan rates, complete stripping of the steel electrode material is avoided and the complete potential range can be studied.

3. CORROSION BEHAVIOUR OF AHA IN AQUEOUS NITRIC ACID SOLUTIONS

3.1. LINEAR SWEEP VOLTAMMETRY (LSV) STUDIES OF SS304L AND SS316L IN THE PRESENCE OF AHA

Linear sweep voltammograms and associated polarisation curves for SS304L an SS316L in AHA concentrations from0.1 to 0.5 mol dm^{-3} are shown in Fig. 2.

Considering first the polarisation curves of Fig. 2b and d, it can be that there is little change in Ecorr, icorr, and the range of passivity with increasing AHA concentration for both steels. The primary difference in the polarisation curves is an increase in transpassive current with increasing AHA concentration.

From the LSVs of Fig. 2a and c, it can be seen that AHA at concentrations from 0.1 to 0.5mol dm–3 significantly increases the oxidation current in the transpassive region for both steels. A larger transpassive current is observed for SS316L compared to SS304L, presumably due to the decreased silica content in SS316L which protects against intergranular corrosion in oxidative acidic environments [15,16]. However, it is interesting to note that while secondary passivation is inhibited by AHA for SS304L at potentials N~1.2 V, it appears to be maintained in SS316L samples.

This project has received funding from the EURATOM research and training programme 2014-2018 under grant agreement No 755171. The content of this deliverable reflects only the author's view. The European Commission is not responsible for any use that may be made of the information it contains.

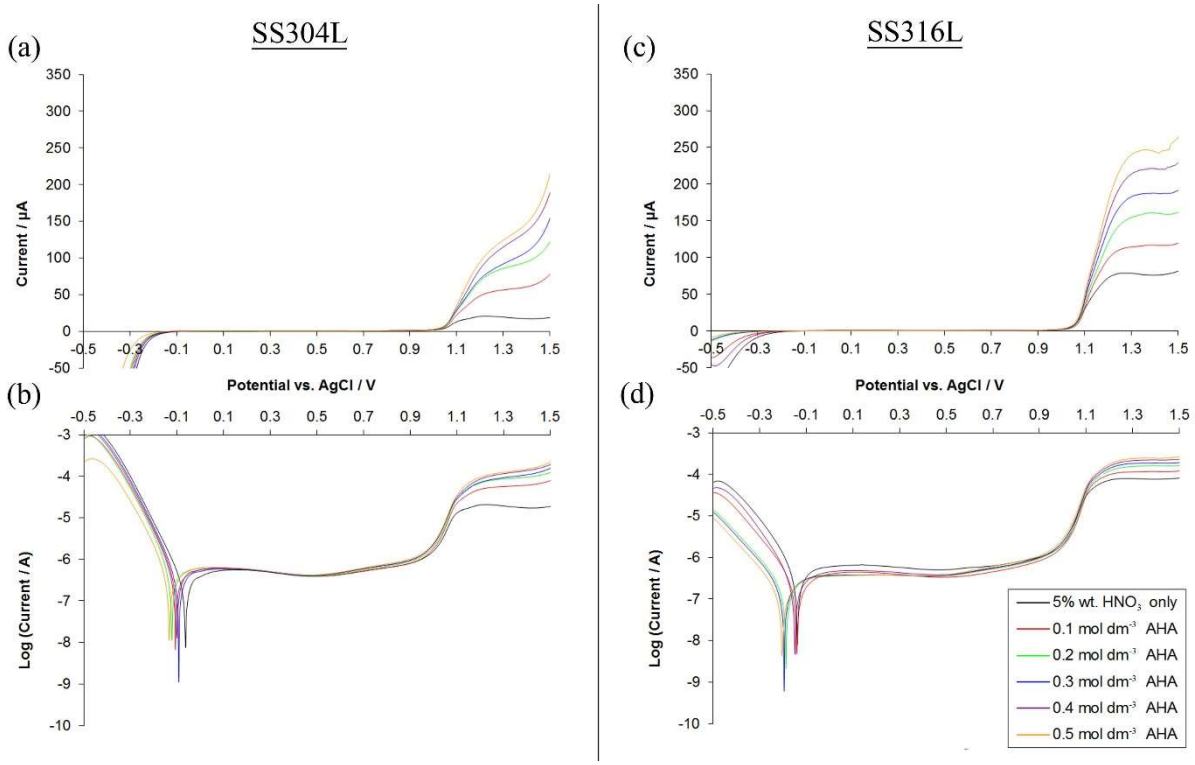

Figure 2. Linear sweep voltammograms (a and c) and polarisation curves (b and d) for SS304L and SS316L in 5% wt. HNO_3 and AHA concentrations from 0.1 to 0.5 mol dm^{-3}

A large increase in transpassive current would initially suggest that extremely rapid dissolution of the steel is occurring. However, visual inspection of both steelwire electrodes revealed no significant changes in surface morphology. Electrochemical studies of AHA oxidation using platinum electrodes [17,18] have reported irreversible oxidation of a range of mono-, di- and tri-hydroxamic acids at 0.555 V vs. Ag/AgCl at pH 4 (0.791 V at pH 0). Thus, this suggests that the transpassive currents of Fig. 2 are not purely due to transpassive dissolution but are rather a convolution of both AHA oxidation and steel dissolution.

3.2. MICROGRAVIMETRIC STUDIES OF SS2343 DISSOLUTION IN THE PRESENCE OF AHA

In order to deconvolute steel dissolution from AHA oxidation, simultaneous linear sweep voltammograms and voltamassograms of SS2343 (as a compositional analogue of SS316L) piezoelectrodes were recorded using the EQCM. Prior to scanning, the open circuit potential of SS2343 was recorded for both 5% wt. HNO_3 alone and in the presence of 0.5 mol dm^{-3} AHA and found to be 0.5 and 0.55 V respectively. Simultaneous linear sweep voltammograms and voltamassograms of SS2343 are shown in Fig.3a and Fig 3b respectively.

Considering first the data for 5% wt. HNO_3 only, it can be seen that the current trace does not mirror the mass trace. Specifically, the voltamassogram of Fig. 3b suggests

This project has received funding from the EURATOM research and training programme 2014-2018 under grant agreement No 755171. The content of this deliverable reflects only the author's view. The European Commission is not responsible for any use that may be made of the information it contains.

that there is no secondary passivation in the transpassive region, while the LSV data of Fig. 3a shows a levelling off of the current typical of passivation. To analyse this region in more detail the mass change was differentiated with respect to voltage. The resulting dΔm/dV vs. potential plot (not shown) reveals a plateau at E > 1.1V, i.e. mass loss continues at a constant rate in this potential region despite the presence of secondary passivation, suggesting that the secondary passive layer is porous in character. Such a layer has been previously observed on 304 stainless steels in sulphuric acid solutions by Song *et al*. [19,20]. They determined that this layer is predominantly non-stoichiometric Fe_2O_3, Cr_2O_3 and NiO with some other constituents such as stoichiometric Fe_3O_4 and metal hydroxides. Importantly, Song *et al*. also find that the Cr content of this layer is significantly lower than that found in the passivating film produced in the primary passivation region of SS304. The comparative lack of Cr in this secondary passivation layer results in a low breakdown potential, explaining the porous character identified from our results above.

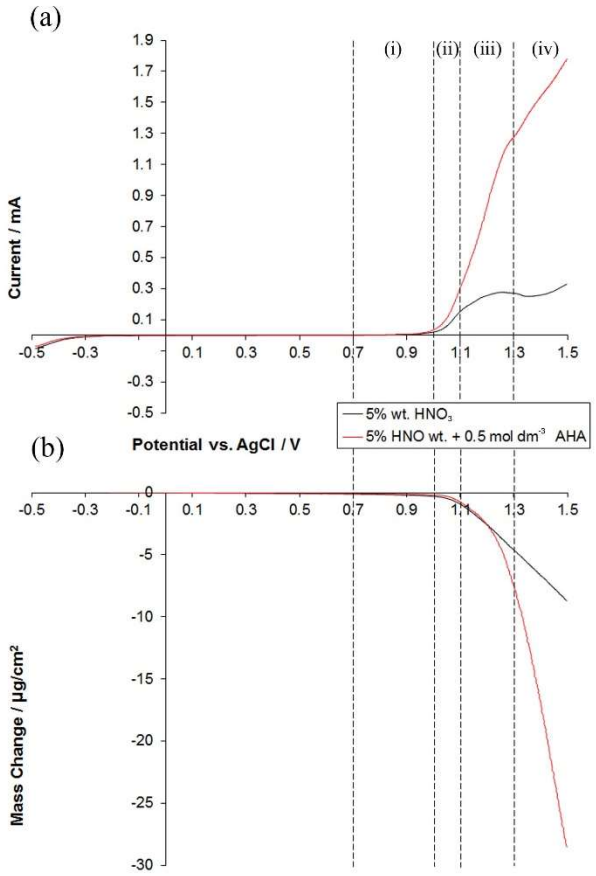

Figure 3. Linear sweep voltammogram (a) and simultaneously recorded voltamassogram (b) for 5% wt. HNO_3 and 0.5 mol dm^{-3} AHA on SS2343 piezoelectrodes.

Based on the above, the LSV for 5% wt. HNO_3 at potentials > 0.7 V can be divided into the following regions as indicated on Fig. 3: (i) Initial onset of transpassivity as Cr^{3+} is converted to higher valency Cr^{6+} in the passive layer [21,22]. (ii) Complete breakdown

This project has received funding from the EURATOM research and training programme 2014-2018 under grant agreement No 755171. The content of this deliverable reflects only the author's view. The European Commission is not responsible for any use that may be made of the information it contains.

of the Cr passive film and uninhibited dissolution of underlying iron as Fe^{3+}. (iii) Secondary passivation, initiated through O^{2-} anions and $Fe^{3+}/Cr^{3+}/Ni^{2+}$ cations meeting at a suitable lattice site [19]. (iv) Oxygen evolution [23]. The observed O_2 evolution current is low in region (iv), with only a slight increase in current apparent. Presumably this last observation is due to the secondary passivation layer restricting solution access to the underlying metal electrode, its porosity notwithstanding.

Considering now the voltamassogram and LSV data for SS2343 in 5% wt. HNO_3 with 0.5 mol dm^{-3} AHA, it can be seen from Fig. 3a that in the presence of AHA there is a larger increase in current with potential at the onset of transpassivity (region (i)) than in the absence of AHA. However, comparison with the simultaneously recorded voltamassogram, Fig 3b, reveals that there is no change in the rate of mass loss from the electrode surface. As discussed above, the larger currents seen in Fig. 3a in the presence of AHA compared to those recorded in its absence are likely associated with AHA oxidation to nitroxyl/hydroxylamine and acetic acid [17,18,24,25]. With regards to Fig. 3b, the electrochemical oxidation of AHA has been previously suggested by Shackleford to occur in solution rather than via a surface adsorbed species [26], explaining why there is no observed difference mass change recorded in this region compared to that seen in HNO_3 only.

Region (iii) shows the greatest difference between experiments conducted in the presence and absence of AHA. From the voltamassogram and LSV of Fig. 3, AHA appears to inhibit secondary passivation at E >1.1 V, most likely by formation of well-known Fe^{3+}-AHA complexes [9] from oxidatively generated free Fe^{3+} at the electrode surface, so interrupting secondary passivation formation and driving transpassive dissolution. Further, dissolution of the steel continues up to 1.5 V, Fig. 3b, the marked change in current at ~1.3 V in Fig. 3a being due to the onset of O_2 evolution at the exposed metal electrode.

SEM images and associated surface roughness values of the SS2343 coated piezoelectrodes employed in Fig. 3 are shown in Fig. 4.

Fig.4c reveals no observable changes in morphology upon cycling in the presence of AHA compared to its absence, Fig. 4b, or even no cycling at all, Fig. 4a. However, comparison of concomitant roughness values for Figs. 4a-c shows a decrease in average surface roughness (R_a) and maximum surface roughness (R_z) in the presence of AHA compared to uncycled piezoelectrodes and those cycled in HNO_3 only, suggesting any corrosive action is uniform in nature and akin to electropolishing of the surface (i.e. removing any surface deposits).

This project has received funding from the EURATOM research and training programme 2014-2018 under grant agreement No 755171. The content of this deliverable reflects only the author's view. The European Commission is not responsible for any use that may be made of the information it contains.

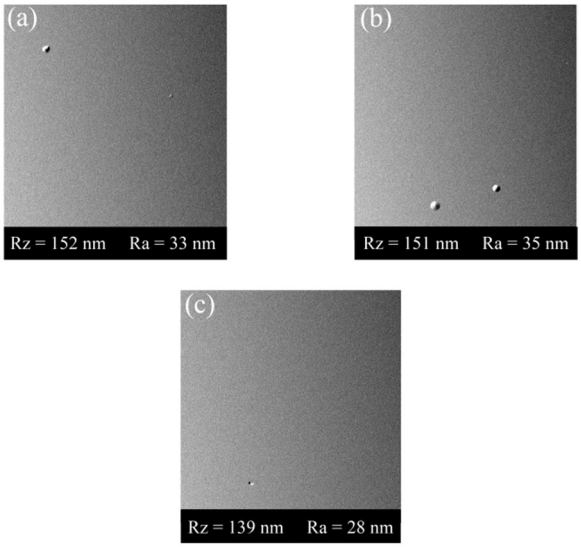

Figure 4. 3000x SEM backscatter images and measured maximum surface roughness (R_z) and average surface roughness (R_a) values of SS2343 piezoelectrodes. (a) Untreated crystal, (b) 5% wt. HNO_3, (c) 5% wt. HNO_3 + 0.5 mol dm^{-3} AHA.

Cycling in AHA also produced a pink solution colouration at the piezoelectrode surface. To determine the origin of this, the solution was sampled post-experiment, diluted and analysed using UV-vis spectrophotometry (not shown). Comparison with absorbance peak values for acetohydroxamatoiron(III) complexes reported by Andrieux *et al.* [9], revealed the presence of the monoacetohydroxamatoiron(III) complex suggesting that electrogenerated Fe(III) is sequestered from the electrode surface in this form.

It is important to note that when iron is freely dissolving with no secondary passivation, region (ii), the rate of mass loss in the presence of AHA is the same as in its absence. Thus, the corrosion accelerating behaviour of AHA is limited to situations where solution redox potential >+1.1 V i.e. in the region associated with secondary passivation in AHA-free solutions. However, few studies exist on the solution potential that obtains in aqueous reprocessing streams. From the scant literature that does exist, the solution potential may potentially be up to 1.15 V, depending on actinide species present, acidity and temperature [27-29]. From our own studies on non-active thermodynamic simulants for Pu(IV) containing systems, potentials as high as 1.1V can be observed at simulant metal ion concentrations as low as 0.1 mmol dm^{-3} [30], a value that would only be expected to be higher at concentrations more typical of reprocessing streams (especially, as may occur in the near future, during recycle of higher burnup fuels) and under certain maloperation conditions such as low pH excursions or high temperature. According to Fig. 3b this would place the solution potential in an area where AHA would increase the rate of SS316L dissolution, suggesting that the use of higher grade steels (e.g. SS310) or transpassive corrosion inhibitors may be necessary if AHA based reprocessing flow sheets are adopted for full scale nuclear fuel recycling in the future.

This project has received funding from the EURATOM research and training programme 2014-2018 under grant agreement No 755171. The content of this deliverable reflects only the author's view. The European Commission is not responsible for any use that may be made of the information it contains.

4. CORROSION BEHAVIOUR OF SO_3-Ph-BTP AND SO_3-Ph-BTPhen IN NITRIC ACID SOLUTIONS

4.1. LINEAR SWEEP VOLTAMMETRY STUDIES OF SS304L AND SS316L IN THE PRESENCE OF SO_3-Ph-BTP AND SO_3-Ph-BTPhen

Linear sweep voltammograms and associated polarisation curves for SS304L and SS316L in SO_3-Ph-BTP concentrations from 1 to 100 mmol dm^{-3} and SO_3-Ph-BTPhen concentrations from 1 to 100 mmol dm^{-3} are shown in Fig. 5 and Fig. 6 respectively.

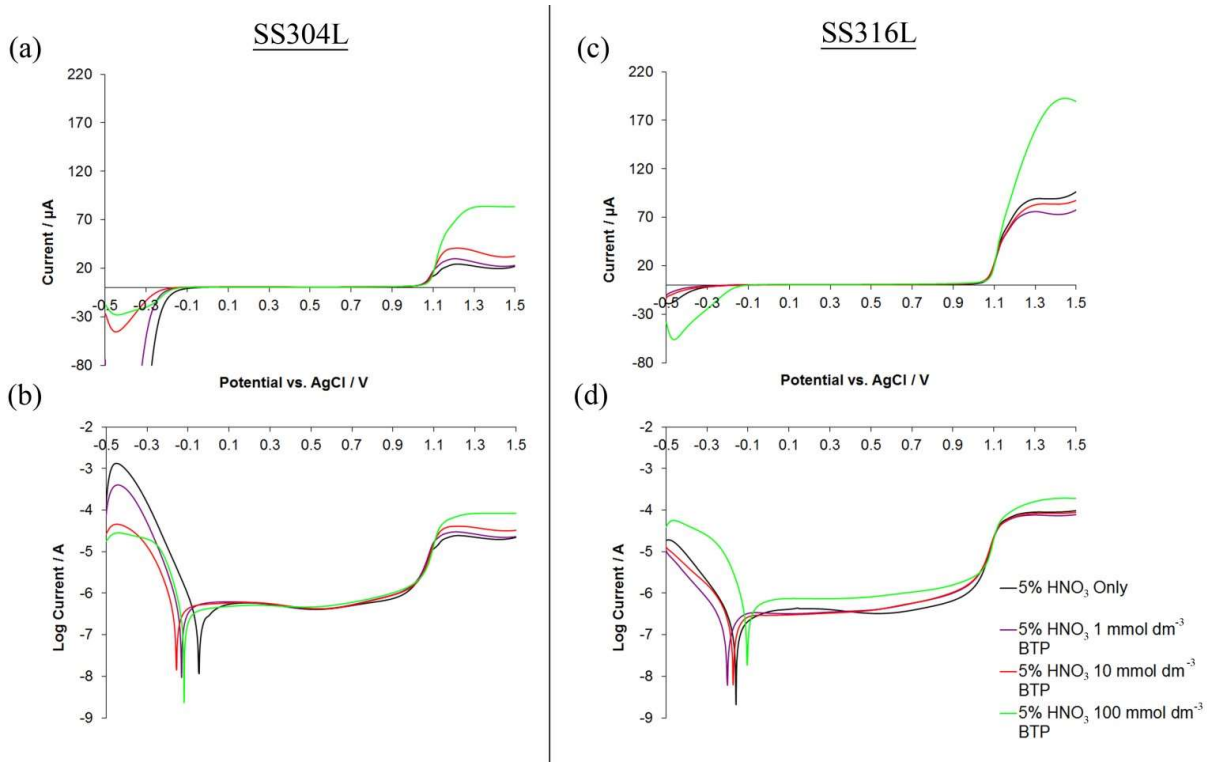

Figure 5: Linear sweep voltammograms (a and c) and polarisation curves (b and d) for SS304L and SS316L in 5% wt. HNO_3 and SO_3-Ph-BTP concentrations from 1 to 100 mmol dm^{-3}.

This project has received funding from the EURATOM research and training programme 2014-2018 under grant agreement No 755171. The content of this deliverable reflects only the author's view. The European Commission is not responsible for any use that may be made of the information it contains.

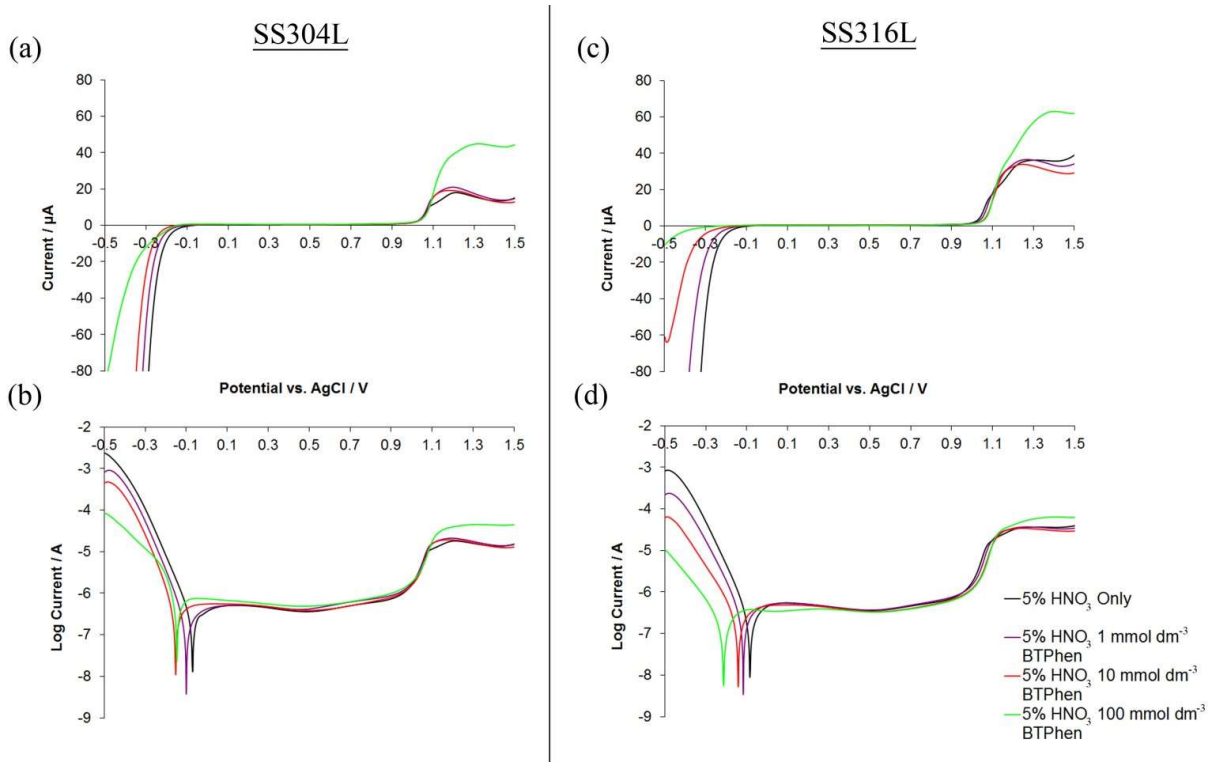

Figure 6: Linear sweep voltammograms (a and c) and polarisation curves (b and d) for SS304L and SS316L in 5% wt. HNO3 and SO3-Ph-BTPhen concentrations from 1 to 100 mmol dm^{-3}.

Considering first the SO_3-Ph-BTP polarisation curves of Fig. 5b and 5d, two effects are observed on both steels with increasing SO_3-Ph-BTP concentration. First, the corrosion potential, E_{corr}, shifts more negative as [SO_3-Ph-BTP] increases, widening the window of steel passivity by up to 110 mV. Second, in the region ~< -0.1V, the current decreases as SO_3-Ph-BTP increases, suggesting that hydrogen evolution at the electrode surface is inhibited by the presence of SO_3-Ph-BTP. Interestingly this latter effect is much greater on SS304L than on SS316L electrodes. This would initially suggest that SO_3-Ph-BTP has a corrosion inhibition effect under the oxidising nitric acid conditions employed.

Looking now at the same polarisation plots for SO_3-Ph-BTPhen, Fig. 6b and 6d, similar corrosion inhibition effects are observed, with E_{corr} shifting more negative as SO_3-Ph-BTPhen concentration increases, widening the window of steel passivity by up to 130 mV. In opposition to SO_3-Ph-BTP, SO_3-Ph-BTPhen inhibition of hydrogen evolution at the electrode surface is much greater on SS316L than SS304L.

Both these effects may be explained by the formation of an adsorbed layer of SO_3-Ph-BTP or SO_3-Ph-BTPhen at the metal-solution interface that forms a barrier against HNO_2, the active corrosive species in this environment [15,31], so inhibiting both oxidative Fe dissolution and the coupled reductive hydrogen evolution reaction in the vicinity of the E_{corr} by hydrophobically restricting electrolyte access to the electrode

This project has received funding from the EURATOM research and training programme 2014-2018 under grant agreement No 755171. The content of this deliverable reflects only the author's view. The European Commission is not responsible for any use that may be made of the information it contains.

surface. In support of this, corrosion inhibition of mild carbon steels through surface adsorption of similar pyridine derivatives in stagnant solution condition acidic environments (similar to those used here) has also been described by other authors [32-34]. However, it should be noted that under the hydrodynamic flow conditions encountered in reprocessing environments, the shear stress is may at least in part lead to desorption of SO_3-Ph-BTP/SO_3-Ph-BTPhen molecules from the steel surface and therefore reduce this corrosion inhibition effect [34].

Turning now to the polarograms for both SO_3-Ph-BTP and SO_3-Ph-BTPhen, Fig. 5a/5c and Fig 6a/6c respectively, it can be seen that the presence of SO_3-Ph-BTP or SO_3-Ph-BTPhen at concentrations > 10 mmol dm^{-3} increases the oxidation current in the trans-passive region (> 1.1 V) for both steels. In the presence of both ligands a larger trans-passive current is observed for SS316L than SS304L, presumably due to the decreased silica content in SS316L which protects against intergranular corrosion in oxidative acidic environments [10,11]. Too, for both steels the oxidative current in the trans-passive region is almost 3x greater in the presence of SO_3-Ph-BTP than SO_3-Ph-BTPhen, suggesting a greater corrosive action of SO_3-Ph-BTP compared to SO_3-Ph-BTPhen.

A large increase in transpassive current would initially suggest that extremely rapid dissolution of the steel is occurring. However, as with studies of AHA corrosion of SS304L and SS316L [35], visual inspection of both steel wire electrodes revealed no significant changes in surface morphology. In order to investigate the background electrochemical behaviour (i.e. oxidation or reduction of the ligand itself) as a possible source of the transpassive current, cyclic voltammograms of 0.1 mol dm^{-3} SO_3-Ph-BTP and 0.1 mol dm^{-3} SO_3-Ph-BTPhen were carried out on a 3 mm glassy carbon electrode. For completion, measurements were also taken in the presence of 0.5 mol dm^{-3} AHA with and without SO_3-Ph-BTP or SO_3-Ph-BTPhen. The results of these experiments are shown in Fig. 7 and Fig.8.

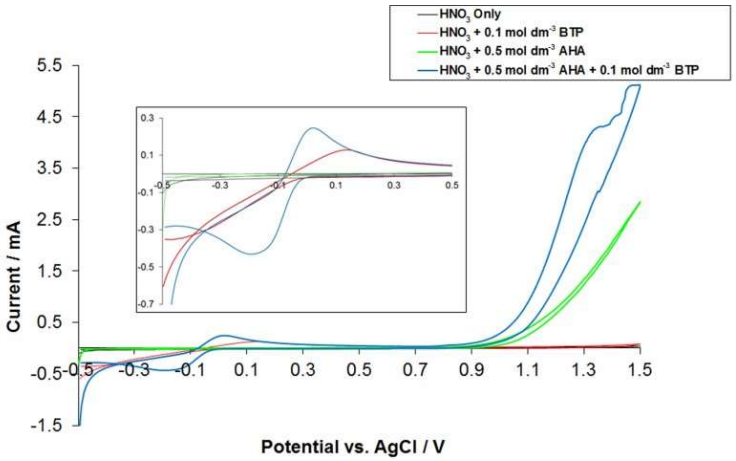

Figure 7: Linear sweep voltammograms of a glassy carbon electrode in 5% wt. HNO_3 and either AHA or SO_3-Ph-BTP.

This project has received funding from the EURATOM research and training programme 2014-2018 under grant agreement No 755171. The content of this deliverable reflects only the author's view. The European Commission is not responsible for any use that may be made of the information it contains.

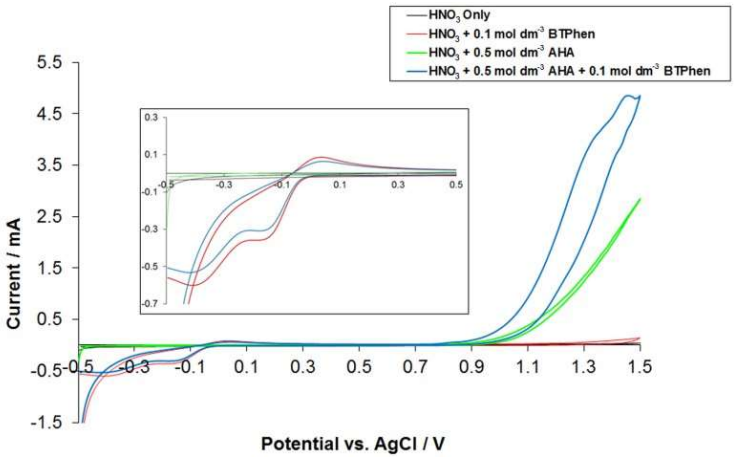

Figure 8. Linear sweep voltammograms of a glassy carbon electrode in 5% wt. HNO_3 and either AHA or SO_3-Ph-BTPhen.

Considering first the background electrochemical behaviour of SO_3-Ph-BTP, Fig. 7, in the presence of HNO_3 only a large reduction wave is observed on the forward scan between -0.5 and -0.05 V. This is then followed by a smaller oxidation peak at 0 to 0.2 V (see inset), with no proximal reduction peak on the reverse scan, suggesting that whatever electrochemical oxidation process is occurring is irreversible. Turning now to SO_3-Ph-BTPhen, Fig. 8, in the presence of HNO_3 a similar reduction wave is observed on the forward scan between -0.5 and -0.1 V. This is then followed again by a smaller oxidation peak at 0 to 0.5 V (see inset), with two reduction peaks on the reverse scan at -0.15 and -0.4 V respectively, suggesting that whatever electrochemical oxidation process is occurring is at least in part reversible.

Importantly, for both SO_3-Ph-BTP and SO_3-Ph-BTPhen there is little electrochemical behaviour at potentials > 1.1 V, suggesting the observed current increase in Fig. 5 and Fig 6 at SO_3-Ph-BTP/BTPhen concentrations > 0.1 mol dm^{-3} is due to increased BTP / BTPhen-promoted transpassive corrosion of the steel (albeit on a scale not visible to the naked eye) rather than any oxidation of the ligand. However, as reported previously [35], AHA in Fig. 7 and 5 is oxidised to hydroxylamine and acetic acid at potentials > 0.9 V and therefore any currents measured at potentials > 1.1 V in the presence of AHA (with or without SO_3-Ph-BTP/SO_3-Ph-BTPhen) are a convolution of steel transpassive dissolution and AHA oxidation.

4.2. MICROGRAVIMETRIC STUDIES OF SS2343 DISSOLUTION IN THE PRESENCE OF SO_3-Ph-BTP AND SO_3-Ph-BTPhen

Simultaneous linear sweep voltammograms and voltamassograms of SS2343 are shown in Fig.9a and Fig 9b respectively.

This project has received funding from the EURATOM research and training programme 2014-2018 under grant agreement No 755171. The content of this deliverable reflects only the author's view. The European Commission is not responsible for any use that may be made of the information it contains.

Considering first the data for 5% wt. HNO_3 only, it can be seen that the current trace does not mirror the mass trace. Specifically, the voltamassogram of Fig. 9b suggests that there is no secondary passivation in the transpassive region, while the LSV data of Fig. 9a shows a levelling off of the current typical of passivation. Such a feature is described in section 3.2 above and our previous publication [35]. If the mass change is differentiated with respect to voltage, the resulting dΔm/dV vs. potential plot (not shown) reveals a plateau at E > 1.1V, i.e. mass loss continues at a constant rate in this potential region despite the presence of secondary passivation. This suggests that the secondary passive layer is porous in character. Such a layer has been previously observed on 304 stainless steels in sulphuric acid solutions by Song *et al*. [19,20]. Through electrochemical and XPS analysis they have determined that this layer is predominantly non-stoichiometric Fe_2O_3, Cr_2O_3 and NiO with some other constituents such as stoichiometric Fe_3O_4 and metal hydroxides. Importantly, Song *et al*. also find that the Cr content of this layer is significantly lower than that found in the passivating film produced in the primary passivation region of SS304. The comparative lack of Cr in this secondary passivation layer results in a low breakdown potential, explaining the porous character identified from our results above.

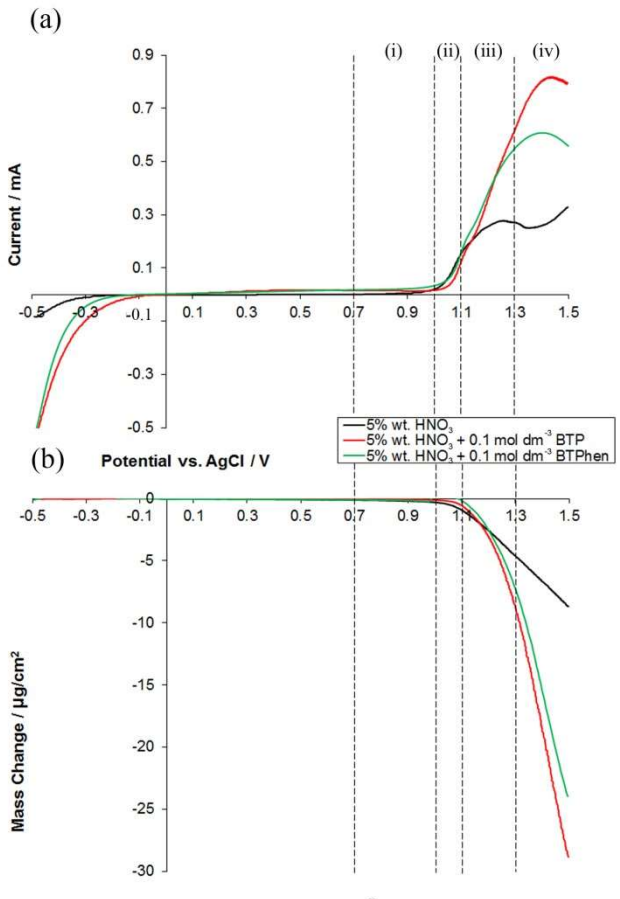

Figure 9: Linear sweep voltammogram (a) and simultaneously recorded voltamassogram (b) for 5% wt. HNO_3 and either 0.1 mol dm^{-3} SO_3-Ph-BTP or 0.1 mol dm^{-3} SO_3-Ph-BTPhen on SS2343 piezoelectrodes.

This project has received funding from the EURATOM research and training programme 2014-2018 under grant agreement No 755171. The content of this deliverable reflects only the author's view. The European Commission is not responsible for any use that may be made of the information it contains.

Based on the above, and as described in section 3.2, the LSV for 5% wt. HNO_3 at potentials > 0.7 V can be divided into the following regions as indicated on Fig. 9: (i) Initial onset of transpassivity as Cr^{3+} is converted to higher valency Cr^{6+} in the passive layer [21,22]. (ii) Complete breakdown of the Cr passive film and uninhibited dissolution of underlying iron as Fe^{3+}. (iii) Secondary passivation, initiated through O^{2-} anions and $Fe^{3+}/Cr^{3+}/Ni^{2+}$ cations meeting at a suitable lattice site [19]. (iv) Oxygen evolution [23]. The observed O_2 evolution current is low in region (iv), with only a slight increase in current apparent. Presumably this last observation is due to the secondary passivation layer restricting solution access to the underlying metal electrode, its porosity notwithstanding.

Considering now the voltamassogram and LSV data for SS2343 in 5% wt. HNO_3 with 0.1 mol dm^{-3} SO_3-Ph-BTP, it can be seen from Fig. 9a that there is little difference in the region of initial onset of transpassive dissolution, Region (i), in the presence or absence of SO_3-Ph-BTP. The same is also generally true for Region (ii), with slightly lower currents recorded in the presence of SO_3-Ph-BTP that are mirrored by a lower of change in mass in the simultaneously recorded voltamassogram of Fig. 9b. Region (iii) shows the greatest difference between experiments conducted in the presence and absence of SO_3-Ph-BTP. Based on the LSV of Fig. 9a, SO_3-Ph-BTP appears to inhibit secondary passivation at E >1.1 V, resulting in a recorded mass loss similar to that observed for AHA (see Fig. 3, section 3.2). This also shows that SO_3-Ph-BTP is more corrosive than AHA, accessing similar corrosion rates at lower concentrations than AHA (0.1 mol dm^{-3} SO_3-Ph-BTP vs. 0.5 mol dm^{-3} AHA), presumably due to the latter's oxidiation at potentials >0.8 V (Fig. 2).

This transpassive enhancement is most likely derived from Fe-SO_3-Ph-BTP complexes formed from oxidatively generated free Fe^{3+} at the electrode surface, so interrupting secondary passivation formation and driving transpassive dissolution. Interestingly the uptake of Fe by SO_3-Ph-BTP results in a distinct colour change in the solution, turning from yellow to black. Attempts to characterise the complex using nuclear magnetic resonance (NMR) spectroscopy and UV-vis spectrophotometry revealed a high degree of magnetic signal noise and extremely high absorbance respectively (not shown), suggesting that complexation results in the formation of a solid iron oxide colloidal dispersion, the black colouration being suspended particles of an FeO_x or FeOH-SO_3-Ph-BTP compound. Further, Fig. 9a also shows that dissolution of the steel continues up to 1.5 V, with a marked change in Region (iv) as the current decreases at ~1.34V. However, as with studies of HNO_3 only, a consistent decrease in mass is recorded microgravimetrically in this potential region (Fig. 9b). Again differentiating the mass change with respect to voltage (not shown), a plateau is revealed at E > ~1.34V, i.e. mass loss continues at a constant rate in this potential region. Thus, this suggests that complete SO_3-Ph-BTP sequestration of dissolved Fe^{3+} from the electrode surface does occur and a secondary passive layer can still form, albeit displaced to a potential > 1.36V.

This project has received funding from the EURATOM research and training programme 2014-2018 under grant agreement No 755171. The content of this deliverable reflects only the author's view. The European Commission is not responsible for any use that may be made of the information it contains.

Turning now to the voltamassogram and LSV data for SS2343 in 5% wt. HNO_3 with 0.1 mol dm^{-3} SO_3-Ph-BTPhen, while currents are higher in Regions (i), (ii) and (iii) of Fig. 9a they generally follow those for SO_3-Ph-BTP up until ~1.28V. At this point the current begins to plateau, resulting in a lower final current at 1.5V compared to SO_3-Ph-BTP, suggesting a lesser degree of transpassive dissolution enhancement compared to SO_3-Ph-BTP, with secondary passivation at potentials >~1.28V. Comparison with the voltamassogram of Fig. 9b shows a total mass loss at 1.5V of 28 µg/cm^2 for SO_3-Ph-BTP compared to 23 µg/cm^2 for SO_3-Ph-BTPhen, supporting the lower observed current in Fig. 9a. Differentiating the mass change with respect to voltage, a plateau is only observed at E > ~1.34V, indicating the onset of secondary passivation. Thus, the change in current observed at 1.34V > E > ~1.28V is presumably indicative of a decrease in the rate of transpassive dissolution enhancement rather than secondary passivation onset.

SEM images and associated measured surface roughness values of the SS2343 coated piezoelectrodes employed in Fig. 9 (not shown) reveal no observable changes in morphology after electrochemical cycling in the presence of either SO_3-Ph-BTP or SO_3-Ph-BTPhen compared to its absence, or even no cycling at all. However, comparison of concomitant roughness values of reveals a small decrease in average surface roughness (R_a) and maximum surface roughness (R_z) in the presence of either SO_3-Ph-BTP or SO_3-Ph-BTPhen compared to un-electrochemically cycled piezoelectrodes and those cycled in HNO_3 only, suggesting any corrosive action is uniform in nature and akin to electropolishing of the surface, i.e. removal of surface deposits from the electrode.

In order to investigate the effect of both SO_3-Ph-BTP and SO_3-Ph-BTPhen under normal operating conditions, further microgravimetric measurements of SS2343 piezoelectrodes in the absence and presence of either 0.1 mol dm^{-3} SO_3-Ph-BTP or SO_3-Ph-BTPhen respectively were performed over longer time periods (~3 hours) without external potential perturbation, while simultaneously measuring the open circuit potential (OCP). The simultaneously recorded mass traces and open circuit potential measurements for these experiments are shown in Fig. 10.

Considering first the recorded open circuit potential for 5% wt. HNO_3 only, Fig. 10(a), it can be seen that the open circuit potential remains steady state at ~0.66V throughout the recording period. Such a value suggests that in 5% wt. HNO_3 SS316L is in a pre-transpassive state, i.e. the Cr passive film is still present, but is being partially and slowly oxidised from Cr(III) to soluble Cr(VI). This is supported by the simultaneously recorded mass trace of Fig. 10(a), which shows a slow dissolution of the steel over the recording period. In order to confirm that such a high potential could be exhibited by SS316L in 5% wt. HNO_3 a further five hour open circuit potential measurement of 5% wt. HNO_3 was carried out using a 3 mm diameter glassy carbon (GC) electrode and AgCl reference.

This project has received funding from the EURATOM research and training programme 2014-2018 under grant agreement No 755171. The content of this deliverable reflects only the author's view. The European Commission is not responsible for any use that may be made of the information it contains.

Despite a slower equilibration period compared to OCP measurements on SS316L, the OCP measured on GC reached an approximate steady state potential of 0.75 V after five hours, confirming the recorded OCP of ~0.66V for SS316L in 5% wt. HNO_3 is plausible.

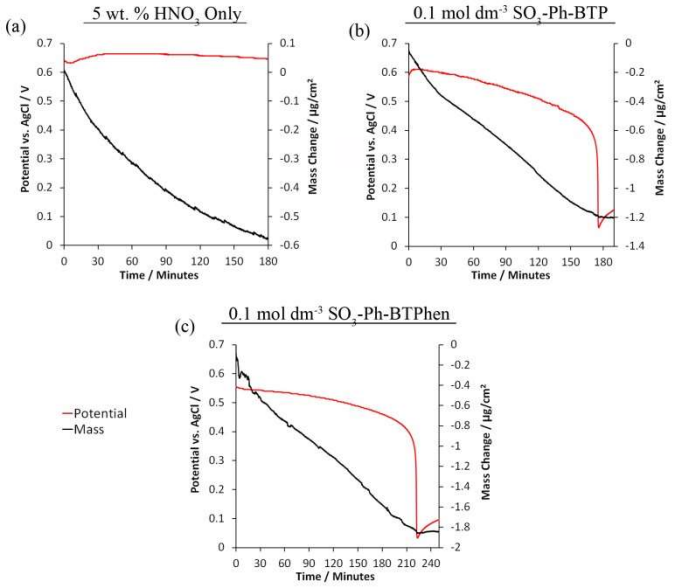

Figure 10: Potentiometry and simultaneously recorded massogram for SS2343 piezoelectrodes in (a) 5% wt. HNO_3 only, (b) 0.1 mol dm^{-3} SO_3-Ph-BTP and (c) 0.1 mol dm^{-3} SO_3-Ph-BTPhen.

Simultaneous OCP and QCM measurements of an SS2343 piezoelectrode in 5% wt. HNO_3 with 0.5 0.1 mol dm^{-3} SO_3-Ph-BTP are shown in Fig. 10(b). It can immediately be seen from Fig. 10(b) that the recorded mass and OCP traces have very different time dependent forms compared to those recorded in the absence of SO_3-Ph-BTP, Fig. 10(a). The OCP slowly decreases while the mass of the electrode rapidly decreases up to ~175 minutes, whereby there is a sudden drop in the potential followed by a simultaneous arrest in recorded mass loss. Similar OCP behaviour has been previously observed in our laboratory for SS316L samples in pH 2.1 H_2SO_4 [36]. Based on work by Evans, Cartledge and Qin [37-39], the dominant electrochemical processes at each step of the OCP behavior of SS316L in H_2SO_4 were interpreted and related to the attack and dissolution of millscale or similar iron surface deposits on the steel. The initial slow drop in potential is suggested by Qin *et al*. [38] to be a result of initial penetration of solution through the iron oxide pores (potentially involving slow acid dissolution of the oxide) causing a sudden large potential drop upon contact with the underlying steel surface. This is in agreement with the work of Bannister and Evans [37] and is also assumed by Itzhak and Aghion [40], who have observed similar potential excursions on hot pressed 316 steel electrodes in pH 0.3 H_2SO_4. The reformation of a new H_2SO_4 stable surface iron oxide through localised exceeding of the iron solubility product results in a subsequent repassivation, arrest in dissolution and slow increase in recorded open circuit potential after the sudden potential drop.

This project has received funding from the EURATOM research and training programme 2014-2018 under grant agreement No 755171. The content of this deliverable reflects only the author's view. The European Commission is not responsible for any use that may be made of the information it contains.

Returning to the OCP trace of Fig. 10(b), while the initial period of solution penetration of oxide pores shows a similar potential trend to that of SS316L in H_2SO_4 solutions, the rapid decrease in potential resulting from contact of HNO_3 with the underlying steel surface at ~ 175 minutes does not, unlike previous H_2SO_4 studies, reach a negative open circuit potential. Thus, while whatever thin surface protective layer present is indeed penetrated, attack of the underlying steel is relatively minor – at least in comparison to that which occurs in sulphuric acid. Secondly, Fig 10(b) shows that repassivation/protection of the steel surface is more rapid compared to SS316L in H_2SO_4 solutions, with a consequent rapid recovery of the open circuit potential and arrest of the recorded mass at > 180 minutes. As this potential and mass behaviour is not shown in the absence of SO_3-Ph-BTP (Fig. 10(a)) it can be inferred that, during the initial dissolution period, SO_3-Ph-BTP complexes the constituents of the millscale/surface iron film resulting initially in more rapid dissolution (-0.5 µg/cm^2 at t = 90 minutes compared to -0.4 µg/cm^2 for HNO_3 only at t = 90 minutes). Furthermore, the lack of any observed passivation in the HNO_3 only data of Fig. 10(a) suggests the repassivation and mass recovery observed at t > 180 minutes in Fig. 10(b) is possibly due to the formation of an adsorbed layer of SO_3-Ph-BTP at the metal-solution interface, rather than the formation of a new HNO_3 stable iron oxide layer – the formation of said oxide layer being inhibited by the complexation of solution released solution Fe(III) with SO_3-Ph-BTP in any case. Such a layer would also restrict electrolyte access to the underlying steel causing an increase in the open circuit potential and is in agreement with linear sweep voltammetry studies of SS316L wire electrodes previously discussed. Such an effect is also observed with addition of 0.1 mol dm^{-3} SO_3-Ph-BTPhen, Fig. 10(c), with similar recorded solution potentials and time to adsorbed layer formation.

Thus, under convection free conditions with no external potential perturbation, equivalent to normal reprocessing operating conditions, both SO_3-Ph-BTP and SO_3-Ph-BTPhen act as corrosion inhibitors rather than corrosion accelerators. However, in the presence of potential perturbations of 1.1 V or greater, equivalent to a maloperations condition, both SO_3-Ph-BTP and SO_3-Ph-BTPhen then act as corrosion accelerators rather than corrosion inhibitors. We shall return to this point below.

In the next section we consider the effect of a combined AHA and SO_3-Ph-BTP/ SO_3-Ph-BTPhen system, such as suggested for use in a EURO-GANEX TRU back extraction [41-43].

4.3. LINEAR SWEEP VOLTAMMETRY STUDIES IN THE PRESENCE OF AHA AND EITHER SO_3-Ph-BTP OR SO_3-Ph-BTPhen

Linear sweep voltammograms and associated polarisation curves for SS304L and SS316L with 0.5 mol dm^{-3} AHA only or 0.5 mol dm^{-3} AHA with either 0.1 mol dm^{-3} SO_3-Ph-BTP or

This project has received funding from the EURATOM research and training programme 2014-2018 under grant agreement No 755171. The content of this deliverable reflects only the author's view. The European Commission is not responsible for any use that may be made of the information it contains.

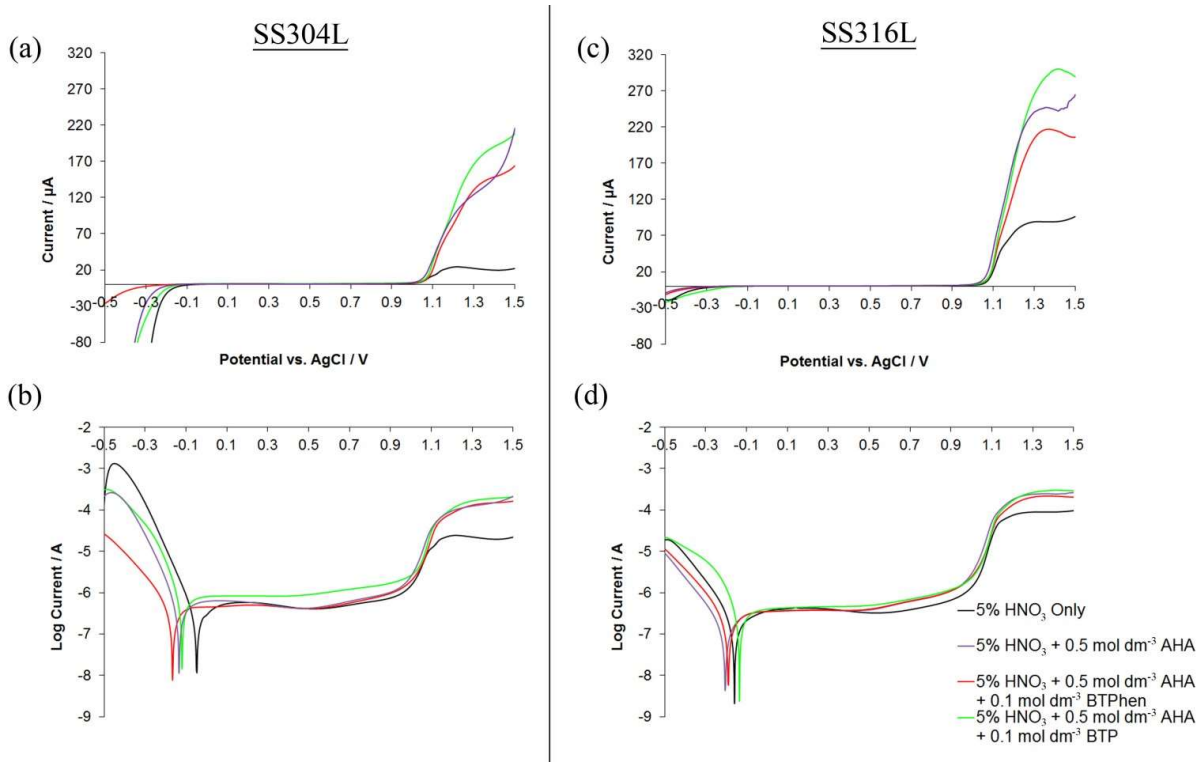

Figure 11. Linear sweep voltammograms (a and c) and polarisation curves (b and d) for SS304L and SS316L in 5% wt. HNO_3 with 0.5 mol dm^{-3} AHA alone or with 0.5 mol dm^{-3} AHA and either 0.1 mol dm^{-3} SO_3-Ph-BTP or 0.1 mol dm^{-3} SO_3-Ph-BTPhen.

SO_3-Ph-BTPhen are shown in Fig. 11. Considering first the LSV and polarisation curves for SS304L, Figs. 11a and b, it can be immediately seen that transpassive currents are considerably higher in the presence of AHA than in the absence. As demonstrated by the CV measurements of AHA on glassy carbon in Fig. 7 and 8, this is due to the oxidation of AHA at potentials > 0.8V. In the presence of added SO_3-Ph-BTPhen, the current in the majority of the transpassive region follows that of AHA alone. However, at potentials > 1.4V currents are lower than those observed for AHA alone, initially suggesting some secondary passivation is occurring or transpassive dissolution enhancement is lessened with the addition of SO_3-Ph-BTPhen. Interestingly at low potentials (E < 0V), while E_{corr} is at approximately the same point as that observed for SO_3-Ph-BTPhen alone (Fig. 6), the current below E_{corr} is substantially reduced, i.e. hydrogen evolution at the steel electrode is significantly inhibited. Thus, it appears that in combination SO_3-Ph-BTPhen and AHA provide a synergistic corrosion inhibition effect against reductive corrosion, presumably through a SO_3-Ph-BTPhen layer forming at the liquid-metal interface. However, in the presence of additional SO_3-Ph-BTP converse behaviour is observed. At low potentials (E < 0V) SO_3-Ph-BTP with AHA currents match that of AHA alone, providing a very similar level of corrosion protection to that observed for SO_3-Ph-BTP only (Fig. 5). However, in the transpassive dissolution region (E > 1V) currents are higher with additional SO_3-Ph-BTP at potentials > 1.2 V than in the presence of AHA alone. Such an observation suggests

This project has received funding from the EURATOM research and training programme 2014-2018 under grant agreement No 755171. The content of this deliverable reflects only the author's view. The European Commission is not responsible for any use that may be made of the information it contains.

higher rates of transpassive steel dissolution are being accessed at a lower potential compared to AHA alone.

Turning now to the LSV and polarisation curves for SS316L, Fig. 11c and d, again a similar trend is observed. For all conditions in Fig. 11c and d transpassive currents are much greater than those recorded on SS304L electrodes, as previously detailed, SO_3-Ph-BTPhen with AHA shows the lowest transpassive current in comparison to SO_3-Ph-BTP with AHA and AHA alone. However, unlike with SS304L electrodes, E_{corr} and the current in the hydrogen evolution region shows little variation between SO_3-Ph-BTPhen with AHA and AHA alone. Considering now SO_3-Ph-BTP with AHA, it can been seen that SS316L transpassive dissolution currents at E > 1.2V are considerably greater in the presence of additional SO_3-Ph-BTP than in the presence of AHA alone, suggesting more rapid dissolution is occurring. Thus, these results initially suggest that AHA alone may be more corrosive than AHA in combination with SO_3-Ph-BTPhen. However, as before, pure voltammetry measurements do not account for additional currents generated at potentials > 0.8V by the oxidation of AHA, therefore microgravimetric measurements are key to understanding the true rate of transpassive dissolution.

4.4. MICROGRAVIMETRIC STUDIES OF SS2343 DISSOLUTION IN THE PRESENCE OF AHA AND EITHER SO_3-Ph-BTP OR SO_3-Ph-BTPhen

Fig.12a and Fig 12b show simultaneous linear sweep voltammograms and voltamassograms respectively of SS2343 in nittic acid, nitric plus AHA and nitric plus AHA plus either SO_3-Ph-BTP or SO_3-Ph-BTPhen.

Considering first the LSV's of Fig. 12a it can be seen that compared to experiments on smaller surface area disk electrodes (Fig. 11), the larger surface area SS2343 piezoelectrodes show not only considerably larger transpassive dissolution currents but also a bigger differentiation between measurements in the presence of AHA alone and those in the presence of additional An/Ln(III) extraction ligands. In particular, the recorded currents for experiments in the presence of both AHA and SO_3-Ph-BTPhen are considerably larger than those recorded for AHA, the antithesis of measurements conducted on SS316L disk electrodes in Figure 11c and d. As such, the small volume and smaller electrode size employed in the disk electrode studies must either: 1) be restricting diffusion of Fe^{3+} into bulk solution, thus increasing the chance of secondary passivation occurring or, 2) result in increased concentrations of SO_3-Ph-BTPhen/ SO_3-Ph-BTP local to the electrode surface, due to the confined volume and slow diffusion away from the electrode of uncomplexed ligand (stagnant conditions), resulting in a much more uniform adsorbed layer at the metal-solution interface, forming a barrier against HNO_2 such as that described previously. Irrespective of which case obtains, the

This project has received funding from the EURATOM research and training programme 2014-2018 under grant agreement No 755171. The content of this deliverable reflects only the author's view. The European Commission is not responsible for any use that may be made of the information it contains.

greater electrode area/larger volume studies of Fig. 12 may be taken to be a more true representation of expected corrosion behaviour for these ligands in larger volume tanks/pipework.

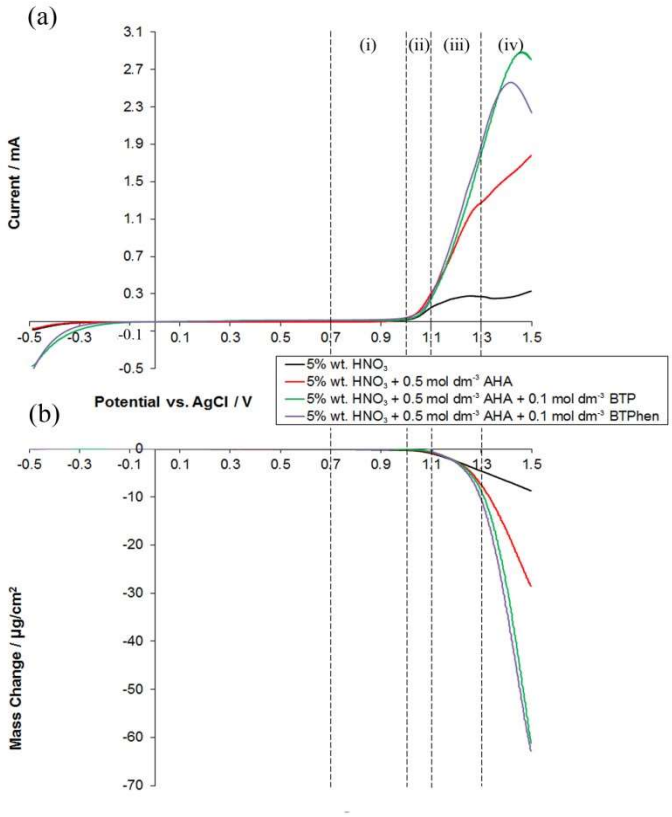

Figure 12. Linear sweep voltammogram (a) and simultaneously recorded voltamassogram (b) for SS2343 piezoelectrodes in 5% wt. HNO_3 with 0.5 mol dm^{-3} AHA alone or with 0.5 mol dm^{-3} AHA and either 0.1 mol dm^{-3} SO_3-Ph-BTP or 0.1 mol dm^{-3} SO_3-Ph-BTPhen.

Turning to the simultaneously recorded voltamassogram of Fig. 12b, it can be seen that both SO_3-Ph-BTP and SO_3-Ph-BTPhen exhibit greater mass loss rates at E > 1.15 V than either 5% wt. HNO_3 only or AHA in 5% wt. HNO_3, total mass loss at 1.5 V being ~6x greater than the mass loss recorded in 5% wt. HNO_3 at the same potential. Mass losses for SO_3-Ph-BTP and SO_3-Ph-BTPhen in the presence of AHA are also 2x that of SO_3-Ph-BTP or SO_3-Ph-BTPhen alone (Fig. 9b). As with studies of SO_3-Ph-BTP and SO_3-Ph-BTPhen in the absence of AHA (Fig. 9), secondary passivation is again observed in the current traces for both SO_3-Ph-BTP and SO_3-Ph-BTPhen in the presence of AHA, Fig. 12a, occurring at 1.46 and 1.4 V for in the presence of SO_3-Ph-BTP and SO_3-Ph-BTPhen respectively. In both cases the potential of secondary passive onset is more anodic than those of 1.36 and 1.34 V previously observed for SO_3-Ph-BTP and SO_3-Ph-BTPhen respectively (Fig. 9). Differentiating the mass change in Fig. 12b with respect to voltage (not shown) reveals a plateau in the rate of mass loss, confirming the onset of secondary passivation at these potentials. Thus, addition of SO_3-Ph-BTP or SO_3-Ph-BTPhen to AHA further enhances transpassive dissolution at E >1.15 V, most likely by

This project has received funding from the EURATOM research and training programme 2014-2018 under grant agreement No 755171. The content of this deliverable reflects only the author's view. The European Commission is not responsible for any use that may be made of the information it contains.

the combined formation of Fe^{3+}-AHA complexes [9] and Fe^{3+}-SO_3-Ph-BTP/SO_3-Ph-BTPhen complexes from oxidatively generated free Fe^{3+} at the electrode surface, interrupting secondary passive layer formation and driving transpassive dissolution.

SEM images and associated surface roughness values of the SS2343 coated piezoelectrodes employed in Fig. 12 (not Shown) reveal a similar electropolishing effect is apparent on a surface exposed to electrochemical cycling in AHA only to that observed in the presence of SO_3-Ph-BTP or SO_3-Ph-BTPhen alone, a feature we have also reported on previously [35]. However, cycling SO_3-Ph-BTP or SO_3-Ph-BTPhen in the presence of AHA, while resulting in only minor observable differences in the surface at the magnification shown (e.g. some tentative shallow pitting), results in significant increases in average surface roughness and maximum surface roughness. Higher magnification SEM images (not shown) reveal that this roughness increase is derived from a general surface wide corrosion of the surface, suggesting that the mechanism of enhanced transpassive corrosion is uniform, with pits occurring at heterogeneous (i.e. SS2343 coating defect) areas only.

In line with previous experiments, microgravimetric measurements of SS2343 piezo-electrodes in the absence and presence of 0.5 mol dm^{-3} AHA with and without 0.1 mol dm^{-3} SO_3-Ph-BTP (as an exemplar) have also been performed over longer time periods (~3 hours) without external potential perturbation, to produce solution conditions equivalent to normal EURO-GANEX operation. The simultaneously recorded mass traces and open circuit potential measurements for these experiments are shown in Fig. 13.

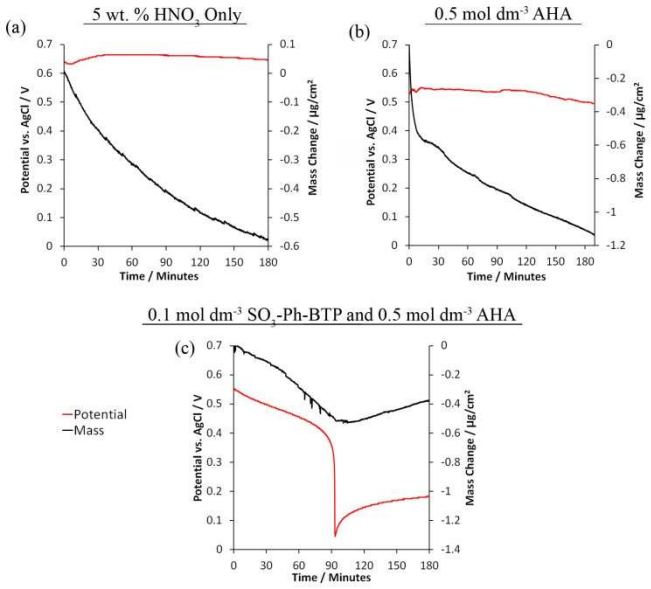

Figure 13. Potentiometry and simultaneously recorded massogram for SS2343 piezoelectrodes in (a) 5% wt. HNO3 only, (b) 0.5 mol dm^{-3} AHA and (c) 0.5 mol dm^{-3} AHA with 0.1 mol dm^{-3} SO_3-Ph-BTP.

This project has received funding from the EURATOM research and training programme 2014-2018 under grant agreement No 755171. The content of this deliverable reflects only the author's view. The European Commission is not responsible for any use that may be made of the information it contains.

Considering first the effect of AHA only, Fig. 13 (b), the recorded open circuit potential remains approximately steady throughout the 3 hour recording period albeit at a slightly lower potential of ~0.54 V, presumably resulting from the reducing solution behaviour of AHA and hydroxylamine, one of the main products of its acid-catalysed hydrolysis [44] (there being a 21% decrease in [AHA] over the 3h recording period, calculated using rate constants for AHA hydrolysis in 1.13 mol dm^{-3} HNO_3 reported by Andrieux *et al.* [9,14]). The simultaneously recorded mass change shows a rapid rate of mass loss within the first 10 minutes of addition which can be attributed to a thinning of any iron oxide/millscale surface film via AHA complexation with Fe^{3+}. However, this quickly recovers to exhibit a similar rate of mass loss to that found in 5% wt. HNO_3 only, Fig. 13(a) – suggesting that the iron oxide/millscale film at the surface is comprised of at least two phases, once of which is susceptible to AHA-complexation driven dissolution, the other requiring the harsher conditions associated with 5% nitric acid solutions to dissolve. Thus, it appears that, with the exception of a lower recorded open circuit potential and a brief initial acceleration of mass loss associated with removal of the less stable constituents of the iron oxide/millscale layer at the surface of ss2343, AHA has very little overall effect on the rate of dissolution of SS2343 in 5% wt. HNO_3.

Turning now to the effect of 0.5 mol dm^{-3} AHA with 0.1 mol dm^{-3} SO_3-Ph-BTP present on SS2343, the same open circuit potential behaviour is observed to that seen for SO_3-Ph-BTP and SO_3-Ph-BTPhen above, Figs 10(b) and 10(c) respectively. However, AHA seems to both affect the initial rate of steel dissolution and result in a more rapid formation of the adsorbed SO_3-Ph-BTP layer, with the potential decrease due to contact with the steel surface occurring earlier at 90 minutes. The earlier onset of formation of the corrosion inhibiting SO_3-Ph-BTP adsorbed layer in the presence of AHA could be due to either the lower steel open circuit potential as a result of the reducing behaviour of AHA and its hydroxylamine hydrolysis product (see above), which allows easier formation of a SO_3-Ph-BTP adsorbed layer under oxidising HNO_3 conditions or increased thinning of any iron oxide/millscale surface film via AHA complexation with Fe^{3+}, resulting in more rapid penetration and formation of the SO_3-Ph-BTP adsorbed layer. In view of the initial rapid dissolution observed early on in Fig. 13(b), which could be related to rapid surface removal of iron deposits, the latter explanation seems most likely, i.e. AHA aids in removal of loose iron from the surface allowing the SO_3-Ph-BTP to form an adsorbed layer with the bare steel surface below. Thus, under convection free conditions with no external potential perturbation, equivalent to normal reprocessing operating conditions, AHA allows more rapid formation of a corrosion inhibiting SO_3-Ph-BTP adsorbed layer.

Without electrochemical mapping throughout a real flowsheet,it is difficult to predict the redox conditions / solution potentials extant in EURO-GANEX process streams.

This project has received funding from the EURATOM research and training programme 2014-2018 under grant agreement No 755171. The content of this deliverable reflects only the author's view. The European Commission is not responsible for any use that may be made of the information it contains.

However, in order to test the effect a potentially oxidative radionuclide may have on open circuit potentials, the same potentiometric/microgravimetric studies described above have also been performed in the presence of 10 mmol dm^{-3} Ce(IV), acting as a Pu (IV) analogue.

4.4. MICROGRAVIMETRIC STUDIES OF SS2343 DISSOLUTION IN THE PRESENCE EXTRACTANTS AND Ce(IV)

Simultaneous OCP and QCM measurements of an SS2343 piezoelectrode in 5% wt. HNO_3 with 10 mmol dm^{-3} ceric ammonium nitrate (Ce(IV)) and in the absence and presence of 0.5 mol dm^{-3} AHA/ 0.1 mol dm^{-3} SO_3-Ph-BTP are shown in Fig. 14.

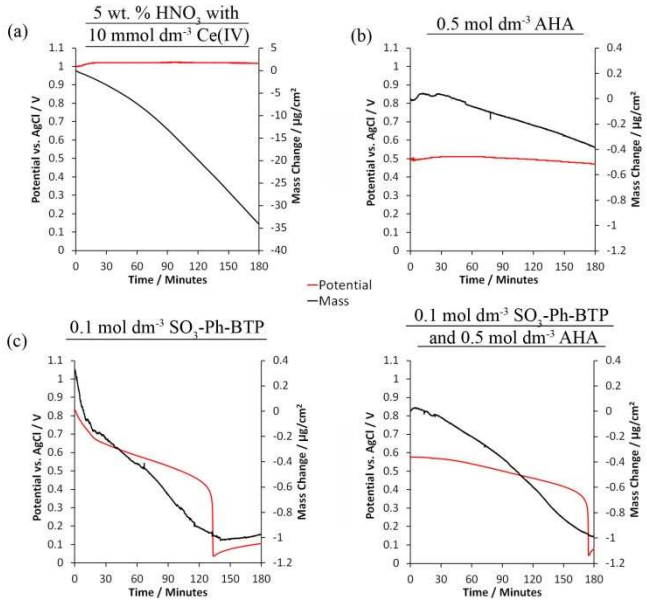

Figure 14. Potentiometry and simultaneously recorded massogram for SS2343 piezoelectrodes in (a) 5% wt. HNO_3 with 10 mmol dm^{-3} Ce(IV), (b) 0.5 mol dm^{-3} AHA with 10 mmol dm^{-3} Ce(IV), (c) 0.1 mol dm^{-3} SO_3-Ph-BTP with 10 mmol dm^{-3} Ce(IV) and (d) 0.5 mol dm^{-3} AHA and 0.1 mol dm^{-3} SO_3-Ph-BTP with 10 mmol dm^{-3} Ce(IV).

Considering first 5% wt. HNO_3 with 10 mmol dm^{-3} Ce(IV) only, Fig. 14(a), Ce(IV) is a highly oxidising cation with an E_0 = +1.72V [45] and this is reflected in the steady state OCP of 1.02V for SS316L in Fig. 14(a). Based on the LSV's for SS316L and SS304L in 5% wt. HNO_3 in Fig. 5, at such a potential the steel will be fully within the transpassive domain and thus expected to be freely corroding. By pushing the steel fully into the transpassive domain the simultaneously recorded rate of mass loss is significantly increased as the protective passive Cr oxide layer is fully oxidized to Cr(VI) allowing attack of the underlying Fe and Ni. Indeed, from Fig. 14(a) total mass loss after 180 minutes is ~58 times greater than that observed in 5% wt. HNO_3 alone, Fig. 13(a), and significant uniform corrosion of the SS2343 piezoelectrode is visible to the naked eye after completion of the experiment.

This project has received funding from the EURATOM research and training programme 2014-2018 under grant agreement No 755171. The content of this deliverable reflects only the author's view. The European Commission is not responsible for any use that may be made of the information it contains.

Turning now to the effect of AHA on SS2343 corrosion in 5% wt. HNO_3 with 10 mmol dm^{-3} Ce(IV), Fig. 14(b), it can be seen that even with Ce(IV) present the recorded open circuit potential of SS2343 remains steady state at ~0.5 V throughout the experiment, similar to that recorded in the presence of AHA in the absence of Ce(IV), Fig. 13(b). Furthermore, some effervescence is observed upon addition of ceric ammonium nitrate to the acidified AHA solution before addition to the QCM cell, the solution remaining colourless not the characteristic yellow colour typical of Ce(IV) solutions above 1 mmol dm^{-3}. The significantly reduced open circuit potential and initial reaction between

$$2Pu^{4+}_{aq} + 2AHA \rightleftharpoons 2Pu(AHA)^{3+} \overset{H^+}{\rightleftharpoons} 2Pu^{4+} + 2NH_3OH^+ + 2CH_3COOH \quad (1)$$

$$2NH_3OH^+ + 2Pu^{4+} \rightarrow 2Pu^{3+} + N_2 + 2H_2O + 4H^+ \quad (2)$$

Ce(IV) and AHA suggests that Ce(IV) is being reduced to Ce(III) before the start of the microgravimetry run. A similar, relatively swift, reduction has been reported by Tkac, Carrott and Barney [43,44,46] for Pu(IV) to Pu(III) in the presence of AHA. The mechanism for this reduction is shown in Eqs. (1) and (2):
Eq. (1) describes the initial complexation of Pu(IV) with AHA followed by the hydrolysis of the complex to form hydroxylamine and acetic acid as well as free Pu(IV). Eq. (2) then describes the reduction of Pu^{4+} to Pu^{3+} by hydroxylamine. Considering the thermodynamic similarity between Pu and Ce [45,47], we expect this mechanism to also apply to Ce(IV). As such, the observed effervescence can be assumed to be N_2 bubbles released by the reduction of Ce(IV) to Ce(III) in Eq. (2). The fast reduction times reported here compared to Tkac, Carrott and Barney [43,44,46] can be attributed to the extremely high concentration ratio of AHA to Ce(IV) (50:1).

Returning to Fig. 14(b), despite some slight variation in the recorded mass within the first 30 minutes of recording, the mass trace shows a similar rate of mass loss to that observed for SS2343 in 5% wt. HNO_3 only, Fig. 13(a). Thus, it appears that while AHA is reducing Ce(IV) to Ce(III) and therefore providing a means of negating attack of the steel surface, through reduction of 4+ oxidation state actinide/lanthanide ions, it does not provide a corrosion inhibition effect similar to di- or tri-hydroxamic acids [48,49].

Turning now to the combined effect of SO_3-Ph-BTP and Ce(IV), Fig. 14(c), within the first 30 minutes the OCP decreases from +0.84V to a level equivalent to that seen for 5% wt. HNO_3 only (~+0.64V), with a simultaneous reduction in the rate of mass loss. After this initial period of potential decrease the same potential trend is observed as that described previously for Fig. 10(c), i.e. slow removal of iron surface deposits followed by formation of an adsorbed layer of SO_3-Ph-BTP at the steel-solution interface. The initial decrease in potential requires further investigation but could be due slow

This project has received funding from the EURATOM research and training programme 2014-2018 under grant agreement No 755171. The content of this deliverable reflects only the author's view. The European Commission is not responsible for any use that may be made of the information it contains.

complexation of Ce(IV) by SO_3-Ph-BTP or reduction of Ce(IV) by SO_3-Ph-BTP. The latter is unlikely as pyridines and bipyridines are not known to be good reductants; indeed, voltammetry of SO_3-Ph-BTP on a glassy carbon electrode, Fig. 7, revealed no oxidation / reduction of SO_3-Ph-BTP in the open circuit potential range of Fig. 14(c). Alternatively, as the rate of mass loss follows the change in potential within the first 30 minutes, this could be a feature of the formation of the protective adsorbed SO_3-Ph-BTP surface film. However, this phenomenon warrants further study to determine if the initial potential suppression is due to complexation or hydrophobic protection of the steel surface.

Finally, simultaneous OCP and QCM measurements of an SS2343 piezoelectrode in 5% wt. HNO_3 with 10 mmol dm^{-3} Ce(IV), 0.5 mol dm^{-3} AHA and 0.1 mol dm^{-3} SO_3-Ph-BTP are shown in Fig. 14(d). Again the open circuit potential behaviour matches that of Fig 14(c), suggesting initial slow dissolution of millscale/iron oxide surface deposits before formation of an adsorbed SO_3-Ph-BTP layer at the metal-solution interface. Furthermore, as described above, the starting potential at the point of electrode insertion (t = 0) is significantly lower than that recorded in the absence of AHA, Fig. 14(a) and Fig. 14(c), there is no rapid mass loss at t <30 minutes observed in solutions of SO_3-Ph-BTP and Ce(IV) only, Fig 14(b) and some effervescence is again observed upon addition of ceric ammonium nitrate. All of these factors suggest that initial reduction of Ce(IV) to Ce(III) is again occurring by AHA and its hydroxylamine hydrolysis product (see above), with subsequent formation of a protective SO_3-Ph-BTP layer.

Thus, the corrosion accelerating behaviour of SO_3-Ph-BTP, SO_3-Ph-BTPhen and AHA is limited to situations where solution redox potentials >+1.1 V, with such ligands actively protecting the surface under normal reprocessing conditions (stagnant flow). Few studies exist on the solution potential that obtains in aqueous reprocessing streams, but from the scant literature that does exist, the solution potential may potentially be up to 1.15 V, depending on actinide species present, acidity, and temperature [27-29]. Indeed, and as shown above, using non-active thermodynamic simulants for Pu(IV)-containing systems (Ce(IV)) potentials as high as 1.02 V can be observed at simulant metal ion concentrations as low as 10 mmol dm^{-3}. Such a potential would only be expected to increase at actinide/lanthanide concentrations more typical of reprocessing streams (especially, as may occur in the near future, during the recycle of higher burnup fuels) and under certain maloperation conditions such as low pH excursions (e.g. as a result of excess HNO_3 introduction), high temperature or a blockage in AHA flow, which as described above under normal operating conditions actively reduces Pu(IV) to Pu(III). Thus, depending on safety case assessment, the use of higher-grade steels (e.g. SS310) or transpassive corrosion inhibitors may be necessary to mitigate the effects of a maloperation if AHA, SO_3-Ph-BTP or SO_3-Ph-BTPhen based reprocessing flowsheets are adopted for full scale nuclear fuel recycling in the future.

This project has received funding from the EURATOM research and training programme 2014-2018 under grant agreement No 755171. The content of this deliverable reflects only the author's view. The European Commission is not responsible for any use that may be made of the information it contains.

5. CORROSION BEHAVIOUR OF SO_3-Ph-BTBP IN NITRIC ACID SOLUTIONS

Linear sweep voltammograms and associated polarisation curves for SS304L electrodes in SO_3-Ph-BTBP concentrations from 0.1 to 100 mmol dm^{-3} are shown in Fig. 15.

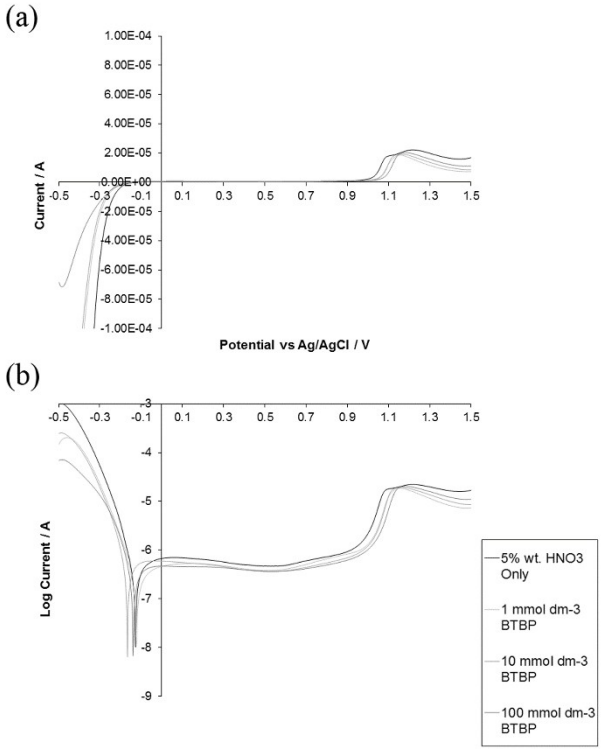

Figure 15. Linear sweep voltammogram (a) and polarisation curve (b) for SS304L in 1.13 mol dm^{-3} HNO_3 and SO_3-Ph-BTBP concentrations from 0.1 to 100 mmol dm^{-3}.

From the LSV and polarisation curve of Fig. 15(a) and (b), it can be seen that there is very little difference in the current across the steel passive range (~-0.1 to 1V) at all SO_3-Ph-BTBP concentrations tested, suggesting SO_3-Ph-BTBP has little effect on the Cr_2O_3/Fe_3O_4 protective passive oxide film. This is further supported by the lack of movement of the corrosion potential, E_{corr}, in the polarisation curve of Fig. 15(b), suggesting no change to the region of steel passivity compared to 1.13 mol dm^{-3} HNO_3 only.

In the region of potential < -0.1V, the current decreases as SO_3-Ph-BTBP increases, suggesting that hydrogen evolution at the electrode surface is inhibited by the presence of SO_3-Ph-BTBP. Similarly in the region of transpassivity, > 1 V, where the Cr(III) passive film is oxidised to soluble Cr(VI) allowing free dissolution of iron as Fe^{3+} [22], currents are slightly lower in the presence of SO_3-Ph-BTBP than in 1.13 mol dm^{-3} HNO_3 only. This would suggest that SO_3-Ph-BTBP has a small corrosion inhibition effect under such oxidising conditions. Both these effects may be explained by the formation of an adsorbed layer of SO_3-Ph-BTBP at the metal-solution interface that forms a barrier

This project has received funding from the EURATOM research and training programme 2014-2018 under grant agreement No 755171. The content of this deliverable reflects only the author's view. The European Commission is not responsible for any use that may be made of the information it contains.

against HNO_2, the active corrosive species in this environment [15,31], inhibiting both Fe dissolution under conditions of transpassive dissolution and reducing hydrogen evolution under conditions of reductive dissolution by hydrophobically restricting electrolyte access to the electrode surface. Indeed, such corrosion inhibition of mild carbon steels through weak surface adsorption of pyridine derivatives in stagnant solution condition acidic environments (similar to those used here) has been previously reported [32-34]. However, under the hydrodynamic flow conditions encountered in reprocessing environments, the shear stress is likely to desorb SO_3-Ph-BTBP molecules from the steel surface and therefore reduce this corrosion inhibition effect [50].

Linear sweep voltammograms and associated polarisation curves for SS316L electrodes in SO_3-Ph-BTBP concentrations from 0.1 to 100 mmol dm^{-3} are shown in Fig. 16.

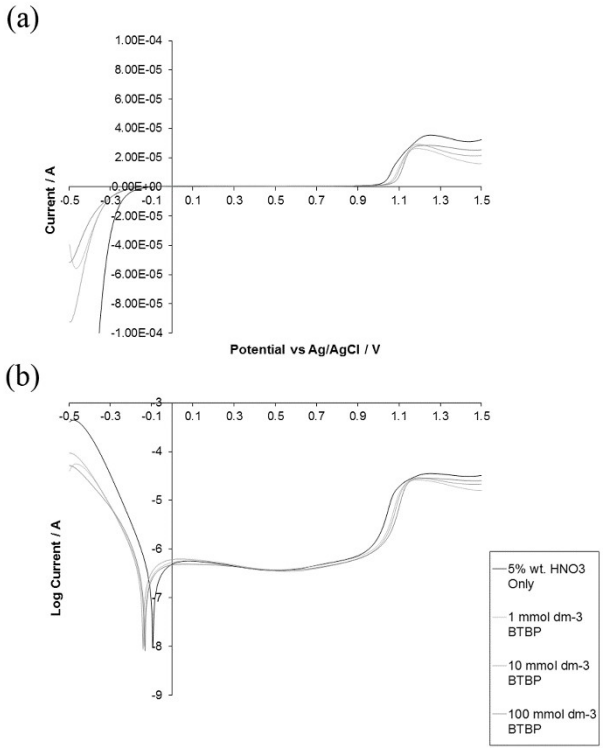

Figure 16. Linear sweep voltammogram (a) and polarisation curve (b) for SS316L in 1.13 mol dm^{-3} HNO^3 and SO_3-Ph-BTBP concentrations from 0.1 to 100 mmol dm^{-3}.

From the LSV and polarisation curve of Fig. 16(a) and (b), it can be seen that again there is very little difference in the current across the steel passive range at all SO_3-Ph-BTBP concentrations tested. As shown in Fig.15 for SS304L electrodes (and discussed above), in the region of active dissolution and transpassive dissolution currents are significantly lower than those recorded in the presence of 1.13 mol dm^{-3} HNO_3 only. Again this suggests the formation of an adsorbed layer of SO_3-Ph-BTBP at the metal-solution interface, providing a barrier that restricts electrolyte access to the electrode surface. However, while measured currents for SS316L in the presence/absence of SO_3-Ph-BTBP

This project has received funding from the EURATOM research and training programme 2014-2018 under grant agreement No 755171. The content of this deliverable reflects only the author's view. The European Commission is not responsible for any use that may be made of the information it contains.

are almost the same in the region of hydrogen evolution as those recorded for SS304L electrodes, Fig. 16(b) and Fig. 15(b) respectively; in the region of transpassive dissolution currents recorded on SS316L electrodes are almost double those of SS304L electrodes. Such an observation may be explained by differences in silica content between SS304L and SS316L (1.000% vs. 0.480% by mass [51,52]). Low Si content stainless steels have been shown to have increased susceptibility to transpassive intergranular corrosion in nitric acid environments [15,53].

The lack of any corrosion enhancement in the presence of SO_3-Ph-BTBP for both SS304L and SS316L is surprising considering the ligands known affinity for actinide/lanthanide 3+ oxidation state species [1-3] and the previously reported ability of similar BTP derivatives to complex strongly with Fe(II) species [54]. This may in part be due to the requirement for a conformational change in SO_3-Ph-BTBP from its preferred *trans*-conformation to the less favoured *cis*-conformation prior to metal binding [5-7], Fig. 17.

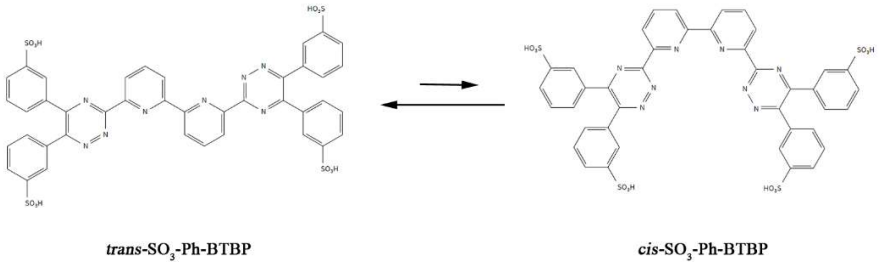

Figure 17. *Cis*- and *trans*- conformations of SO_3-Ph-BTBP.

Such a requirement for a conformational change has been proposed, at least in part, to be responsible for slow kinetics of extraction of both An(III) and Ln(III) species by hydrophobic $CyMe_4$ based versions of BTBP compared to $CyMe_4$ based equivalents of BTP and BTPhen [5-7]. Thus, we would expect such extraction kinetics to also be slow for Fe^{3+} extraction, resulting in the lack of an observed increase in the rate of reductive or transpassive dissolution for both SS304L and SS316L (Figs. 15 and 16). This conclusion is in keeping with our findings above that the kinetically faster hydrophilic sulfonated derivatives of BTPhen and BTP act as corrosion accelerators in the transpassive regime..

This project has received funding from the EURATOM research and training programme 2014-2018 under grant agreement No 755171. The content of this deliverable reflects only the author's view. The European Commission is not responsible for any use that may be made of the information it contains.

6. CONCLUSIONS AND FURTHER WORK

Under normal operation conditions, the open circuit potential of 5% wt. HNO_3 is on the edge of the transpassive domain of common process steel 304L and 316L.
AHA has been shown to have little effect on either steel passivation or dissolution at applied potentials < 1.1 V. However, at transpassive dissolution potentials > 1.1 V, AHA complexes with Fe^{3+}, inhibiting secondary passivation and driving transpassive dissolution of both SS304L and SS316L. In this context, which represents a maloperations condition, it presents a corrosion risk.

SO_3-Ph-BTP or SO_3-Ph-BTPhen under stagnant flow conditions result in the formation of a thin absorbed ligand layer at the metal-solution interface. This layer forms a barrier against HNO_2, the active corrosive species in this environment at the electrode surface, acting as a corrosion inhibitor. However, under oxidative maloperation conditions, e.g. potentials > 1.1 V, SO_3-Ph-BTPhen and SO_3-Ph-BTP enhance transpassive dissolution through Fe^{3+} sequestration. In this maloperations context, they present a corrosion risk.

In the presence of additional AHA and under normal operating conditions, the absorbed SO_3-Ph-BTP ligand layer is more rapidly formed at the metal-solution interface. However, under oxidative maloperation conditions i.e. potentials > 1.1 V, both SO_3-Ph-BTPhen/SO_3-Ph-BTP and AHA enhance transpassive dissolution through Fe^{3+} sequestration, resulting in a significantly enhanced dissolution rate compared to either chemical in isolation. Again, in this maloperations context, they represent a corrosion risk.

Finally, tests in the presence of a potentially oxidative radionuclide ion (Ce(IV) acting as a Pu(IV) analogue) show that AHA rapidly reduces Ce(IV) to Ce(III), inhibiting oxidative attack of process steels. Further, the corrosion inhibiting absorption of SO_3-Ph-BTP at the steel surface persists in the presence of Ce(IV), even in the absence of AHA. Thus, all three of these ligands may act to inhibit corrosion due to solution-phase imposed oxidative stresses – either by reduction of the entity causing the stress or by hydrophobic protection of the steel surface.

In the case of SO_3-Ph-BTBP, SS304L steels show no change in either their range of passivation or corrosion potential (E_{corr}) up to ligand concentrations of 100 mmol dm^{-3}. When electrochemically driven cathodic and into a region of active dissolution, hydrogen evolution is found to be decreased in the presence of SO_3-Ph-BTBP. Conversely, if SS304L is driven anodically into the region of transpassive dissolution SO_3-Ph-BTBP has been shown to reduce the rate of transpassive dissolution. The lack of any obvious corrosion acceleration due to Fe^{3+} complexation may be attributed to the

This project has received funding from the EURATOM research and training programme 2014-2018 under grant agreement No 755171. The content of this deliverable reflects only the author's view. The European Commission is not responsible for any use that may be made of the information it contains.

complexation kinetics of SO_3-Ph-BTBP as a result of a required *trans*- to *cis*-conformational change.

Thus, the hierarchy of TRU ligand corrosivity at potentials > 1.1 V (equivalent to those under maloperation) is as follows: SO_3-Ph-BTBP < AHA < SO_3-Ph-BTPhen < SO_3-Ph-BTP.

Recommendations for further work: Given the uncertainties as to the redox stresses that exist throughout the GANEX process, it is recommended that a map of the solution redox potentials that obtain throughout flowsheet is compiled – both under normal and maloperation conditions.

Such a map would also allow for an assessment of the potential role of (particularly) aqueous phase complexants in decreasing the oxidative power of potential solution phase oxidants (such as we suspect is occurring in the case of Ce(IV) (as a Pu surrogate) with SO_3-Ph-BTP). However, the role of the aqueous phase ligands as corrosion inhibitors via the formation of hydrophobic protective film, comprised of the adsorbed ligands, at the steel surface also needs to be explored – especially under the high shear flow conditions that may occur in modern plant such as centrifugal contactors.

The work reported here has indicated the potential vulnnerability of common process steels to corrosion damage, especially under maloperation conditions. Thus it is also recommended that studies are repeated using higher grade steels that may be used as process alternatives (e.g. SS310, 18/10 NAG) and in the presence of corrosion inhibiting additives that may be sympathetic to the overall GANEX chemistry. One candidate here is CDTA whose action in this regard will be discussed below.

Finally, as alternative ligands are currently being assessed for use in GANEX-2, these too should be subject to corrosion vulnerability assessments. Thus, it is recommended that the studies described above are repeated in the presence of the new aqueous phase extraction agent, py-tri-diol.

This project has received funding from the EURATOM research and training programme 2014-2018 under grant agreement No 755171. The content of this deliverable reflects only the author's view. The European Commission is not responsible for any use that may be made of the information it contains.

REFERENCES

[1] A. Geist, U. Mullich, G. Modolo, and A. Wilden, Selective aqueous complexation of actinides with hydrophilic BTP and BTBP: Towards improved i-SANEX processes, Organisation for Economic Co-operation and Development - Nuclear Energy Agency, San Francisco, USA, 2012, pp. 1-9.

[2] P.J. Panak and A. Geist, Complexation and Extraction of Trivalent Actinides and Lanthanides by Triazinylpyridine N-Donor Ligands, Chem. Rev., 113 (2013) 1199-1236.

[3] A. Geist, U. Mullich, D. Magnusson, P. Kaden, G. Modolo, A. Wilden, and T. Zevaco, Actinide(III)/Lanthanide(III) Separation Via Selective Aqueous Complexation of Actinides(III) using a Hydrophilic 2,6-Bis(1,2,4-Triazin-3-Yl)-Pyridine in Nitric Acid, Solvent Extr. Ion Exch., 30 (2012) 433-444.

[4] M.J. Hudson, C.E. Boucher, D. Braekers, J.F. Desreux, M.G.B. Drew, M.R.S. Foreman, L.M. Harwood, C. Hill, C. Madic, F. Marken, and T.G.A. Youngs, New bis(triazinyl) pyridines for selective extraction of americium(III), New J. Chem., 30 (2006) 1171-1183.

[5] F.W. Lewis, L.M. Harwood, M.J. Hudson, M.G.B. Drew, A. Wilden, M. Sypula, G. Modolo, T. Vu, J. Simonin, G. Vidick, N. Bouslimani, and J.F. Desreux, From BTBPs to BTPhens: The effect of ligand pre-organisation on the extraction properties of quadridentate bis-triazine ligands, Proc. Chem., 7 (2012) 231-238.

[6] F.W. Lewis, L.M. Harwood, M.J. Hudson, M.G.B. Drew, V. Hubscher-Bruder, V. Videva, F. Arnaud-Neu, K. Stamberg, and S. Vyas, BTBPs versus BTPhens: Some reasons for their differences in properties concerning the partitioning of minor actinides and the advantages of BTPhens, Inorg. Chem., 52 (2013) 4993-5005.

[7] G. Benay, R. Schurhammer, and G. Wipff, Basicity, complexation ability and interfacial behavior of BTBPs: a simulation study, Phys. Chem. Chem. Phys., 13 (2011) 2922-2934.

[8] F.P.L. Andrieux, C. Boxall, I. May, and R.J. Taylor, The hydrolysis of hydroxamic acid complexants in the presence of non-oxidising metal ions 2: Neptunium (IV) ions, J. Solution Chem., 37 (2008) 215-232.

[9] F.P.L. Andrieux, C. Boxall, and R.J. Taylor, Acetohydroxmatoiron(III) Complexes: Thermodynamics of Formation and Temperature Dependent Speciation, J. Solution Chem., 37 (2008) 1511-1527.

[10] C. Donik, I. Paulin, and M. Jenko, Influence of MnS inclusions on the corrosion of austenitic stainless steels, Mater. Tehnol., 44 (2010) 67-72.

[11] G. Sauerbrey, Verwendung von Schwingquarzen zur Wägung dünner Schichten und zur Mikrowägung, Z. Phys., 155 (1959) 206-222.

[12] C. Gabrielli, M. Keddam, and R. Torresi, Calibration of the Electrochemical Quartz Crystal Microbalance, J. Electrochem. Soc., 139 (1991) 2657-2660.

[13] G.L. Borges, K.K. Kanazawa, J.G. Gordon, K. Ashley, and J. Richer, An in-situ electrochemical quartz crystal microbalance study of the underpotential deposition of copper on Au(111) electrodes, J. Electroanal. Chem., 364 (1994) 281-284.

[14] F.P.L. Andrieux, C. Boxall, and R.J. Taylor, The hydrolysis of hydroxamic acid complexants in the presence of non-oxidising metal ions 1: Ferric Ions, J. Solution Chem., 36 (2007) 1201-1217.

[15] P. Fauvet, F. Balbaud, R. Robin, Q.T. Tran, A. Mugnier, and D. Espinoux, J. Nucl. Mater., 375 (2008) 52-64.

This project has received funding from the EURATOM research and training programme 2014-2018 under grant agreement No 755171. The content of this deliverable reflects only the author's view. The European Commission is not responsible for any use that may be made of the information it contains.

[16] J.S. Armijo, Corrosion, 24 (1968) 24-30.
[17] J.A. Amberson and G. Svehla, Anal. Proc. (London), 23 (1986) 443-446.
[18] D. Arrigan, B. Deasy, J.D. Glennon, B. Johnston, and G. Svehla, Analyst, 118 (1993) 355-359.
[19] G.L. Song, C.N. Cao, and H.C. Lin, Corros. Sci., 36 (1994) 165-169.
[20] G. Song, Corros. Sci., 47 (2005) 1953-1987.
[21] C.-O.A. Olsson and D. Landolt, Electrochim. Acta, 48 (2003) 1093-1104.
[22] N. Padhy, R. Paul, U.K. Mudali, and B. Raj, Appl. Surf. Sci., 257 (2011) 5088-5097.
[23] M. Pourbaix, Iron, in: M. Pourbaix (Ed.), Atlas of electrochemical equilibria in aqueous solutions, NACE International, 1974, pp. 307-321.
[24] A. Samuni and S. Goldstein, J. Phys. Chem. A, 115 (2011) 3022-3028.
[25] T.R. Oliver and W.A. Waters, J. Chem. Soc. B, (1971) 677-681.
[26] S. Shackleford, Development of an EQCM based sensor for metal ions. 114-116. 2002. University of Central Lancashire. http://ethos.bl.uk/OrderDetails.do?uin=uk.bl.ethos.272808
[27] B. Gwinner, M. Auroy, D. Mas, A. Saint-Jevin, and S. Pasquier-Tilliette, J. Nucl. Mater., 428 (2012) 110-116.
[28] D.N. Hess, L. Rice, B. Willis, E.S. Snavely, and W.E. Clark, Corrosion of stainless steel in acidic nitrate waste solutions from processing stainless steel reactor fuels. ORNL-3474, 1-35. 1963. USA, Oak Ridge National Laboratory.
[29] C. Kato, F. Ueno, M. Yamamoto, Y. Ban, G. Uchiyama, Y. Nojima, and S. Fujine, ECS Trans., 53 (2013) 45-55.
[30] G. Le Gurun, C. Boxall, and R.J. Taylor, Modelling the photocatalytic reduction of actinide and lanthanide ions: A study by photopotentiometry, ECS Meeting Abstracts: 207th Meeting of the Electrochemical Society, Quebec City, Canada, 2005.
[31] D. Sicsic, F. Balbaud-Celerier, and B. Tribollet, Mechanism of Nitric Acid Reduction and Kinetic Modelling, Eur. J. Inorg. Chem., 2014 (2014) 6174-6184.
[32] S.A. Abd El-Maksoud and A.S. Fouda, Some pyridine derivatives as corrosion inhibitors for carbon steel in acidic medium, Mater. Chem. Phys., 93 (2005) 84-90.
[33] U. Ergun, D. Yuzer, and K.C. Emregul, The inhibitory effect of bis-2,6-(3,5-dimethylpyrazolyl)pyridine on the corrosion behaviour of mild steel in HCl solution, Mater. Chem. Phys., 109 (2008) 492-499.
[34] K. Tebbji, H. Oudda, B. Hammouti, M. Benkaddour, M. El Kodadi, and A. Ramdani, Inhibition effect of two organic compounds pyridine-pyrazole type in acidic corrosion of steel, Colloids and Surfaces A: Physicochemical and Engineering Aspects, 259 (2005) 143-149.
[35] R.J. Wilbraham and C. Boxall, The effect of acetohydroxamic acid on stainless steel corrosion in nitric acid, Electrochemistry Communications, 62 (2016) 52-55.
[36] R.J. Wilbraham. Surface Decontamination by Photocatalysis. 1-300. 2012. Lancaster University. Ref Type: Thesis/Dissertation
[37] L.C. Bannister and U.R. Evans, CLXXVII. - The passivity of metals. Part V. The potential-time curves of some iron alloys, J. Soc. Chem., (1930) 1361-1374.
[38] Z. Qin, B. Demko, J.J. Noël, D.W. Shoesmith, F. King, R. Worthingham, and K. Keith, Localized dissolution of millscale-covered pipeline steel surfaces, Corrosion, 60 (2004) 906-914.
[39] G.H. Cartledge, The activation and passivation of stainless steel in aerated sulfuric acid, J. Electrochem. Soc., 104 (1957) 420-426.

This project has received funding from the EURATOM research and training programme 2014-2018 under grant agreement No 755171. The content of this deliverable reflects only the author's view. The European Commission is not responsible for any use that may be made of the information it contains.

[40] D. Itzhak and E. Aghion, Corrosion behaviour of hot-pressed austenitic stainless steel in H2SO4 solutions at room temperature, Corros. Sci., 23 (1983) 1085-1094.
[41] C.G. Bathke, B.B. Ebbinghaus, B.A. Collins, B.W. Sleaford, K.R. Hase, M. Robel, R.K. Wallace, K.S. Bradley, J.R. Ireland, G.D. Jarvinen, M.W. Johnson, A.W. Prichard, and B.W. Smith, The attractiveness of materials in advanced nuclear fuel cycles for various proliferation and theft scenarios, Nucl. Technol., 179 (2012) 5-30.
[42] K. Bell, C. Carpentier, M.J. Carrott, A. Geist, C. Gregson, X. Heres, D. Magnusson, R. Malmbeck, F. McLachlan, G. Modolo, U. Mullich, M. Sypula, R.J. Taylor, and A. Wilden, Progress towards the development of a new GANEX process, Proc. Chem., 7 (2012) 392-397.
[43] M.J. Carrott, K. Bell, J. Brown, A. Geist, C. Gregson, X. Heres, C. Maher, R. Malmbeck, C. Mason, G. Modolo, U. Mullich, M. Sarsfield, A. Wilden, and R.J. Taylor, Development of a new flowsheet for co-separating the transuranic actinides: The "EURO-GANEX" process, Solvent Extr. Ion Exch., 32 (2014) 447-467.
[44] P. Tkac, M. Precek, and A. Paulenova, Redox reactions of Pu(IV) and Pu(III) in the presence of acetohydroxamic acid in HNO3 solutions, Inorg. Chem., 48 (2009) 11935-11944.
[45] L.R. Morss, Yttrium, Lanthanum and the Lanthanide Elements, in: A.J. Bard, R. Parsons, and J. Jordan (Eds.), Standard Potentials in Aqueous Solution, Marcel Dekker, 1985, pp. 587-631.
[46] G.S. Barney, A kinetic study of the reaction of plutonium(IV) with hydroxylamine, Journal of Inorganic and Nuclear Chemistry, 38 (1976) 1677-1681.
[47] L. Martinot and J. Fuger, The Actinides, in: A.J. Bard, R. Parsons, and J. Jordan (Eds.), Standard Potentials in Aqueous Solution, Marcel Dekker, 1985, pp. 631-675.
[48] A. Alagta, I. Felhosi, I. Bertoti, and E. Kalman, Corrosion protection properties of hydroxamic acid self-assembled monolayer on carbon steel, Corros. Sci., 50 (2008) 1644-1649.
[49] A. Alagta. Investigation of carbon steel corrosion inhibition by hydroxamic acids. 1-92. 2009. Budapest University of Technology and Economics. 17-12-2009.
Ref Type: Thesis/Dissertation
[50] Kosari, A.; Moayed, M. H.; Davoodi, A.; Parvizi, R.; Momeni, M.; Eshghi, H.; Moradi, H. (2014). Electrochemical and quantum chemical assessment of two organic compounds from pyridine derivatives as corrosion inhibitors for mild steel in HCl solution under stagnant condition and hydrodynamic flow. Corros. Sci. 78, 138-150.
[51] Hayward, T. M.; Svishchev, I. M.; Makhija, R. C. (2003). Stainless steel flow reactor for supercritical water oxidation: corrosion tests. Journal of Supercritical Fluids 27 (3), 275-281.
[52] Caire, J. P.; Laurent, F.; Cullie, S.; Dalard, F.; Fulconis, J. M.; Delagrange, H. (2003). AISI 304 L stainless steel decontamination by a corrosion process using cerium IV regenerated by ozone - Part I: Study of the accelerated corrosion process. J. Appli. Electrochem. 33 (8), 703-708.
[53] Armijo, J. S. (1968). Intergranular Corrosion of Nonsensitized Austenitic Stainless Steels. Corrosion 24 (1), 24-30.
[54] Byrne, J. P.; Kitchen, J. A.; Gunnlaugsson, T. (2014). The btp [2,6-bis(1,2,3-triazol-4-yl)pyridine] binding motif: a new versatile terdentate ligand for supramolecular and coordination chemistry. Chem. Soc. Rev. 43 (15), 5302-5325.

This project has received funding from the EURATOM research and training programme 2014-2018 under grant agreement No 755171. The content of this deliverable reflects only the author's view. The European Commission is not responsible for any use that may be made of the information it contains.

STUDY OF PROCESS STEEL CORROSION IN THE PRESENCE OF HYDRAZINE

1. INTRODUCTION

In the EURO-GANEX 1st cycle, DEHiBA in OK or TPH is used to selectively extract U, Tc and Np, the latter two species being subsequently reduced and scrubbed back into the aqueous phase using hydrazine, leaving a pure U product in the DEHiBA organic phase. The effect of hydrazine on the corrosion of process steels foreseen for use in the GANEX process therefore needs to be explored. However, hydrazine has been used as a corrosion inhibitor. Thus, its study in the context of the GANEX process may be especially useful given the corrosion vulnerabilities highlighted in the last section.

Hydrazine and hydrazine derivatives have been utilised as corrosion inhibitors in various environments as early as the 1950s [1]. A considerable literature base exists on the mechanism of hydrazine corrosion inhibition of mild/carbon steels in aggressive ions such as Cl^- and SO_4^{2-} [2-5]. The mechanism of inhibition is believed to be through adsorption of a hydrazine film at anodic pore sites, causing a blocking of such sites and an overall reduction in corrosive attack through pitting [5]. Indeed, a number of hydrazine derivatives have been developed to improve adsorption and complex film formation on mild/carbon steels of the form $FeX_2(N_2H_4)_2$ in order to allow their deployment in chloride environments such as ground waters [3-5].

The use of hydrazine for corrosion suppression on stainless steels of the type foreseen for use in a scaled-up GANEX process is somewhat more limited compared to the mild and carbon steel literature. Hydrazine is commonly used in nuclear power plant boilers (light water reactors) as a corrosion inhibitor [6]. As hydrazine passes through the boiler it is either oxidised, thermally decomposed or radiolysed [7]. The first of these reactions is of most interest with regards to corrosion inhibition. If hydrazine contacts an un-oxidised metal surface it slowly oxidises with the net reaction:

$$N_2H_2 + O_2 \rightarrow N_2 + 2H_2O \quad (1)$$

The removal of dissolved oxygen in the primary loop reduces anodic dissolution of the stainless steel used in the boiler structure, with iron corrosion rates directly proportional to dissolved O_2 concentration, preventing intergranular corrosion. Furthermore, the formation of 3+ oxidation state iron oxide scale particles are also prevented through the reduction of Fe oxides and hydroxides:

This project has received funding from the EURATOM research and training programme 2014-2018 under grant agreement No 755171. The content of this deliverable reflects only the author's view. The European Commission is not responsible for any use that may be made of the information it contains.

$$N_2H_4 + 6Fe_2O_3 \rightarrow N_2 + 2H_2O + 4Fe_3O_4 \quad (2)$$

$$N_2H_4 + 2Fe_2O_3 \rightarrow N_2 + 2H_2O + 4FeO \quad (3)$$

$$N_2H_4 + 2FeO \rightarrow 2Fe + N_2 + 2H_2O \quad (4)$$

$$N_2H_4 + 4Fe(OH)_3 \rightarrow 4Fe(OH)_2 + N_2 + 4H_2O \quad (5)$$

Hydrazine also has some effect on the generation of hydrogen peroxide by gamma radiolysis of water. The effect of hydrazine on reactor pressure vessel/primary containment vessel steel under gamma irradiation has been reported by Nakano *et al.* [8]. In an N_2 atmosphere hydrazine was found to not only reduce corrosion rates of the tested stainless steels through removal of oxygen directly but also through the removal of hydrogen peroxide which may also generate oxygen indirectly through the reaction:

$$H_2O_2 \rightarrow H_2O + 0.5\ O_2 \quad (6)$$

The most pertinent work with regards to the effect of hydrazine on reprocessing steel corrosion is that by Abraham *et al.* [9]. The authors tested SS304L plate coupons in 2 mol dm^{-3} boiling HNO_3 in the presence and absence of up to 83 mmol dm^{-3} hydrazine. Two corrosion inhibition effects in the presence of hydrazine are noted by the authors.

First, the recorded corrosion potential is shown to be significantly more cathodic in the presence of hydrazine than in its absence. This is attributed by the authors to a change in the amount of HNO_2 in solution, the electrochemically active species involved in controlling the steel corrosion potential in higher concentrations of nitric acid [10]. Hydrazine is frequently used as a stabiliser to supress oxidation of iron and plutonium in PUREX streams through the removal of nitrous acid [11] and reacts with HNO_2 via:

$$N_2H_5^+ + HNO_2 \rightarrow HN_3 + 2H_2O + H^+ \quad (7)$$

$$HN_3 + HNO_2 \rightarrow N_2O + N_2 + H_2O \quad (8)$$

HNO_2 controls the potential by production of NO_2 and NO through an autocatalytic process, details of which can be found later in this report and in [12]. However, the reduction of these species has a highly oxidising E^0 of ~0.8V. Thus, by removing HNO_2 with hydrazine it can seen why a more cathodic E_{corr} is observed.

Secondly, the authors report the tentative observation of a secondary passive region at >1V vs. SCE in the presence of hydrazine [11]. They attribute this to the reduction of Cr(VI) absorbed transpassive products to insoluble Cr(III) species by hydrazine:

$$4CrO_4H^- + 3N_2H_5^+ + 13H^+ + 8H_2O \rightarrow 4[Cr(OH_2)_6]^{3+} + 3N_2 \quad (9$$

This project has received funding from the EURATOM research and training programme 2014-2018 under grant agreement No 755171. The content of this deliverable reflects only the author's view. The European Commission is not responsible for any use that may be made of the information it contains.

However, it should be noted that polarisation results for this region in the absence of hydrazine are not presented and no further surface analysis is carried out by the authors to support the above reduction of Cr(VI) species to Cr(III).

Thus, in the following sections the effect of 1.5 mol dm^{-3} HNO_3 and 0.2 mol dm^{-3} hydrazine, the same as that in the suggested flowsheet for 1st cycle EURO-GANEX, at RTP on two different process steels is explored, namely SS316L and 18/10 NAG (Nitric Acid Grade). The latter grade is specialist grade of nitric acid resistant stainless steel plate used in dissolvers or areas of high temperature/high nitric acid in the Thermal Oxide Reprocessing Plant (THORP) at Sellafield, Cumbria, UK and constitutes our first exploration of alternative process steels as recommended at the end of the last section.

2. EXPERIMENTAL

As hydrazine is available in much greater quantities than any of the previously tested extraction ligands, a larger volume traditional corrosion cell configuration was used for experiments reported here. 450 ml of 1.5 mol dm^{-3} HNO_3 was used in a 1 L flat bottom flask per experiment. When hydrazine was used, a concentration of 0.2 mol dm^{-3} was added prior to solution sparging (see below).

Working electrodes were created from 100 mm long, 12.7 mm diameter SS316L rod (Goodfellow, UK) and a one and a half inch diameter 18/10 NAG plate sample (Sellafield Ltd., Cumbria, UK). In the latter materials the plate was cut so that the face of the electrode was created from material in the rolling direction with a depth of about 30 mm. Both materials were then turned down on a metal working lathe to a cylinder with a diameter of 9.65 mm and degreased of machine oil by repeatedly washing with toluene before mounting. Samples were first mounted onto threaded brass rod supports using a conductive silver-loaded epoxy (RS Components Ltd., Northants, UK) before casting the entire assembly in epoxy resin (CY1300, Aeorpia Ltd., UK) at 60°C.

Before each experiment working electrodes were polished using decreasing grades of SiC paper (240, 600, 800 and 1200 grit), followed by diamond polishing pastes (10, 6, 3 and 1 µm). Immediately before immersion in test solutions, samples were given a final clean/degrease using successive washes of acetone, deionised water and methanol respectively, as per ASTM G1-03 [13]. The electrode was then mounted on a threaded SS304L stainless steel rod sealed in glass so that only the steel working electrode face is exposed to solution.

The reference electrode was carefully setup to avoid any chloride contamination of the nitric acid solution. First, a saturated calomel (SCE) double junction reference electrode

This project has received funding from the EURATOM research and training programme 2014-2018 under grant agreement No 755171. The content of this deliverable reflects only the author's view. The European Commission is not responsible for any use that may be made of the information it contains.

was prepared (EDT, UK), with an outer junction fill of 1 mol dm^{-3} KNO_3. This was then further placed in a CoralPor™ fritted luggin capillary with the tip placed next to the steel surface, creating a triple junction system. To complete the three electrode cell, two large area platinum mesh counter electrodes were immersed in solution to give an even current distribution around the working electrode.

Linear sweep voltammetry (LSV) and linear polarisation resistance (LPR) were used as the predominant experimental techniques to assess *in situ* corrosion behaviour. Both measurements were carried out according to the relevant ASTM standards [14,15].

After an open circuit potential (OCP) equilibration period of 2-3 hours, an initial small window (-25 mV to + 25 mV of OCP) linear polarisation resistance (LPR) measurement was taken to ascertain the corrosion rate of the steel. After this initial scan a larger window LSV was performed from -0.2V vs. OCP to +1.5V vs. the reference electrode to determine the general electrochemical corrosion behaviour of the steel in the presence of varying concentrations of hydrazine. All such electrochemical experiments described here are performed at scan rates of 0.5 mV/s. Solutions were also either sparged with air or N_2 for one hour prior to electrode immersion and during the equilibration period to investigate the effects of the presence and absence of oxygen respectively.

All experiments were performed in triplicate.

3. STUDIES OF SS316L IN 1.5 mol dm^{-3} HNO_3 WITH AND WITHOUT HYDRAZINE

Before discussing the results of the large LSV measurements it is first useful to again define the regions expected in a typical potential vs. current plot obtained using this method. An example annotated LSV plot of the SS316L rod electrode in 1.15 mol dm^{-3} HNO_3 is shown in Figure 1.

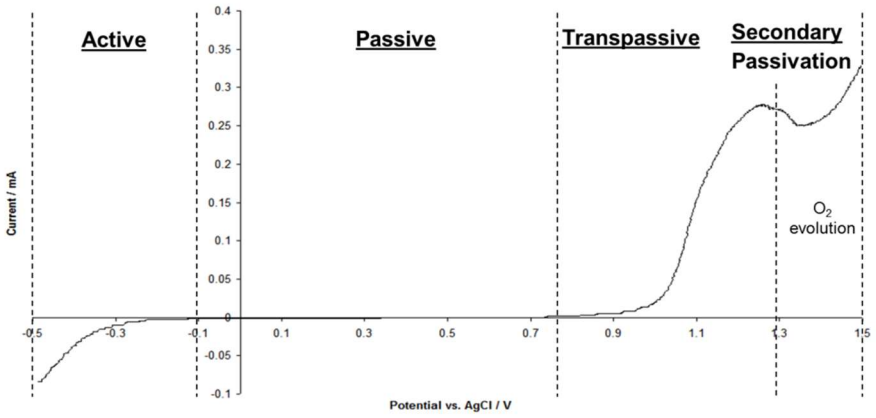

Figure 1: Annotated LSV of a 10 mm area SS316L rod electrode in 1.15 mol dm^{-3} HNO_3.

This project has received funding from the EURATOM research and training programme 2014-2018 under grant agreement No 755171. The content of this deliverable reflects only the author's view. The European Commission is not responsible for any use that may be made of the information it contains.

At the most cathodic applied potentials, the electrode is said to be actively corroding and a reduction current is observed due to hydrogen evolution. As the potential increases anodically a point is reached at which a Cr_2O_3 passive film can exist. This oxide film blocks further attack of the underlying metal and the surface is said to be 'passivated', i.e. no net mass change is occurring as indicated by the extremely low currents in this region. As the potential becomes more anodic the insoluble Cr(III)oxide passive film begins to become slowly oxidised to a soluble Cr(VI) oxide and the metal surface becomes 'transpassive', beginning again to corrode as indicated by the steadily increasing positive current. Some of the observed current above +1.2V may be due to the evolution of oxygen through breakdown of the solvent. Alternatively, secondary passivation may occur, whereby the rate of current increase slows as the anodic potential increases. Within this region dissolution does still occur, but is partially inhibited by a porous layer predominantly – but not exclusively – comprised of the iron oxide, hematite, generated at the steel surface due to the local solubility product of iron being exceeded as a considerable amount of Fe^{3+} ions are dissolved from the metal.

LSV and Tafel (log current density vs. potential) plots for the triplicate experiments performed on SS316L in the absence of N_2H_2 and purged with air are shown in Figure 2.

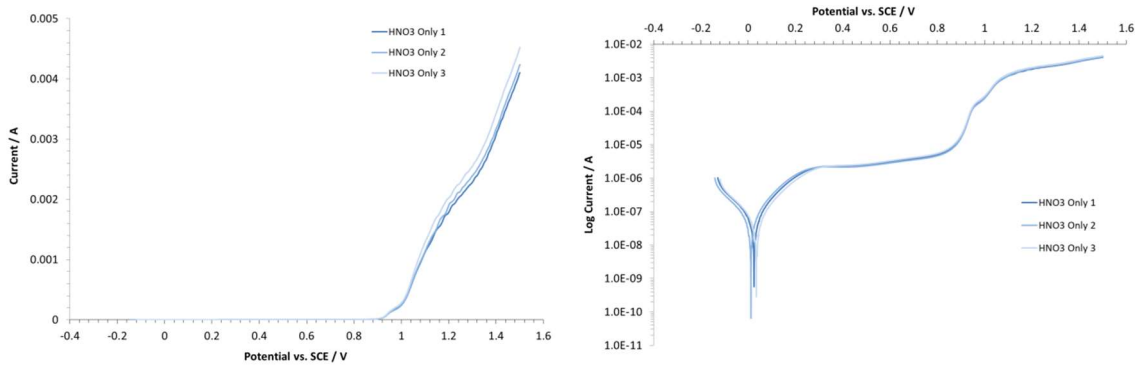

Figure 2: LSV (left) and Tafel plot (right) of a SS316L rod electrode in 1.5 mol dm^{-3} HNO_3. Results are shown in triplicate. Solutions were sparged with air.

From Figure 2 it can be seen that repeatability is excellent between experiments. The onset of transpassive dissolution occurs at approximately 0.9V vs. SCE, with very little secondary passivation apparent at potentials >1.3 V vs. SCE.

The same experimental series overlaid with triplicate experiments performed in the same concentration of nitric acid, but in the presence of 0.2 mol dm^{-3} hydrazine are shown in Figure 3.

This project has received funding from the EURATOM research and training programme 2014-2018 under grant agreement No 755171. The content of this deliverable reflects only the author's view. The European Commission is not responsible for any use that may be made of the information it contains.

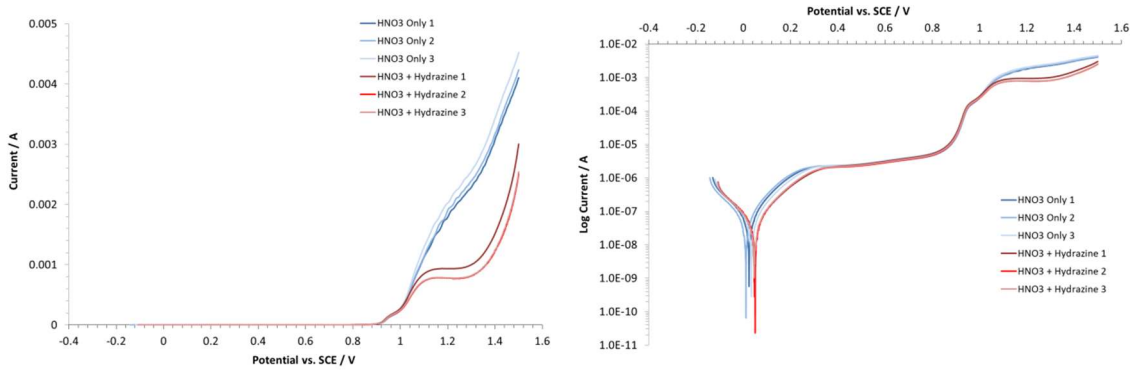

Figure 3: LSV (left) and Tafel plot (right) of a SS316L rod electrode in 1.5 mol dm^{-3} HNO_3 only and 1.5 mol dm^{-3} HNO_3 with 0.2 mol dm^{-3} hydrazine. Results are shown in triplicate. Solutions were sparged with air.

Several differences can be identified between the two data sets. First, E_{corr} in the presence of hydrazine is shifted ~30 mV more positive of that measured in experiments of HNO_3 only. Secondly, in the range between E_{corr} and the region of primary passivation, it can be seen that the anodic tafel arm exhibits a reduced current in the presence of hydrazine compared to HNO_3 only. Finally, and most significantly, at potentials between 1 and 1.4 V vs. SCE a new current region of secondary passivation is observed in the presence of hydrazine, with transpassive dissolution accelerating above 1.4 V only.

To qualitatively assess the degree of physical corrosion extant in both experiments, SEM images were taken before and after electrochemical scanning of the SS316L electrode in both the presence and absence of hydrazine. Imaging was performed using a JEOL 6010-LV (JEOL UK Ltd., Herts, UK) at 20 keV using both secondary electron (SEI) and backscatter topographic mode (BET). In the latter mode, strong topographic contrast is produced by collecting back-scattered electrons from one side above the specimen using an asymmetrical, directional back scattered electron detector. The resulting contrast appears as illumination of the topography from that side. This mode is especially useful for understanding 3D physical features that may be difficult to interpret in inherently 2D traditional SEI images.

Examples of surface images taken at 400x (SEI) and 800x (BET) of an SS316L electrode in various conditions are shown in Table 1. Considering first the post-polishing images therein, some minor scratches are still present as a result of hand polishing as well as small amounts of diamond paste particles that have not been fully removed by the post-polish washes. Turning now to the post-electrochemical scanning images in the presence of 1.5 mol dm^{-3} HNO_3 only, slightly more particulate material is apparent in the SEI image compared to that in the previous post-polishing image. This may be due to some general corrosive roughening of the surface, i.e. a form of transpassive uniform corrosion.

This project has received funding from the EURATOM research and training programme 2014-2018 under grant agreement No 755171. The content of this deliverable reflects only the author's view. The European Commission is not responsible for any use that may be made of the information it contains.

Table 1: SEM images taken at 400x (SEI) and 800x (BET) of an SS316L electrode in various conditions.

Air	Before Scanning to +1.5V vs. SCE	After Scanning to +1.5 V vs. SCE - HNO_3 Only	After Scanning to +1.5 V vs. SCE - HNO_3 and Hydrazine
SEI	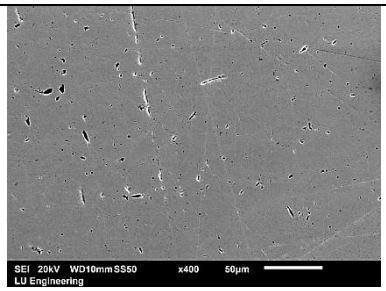	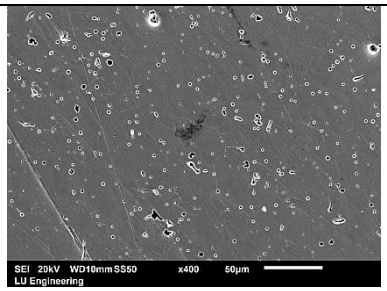	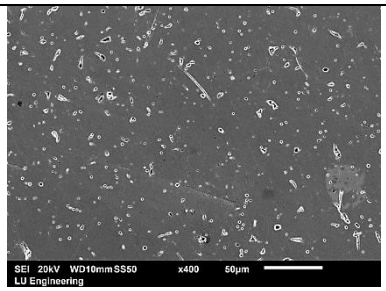
BET	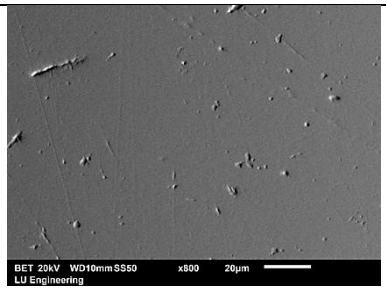	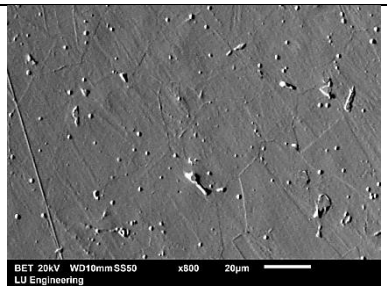	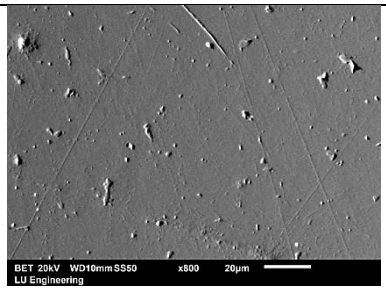

Such mild uniform corrosion has been observed previously on SS316L equivalent quartz crystal piezoelectrodes scanned to similar potentials [16]. However, while hard to see from the SEI image, the BET image clearly shows that steel grain boundaries are now visible post-scanning, i.e. intergranular corrosion of the steel has occurred (see below).

Finally, in the presence of N_2H_4, again slightly more particulate material is apparent in the post-electrochemical scanning SEI image compared to the post-polishing image. However, the amount is similar to that seen in the post-electrochemical scanning image in HNO_3 only. Interestingly in the post-scanning BET image of the surface studied in hydrazine, no grain boundaries are apparent. SEM examination at higher magnification, Figure 4, does reveal show some mild intergranular corrosion; however, as shown in Table 1, it is significantly reduced compared to that seen in the absence of N_2H_4.

The causes and mechanism of intergranular corrosion in stainless steels in nitric acid are well reported [17]. The susceptibility of stainless steel to failure in boiling 8 mol dm^{-3} HNO_3 is the result of one or more of the following processes: (i) intergranular corrosion due to sensitization, (ii) intergranular corrosion due to impurity segregation at grain boundaries, (iii) transpassive dissolution of passive films, and (iv) selective corrosion of welds [18]. In the SS316L electrode used here processes (ii) and (iii) are most applicable to the observed intergranular corrosion morphologies of Table 1 and Figure 4.

This project has received funding from the EURATOM research and training programme 2014-2018 under grant agreement No 755171. The content of this deliverable reflects only the author's view. The European Commission is not responsible for any use that may be made of the information it contains.

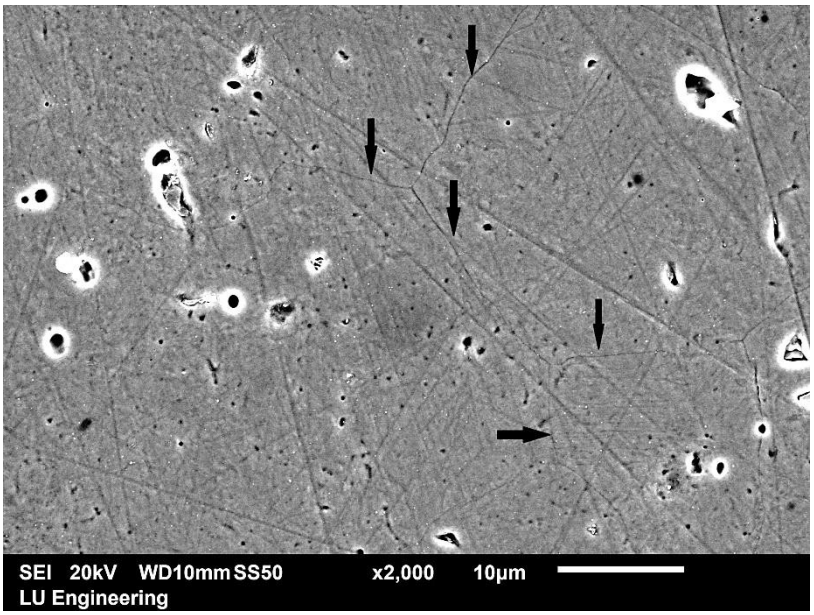

Figure 4: 2000x SEI image of a SS316L electrode after electrochemical scanning to +1.5 V in 1.5 mol dm^{-3} HNO_3 and 0.2 mol dm^{-3} hydrazine. Annotation has been added to highlight intergranular grain boundaries.

As per the general description of a linear sweep voltammogram, Figure 1, if a significantly oxidising potential is applied to a stainless steel electrode then transpassive dissolution of the passivating Cr^{3+} oxide surface film to Cr^{6+} soluble species will occur, resulting in attack of the underlying Fe/Cr/Ni bulk steel matrix. Putative transpassive attack in nuclear reprocessing systems may be a response to the combination of both the highly anodic E^0 of the HNO_2/NO_2 and NO autocatalytic coupling that increases with HNO_3 concentration (see above and [12]) and the higher temperatures in nuclear systems as a result of radionuclide decay. The result is a more positive E_{corr} (corrosion potential), which determines whether or not transpassive dissolution can occur. A summary of expected E_{corr} in acid media used nuclear reprocessing systems under various conditions is shown in Figure 5. Please note the reversal of the potential axis.

From Figure 5 it can be seen that LSV and Tafel plots of Figures 2 and 3 allow for simulation of corrosion behaviour over a broad range of expected and maloperation conditions that may occur in a reprocessing flowsheet. For example, if high acidity hot nitric acid were to enter this stage from head end accidentally pushing E_{corr} to ~ 1 V, such an oxidative insult can be quickly simulated by potentiostatically scanning to ~ 1 V.

Returning to the impurities induced susceptibility of stainless steels to intergranular corrosion, many minor elements introduced during manufacture, such as Si, Mn, S, P, B, segregate to grain boundaries after solution annealing and heat treatments. Such segregation results in the formation of weak passive films at grain boundaries, which

This project has received funding from the EURATOM research and training programme 2014-2018 under grant agreement No 755171. The content of this deliverable reflects only the author's view. The European Commission is not responsible for any use that may be made of the information it contains.

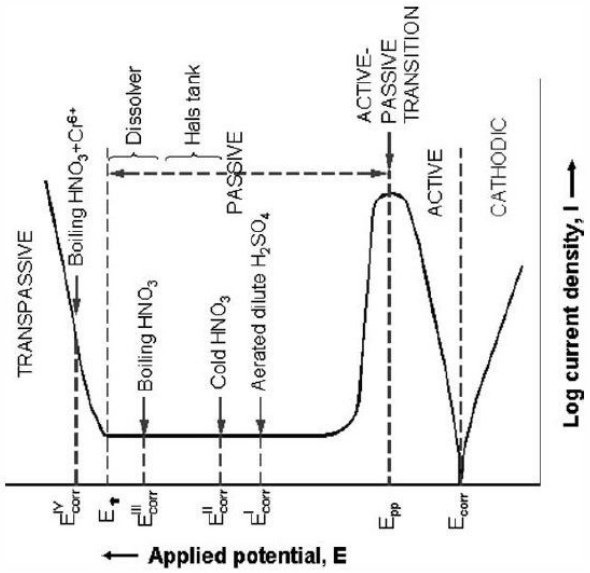

Figure 5: Schematic polarization diagram showing the corrosive zones seen for austenitic stainless steels in nitric acid environments in reprocessing plants [19]. ***Note the reversal of the Applied Potential axis compared to that employed in Figure 1 and everywhere else in this report. This is solely due to the sign convention adopted by the authors of the source reference from which this figure is extracted.***

rapidly dissolve at the point of transpassivity or pre-transpassivity leading to selective intergranular corrosion. For example, MnS inclusions are well known pitting initiation points in chloride media due to their high solubility and have a similar deleterious effect in nitric acid [19]. Similarly boron, at levels as low as 30 ppm, can form dichromium boride (Δ-Cr2B) along grain boundaries, locally weakening Cr film resistance [20].

In a reprocessing plant SS316L is typically used for waste storage containers but also structural work exposed to seawater or steam separator plates. It is therefore important to test it under direct reprocessing stream conditions in the case of maloperation scenarios, for example use of the wrong steel grade in pipe manufacture or leakage into SS316L waste tanks. The measured elemental composition of the SS316L rod electrode used in these studies is shown in Table 2.

Table 2: SEM-EDS/XRF derived chemical composition of SS316L steel sample. Values are shown in wt. %.

	Al	Si	P	S	Ti	V	Cr	Mn	Fe	Ni	Cu	Mo	W	Zr
SS316L	0.03	0.46	N/D	0.11	0.023	0.08	18.124	1.64	66.397	10.791	0.455	1.865	0.24	0.002

From Table 2 it can be seen that many elements detrimental to nitric acid use are present at concentrations that may cause weak local passive films. Mn is greater than 1 wt.% and S is greater than 0.5 wt.% which may lead to formation of MnS inclusions (see above and

This project has received funding from the EURATOM research and training programme 2014-2018 under grant agreement No 755171. The content of this deliverable reflects only the author's view. The European Commission is not responsible for any use that may be made of the information it contains.

[19]). A Si content of 0.46 wt.% may also cause issues with intergranular attack. A Si content of between 0.4 and 1% Si content is well known to cause excessive intergranular attack [21]. Other minor elements, with the exception of P which remains low in this material, have been shown to have very little corrosion effect in boiling nitric acid tests [17;22].

Thus, for the SEM results of Table 1, the origin of intergranular corrosion in the SS316L electrode is therefore a combination of the potential scan that has been applied as well as the minor element sensitivity of the material. The latter is explored more in the studies of 18/10 NAG in the next section.

Returning to the LSV results of Figure 3, the differences observed upon the addition of hydrazine may be explained thus. First, the smaller currents observed in the anodic arm of the corresponding tafel plot suggests that some mild corrosion inhibition is occurring in the presence of hydrazine compared to in its absence. The degree of this corrosion inhibition may be better understood by looking at the linear polarisation resistance (LPR) measurements taken prior to the linear sweep voltammogram of Figure 3.

Full details of this method and how the corrosion rate is derived may be found in the ASTM standards G59 – 97 and G102 - 89 [14;15]. Briefly, a small window polarisation is made either side of OCP (25 mV) at a slow scan speed (0.5 mV/s). The corrosion current (i_{corr}) is calculated using the polarisation resistance (R_p) determined from a linear regression around the corrosion potential and measurement of anodic (b_a) and cathodic (b_c) transfer coefficients from the corresponding arms of the tafel plot. i_{corr}, the sample equivalent weight, surface area and density are then used to determine the corrosion rate, expressed in µm/yr or nm/yr. The results of this analysis for the SS316L electrodes polarised in 1.5 mol dm^{-3} HNO_3 in the absence/presence of 0.2 mol dm^{-3} hydrazine are shown in Figure 6.

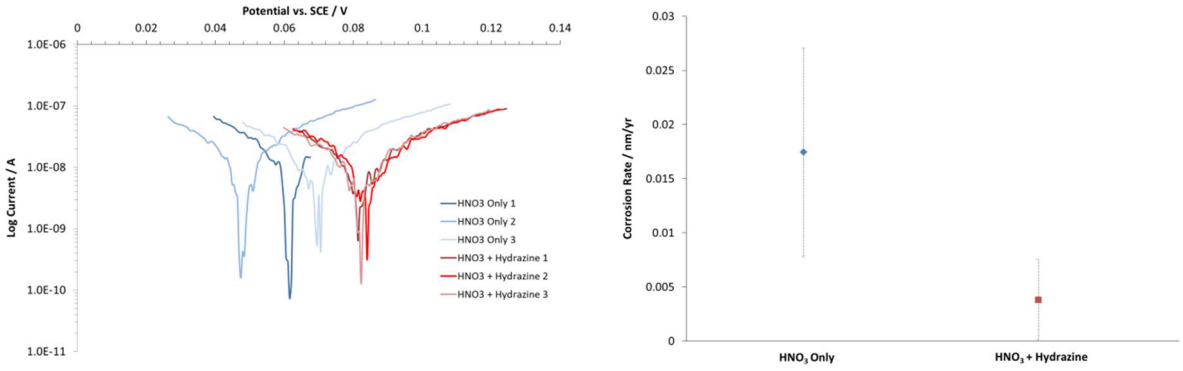

Figure 6: Triplicate LPR scans (left) and derived corrosion rates (right) for SS316L rod electrodes in 1.5 mol dm^{-3} HNO_3 in the presence/absence of 0.2 mol dm^{-3} hydrazine under air.

This project has received funding from the EURATOM research and training programme 2014-2018 under grant agreement No 755171. The content of this deliverable reflects only the author's view. The European Commission is not responsible for any use that may be made of the information it contains.

From Figure 6 it can be seen that as well as a small but significant difference between the open circuit potential (OCP) recorded in the presence of hydrazine (denoted by the position of E_{corr} in this case), the slightly lower currents observed in the anodic tafel arm in the presence of hydrazine, more easily seen in Figure 3, also results in a small but significant decrease in the calculated corrosion rate.

While a more substantial change in E_{corr} with addition of hydrazine in boiling 2 mol dm^{-3} HNO_3 has been previously reported by Abraham *et al*. [9], a similar reduced anodic response has also been reported by the authors. They attribute this to the scavenging of HNO_2 by hydrazine, shown in Eq. (7) and (8), and an associated inhibition of the HNO_2-catalysed reduction of HNO_3.This may be explained as follows. The global reaction of reduction of nitric acid is given by:

$$HNO_3 + H^+ + e^- \rightarrow NO_2 + H_2O \quad (9)$$

And is followed by a heterogeneous mechanism [23]:

$$NO_2 + e^- \rightarrow NO_2^- \quad (10)$$

$$NO_2^- + H^+ \rightarrow HNO_2 \quad (11)$$

$$HNO_2 + HNO_3 \rightarrow 2NO_2 + H_2O \quad (12)$$

In parallel the following reactions also occur:

$$NO_2 + e^- \rightarrow NO_2^- \quad (13)$$

$$NO^-_2 + H^+ \rightarrow HNO_2 \quad (14)$$

$$HNO_2 + HNO_3 \rightarrow 2NO_2 + H_2O \quad (15)$$

As noted in the introductory section, HNO_2 is considered the electroactive species in this reaction scheme, causing reduction of nitric acid to NO_2 and H_2O. Indeed as per the introduction to this report, nitric acid reduction is an autocatalytic mechanism which constitutes a charge transfer step and a chemical reaction which regenerates the electroactive species as shown by the above reactions. This results in the formation of an extra half mole of nitrous acid for each mole of nitrous acid destroyed [9]. Importantly, the solution redox potential (and thus the potential of the stainless steel) is actually a result of the oxidation of NO_2 to NO_3^- and NO to NO_3^-:

This project has received funding from the EURATOM research and training programme 2014-2018 under grant agreement No 755171. The content of this deliverable reflects only the author's view. The European Commission is not responsible for any use that may be made of the information it contains.

$$NO_2 + H_2O \rightarrow NO_3^- + 2H^+ + e^- \quad (16)$$

$$NO + 2H_2O \rightarrow NO_3^- + 4H^+ + 3e^- \quad (17)$$

Which has a highly anodic thermodynamic potential of ~0.8V vs. SCE. As the generation of NO_2 and NO is very much dependent on the ratio of HNO_2 to HNO_3, as shown by Eq. (10) to (15), excess HNO_2 will result in more anodic potentials and a decrease in HNO_2 concentration will result in more cathodic potentials being imposed on the immersed stainless steel.

Thus, returning to the observed decrease in corrosion rate in Figure 6, scavenging of HNO_2 by hydrazine, previously shown in Eq. 7 and 8, should reduce the applied potential and also reduce the anodic corrosion current as a result, a conclusion also reached by Abraham *et al.* [9] under boiling nitric acid conditions. While the latter is true here the former is not, i.e. a slightly higher measured E_{corr} is instead observed and this is returned to later in this section.

Of more interest, compared to the small variation in corrosion rate, is the significant current differences recorded in the transpassive dissolution regime above 1V vs. SCE in the presence of hydrazine, a magnification of which is shown in Figure 7.

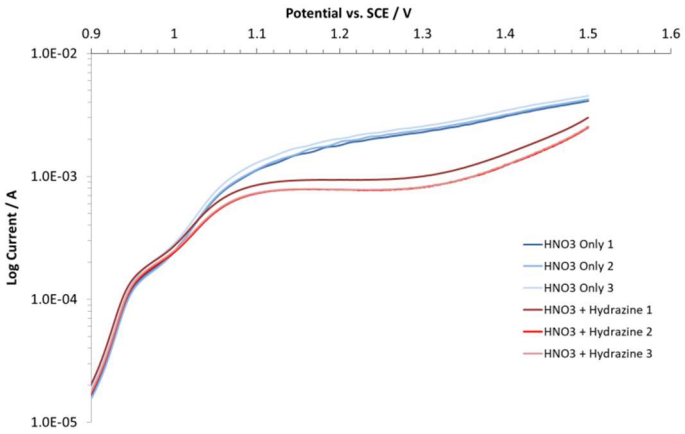

Figure 7: Tafel plot magnification of the potential range 0.9 to 1.6V for a SS316L rod electrode in 1.5 mol dm^{-3} HNO_3 only 1.5 mol dm^{-3} and HNO_3 with 0.2 mol dm^{-3} hydrazine.

As described in the introduction, the reduced current in the presence of hydrazine in this region is suggested by Abraham *et al.* to be due to reduction of soluble Cr(VI) species to Cr(III) by hydrazine *via*:

$$4CrO_4H^- + 3N_2H_5^+ + 13H^+ + 8H_2O \rightarrow 4[Cr(OH_2)_6]^{+3} + 3N_2 \quad (18)$$

This project has received funding from the EURATOM research and training programme 2014-2018 under grant agreement No 755171. The content of this deliverable reflects only the author's view. The European Commission is not responsible for any use that may be made of the information it contains.

the above reaction stabilising Cr at grain boundaries and generally across the surface, so reducing intergranular corrosion. However, assuming that the reduction of Cr(VI) to Cr(III) by hydrazine is the primary mechanism in the inhibition of transpassive corrosion on SS316L, then why does this inhibition not occur until the scanned potential is greater than 1V vs. SCE? Indeed, no decrease in the transpassive current is observed in the pre-transpassive and general transpassive region below 1V vs. SCE. This may simply be a kinetics issue. However, a factor not considered by Abraham *et al.* is that secondary passivation may also occur in this region, as described for the example LSV shown in Figure 1. Secondary passivation has been shown to readily occur for AISI 316L [24] and SS304 [25;26] in the >1V vs. SCE region. The secondary passive layer is predominantly non-stoichiometric Fe_2O_3, Cr_2O_3 and NiO with some other constituents such as stoichiometric Fe_3O_4 and metal hydroxides. The Cr content of this layer is significantly lower than that found in the passivating film produced in the primary passivation region of either SS304 or SS316L. The comparative lack of Cr in this secondary passive layer results in a low breakdown potential, giving the layer a porous character, a subject we reported on in our previous studies on the effect of AHA on SS316L corrosion [16]. In the case of the latter, the AHA effect on secondary passiviation is to complex with dissolved Fe^3, significantly enhancing transpassive dissolution by inhibiting the predominantly iron oxide based layer formation.

In the results of Figure 7 it could be suggested that the reverse is instead occurring, i.e. that hydrazine acts to stabilise Fe in the 3+ or lower oxidation state, strengthening the secondary passive film. As shown in Eq. (2) to (5) and [6;7], the application of hydrazine in supercritical water conditions causes reduction of higher oxidation number iron oxides/hydroxides to more stable lower oxidation states, which would enhance surface protection. Alternatively, it has been reported that in groundwaters or chloride containing solutions hydrazine and its compounds can form tetragonal complexes of the type $FeX_2(N_2H_4)_2$ which contain bridging and bidentate hydrazine groups [4;5]. Such complexes adsorb at the metal-solution interface, forming a barrier against aggressive solutions reaching the metal surface. In this case it could be foreseen that a similar process may occur, i.e. an adsorbed hydrazine-Fe layer restricting HNO_2 access to the surface.

Surface characterisation techniques that yield speciation information, such as XPS, would be useful here in order to determine which process of the above described processes is most likely to be responsible. However, even in the absence of such information, it is clear from the above results that in air sparged nitric acid solutions hydrazine has a significant corrosion inhibition effect under oxidative maloperation conditions.

The data of Figures 2-4 and 6 & 7 were recorded in air sparged solutions. Experiments

This project has received funding from the EURATOM research and training programme 2014-2018 under grant agreement No 755171. The content of this deliverable reflects only the author's view. The European Commission is not responsible for any use that may be made of the information it contains.

have also been performed under N_2 – purged conditions to allow comparison of the above data with results achieved in the absence of oxygen (a known corrosion accelerator). LSV and Tafel plots for the triplicate experiments performed on SS316L in the absence of hydrazine and purged with N_2 are shown in Figure 8.

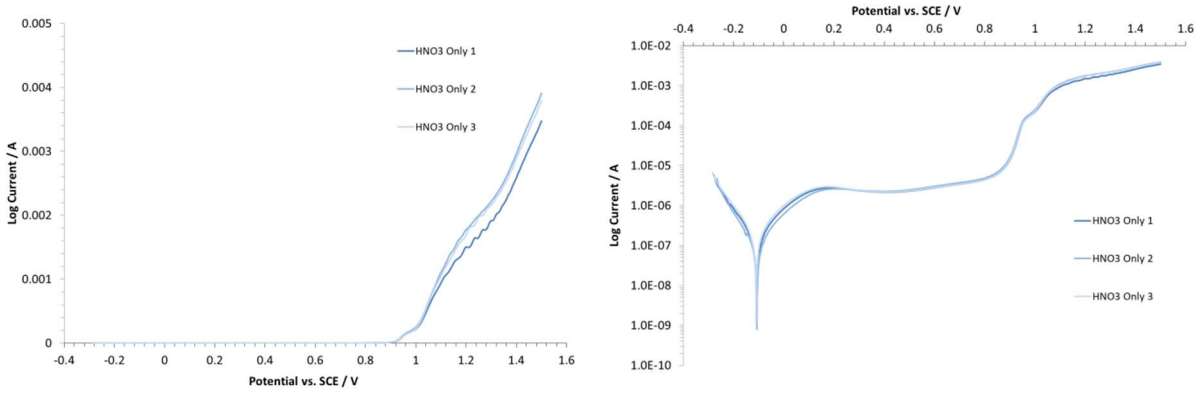

Figure 8: LSV (left) and Tafel plot (right) of a SS316L rod electrode in 1.5 mol dm^{-3} HNO_3. Results are shown in triplicate. Solutions were sparged with N_2.

In order to aid comparison by the reader between conditions, a single experiment from each atmosphere condition is shown in the Tafel plots of Figure 9.

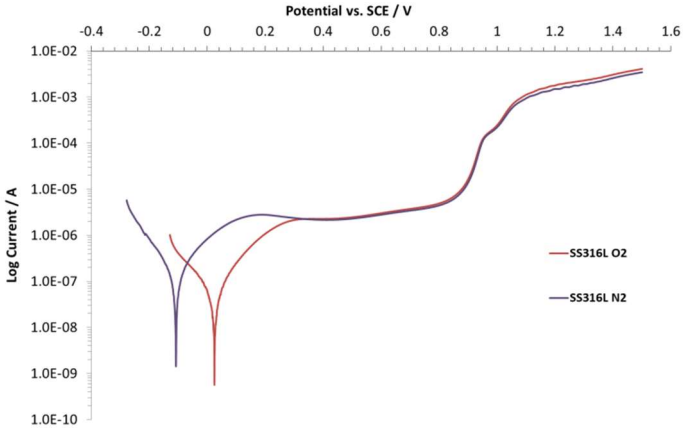

Figure 9: Tafel plot of a SS316L rod electrode in 1.5 mol dm^{-3} sparged with either air or N_2.

Figure 9 reveals that the tafel traces are very similar in the passive and transpassive regions, with only a slight decrease in the recorded transpassive current at 1.5V of 3.9 mV vs. 4.4 mV in air. However, around E_{corr} quite obvious differences are apparent. First, E_{corr} is more cathodic under nitrogen, being closer to ~-0.2V than the previous ~0V under air. Secondly, the i_{corr} and general current density is larger in the absence of air compared to the presence.

The effect of oxygen on stainless steel corrosion is highly dependent on the anions

This project has received funding from the EURATOM research and training programme 2014-2018 under grant agreement No 755171. The content of this deliverable reflects only the author's view. The European Commission is not responsible for any use that may be made of the information it contains.

present in the solution environment. In the case of combinations of nitric acid and dissolved oxygen, the effect of dissolved oxygen on the open circuit potential and potentiodynamic polarisation behaviour of SS304L has been reported by Khobragade *et al.* [27].

The findings of Khobragade *et al.* can be exported to our work on SS316L reported here. Considering first the shift in E_{corr} of SS316L, while in part influenced by the solution potential of the system controlled by the NO_3^-/NO_2^- couple, see Eq. (16-17) and [23], the E_{corr} of SS316L is predominantly dictated by the passive film surface state. The passive film of Cr_2O_3 on a stainless steel surface can act as a p-type semiconductor and has cation vacancies as a result. Vacancy defects in most oxide surfaces display a strong interaction with molecules such as O_2 and H_2O. O_2 may be reduced to form O^{2-} ions as one of the mixed potential (measured as E_{corr}) determining half reactions at the steel surface, joining and enhancing the passive film. The coupled oxidation half reaction is most likely the oxidation of one of the alloying elements, most likely Cr, at the metal-metal oxide interface. Nitrate ions may compete with the reductively formed oxide ions for adsorption on the film surface, inhibiting film formation and driving dissolution. However, this nitrate-associated effect aside, the open circuit potentials measured on SS316L reported here is shifted towards passivity under aerated conditions as the oxygen drives Cr_2O_3 layer formation. Conversely, in the absence of oxygen, passive layer formation is inhibited in comparison to aerated solutions, causing a shift towards active dissolution as well as consequent increases in i_{corr} and overall corrosion rate, as observed in Figure 9.

Considering the importance of oxygen in forming the passive layer, the difference highlighted above may also explain why a small anodic rather than cathodic shift in E_{corr} is observed in the presence of hydrazine under aerated conditions, Figure 3. As noted by Abraham *et al.* [9] and described in Eq. (7) and (8), the effect of hydrazine is to scavenge HNO_2, reducing corrosion rates and shifting E_{corr} more cathodic. It may also act as an adsorbed layer restricting electrolyte access to the steel surface [4;5]. In the case of the latter, a restriction of NO_3^- to the surface would allow less competition between solution NO_3^- and O^{2-} ions formed directly as a result of the reduction of dissolved oxygen at the steel surface in the formation of the passive film on the SS316L electrode described above. The result is a slight anodic shift in E_{corr} as a response to the presence of a more protective passive layer.

Turning now to the effect of hydrazine under deaerated conditions, triplicate experiments performed in the same concentration of nitric acid, but in the presence of 0.2 mol dm^{-3} hydrazine are shown in Figure 10.

This project has received funding from the EURATOM research and training programme 2014-2018 under grant agreement No 755171. The content of this deliverable reflects only the author's view. The European Commission is not responsible for any use that may be made of the information it contains.

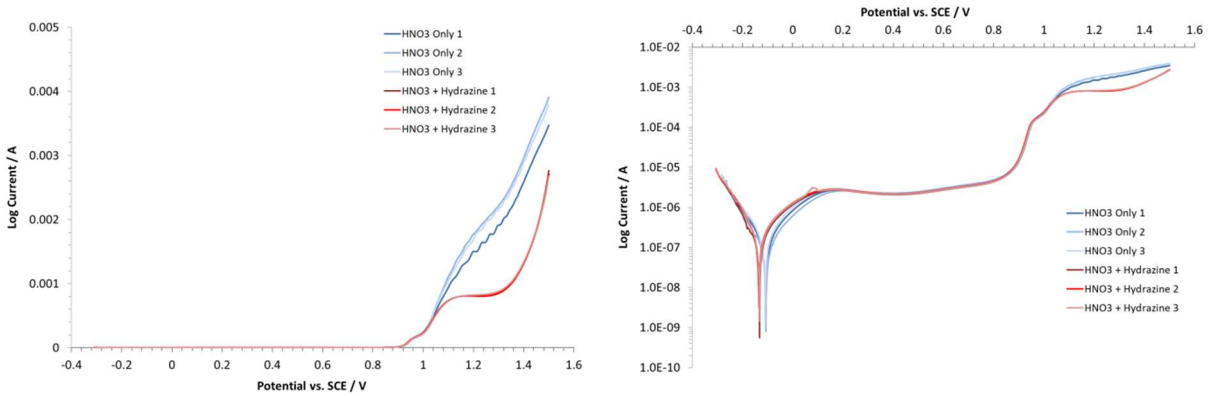

Figure 10: LSV (left) and Tafel plot (right) of a SS316L rod electrode in 1.5 mol dm^{-3} HNO_3 only 1.5 mol dm^{-3} HNO_3 with 0.2 mol dm^{-3} hydrazine. Results are shown in triplicate. Solutions were sparged with N_2.

As can be seen from Figure 10, hydrazine has an almost identical inhibition effect in the transpassive region as that seen in the aerated experiments shown in Figure 3 above. Examples of surface images taken at 400x (SEI) and 800x (BET) of an SS316L electrode post-electrochemical scanning under the conditions used in Figure 10 are shown in Table 3.

From the images of Table 3 it can be seen that almost identical morphology results to those of Table 1 are achieved in the absence/presence of hydrazine, i.e. the corrosion inhibition effect of hydrazine maintains under N_2 atmospheres.

Returning to Figure 10, of particular interest is the effect of hydrazine on the position of E_{corr} under N_2 atmospheres. This can more clearly be seen in the LPR analysis performed to determine the corrosion rate shown in Figure 11.

Unlike results in air, under N_2 a very slight cathodic shift in E_{corr} is observed in the presence of hydrazine. As there is no oxygen under such conditions to affect the passive film, the slight cathodic shift may instead be simply due to the scavenging of HNO_2, as noted by Abraham *et al.* [9] and described in Eq. (7) and (8). Interestingly, corrosion rates in the absence and presence of hydrazine under an N_2 atmosphere are not significantly different; suggesting that while the oxide layer may have an adsorbed layer of hydrazine at the surface and contain a higher proportion of oxygen compared to that formed in the absence of hydrazine (see above), the corrosion rate is not significantly improved, remaining in the 10's of pm/yr region.

This project has received funding from the EURATOM research and training programme 2014-2018 under grant agreement No 755171. The content of this deliverable reflects only the author's view. The European Commission is not responsible for any use that may be made of the information it contains.

Table 3: SEM images taken at 400x (SEI) and 800x (BET) of an SS316L electrode in various condition under N_2.

N_2	Before Scanning to +1.5V vs. SCE	After Scanning to +1.5 V vs. SCE - HNO_3 Only	After Scanning to +1.5 V vs. SCE - HNO_3 and Hydrazine
SEI	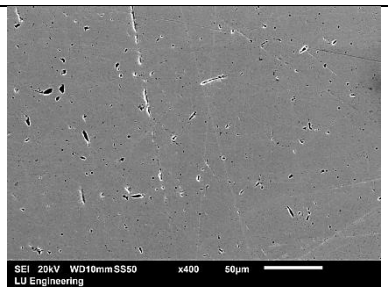	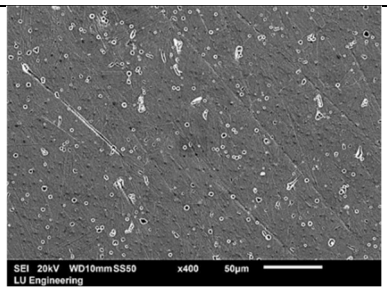	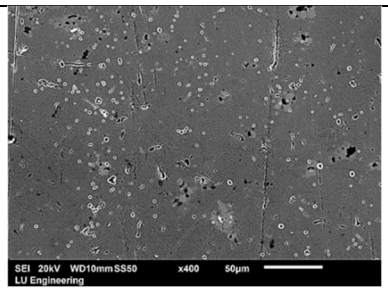
BET	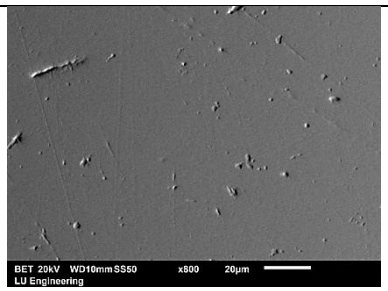	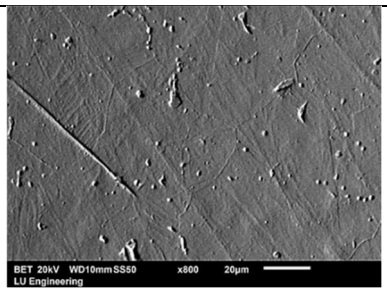	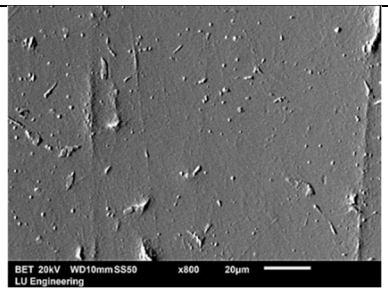

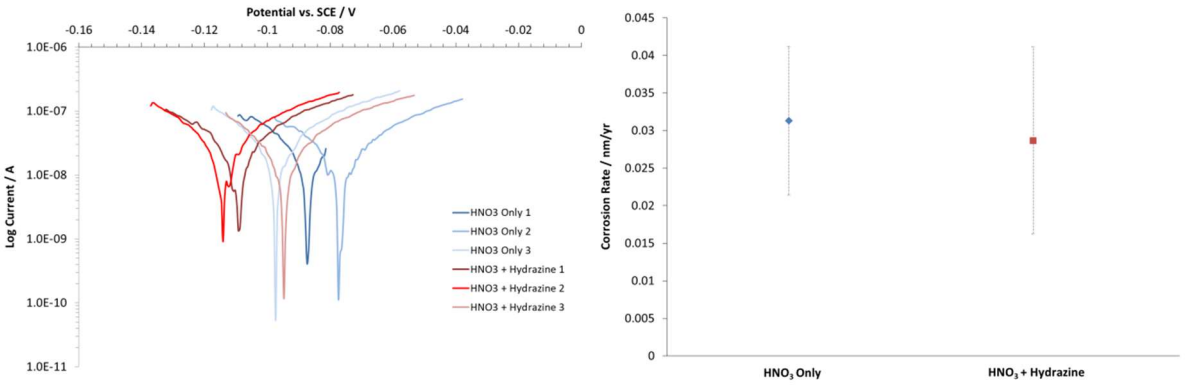

Figure 11: Triplicate LPR scans (l) and derived corrosion rates (r) for SS316L rod electrodes in 1.5 mol dm^{-3} HNO_3 in the presence/absence of 0.2 mol dm^{-3} hydrazine under N_2.

This project has received funding from the EURATOM research and training programme 2014-2018 under grant agreement No 755171. The content of this deliverable reflects only the author's view. The European Commission is not responsible for any use that may be made of the information it contains.

4. STUDIES OF 18/10 NAG IN 1.5 mol dm^{-3} HNO_3 WITH AND WITHOUT HYDRAZINE

As mentioned in the introduction to this section above, 18/10 NAG is a specific stainless steel grade utilised in dissolvers or areas of high temperature/high nitric acid in the Thermal Oxide Reprocessing Plant (THORP) at Sellafield, Cumbria, UK. We have therefore conducted some preliminary tests on this material as part of an exploration of alternative process steels discussed in the Recommendations for Further Work presented at the end of the previous section. The tested composition of the plate sample used in this study alongside the SS316L rod composition of Table 2 is shown in Table 4.

Table 4: SEM-EDS/XRF derived chemical composition of 18/10 NAG plate steel sample. Values are shown in wt.%.

	Al	Si	P	S	Ti	V	Cr	Mn	Fe	Ni	Cu	Mo	W	Zr
SS316L	0.03	0.46	N/D	0.11	0.023	0.08	18.124	1.64	66.397	10.791	0.455	1.865	0.24	0.002
18/10NAG	0.03	0.26	0.03	0.06	0.025	0.037	18.919	1.07	69.171	10.338	0.083	0.043	0.14	0.005

18/10 NAG has a carefully controlled elemental composition in order to limit intergranular corrosion damage in nitric acid. First, S is kept as low as possible and Mn is kept to ~1 wt.% or below to reduce the formation of MnS inclusions [19]. Secondly copper is kept below 0.1 wt.% as it enhances selective corrosion attack [17;22]. Importantly, Si is also kept below 0.4 wt.%, being closer to 0.2 wt.%, which has been shown to provide optimum intergranular resistance [21]. Finally, it can be seen that Mo content is significantly reduced vs. SS316L. Mo is reduced to very low levels in the alloy for two reasons namely, (i) to increase ferrite formation, and (ii) in the presence of Mo submicroscopic sigma precipitation can occur during multipass welding of steel components (said sigma phase preferentially dissolving in hot oxidizing nitric acid leading to excessive corrosion rates at welds).

The 18/10 NAG plate electrodes were subjected to the same air and N_2 atmosphere electrochemical corrosion tests as in the previous section. LSV and Tafel plots for the triplicate experiments performed on 18/10 NAG in the absence of hydrazine and purged with air are shown in Figure 12.

Figure 12 again shows that the current experimental method produces highly repeatable results. In order to aid comparison by the reader between materials, a single NAG 18/10 and SS316L experiment under the same air atmosphere condition is shown in the LSV and Tafel plots of Figure 13.

This project has received funding from the EURATOM research and training programme 2014-2018 under grant agreement No 755171. The content of this deliverable reflects only the author's view. The European Commission is not responsible for any use that may be made of the information it contains.

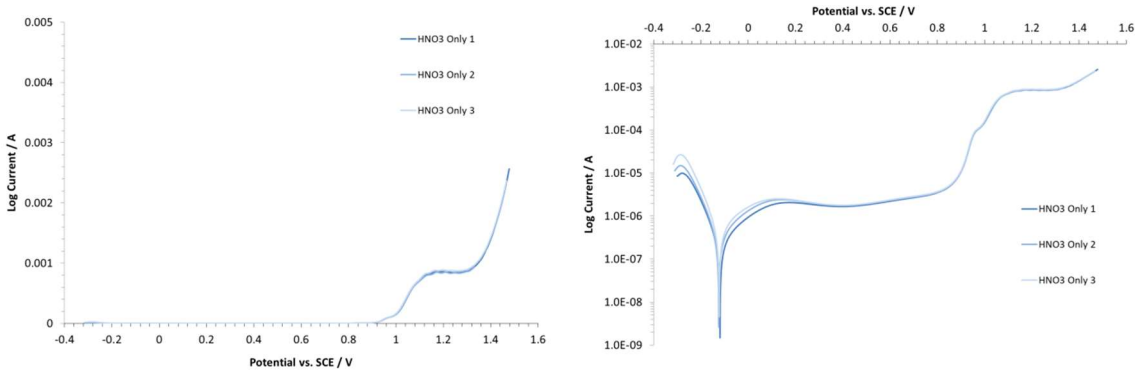

Figure 12: LSV (left) and Tafel plot (right) of 18/10 NAG electrodes in 1.5 mol dm^{-3} HNO_3. Results are shown in triplicate. Solutions were sparged with air.

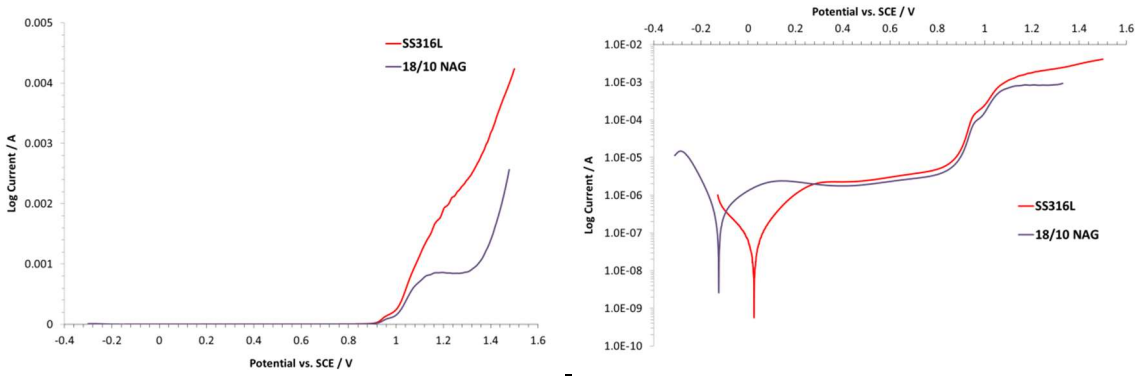

Figure 13: LSV and Tafel plots of a SS316L and 18/10 NAG electrode in 1.5 mol dm^{-3} HNO_3.sparged with air.

Figure 13 clearly highlights the significantly improved corrosion resistance of 18/10 NAG to SS316L under oxidising nitric conditions. First, lower currents are observed in the passive and pre-transpassive regions compared to SS316L. Secondly, the passive range is extended vs. SS316, with E_{corr} occurring at a considerably lower potential. Finally, secondary passivation is greatly enhanced above 1V, presumably due to the decrease in both Mo and Si (i.e. enhanced ferritic phases and reduced intergranular attack). Interestingly, despite the improvements at higher anodic scanning potentials, the anodic and cathodic tafel arms appear to be at a higher current in 18/10 NAG than SS316L. This would suggest that higher corrosion rates are occurring under open circuit potential conditions compared to SS316L. This is explored later in this section.

The same 18/10 NAG experimental series overlaid with triplicate experiments performed in the same concentration of nitric acid, but in the presence of 0.2 mol dm^{-3} hydrazine are shown in Figure 14.

This project has received funding from the EURATOM research and training programme 2014-2018 under grant agreement No 755171. The content of this deliverable reflects only the author's view. The European Commission is not responsible for any use that may be made of the information it contains.

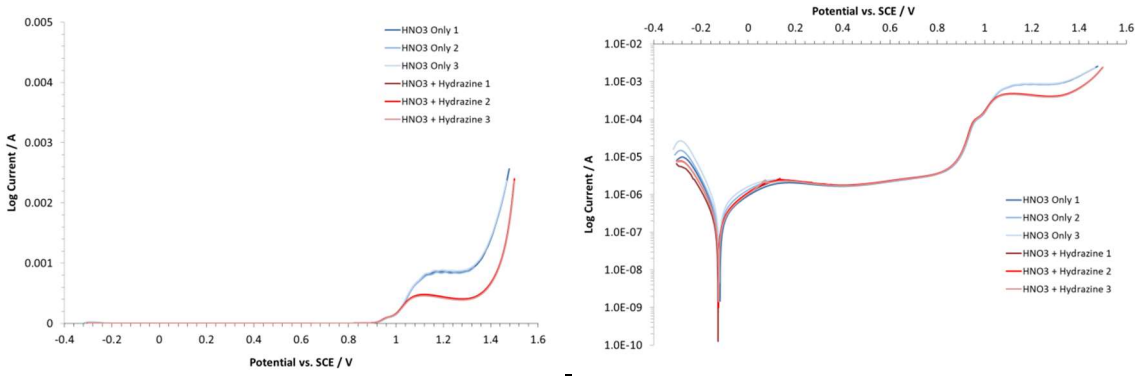

Figure 14: LSV (left) and Tafel plot (right) of 18/10 NAG electrodes in 1.5 mol dm^{-3} HNO_3 only and 1.5 mol dm^{-3} HNO_3 with 0.2 mol dm^{-3} hydrazine. Results are shown in triplicate. Solutions were sparged with air.

As per SS316L studies, hydrazine significantly reduces transpassive currents and stabilises the secondary passivation layer at potentials >1V. Interestingly, on 18/10 NAG there are no significant changes in either the tafel arms or E_{corr} position when hydrazine is present in solution. In order to further study this, again a small window LPR analysis was performed. The results of this analysis for a 18/10 NAG electrode polarised in 1.5 mol dm^{-3} HNO_3 in the absence/presence of 0.2 mol dm^{-3} hydrazine are shown in Figure 15.

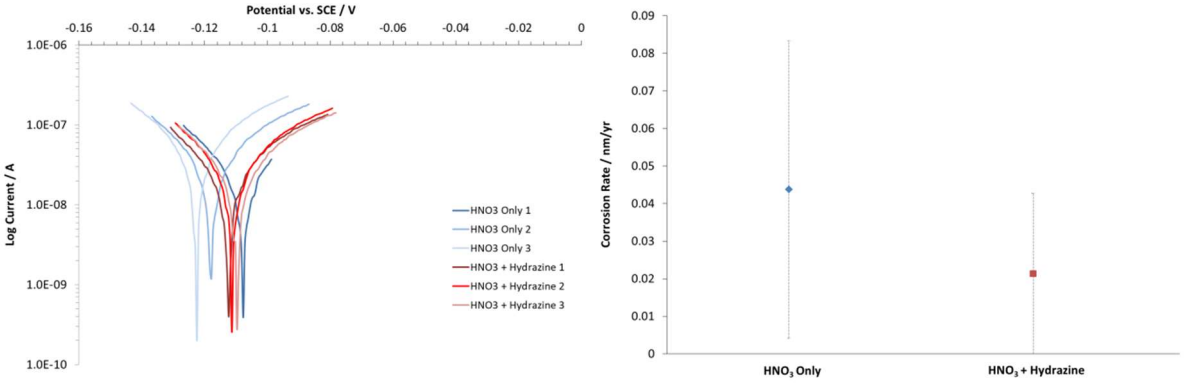

Figure 15: Triplicate LPR scans (l) and derived corrosion rates (r) for 18/10 NAG electrodes in 1.5 mol dm^{-3} HNO_3 in the presence/absence of 0.2 mol dm^{-3} hydrazine under air.

Figure 15 confirms the lack of any difference in E_{corr} in the presence of hydrazine vs. HNO_3 only. Further, calculated corrosion rates are also within error of each other, i.e. under normal non-potentiometrically controlled conditions hydrazine has no effect on the corrosion behaviour of 18/10 NAG. Interestingly, the variance in corrosion rate in nitric acid generally is significantly greater for 18/10 NAG than SS316L. As per Figure 13 as well as Figure 15, E_{corr} is also closer to SS316L experiments performed under nitrogen, than those performed under air.

This project has received funding from the EURATOM research and training programme 2014-2018 under grant agreement No 755171. The content of this deliverable reflects only the author's view. The European Commission is not responsible for any use that may be made of the information it contains.

This would suggest that while 18/10 NAG performance at high anodic potentials (such as those in boiling nitric acid) is excellent, at lower potentials where pitting and active corrosion rather than intergranular corrosion dominate, 18/10 NAG is not quite as protective as SS316L steel grades – although it does still offer excellent protection.

This slight reduction in performance of 18/10 NAG compared to that of SS316L at low overpotentials may in part be due to the considerably lower Mo content in 18/10 NAG, as shown in Table 4. Whilst reducing Mo in the steel imparts benefits to the stabilisation of secondary passivation films and intergranular sensitisation during welding, enriching of Cr oxide films with Mo(IV) or Mo(VI) is well known to mitigate the breakdown of the passive film preceding the initiation of localized corrosion and promote the passive film repair after breakdown [28]. As such, a Mo containing steel such as SS316L would be expected to have a stronger passive film under localised or active corrosion conditions.

This project has received funding from the EURATOM research and training programme 2014-2018 under grant agreement No 755171. The content of this deliverable reflects only the author's view. The European Commission is not responsible for any use that may be made of the information it contains.

5. CONCLUSIONS AND FURTHER WORK

The addition of hydrazine is found to cause two important observable effects:

(1) The corrosion potential (E_{corr}) in the presence of hydrazine in aerated solutions such as those that might be expected to obtain in reprocessing plant is shifted ~30 mV more positive resulting in movement of the anodic tafel arm towards the region of primary passivation.

(2) More importantly, currents within the transpassive range are significantly reduced in both the N_2 and air sparged solutions, suggesting a stabilisation of a secondary passivation layer in the presence of hydrazine and resistance to intergranular attack.

18/10 NAG steel is found to exhibit significantly greater corrosion resistance in the transpassive region than SS316L.

Recommendations for further work: Given the inhibiting effect of hydrazine on transpassive corrosion on SS316L, a surface analysis-based study of the nature of the passive layer on 316L in the presence of hydrazine should be conducted so as to better understand the mechanism of this protection.

Studies of the effect that hydrazine has on the transpassive corrosion processes observed in the presence of AHA, SO_3-Ph-BTP, SO_3-Ph-BTPhen should also be conducted in order to determine whether there is any additional protection afforded over and above that provided by the AHA hydrolysis product, hydroxylamine.

Finally, studies of the effect of those ligands that have so far shown the greatest corrosion accelerating properties on 316L and 304L stainless steels, i.e. AHA, SO_3-Ph-BTP and SO_3-Ph-BTPhen, should be repeated on 18/10 NAG to determine if the latter steel offers better protection under maloperations conditions in the presence of the ligands in question.

This project has received funding from the EURATOM research and training programme 2014-2018 under grant agreement No 755171. The content of this deliverable reflects only the author's view. The European Commission is not responsible for any use that may be made of the information it contains.

REFERENCES

[1] E.R. Woodward, *Power* **97**(91) (1953)
[2] V.K. Gouda, S.M. Sayed, *Corrosion Science* **13** (1973), pp647-652
[3] G.S. Suresh, C.L. Araviada, M.F. Ahamed, S.M. Mayanna, *Indian Journal of Chemical Technology* **6** (1999), pp.301-304
[4] A.S. Fouda, S.A. Abd El-Maksoud, A. El-Hossiany, A. Ibrahim, *International Journal of Electrochemical Science* **14** (2019), pp2187-2207
[5] N.C. Subramanyam, B.S. Sheshadri, S.M. Mayanna, *Key Engineering Materials* **20-28** (1988), pp3007-3021
[6] S.V. Jovanovic, T. Zakharov, H. Mulye, D. Kim, K-A. Fagan, *Analytical Methods* **7**(23) (2015), pp9825-9834
[7] O.P. Arkhipov, V.L. Bugaenko, S.A. Kabakchi, V.I. Pashevich, *Atomic Energy* **82**(2) (1997). pp92-98
[8] J. Nakano, Y. Kaji, M. Yamamoto, T. Tsukada, *Journal of Nuclear Science and Technology* **51**(7-8) (2014), pp977-986
[9] G.J. Abraham, V. Kain, G.K. Dey, *Journal of Nuclear Materials* 397 (2010), pp55-60
[10] M.T. Beck, D.A. Durham, *Journal of Inorganic and Nuclear Chemistry* **32** (1970), pp1971-1977
[11] S.V. Kumar, M.N. Nadkarni, A. Ramanujam, M. Venkatesan, V. Gopalakrishnan, J.A. Kazi, BARC Report No. 782 (1974)
[12] R.C. Williamson, *Mechanisms of Fixed Contamination of Commonly Engineered Surfaces*, Ph.D. Thesis, Lancaster University (2018).
[13] ASTM International. Standard Practice for Preparing, Cleaning and Evaluating Corrosion Test Specimens. G1-03, 1-12. 2011.
[14] ASTM International. Standard Test Method for Conducting Potentiodynamic Polarization Resistance Measurements. G59 - 97, 1-4. 2014.
[15] ASTM International. Standard Practice for Calculation of Corrosion Rates and Related Information from Electrochemical Measurements. G102 - 89, 1-8. 2015.
[16] R.J. Wilbraham, C. Boxall, *Electrochemistry Communications* **62** (2016), pp52-55
[17] B. Raj, U.K. Mudali, *Progress in Nuclear Energy* **48** (2006), pp283-313
[18] V. Cihal, *Intergranular Corrosion of Steels and Alloys (Materials Science Monographs)*, Elsevier (1984), ISBN 0444996443.
[19] D.F. Steele, *Atom: Monthly Bulletin of the United Kingdom Atomic Energy Authority* **353** (1986) pp5-9
[20] T. Gladman, *Materials Performance (*1989), pp60-61
[21] R. Robin, F. Miserque, V. Spagnol, *Journal of Nuclear Materials* **375** (2008), pp65-71
[22] A. Pardo, M.C. Merino, J. Botella, M. Carboneras, V. Matres, F. Viejo, R. Arrabal, *Corrosion Engineering, Science and Technology* **41**(2) (2006), pp122-129
[23] V.P. Razygraev, M.V. Lebedeva, S.A. Kabakchi, E.Y. Ponomareva, R.S. Balovneva, L.P. Lobanova, *Journal of Applied Chemistry of the USSR* **61** (1988)
[24] I. Betova, M. Bojinov, T. Laitinen, K. Mäkelä, P. Pohjanne, T. Saario, *Corrosion Science* **44** (2002), pp2675-2697
[25] G.L. Song, C.N. Cao, H.C. Lin, *Corrosion Science* **36** (1994), pp165-169.

This project has received funding from the EURATOM research and training programme 2014-2018 under grant agreement No 755171. The content of this deliverable reflects only the author's view. The European Commission is not responsible for any use that may be made of the information it contains.

[26] G. Song, Corrosion Science **47** (2005), pp1953-1987.

[27] N.N. Khobragade, A.V. Bansod, A.P. Patil, Materials Research Express **5** (2018), pp046526

[28] Z. Wang, E-M. Paschalidou, A. Seyeux, S. Zanna, V. Maurice, P. Marcus, Frontiers in Materials **6**(232) (2019), pp1-12

This project has received funding from the EURATOM research and training programme 2014-2018 under grant agreement No 755171. The content of this deliverable reflects only the author's view. The European Commission is not responsible for any use that may be made of the information it contains.

STUDY OF PROCESS STEEL CORROSION IN THE PRESENCE OF TRANS-1,2-DIAMINOCYCLOHEXANE-N,N,N',N'-TETRAACETICACID (CDTA)

1. INTRODUCTION

CDTA is utilised at the start of the 2nd cycle in the EURO-GANEX process. CDTA is fed from a constant head feed tank into the primary separation stream to prevent extraction of FPs (particularly zirconium (IV) and palladium (II) [1]) in the next Transuranium element (TRU) extraction and scrub through the formation of Zr and Pd complexes in the aqueous phase. At the start of the 2nd cycle the nitric acid concentration is still relatively high, 7.408 mol dm^{-3}, the U-stripped aqueous input stream coming from the primary separation step after fuel dissolution. The added CDTA concentration at this stage is expected to be 0.104 mol dm^{-3}.

CDTA complexed with Zr at a lower concentration (0.033 mol dm^{-3}) will also be apparent in the resultant FP loaded nitric acid stream generated by the TRU extraction and scrub step at the start of the 2nd cycle. Some residual hydrazine is also expected in this stream (0.023 mol dm^{-3}) having been carried through from the 1st cycle uranium scrub and the nitric acid concentration is also expected to be lower at 3.74 mol dm^{-3} [2]. Thus, with regards to process steel corrosion, two scenarios need to be assessed:

1) CDTA in nitric acid concentrations of ~7.4 mol dm^{-3} and 3.74 mol dm^{-3} HNO_3
2) CDTA and hydrazine in nitric acid concentrations of ~7.4 and 3.74 mol dm^{-3} HNO_3.

In this section, the first of these scenarios is assessed (CDTA in nitric acid only), with the latter scenario being recommended for furtherwork.

Hitherto CDTA has seen no studies performed with regards to exploring its corrosion effects on metallic surfaces in aqueous conditions. However, the similarly structured sister complexant Ethylenediaminetetraacetic acid (EDTA), Figure 1, has been previously studied with regards to its corrosion properties in a couple of different areas of the nuclear fuel cycle.

EDTA is commonly used to remove iron oxide scales (specifically magnetite) from secondary cooling loops in Pressurised Water Reactors (PWR's), through chelation of corroding ions. Furthermore, EDTA has been shown to be a cathodic stimulant for process steel corrosion in pH 9 high temperature water (70-150°C), carboxylic groups within the structure reducing to aldehydes and driving more rapid anodic steel oxidation even in the absence of oxygen [3].

This project has received funding from the EURATOM research and training programme 2014-2018 under grant agreement No 755171. The content of this deliverable reflects only the author's view. The European Commission is not responsible for any use that may be made of the information it contains.

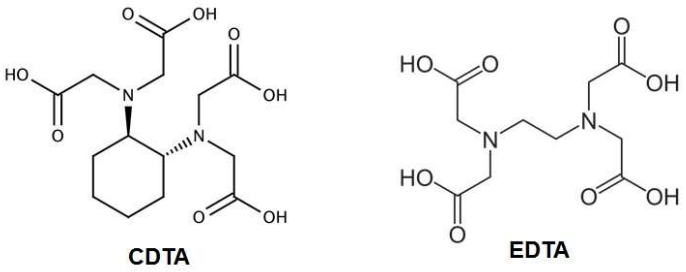

Figure 1: Chemical Structures of CDTA and EDTA.

The effect of EDTA on the corrosion of aluminium has also been studied by Treacy *et al.* [4], aluminium having some use in power plant heat exchangers. Again in pH 9 alkaline solutions (this time at 25°C) significant enhancement of anodic Al corrosion was observed. However, in solutions of pH 4 or less, no observable corrosion enhancement or inhibition was apparent. Such an observation is attributed by the authors to the relative stability of the $Al(EDTA)^-$ complex, which is thermodynamically favoured in alkaline conditions only.

Assuming the corrosion enhancement of metals is related to the relative thermodynamic stability of the complex formed, as per Treacy *et al.* [4], it is therefore useful to compare relative stabilities/extraction properties of CDTA complexes of the primary elemental constituents of process steels, Fe and Cr, in nitric acid solutions. The thermodynamic stability of Fe(II) CDTA complexes has been previously reported by Piché and Larachi [5] and the extraction efficiency of CDTA for Fe, Cr and Ni has been reported by Bell *et al.*[1]. In both cases Fe is shown to have only a minor affinity with CDTA, with Ni and Cr even less likely to form stable complexes in 3 mol dm^{-3}. Thus, it would be expected that CDTA has very little effect on corrosion of stainless steels in nitric acid. Nevertheless, the following section describe experimental work aimed at quantifying the degree of corrosion of SS304L and SS316L that can be expected in nitric acid solutions of 3 mol dm^{-3} and 7.5 mol dm^{-3}.

2. EXPERIMENTAL

2.1. SS304L AND SS316L STAINLESS STEEL WIRE STUDIES IN 3 AND 7 mol dm^{-3} HNO_3

Stainless steel wire experiments have been conducted in a small volume electrochemical cell (200 µl) in order to allow high ligand concentrations to be achieved. Working electrodes were constructed using 10 mm diameter SS316L and SS304L wire in glass Pasteur pipettes, backfilled with epoxy resin and polished using decreasing SiC paper grades and 6, 3 and 1 µm diamond polishing pastes. To complete the three electrode cell, a Ag/AgCl reference electrode and coiled platinum wire

This project has received funding from the EURATOM research and training programme 2014-2018 under grant agreement No 755171. The content of this deliverable reflects only the author's view. The European Commission is not responsible for any use that may be made of the information it contains.

counter electrode were inserted via simple PTFE manifold. An image of the completed cell is shown in Figure 2.

Linear sweep voltammetry (LSV) was used as the predominant experimental technique to assess *in situ* corrosion behaviour. After an open circuit potential (OCP) equilibration period of 2-3 hours, an initial small window (-25 mV to + 25 mV of OCP) linear polarisation resistance (LPR) measurement was taken to ascertain the corrosion rate of the steel (see below). After this initial scan a larger window LSV was performed from -0.25V to +1.25V of OCP to determine the general electrochemical corrosion behaviour of the steel in the presence of varying concentrations of CDTA. All such electrochemical experiments described here are performed at scan rates of 0.5 mV/s. Solutions were also oxygenated during the equilibration period to ensure a maximum amount of dissolved oxygen was present in solution.

Experiments were conducted in both 3 mol dm^{-3} and 7.5 mol dm^{-3} nitric acid solutions with CDTA added at concentrations of 0, 10 and 100 mmol dm^{-3}. Finally all steel wire experiments were performed in triplicate in order to assess the significance of the LPR determined corrosion rate.

2.2. 18/10 NAG AND SS316L STAINLESS STEEL DISK ELECTRODE STUDIES IN 1.5 mol dm^{-3} HNO_3

For large area macro electrode studies, a larger volume traditional corrosion cell configuration was used for experiments. 450 ml of 1.5 mol dm^{-3} HNO_3 was used in a 1 L flat bottom flask. CDTA was used at concentration of 10 mmol dm^{-3} CDTA was added and mixed until dissolved prior to solution sparging.

Working electrodes were created from 100 mm long, 12.7 mm diameter SS316L rod (Goodfellow, UK) and a one and a half inch diameter 18/10 NAG plate sample (Sellafield Ltd., Cumbria, UK). In the latter materials the plate was cut so that the face of the electrode was created from material in the rolling direction with a depth of about 30 mm. Both materials were then turned down on a metal working lathe to a cylinder with a diameter of 9.65 mm and degreased of machine oil by repeatedly washing with toluene before mounting. Samples were first mounted onto threaded brass rod supports using a conductive silver-loaded epoxy (RS Components Ltd., Northants, UK) before casting the entire assembly in epoxy resin (CY1300, Aeorpia Ltd., UK) at 60°C.

Before each experiment working electrodes were polished using decreasing grades of SiC paper (240, 600, 800 and 1200 grit), followed by diamond polishing pastes (10, 6, 3 and 1 µm). Immediately before immersion in test solutions, samples were given a final clean/degrease using successive washes of acetone, deionised water and methanol

This project has received funding from the EURATOM research and training programme 2014-2018 under grant agreement No 755171. The content of this deliverable reflects only the author's view. The European Commission is not responsible for any use that may be made of the information it contains.

respectively, as per ASTM G1-03 [5]. The electrode was then mounted on a threaded SS304L stainless steel rod sealed in glass so that only the steel working electrode face is exposed to solution.

The reference electrode was carefully setup to avoid any chloride contamination of the nitric acid solution. First, a saturated calomel (SCE) double junction reference electrode was prepared (EDT, UK), with an outer junction fill of 1 mol dm^{-3} KNO_3. This was then further placed in a CoralPor™ fritted luggin capillary with the tip placed next to the steel surface, creating a triple junction system. To complete the three electrode cell, two large area platinum mesh counter electrodes were immersed in solution to give an even current distribution around the working electrode.

Linear sweep voltammetry (LSV) and linear polarisation resistance (LPR) were used as the predominant experimental techniques to assess *in situ* corrosion behaviour. Both measurements were carried out according to the relevant ASTM standards [6,7].
After an open circuit potential (OCP) equilibration period of 2-3 hours, an initial small window (-25 mV to + 25 mV of OCP) linear polarisation resistance (LPR) measurement was taken to ascertain the corrosion rate of the steel. After this initial scan a larger window LSV was performed from -0.2V vs. OCP to +1.5V vs. the reference electrode to determine the general electrochemical corrosion behaviour of the steel in the presence of varying concentrations of hydrazine. All such electrochemical experiments described here are performed at scan rates of 0.5 mV/s.

Finally all disk electrode experiments were performed in triplicate in order to assess the significance of the LPR determined corrosion rate and repeatability of experimentally determined polarisation plots.

3. SS304L AND SS316L STAINLESS STEEL WIRE WITH AND WITHOUT CDTA

3.1. STUDIES IN 3 mol dm^{-3} HNO_3

Example LSV and Tafel (log current density vs. potential) plots from one of the triplicate experiments performed on SS316L in the presence of 0, 10 and 100 mmol dm^{-3} CDTA are shown in Figure 4.

This project has received funding from the EURATOM research and training programme 2014-2018 under grant agreement No 755171. The content of this deliverable reflects only the author's view. The European Commission is not responsible for any use that may be made of the information it contains.

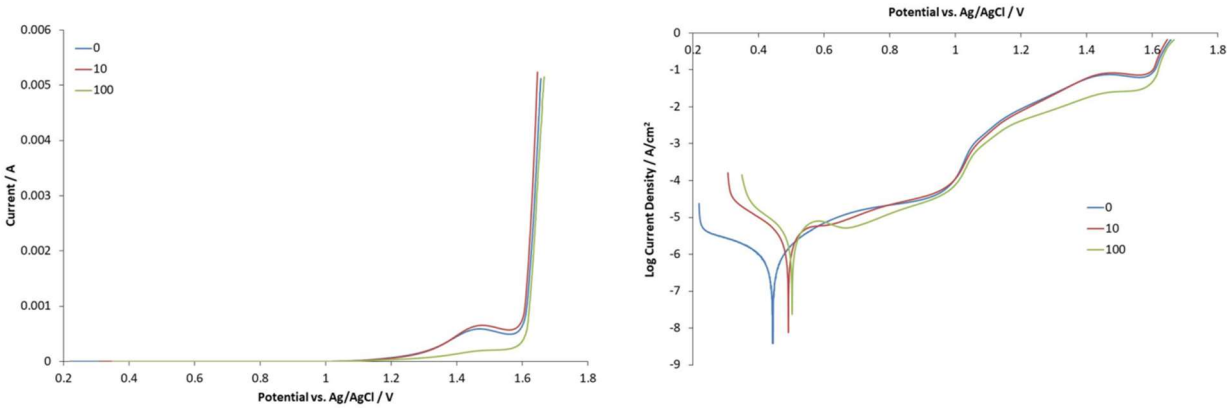

Figure 4: LSV (left) and Tafel plot (right) of a SS316L wire electrode in 3 mol dm^{-3} HNO_3 in the presence of 0, 10 and 100 mmol dm^{-3} CDTA.

At 0 and 10 mmol dm^{-3} CDTA, the LSV scans show little difference between each other, both in the passive and transpassive regions, suggesting there is no significant process steel corrosion enhancement or inhibition at potentials that may be expected under either normal or oxidative maloperation conditions. However, at a higher CDTA concentration of 100 mmol dm^{-3} passive and transpassive currents appear to be significantly reduced vs. either nitric acid alone or at a lower CDTA concentration of 10 mmol dm^{-3}. Such an observation would initially suggest that at a concentration of 100 mmol dm^{-3} CDTA is acting as a corrosion inhibitor, reducing the rate of SS316L steel dissolution. Alternatively as the potential is greater than 1.2 V the observed effect could be some stabilising of the solvent against oxygen evolution.

In the active region, there is some shift in the corrosion potential, E_{corr}, between the triplicate scans performed, as shown in Figure 5, which compares triplicate experiments in 3 mol dm^{-3} HNO_3 only (A) and triplicate experiments in 3 mol dm^{-3} HNO_3 with 10 mmol dm^{-3} CDTA (B). However, importantly the overall shape of the Tafel slopes in the active/initial passive region (<1 V) remains approximately the same across experiments in the presence (Figure 5(B)) and absence (Figure 5(A)) of CDTA. Further, in the region of transpassivity (>1 V) and in both the absence and presence of CDTA the data recorded between experimental runs is almost identical, highlighting the validity of the corrosion inhibition results described for the transpassive region above.

Returning to Figure 4, there is some repeatable increase in the current of the cathodic Tafel arm in the presence of both 10 mmol dm^{-3} and 100 mmol dm^{-3} CDTA concentrations compared to the current observed in the absence of CDTA. This may indicate some cathodic breakdown of carboxylic groups within the structure reducing to aldehydes, as observed by Palmer and Boden in high temperature water carbon steel corrosion [3], leading to an increase in the cathodic current. However, despite the current increase of the cathodic Tafel arm there is no concurrent increase in the anodic

This project has received funding from the EURATOM research and training programme 2014-2018 under grant agreement No 755171. The content of this deliverable reflects only the author's view. The European Commission is not responsible for any use that may be made of the information it contains.

Tafel arm, suggesting that despite structural changes within the CDTA molecule there is no effect on the anodic corrosion rate of the SS316L steel.

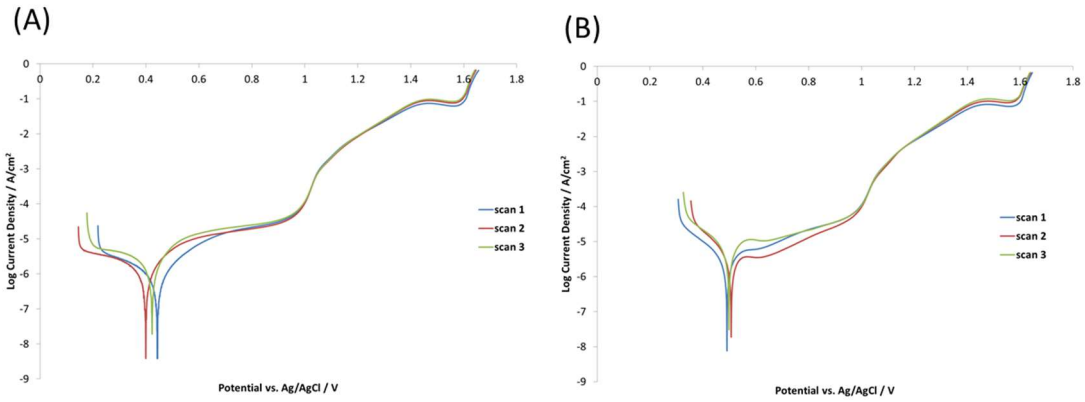

Figure 5: Tafel plots of three separate experiments performed on a SS316L wire electrode in the presence of (A) 3 mol dm^{-3} HNO_3 only and (B) 3 mol dm^{-3} HNO_3 with 10 mmol dm^{-3} CDTA.

The average recorded O.C.P of an SS316L wire electrode across three experiments after two hours immersion in 3 mol dm^{-3} HNO_3 and 0, 10 and 100 mmol dm^{-3} CDTA is shown in Figure 6.

As per the shift in E_{corr} observed in the Tafel plots of Figure 4, the recorded O.C.P. is significantly increased anodically by ~100 mV in the presence of either 10 or 100 mmol dm^{-3} CDTA. This suggests that there is a degree of oxidative stress being generated on the steel, presumably in response to the reduction of carboxylic acid groups to aldehyde groups in the CDTA molecule.

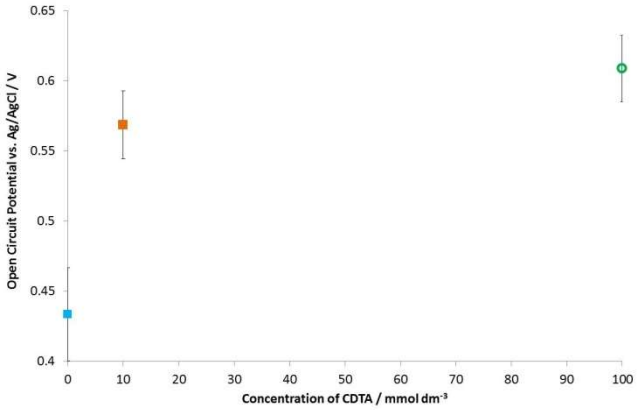

Figure 6: Open circuit potential of an SS316L wire electrode after two hours immersion in 3 mol dm^{-3} HNO_3 in the presence of 0, 10 and 100 mmol dm^{-3} CDTA.

This project has received funding from the EURATOM research and training programme 2014-2018 under grant agreement No 755171. The content of this deliverable reflects only the author's view. The European Commission is not responsible for any use that may be made of the information it contains.

In order to ascertain whether this oxidative stress has any effect on the corrosion rate of the SS316L steel electrode, the corrosion rate was determined using the linear polarisation resistance (LPR) method. Full details of this method and how the corrosion rate is derived may be found in the ASTM standards G59 – 97 and G102 - 89 [6;7]. Briefly, a small window polarisation is made either side of OCP (25 mV) at a slow scan speed (0.5 mV/s). The corrosion current (i_{corr}) is calculated using the polarisation resistance (Rp) determined from a linear regression around the corrosion potential and anodic (b_a) and cathodic (b_c) Tafel arms. i_{corr}, the sample equivalent weight, surface area and density are then used to determine the corrosion rate, expressed in µm/yr or nm/yr.

The results of this analysis for SS316L wire electrodes polarised in 3 mol dm^{-3} HNO_3 in the presence of 0, 10 and 100 mmol dm^{-3} CDTA are shown in Figure 7.

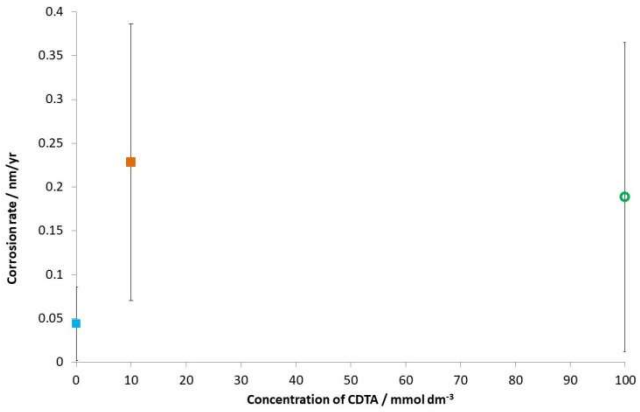

Figure 7: LPR derived corrosion rates for SS316L wire electrodes in 3 mol dm^{-3} HNO_3 in the presence of 0, 10 and 100 mmol dm^{-3} CDTA.

From Figure 7 it can be seen that corrosion rates across all conditions are very low (100's of pm a year). Further, no significant difference in corrosion rate is observed in the presence of both 10 and 100 mmol dm^{-3} added CDTA. Thus, despite cathodic stimulation induced by the CDTA molecule, CDTA appears to have very little effect on the corrosion of SS316L steel in 3 mol dm^{-3}, neither acting as a corrosion accelerator or corrosion inhibitor.

SS304L wire electrodes have also been tested under the same conditions. Example LSV and Tafel plots from one of the triplicate experiments performed on SS304L in the presence of 0, 10 and 100 mmol dm^{-3} CDTA are shown in Figure 8.

This project has received funding from the EURATOM research and training programme 2014-2018 under grant agreement No 755171. The content of this deliverable reflects only the author's view. The European Commission is not responsible for any use that may be made of the information it contains.

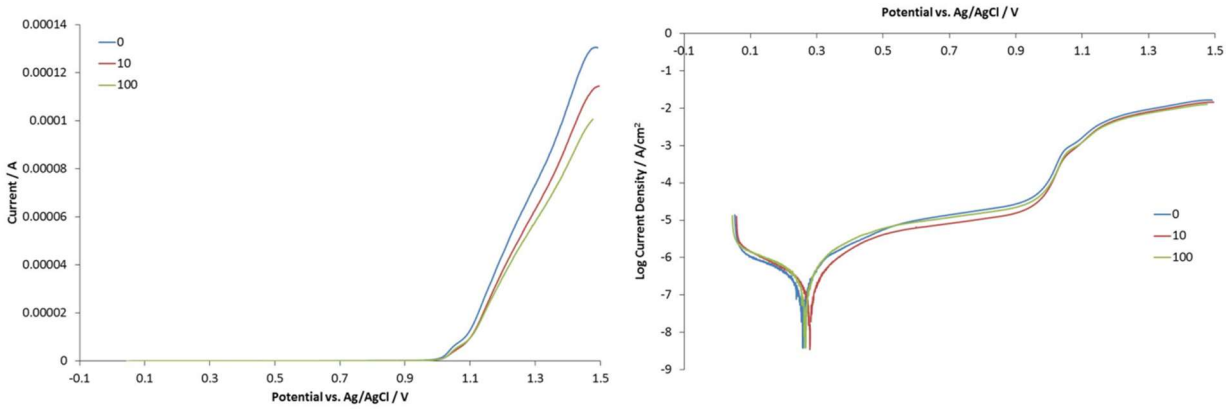

Figure 8: LSV (left) and Tafel plot (right) of a SS304L wire electrode in 3 mol dm^{-3} HNO_3 in the presence of 0, 10 and 100 mmol dm^{-3} CDTA.

As discussed in the second experimental section of this report and in our associated publication on the corrosion effect of AHA on process steels [8], significantly larger currents are observed in the recorded transpassive dissolution currents of Figure 4 for SS316L compared to those of SS304L shown in Figure 8. This has been attributed to the difference in silica content between the two materials [9].

In the active dissolution region no significant differences are observed in the presence or absence of CDTA. Intriguingly there is also no variation in the cathodic arm of the recorded Tafel plot such as that seen in the SS316L experiments of Figure 4. This would suggest there is no cathodic stimulation of corrosion for SS304L, i.e. CDTA is not readily reducing from carboxylic to aldehyde groups. As SS304L shows considerably improved corrosion resistance in nitric acid compared to either SS316L (Figure 4) or carbon steel [3], it could be envisaged that coupling of the cathodic reduction of CDTA with the anodic oxidation of SS304L can only occur if there is a reasonable anodic oxidation half reaction of the steel already occurring, i.e. if the steel is already significantly corroding in nitric acid. However, further electrochemical studies are required to confirm such a hypothesis. Interestingly, and again unlike in the SS316L experiments of Figure 4, increasing CDTA concentration appears to slightly reduce the recorded current in the transpassive regime. Such an observation may suggest that CDTA could be acting as a mild corrosion inhibitor, reducing the rate of SS304L steel dissolution.

In order to understand the background voltammetric behaviour of CDTA across the whole potential window (and in particular the transpassive dissolution range), cyclic voltammograms (CV) on a 3 mm glassy carbon electrode (GC) were also performed in 3 mol dm^{-3} HNO_3 with increasing CDTA concentrations. The results of this analysis are shown in Figure 9.

This project has received funding from the EURATOM research and training programme 2014-2018 under grant agreement No 755171. The content of this deliverable reflects only the author's view. The European Commission is not responsible for any use that may be made of the information it contains.

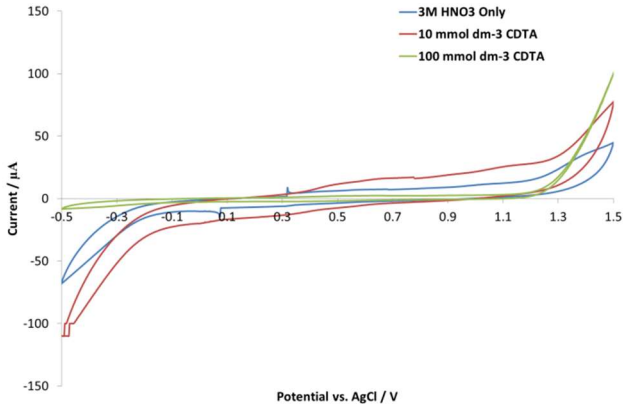

Figure 9: Cyclic Voltammograms of a 3 mm diameter glassy carbon electrode in 3 mol dm^{-3} HNO_3 in the presence of 0, 10 and 100 mmol dm^{-3} CDTA.

While there are some small variations in current with [CDTA] at potentials greater than 1.2 V and less than -0.2 V, such differences are small and unlikely to account for the significantly lower currents observed in the presence of CDTA in the transpassive region, as reported in Figure 8 and Figure 4. Thus, the reduced currents of Figure 8 and Figure 4 are most likely CDTA derived transpassive corrosion inhibition, rather than electrochemical oxidation or reduction of CDTA, such as that reported previously for GC scans of AHA in nitric acid [8]. Considering that under maloperation conditions it is expected that oxidative potentials could reach as high as +1.1V, such CDTA derived corrosion inhibition at potentials >+1V suggests that rather than being detrimental to process steels employed in a EURO-GANEX reprocessing plant, CDTA instead provides some mitigation of process steel corrosion in the event of an oxidative maloperation.

The average recorded O.C.P of an SS304L wire across 3 experiments after 2h immersion in 3 mol dm^{-3} HNO_3 and 0, 10 and 100 mmol dm^{-3} CDTA are shown in Figure 10.

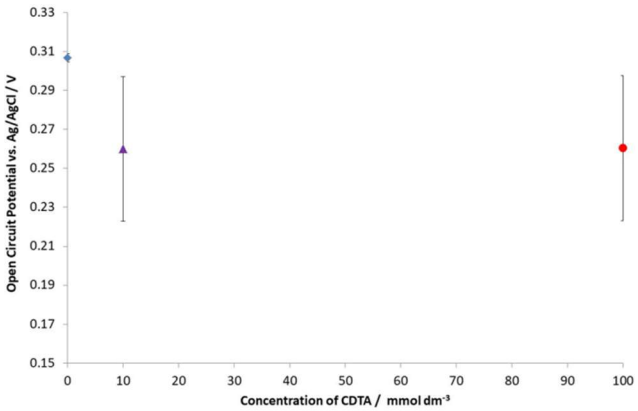

Figure 10: Open circuit potential of an SS304L wire electrode after two hours immersion in 3 mol dm^{-3} HNO_3 in the presence of 0, 10 and 100 mmol dm^{-3} CDTA.

This project has received funding from the EURATOM research and training programme 2014-2018 under grant agreement No 755171. The content of this deliverable reflects only the author's view. The European Commission is not responsible for any use that may be made of the information it contains.

From Figure 10 it can be seen that the recorded O.C.P. values in the presence of CDTA are significantly lower than those recorded in 3 mol dm^{-3} HNO_3 alone, the reverse of measurements on SS316L wire electrodes, Figure 6. As per the large LSV results discussed above, this would suggest that CDTA has some mild reductive effect on SS304L steel at this nitric acid concentration, which could also be inferred to also reduce oxidative dissolution of the steel surface.

In order to ascertain whether this reductive stress has any effect on the corrosion rate of the SS304L steel electrode, the corrosion rate was again determined using the linear polarisation resistance (LPR) method. The results of this analysis for SS304L wire electrodes polarised in 3 mol dm^{-3} HNO_3 in the presence of 0, 10 and 100 mmol dm^{-3} CDTA are shown in Figure 11.

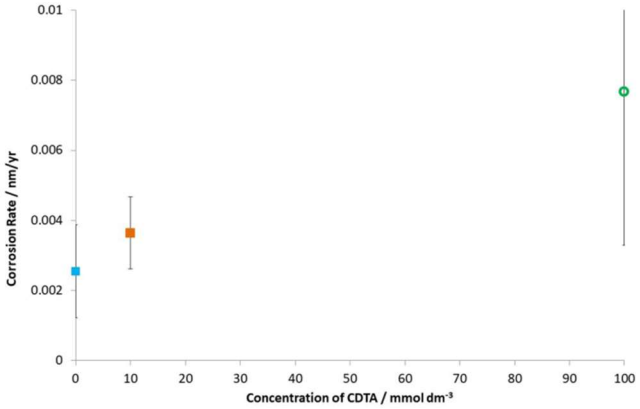

Figure 11: LPR derived corrosion rates for SS304L wire electrodes in 3 mol dm^{-3} HNO_3 in the presence of 0, 10 and 100 mmol dm^{-3} CDTA.

From Figure 11 it can be seen that corrosion rates across all conditions are significantly lower than SS316L (picometers per year). Further, no significant difference in corrosion rate is observed in the presence of both 10 and 100 mmol dm^{-3} added CDTA. Thus, despite the observed more cathodic O.C.P. values recorded in the presence of CDTA, CDTA appears to have very little effect on the corrosion of SS304L steel in 3 mol dm^{-3}, neither acting as a corrosion accelerator or corrosion inhibitor.

3.2. STUDIES IN 7.5 mol dm^{-3} HNO_3

Example LSV and Tafel (log current density vs. potential) plots from one of the triplicate experiments performed on SS316L in the presence of 0, 10 and 100 mmol dm^{-3} CDTA in 7.5 mol dm^{-3} HNO_3 solutions are shown in Figure 12.

This project has received funding from the EURATOM research and training programme 2014-2018 under grant agreement No 755171. The content of this deliverable reflects only the author's view. The European Commission is not responsible for any use that may be made of the information it contains.

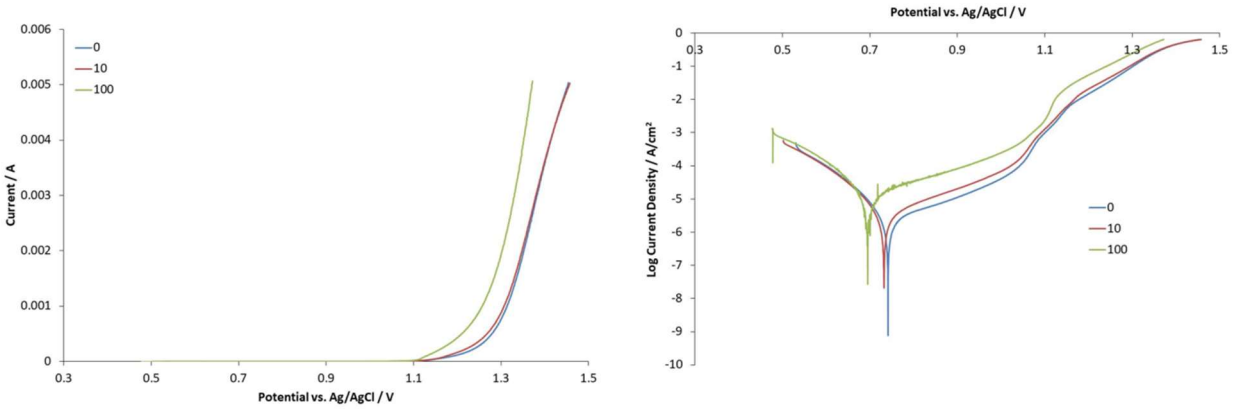

Figure 12: LSV (left) and Tafel plot (right) of a SS316L wire electrode in 7.5 mol dm^{-3} HNO_3 in the presence of 0, 10 and 100 mmol dm^{-3} CDTA.

Unlike at [HNO_3] =- 3 mol dm^{-3} above, both passive and transpassive currents are increased in the presence of 100 mmol dm^{-3} CDTA. A preliminary conclusion would be that at this higher [HNO_3], CDTA acts to accelerate corrosion under transpassive conditions. However, further tests are required to confirm that this is not simply some oxidation effect of the CDTA molecule and is indeed an enhancement of SS316L steel corrosion. Thus, in order to understand the background voltammetric behaviour of CDTA across the whole potential window at this acidity, cyclic voltammograms (CV) on a 3 mm glassy carbon electrode (GC) were again performed in 7.5 mol dm^{-3} HNO_3 with increasing CDTA concentrations. The results of this analysis are shown in Figure 13.

Several observations can be made from Figure 13. First, the OCP and therefore the potential of scan initiation is more anodic than that recorded at 3 mol dm^{-3} HNO_3 in Figure 9, ~0.94V vs. ~0.68V. Second, larger reduction currents for 7.5 mol dm^{-3} nitric acid are observed in Figure 13 vs. those recorded at a concentration of 3 mol dm^{-3} HNO_3 in Figure 13 – with clear hysteresis being present at ~0.4V in the former.

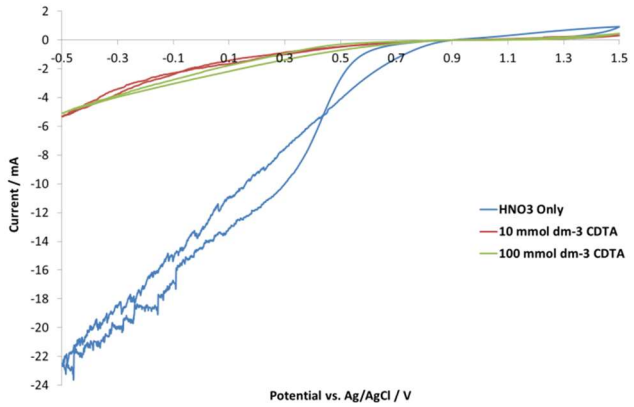

Figure 13: Cyclic Voltammograms of a 3 mm diameter glassy carbon electrode in 7.5 mol dm^{-3} HNO_3 in the presence of 0, 10 and 100 mmol dm^{-3} CDTA.

This project has received funding from the EURATOM research and training programme 2014-2018 under grant agreement No 755171. The content of this deliverable reflects only the author's view. The European Commission is not responsible for any use that may be made of the information it contains.

The electrochemical reduction of nitric acid has been well described at temperatures up to 100ºC by Baulbard *et al.* [10]. In an electrochemical reduction process the nitric acid molecule is not directly reduced; it is reduced through an autocatalytic mechanism involving an electrochemical step and a chemical reaction regenerating the active species, shown in reactions (1) and (2):

$$(HNO_2)_{el.} + H^+ + e^- + s = (NO)_{ads} + H_2O \quad (1)$$

$$HNO_3 + (NO)_{ads} = (HNO_2)_{el.} + (NO_2)_{ads} \quad (2)$$

Where *s* represents a free adsorption site.

HNO_2 is the electroactive species (as denoted by *el.*) in this reaction scheme, reaction (1) being the charge transfer step for the reduction of nitrous acid into nitrogen monoxide. The regeneration reaction (2) is heterogeneous and regenerates the active species HNO_2 from HNO_3 as well as producing NO_2. The rate of regeneration is therefore dependent on the nitric acid concentration. The regeneration reaction is rapid for high HNO_3 concentrations (>9 mol dm^{-3}) and slow for low concentrations (4 to 9 mol dm^{-3} HNO_3). The relative slow speed of the regeneration reaction (2) vs. the charge transfer step of reaction (1) causes the appearance of the hysteresis phenomenon observed in Figure 13.

Returning to Figure 13, the final observation that can be made is the effect of CDTA on nitric acid reduction at this concentration. CDTA at both 10 and 100 mmol dm^{-3} significantly reduces the observed reduction current for nitric acid in the region -0.5 to +0.7V. Such an observation could be the result of one of two different processes, either scavenging of nitrous acid by CDTA or alternatively CDTA blocking adsorption sites for NO, inhibiting the generation of the electroactive species HNO_2, see equation 2.

In the first process removal of nitrous acid (the electroactive species) would result in decreased currents in the CV of Figure 13. However, no information on the nitrous scavenging properties of CDTA is available and further, while metal complexes of EDTA can act as efficient nitric oxide scavengers, no studies have described examples of EDTA scavenging of nitrous acid. Thus, of the two processes the second process seems the more plausible. Adsorption of EDTA onto glassy carbon surfaces is well known and proceeds via an interaction of EDTA carboxylic acid groups at –COH surface sites [11]. Considering CDTA has the same tetra carboxylic acid group structure as EDTA, it would be expected that a similar adsorption process would also readily occur with CDTA. As a result, a layer of CDTA would already be pre-adsorbed at the GC electrode surface before electrochemical scanning, restricting the ability of NO to surface adsorb and reducing the regeneration of HNO_3 to HNO_2 shown in equation (2). As reduction of

This project has received funding from the EURATOM research and training programme 2014-2018 under grant agreement No 755171. The content of this deliverable reflects only the author's view. The European Commission is not responsible for any use that may be made of the information it contains.

nitrous acid is responsible for charge transfer via equation (1), the consequence of NO adsorption site blocking in equation (2) is smaller reduction currents at <1 V, as observed in Figure 13. Further, from Figure 13 it can be seen that 10 mmol dm^{-3} CDTA is enough to completely cover the electrode surface, as no further decrease in reduction current at <1 V is observed at the higher 100 mmol dm^{-3} CDTA concentration.

Returning to Figure 12, it is therefore surprising that enhanced transpassive currents are observed at the higher CDTA concentrations. The standard potential of the NO_3^- /HNO_2 couple is well known to control the redox potential and corrosion rate of process steels in nitric acid [12], thus, inhibition of the electroactive charge transfer reaction by CDTA would be expected to reduce steel corrosion not enhance it.

In order to explore reproducibility between experiments, the complete triplicate series in the absence of CDTA, Figure 14(A), and in the presence of 100 mmol dm^{-3} CDTA (said concentration showing the apparent transpassive increase in Figure 12), Figure 14(B), on a SS316L wire electrode are shown in Figure 14.

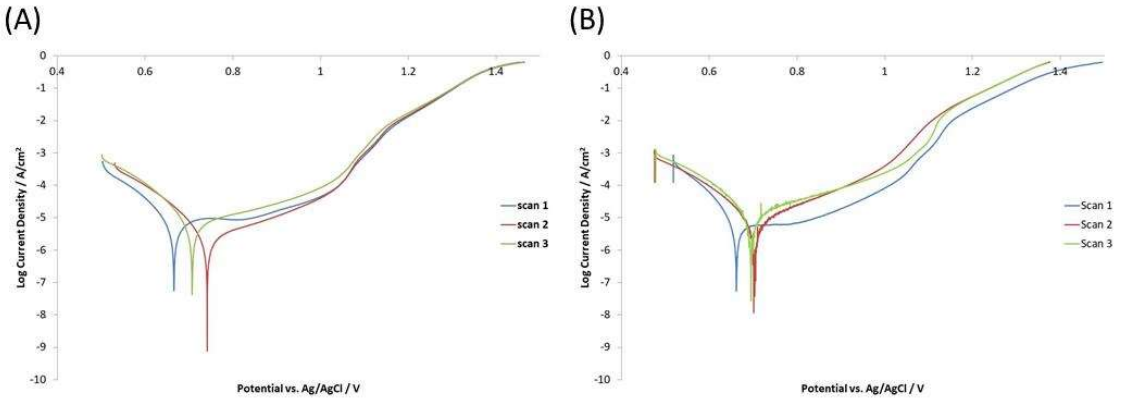

Figure 14: Tafel plots of three separate experiments performed on a SS316L wire electrode in the presence of (A) 7.5 mol dm^{-3} HNO_3 only and (B) 7.5 mol dm^{-3} HNO_3 with 100 mmol dm^{-3} CDTA.

In the absence of CDTA, and as per the results for 3 mol dm^{-3} HNO_3, some variations in E_{corr} and passive currents at <1 V are observed in Figure 14(A). However, in the presence of 100 mmol dm^{-3} CDTA it can be seen that as well as more significant current variations in the passive region at <1 V, there is also more considerable variation in the recorded current in the transpassive region. Thus, in the presence of this CDTA concentration repeatability is low and the observed additional transpassive current previously described is actually within error of data recorded in the absence of CDTA or with a lower concentration of 10 mmol dm^{-3} CDTA.

The average recorded O.C.P of an SS316L wire electrode across three experiments after

This project has received funding from the EURATOM research and training programme 2014-2018 under grant agreement No 755171. The content of this deliverable reflects only the author's view. The European Commission is not responsible for any use that may be made of the information it contains.

two hours immersion in 7.5 mol dm^{-3} HNO_3 and 0, 10 and 100 mmol dm^{-3} CDTA is shown in Figure 15. From this, it can be seen that the recorded open circuit potential in 7.5 mol dm^{-3} HNO_3 is significantly higher than that recorded in 3 mol dm^{-3} HNO_3 (0.758 ± 0.016 V vs. 0.434 ± 0.033 V), the increased oxidative stress being derived from the additional concentration of nitrous acid, the electroactive species responsible for facilitating nitric control of the observed O.C.P. [10]. Despite the average O.C.P. of the 100 mol dm^{-3} CDTA condition being lower than that of both HNO_3 only and 10 mmol dm^{-3} CDTA, all conditions are within error of each other, i.e. such an observed difference is not significant.

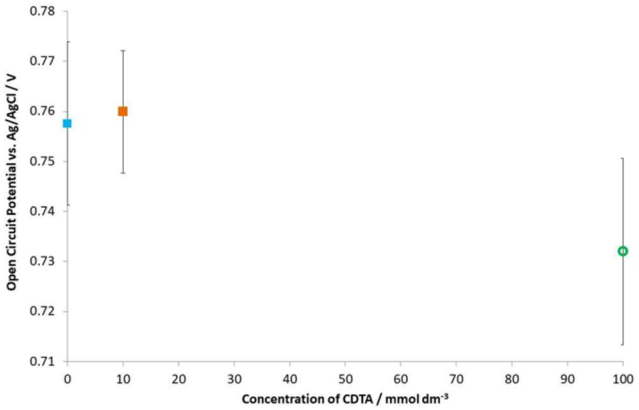

Figure 15: Open circuit potential of an SS316L wire electrode after two hours immersion in 7.5 mol dm^{-3} HNO_3 in the presence of 0, 10 and 100 mmol dm^{-3} CDTA.

In order to ascertain whether CDTA therefore has any effect on the corrosion rate of the SS316L steel electrode, the corrosion rate was again determined using the linear polarisation resistance (LPR) method. The results of this analysis for SS316L wire electrodes polarised in 3 mol dm^{-3} HNO_3 in the presence of 0, 10 and 100 mmol dm^{-3} CDTA in 7.5 mol dm^{-3} HNO_3 are shown in Figure 16.

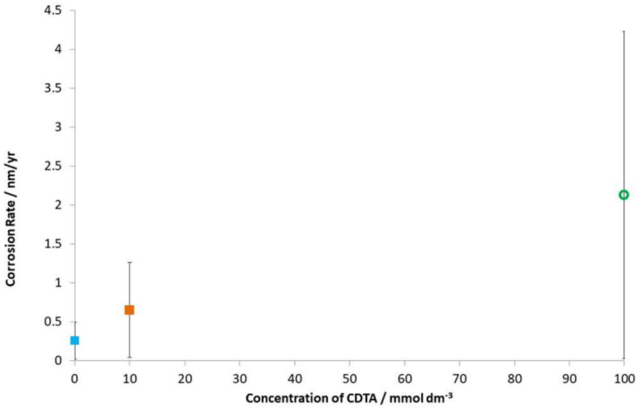

Figure 16: LPR derived corrosion rates for SS316L wire electrodes in 7.5 mol dm^{-3} HNO_3 in the presence of 0, 10 and 100 mmol dm^{-3} CDTA.

This project has received funding from the EURATOM research and training programme 2014-2018 under grant agreement No 755171. The content of this deliverable reflects only the author's view. The European Commission is not responsible for any use that may be made of the information it contains.

From Figure 16 it can be seen that despite the considerable increase in corrosion rate compared to studies in 3 mol dm^{-3} HNO_3, no significant difference in corrosion rate is observed in the presence of both 10 and 100 mmol dm^{-3} additionally added CDTA. Thus, CDTA appears to have very little effect on the corrosion of SS316L steel in 7.5 mol dm^{-3}, neither acting as a corrosion accelerator or corrosion inhibitor.

SS304L wire electrodes have also been tested under the same conditions. Example LSV and Tafel plots from one of the triplicate experiments performed on SS304L in the presence of 0, 10 and 100 mmol dm^{-3} CDTA are shown in Figure 17.

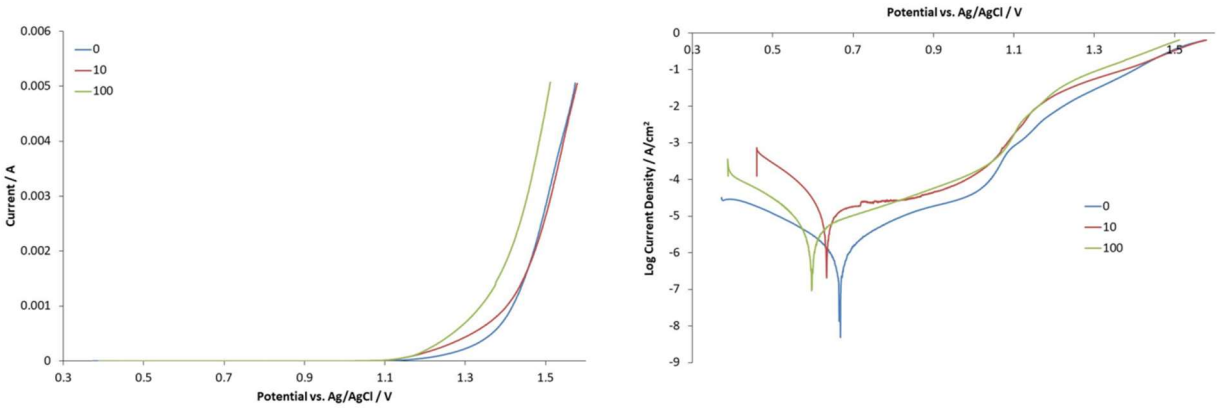

Figure 17: LSV (left) and Tafel plot (right) of a SS304L wire electrode in 7.5 mol dm^{-3} HNO_3 in the presence of 0, 10 and 100 mmol dm^{-3} CDTA.

Again, and unlike at a lower HNO_3 concentration of 3 mol dm^{-3}, both passive and transpassive currents appear to be increased in the presence of 100 mmol dm^{-3} CDTA in an almost identical way to that of SS316L. Further, transpassive currents are almost identical to those recorded for SS316L electrodes in Figure 17. This suggests that the difference in silicon content between SS304L and SS316L has little transpassive protective effect at such a high HNO_3 concentration (see below).

Returning to the higher currents observed in the transpassive region in the presence of 100 mmol dm^{-3}, the complete triplicate series in the absence of CDTA, Figure 18(A), and in the presence of 100 mmol dm^{-3} CDTA (which shows the apparent transpassive increase, Figure 17), Figure 18(B), on a SS304L wire electrode are shown in Figure 18.

This project has received funding from the EURATOM research and training programme 2014-2018 under grant agreement No 755171. The content of this deliverable reflects only the author's view. The European Commission is not responsible for any use that may be made of the information it contains.

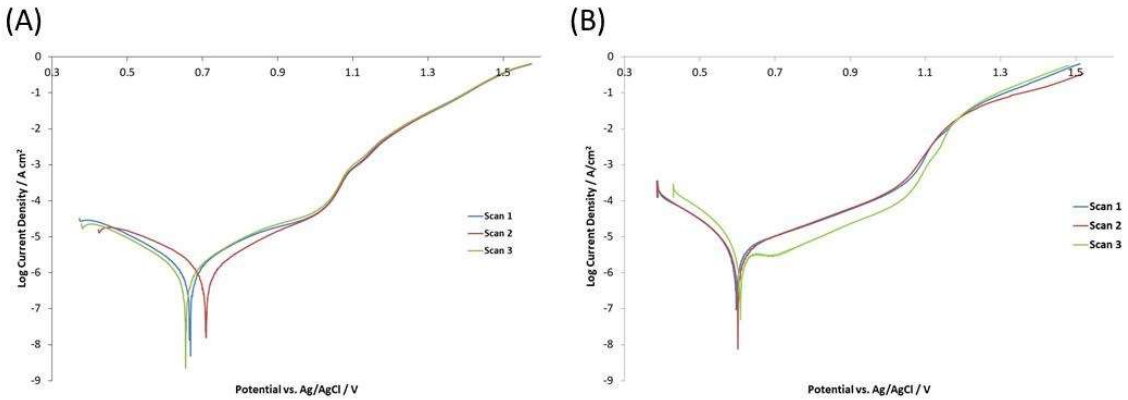

Figure 18: Tafel plots of three separate experiments performed on a SS304L wire electrode in the presence of (A) 7.5 mol dm^{-3} HNO_3 only and (B) 7.5 mol dm^{-3} HNO_3 with 100 mmol dm^{-3} CDTA.

As per SS316L studies in the absence of CDTA, some variations in E_{corr} and passive currents at <1 V are observed in Figure 18(A). However, in the presence of 100 mmol dm^{-3} CDTA it can be seen that as well as more significant current variations in the passive region for one experiment at <1 V, there is also considerable variation in the recorded current in the transpassive region. Thus, in the presence of this CDTA concentration repeatability is low and the observed additional transpassive current previously described is actually within error of data recorded in the absence of CDTA or with a lower concentration of 10 mmol dm^{-3} CDTA.

The average recorded O.C.P of an SS304L wire electrode across three experiments after two hours immersion in 7.5 mol dm^{-3} HNO_3 and 0, 10 and 100 mmol dm^{-3} CDTA is shown in Figure 19.

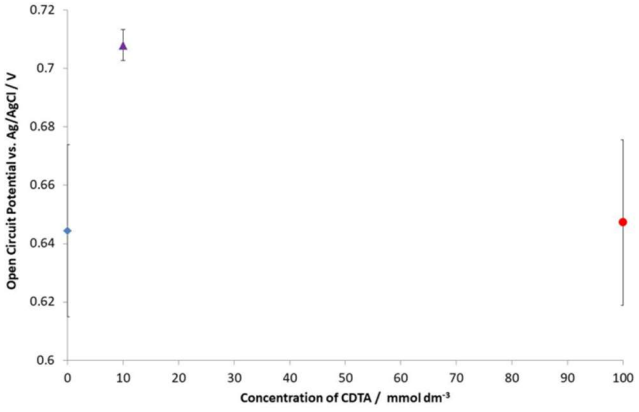

Figure 19: Open circuit potential of an SS304L wire electrode after two hours immersion in 7.5 mol dm^{-3} HNO_3 in the presence of 0, 10 and 100 mmol dm^{-3} CDTA.

From Figure 19 it can be seen that while the O.C.P anodically increases in the presence

This project has received funding from the EURATOM research and training programme 2014-2018 under grant agreement No 755171. The content of this deliverable reflects only the author's view. The European Commission is not responsible for any use that may be made of the information it contains.

of 10 mmol dm^{-3} CDTA, it returns to the same values as those recorded in the presence of 7.5 mol dm^{-3} HNO_3 only upon increasing to 100 mmol dm^{-3} CDTA.

In order to ascertain whether the observed oxidative increase at 10 mmol dm^{-3} CDTA has any effect on the corrosion rate of the SS304L steel electrode, the corrosion rate was determined using the linear polarisation resistance (LPR) method. The results of this analysis for SS304L wire electrodes polarised in 3 mol dm^{-3} HNO_3 in the presence of 0, 10 and 100 mmol dm^{-3} CDTA in 7.5 mol dm^{-3} HNO_3 are shown in Figure 20.

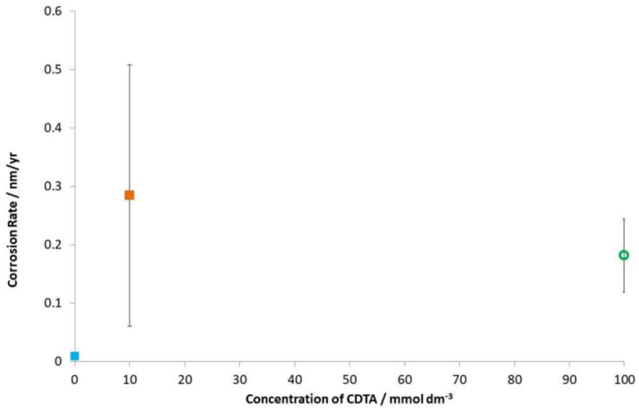

Figure 20: LPR derived corrosion rates for SS304L wire electrodes in 7.5 mol dm^{-3} HNO_3 in the presence of 0, 10 and 100 mmol dm^{-3} CDTA.

Several observations can be made from Figure 20.

First, corrosion rates of SS304L are again within error of those recorded on SS316L electrodes in 7.5 mol dm^{-3} HNO_3 with varying concentrations of CDTA, as shown in Figure 16. As discussed above, it would usually be expected that SS304L should have superior corrosion resistance in nitric acid compared to SS316L [8], although most previous studies comparing SS304L and SS316L have only looked at the corrosion rate of both steels at temperatures greater than 50°C [12]. Thus, potentially the higher nitric acid concentration of 7.5 mol dm^{-3} negates any alloying elemental benefits that usually are apparent in lower nitric concentrations under non-oxidative maloperation conditions (see above).

Second, there a significant increase in corrosion rate in the presence of either 10 or 100 mmol dm^{-3} CDTA vs. 7.5 mol dm^{-3} HNO_3. This would suggest that CDTA has a mild corrosion acceleration effect on SS304L steel under such conditions. However, it should be noted that 1) there is a significant increase in error in the calculated corrosion rate in the presence of CDTA and 2) the increase in corrosion rate is only small (+0.1 nm/yr).

This project has received funding from the EURATOM research and training programme 2014-2018 under grant agreement No 755171. The content of this deliverable reflects only the author's view. The European Commission is not responsible for any use that may be made of the information it contains.

4. 18/10 NAG AND SS316L STAINLESS STEEL DISK ELECTRODE STUDIES

4.1. STUDIES IN 1.5 mol dm^{-3} HNO_3 AND CDTA

Preliminary experiments on the effect of CDTA on SS316L rod and 18/10 NAG plate electrodes have also been carried out for the same reasons as in the section on the effect of hydrazine on the corrosion of prcoess steels above. Further, and as noted in the introduction, CDTA and residual N_2H_4 in nitric acid concentrations up to 3.74 mol dm^{-3} HNO_3 is suggested for use at the start of the 2nd cycle in the EURO-GANEX process. Thus, while a lower nitric acid concentration of 1.5 mol dm^{-3} is studied here, the combinational effect of hydrazine and CDTA is also explored.

LSV and Tafel plots for single run experiments performed on SS316L rod electrodes in air-purged 1.5 mol dm^{-3} nitric acid in the presence 0.01 mol dm^{-3} CDTA are shown in Figure 21.

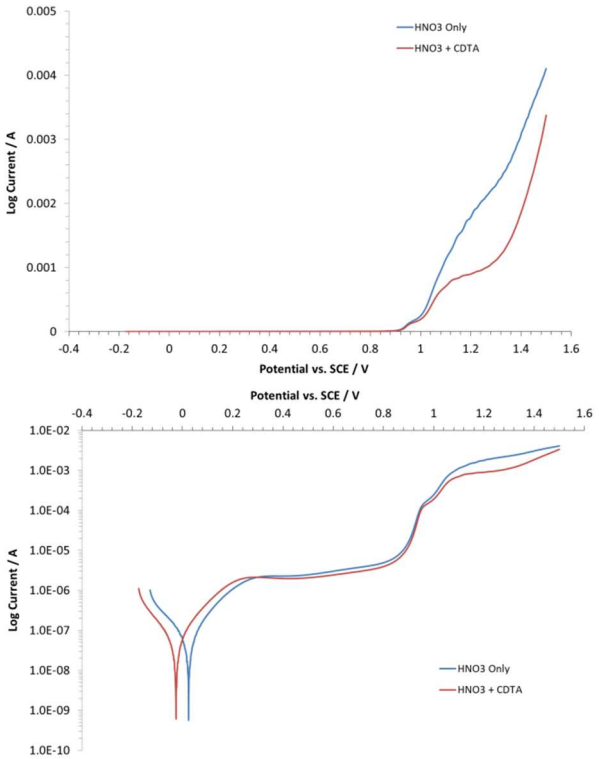

Figure 21: LSV (left) and Tafel plot (right) of SS316L electrodes in 1.5 mol dm^{-3} HNO_3 in the absence and presence of 0.01 mol dm^{-3} CDTA. Solutions were sparged with air.

In the previous section, some inhibition of transpassive dissolution at potentials >1V was observed in studies of SS316L and SS304L wire electrodes in 3 mol dm^{-3} HNO_3 containing 10 and 100 mmol dm^{-3} CDTA. However, on the larger bulk electrodes of

This project has received funding from the EURATOM research and training programme 2014-2018 under grant agreement No 755171. The content of this deliverable reflects only the author's view. The European Commission is not responsible for any use that may be made of the information it contains.

Figure 21 the reduction in transpassive current at >1V is considerably greater and more clear than the previous small electrode area wire studies. Interestingly, and unlike when N_2H_4 is added to the solution, CDTA does not appear to stabilise the secondary passive layer, i.e. recorded transpassive currents are still increasing between ~1.1 and ~1.3V, despite the overall reduction in current within this region. This would suggest that the inhibitive action of CDTA is more akin to restricting solution access to the electrode surface, rather than reducing iron oxide species. As noted in the previous section, CDTA-Fe(II) complexes are known to occur, thus it can be seen that a similar complex could form at the exposed iron surface caused by secondary passivation. The resulting complex layer would then act as a barrier against aggressive agents reaching the metal surface, i.e. an adsorbed CDTA-Fe layer restricting HNO_2 access to the surface.

Returning to Figure 21, the other difference of note is a shift in E_{corr} to a more cathodic potential in the presence of CDTA. Again in order to explore this in more detail a small window LPR scan was also carried out. The results of this scan and the subsequently calculated corrosion rate are shown in Figure 22.

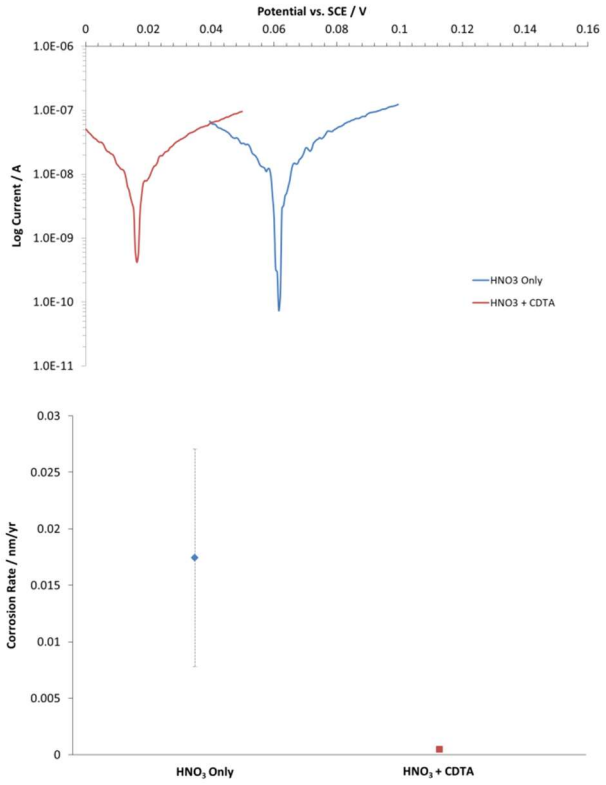

Figure 22: LPR scans (left) and derived corrosion rates (right) for SS316L electrodes in 1.5 mol dm^{-3} HNO_3 in the presence/absence of 0.01 mol dm^{-3} CDTA under air.

From Figure 22 it can be seen that OCP in the presence of 0.01 mol dm^{-3} CDTA is indeed more cathodic than that measured in the absence of CDTA. Furthermore, the preliminary calculated corrosion rate also appears to be reduced in the presence of

This project has received funding from the EURATOM research and training programme 2014-2018 under grant agreement No 755171. The content of this deliverable reflects only the author's view. The European Commission is not responsible for any use that may be made of the information it contains.

CDTA vs. HNO_3 only. However, it should be noted that further experiments are required to confirm whether such a corrosion rate reduction is significant (i.e. error determination through triplicate studies). As per the discussion of the reduced transpassive dissolution of Figure 21, assuming CDTA is indeed providing a surface absorbed complex layer then this may make the measured open circuit potential more cathodic by restricting the access of HNO_2 to the electrode surface, said HNO_2 typically resulting in a high E_0 due to the autocatalytic reduction cycle discussed previously.

Data has also been recorded under N_2 purged conditions. LSV and Tafel plots for single run experiments performed on SS316L rod electrodes in 1.5 mol dm^{-3} nitric acid in the presence 0.01 mol dm^{-3} CDTA and purged with N_2 are shown in Figure 23. The same LPR analysis has also been performed under these conditions, results shown in Figure 24.

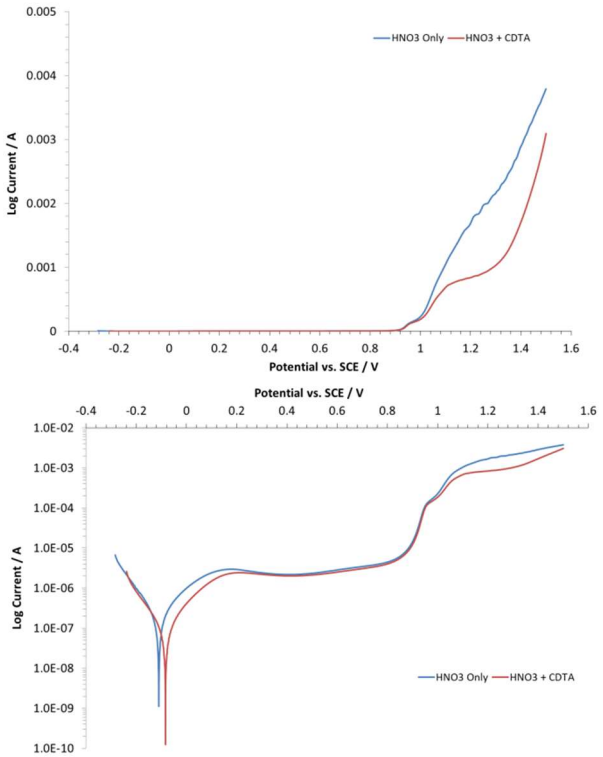

Figure 23: LSV (left) and Tafel plot (right) of SS316L electrodes in 1.5 mol dm^{-3} HNO_3 in the absence and presence of 0.01 mol dm^{-3} CDTA. Solutions were sparged with N_2.

Considering first Figure 23, the transpassive corrosion inhibition behaviour at >1V under N_2 is almost identical to that recorded under aerated conditions, Figure 21, suggesting such CDTA corrosion inhibition action is exclusive of atmospheric conditions. Turning now to Figure 24, the corrosion rate at open circuit potential in the presence of CDTA is also reduced to a similar degree as that observed in aerated conditions. However, interestingly, and unlike in studies of the effect of hydrazine on SS316L corrosion in an N_2 atmosphere, open circuit potential is shifted more anodic in the presence of CDTA.

This project has received funding from the EURATOM research and training programme 2014-2018 under grant agreement No 755171. The content of this deliverable reflects only the author's view. The European Commission is not responsible for any use that may be made of the information it contains.

As described in the previous section, the E_{corr} of SS316L is predominantly dictated by the passive film surface state. O_2 molecules dissociate to form O^{2-} ions and join and enhance the passive film. Conversely, NO_3^- competes for adsorption on the film surface, inhibiting film formation and driving dissolution. Thus, the open circuit potential is shifted towards passivity under aerated conditions as the Cr_2O_3 strengthens in the presence of dissociated oxygen molecules. Conversely, in the absence of oxygen, passive layer formation is inhibited by more adsorption of NO^{3-} species causing a shift towards active dissolution.

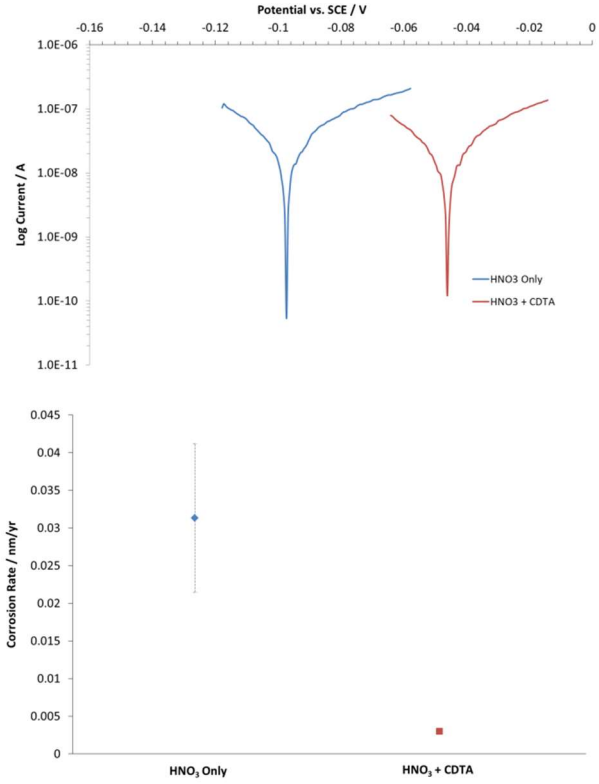

Figure 24: LPR scans (left) and derived corrosion rates (right) for SS316L electrodes in 1.5 mol dm^{-3} HNO_3 in the presence/absence of 0.01 mol dm^{-3} CDTA under N_2.

Thus, one possible explanation for the anodic shift in the corrosion potential observed upon addition of CDTA in Figures 23 and 24 is that the adsorbed CDTA layer restricts NO_3^- access to the steel surface allowing less competition between NO_3^- and O^{2-} ions in the formation of the passive film on the SS316L electrode described above, i.e. the pre-immersion air formed Cr_2O_3 layer predominates. The result is a slight anodic shift in E_{corr} as a response to a more protective passive layer. Note, unlike with hydrazine no concomitant scavenging of HNO_2 also occurs (which would produce a more cathodic OCP) and so the overall effect is an anodic shift in E_{corr}.

This project has received funding from the EURATOM research and training programme 2014-2018 under grant agreement No 755171. The content of this deliverable reflects only the author's view. The European Commission is not responsible for any use that may be made of the information it contains.

4.2. STUDIES IN 1.5 mol dm^{-3} HNO_3, CDTA AND HYDRAZINE

LSV and Tafel plots for single run experiments performed on SS316L rod electrodes in 1.5 mol dm^{-3} nitric acid in the presence of 1.5 mol dm^{-3} HNO_3 and 0.2 mol dm^{-3} hydrazine with and without 0.01 mol dm^{-3} CDTA and purged with air are shown in Figure 25.

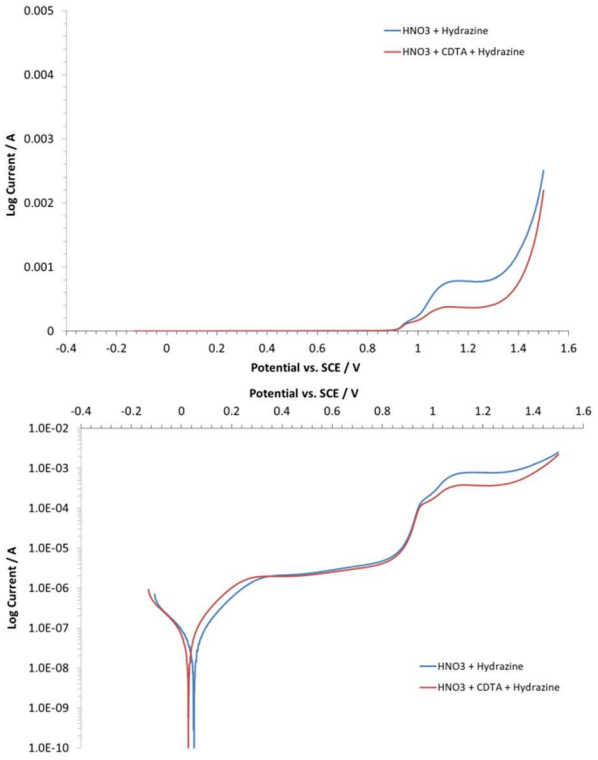

Figure 25: LSV (left) and Tafel plot (right) of SS316L electrodes in 1.5 mol dm^{-3} HNO_3 with 0.2 mol dm^{-3} hydrazine in the absence and presence of 0.01 mol dm^{-3} CDTA. Solutions were sparged with air.

The considerable enhancement of the secondary passive layer at >1V in the presence of hydrazine is clearly shown in Figure 25. Interestingly, the addition of CDTA seems to have a similar effect to that in the absence of hydrazine, Figure 21, i.e. transpassive currents are lowered further but the overall shape of the LSV/Tafel curve remains unchanged.

Thus, it would appear that both hydrazine and CDTA can act in combination to inhibit transpassive corrosion if both are present in solution. The most likely mechanism would thus be a reduction of secondary passive layer iron oxide species by hydrazine, stabilising the secondary partially-passive layer, and subsequent or simultaneous formation of an adsorbed CDTA surface layer that further inhibits electrolyte access to the partially-passive steel surface.

This project has received funding from the EURATOM research and training programme 2014-2018 under grant agreement No 755171. The content of this deliverable reflects only the author's view. The European Commission is not responsible for any use that may be made of the information it contains.

The results of LPR scans and the subsequently calculated corrosion rate are shown in Figure 26.

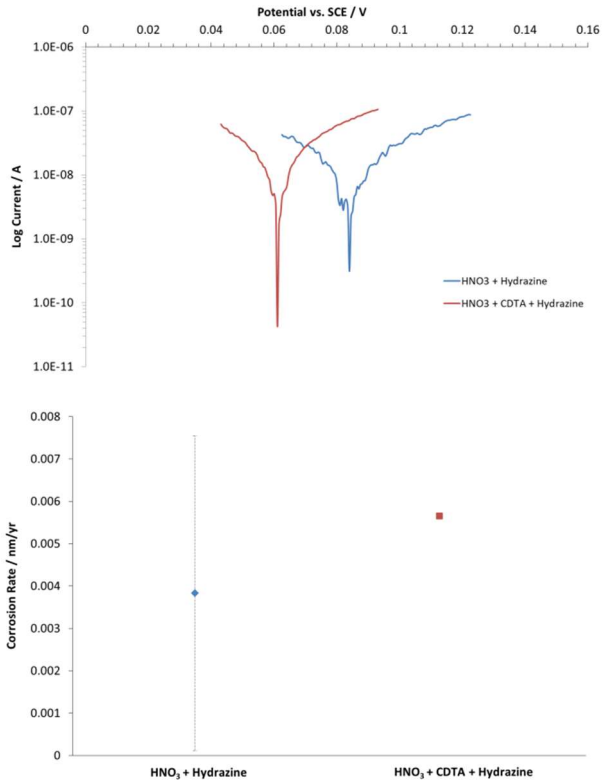

Figure 26: LPR scans (I) and derived corrosion rates (r) for SS316L electrodes in 1.5 mol dm^{-3} HNO_3 and 0.2 mol dm^{-3} hydrazine in the presence/absence of 0.01 mol dm^{-3} CDTA under air.

Despite the additional protection at transpassive potentials, no significant improvement in corrosion rate is seen around open circuit potential. However, as per Figure 22, it appears that the presence of CDTA in solution does still cause a cathodic shift in the open circuit potential over and above that observed in the presence of hydrazine. This would suggest that CDTA is perhaps the dominant surface complexant under such conditions, i.e. a surface CDTA layer is preferentially adsorbed over a bidentate hydrazine complexed surface film, the switch from one adsorbed film to the other having no particular benefit with regards to reducing corrosion above that already provided in the presence of an adsorbed hydrazine film alone.

LSV and Tafel plots for single run experiments performed on 18/10 NAG electrodes in 1.5 mol dm^{-3} nitric acid in the presence 0.01 mol dm^{-3} CDTA and purged with air are shown in Figure 27.

This project has received funding from the EURATOM research and training programme 2014-2018 under grant agreement No 755171. The content of this deliverable reflects only the author's view. The European Commission is not responsible for any use that may be made of the information it contains.

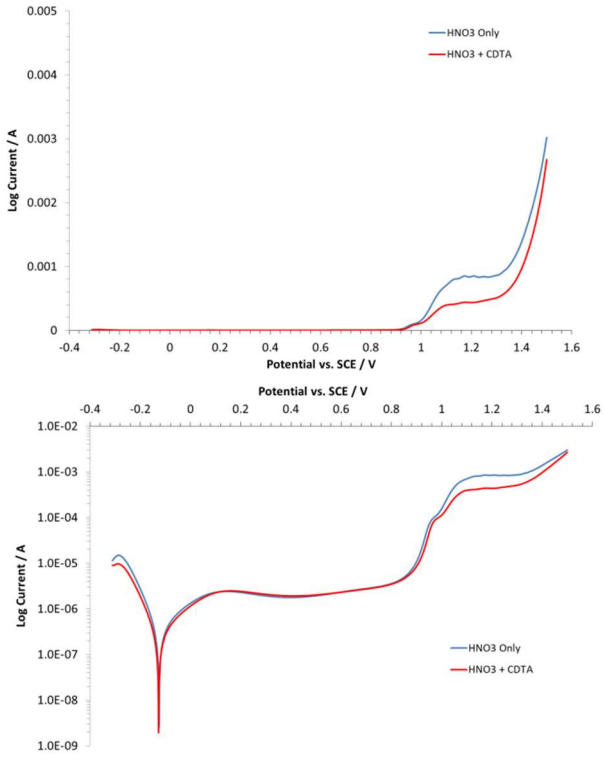

Figure 27: LSV (left) and Tafel plot (right) of 18/10 NAG electrodes in 1.5 mol dm^{-3} HNO_3 in the absence and presence of 0.01 mol dm^{-3} CDTA. Solutions were sparged with air.

Figure 27 reveals an almost identical reduction in transpassive current at >1V to that seen in SS316L studies, Figure 21. Interestingly, and again the same as that observed in Figure 21 for the SS316L electrode, CDTA does not appear to stabilise the secondary passive layer, i.e. the same LSV shape is maintained between ~1.1 and ~1.3V. Instead transpassive currents are evenly reduced across the entire transpassive range; again suggesting restriction of electrolyte to the electrode surface is the predominant corrosion inhibition mechanism rather than reduction and stabilisation of the secondary partially-passive layer.

The results of LPR scans and the subsequently calculated corrosion rate are shown in Figure 28.

Unlike the previous studies on SS316L electrodes, Figure 28 shows that OCP varies little in the presence of CDTA. Similarly, calculated corrosion rates in the presence of CDTA remain very close to within error of those recorded in HNO_3 alone. Such behaviour is almost identical to that described for 18/10 NAG electrodes in the presence of hydrazine. This would support the previous conclusion that the 18/10 NAG passive film at low cathodic potentials is not as protective as that formed on SS316L, again supported by the high variance in corrosion rates recorded in triplicate experiments for

This project has received funding from the EURATOM research and training programme 2014-2018 under grant agreement No 755171. The content of this deliverable reflects only the author's view. The European Commission is not responsible for any use that may be made of the information it contains.

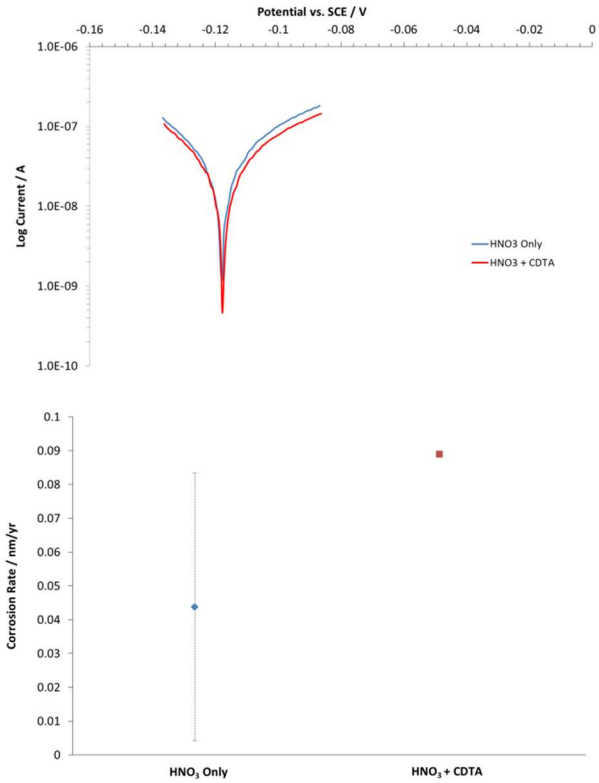

Figure 28: LPR scans (left) and derived corrosion rates (right) for 18/10 NAG electrodes in 1.5 mol dm^{-3} HNO_3 in the presence/absence of 0.01 mol dm^{-3} CDTA under air.

the HNO_3 only condition. It would appear that this reduced effectiveness of the 18/10 NAG passive film compared to SS316L also reduces the effectiveness of adsorbed surface film inhibitors such as CDTA and hydrazine at reducing active dissolution.

LSV and Tafel plots for single run experiments performed on 18/10 NAG electrodes in 1.5 mol dm^{-3} nitric acid in the presence of 1.5 mol dm^{-3} HNO_3 and 0.2 mol dm^{-3} hydrazine with and without 0.01 mol dm^{-3} CDTA and purged with air are shown in Figure 29.

The considerable enhancement of the secondary passive layer at applied potentials greater than 1V in the presence of hydrazine is clearly shown in Figure 29. Furthermore, the addition of CDTA again has a similar effect to that in the absence of hydrazine, Figure 27, i.e. transpassive currents are lowered further but the overall shape of the LSV/Tafel curve remains unchanged. This makes the transpassive currents up to 1.4V the lowest yet recorded, being in the region of ~100µA, compared to just over a 1 mA in the presence of HNO_3 only, see Figure 27. Thus, it would again appear that both hydrazine and CDTA can act in combination to inhibit transpassive corrosion if both are present in solution.

This project has received funding from the EURATOM research and training programme 2014-2018 under grant agreement No 755171. The content of this deliverable reflects only the author's view. The European Commission is not responsible for any use that may be made of the information it contains.

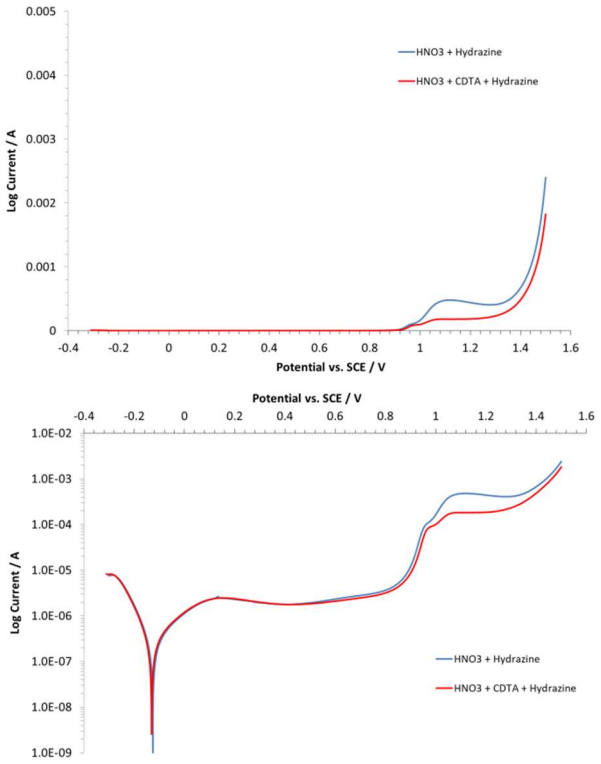

Figure 29: LSV (left) and Tafel plot (right) of 18/10 NAG electrodes in 1.5 mol dm^{-3} HNO_3 with 0.2 mol dm^{-3} hydrazine in the absence and presence of 0.01 mol dm^{-3} CDTA. Solutions were sparged with air.

Finally, the results of LPR scans and the subsequently calculated corrosion rate are shown in Figure 30.

From Figure 30, it can be seen that the corrosion rate at OCP in the presence of CDTA and hydrazine appears slightly higher than that measured in hydrazine and HNO_3 only. Furthermore the measured OCP is slightly more cathodic in the presence of CDTA and hydrazine compared to in the absence of CDTA. Again such results should be treated with caution until triplicate studies are performed, but if a slight corrosion enhancement is indeed occurring, overall increase in corrosion rate is very low, being of the order of 10's of pm/yr.

This project has received funding from the EURATOM research and training programme 2014-2018 under grant agreement No 755171. The content of this deliverable reflects only the author's view. The European Commission is not responsible for any use that may be made of the information it contains.

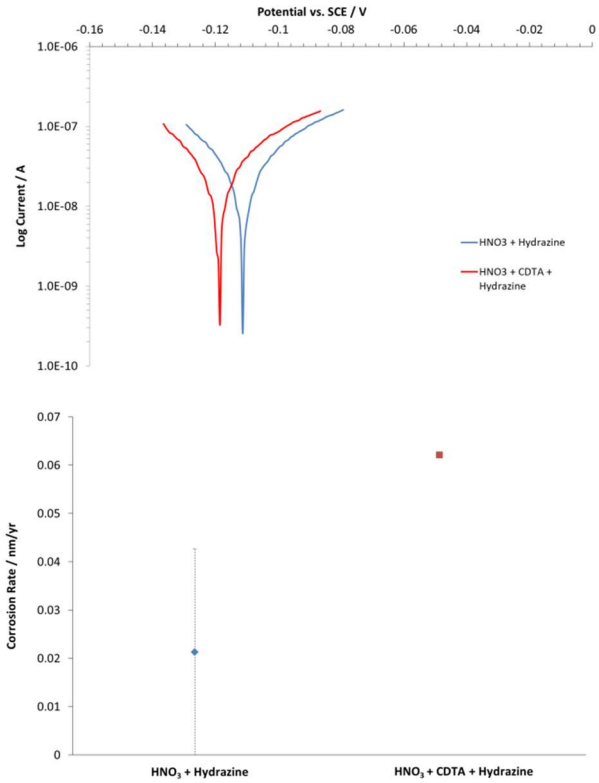

Figure 30: LPR scans (l) and corrosion rates (r) for 18/10 NAG electrodes in 1.5 mol dm^{-3} HNO_3, 0.2 mol dm^{-3} hydrazine in the presence/absence of 0.01 mol dm^{-3} CDTA under air.

This project has received funding from the EURATOM research and training programme 2014-2018 under grant agreement No 755171. The content of this deliverable reflects only the author's view. The European Commission is not responsible for any use that may be made of the information it contains.

5. CONCLUSIONS AND FURTHER WORK

Linear sweep voltammetry (LSV), Linear Polarisation Resistance (LPR) and Open Circuit Potential (OCP) studies have been conducted into the corrosion of SS304L and SS316L wire electrodes in 3 and 7.5 mol dm^{-3} HNO_3 at CDTA concentrations of 0, 10 and 100 mmol dm^{-3}.

In 3 mol dm^{-3} HNO_3 CDTA has little effect on corrosion of either SS316L or SS304L steels under both normal and oxidative maloperation conditions. Indeed on SS304L steels some mild corrosion inhibition is observed under conditions of oxidative maloperation, suggesting CDTA may actually be beneficial to plant material resistance under such conditions.

Both steels undergo more rapid corrosion in 7.5 mol dm^{-3} HNO_3. However, little difference in either normal operation corrosion rates or maloperation currents are observed between the two steel types despite differences in minor element composition. Under normal operation conditions there is no significant increase in corrosion rate in the presence of CDTA at all concentrations tested. Under oxidative maloperation conditions greater current variation between experiments is observed in the transpassive region upon addition of 100 mmol dm^{-3} CDTA, but no significant increase in transpassive dissolution is found. Interestingly, baseline electrochemical behaviour studies in 7.5 mol dm^{-3} HNO_3 suggest CDTA acts to inhibit the electroactive species HNO_2, which could reduce the redox potential and therefore potentially mitigate against corrosion in particularly oxidising nitric acid environments.

Studies using high surface area SS316L and 18/10 NAG electrodes have provided further data for systems closer to realistic EURO-GANEX conditions and with observable surface morphologies.

While LSV/Tafel curves for hydrazine-nitric acid systems shows the stabilisation of a secondary passive layer in the region of transpassive dissolution (where intergranular corrosion may occur), such a stabilisation is not observed with CDTA. However, transpassive currents are still reduced at transpassive potentials, suggesting that the inhibitive action of CDTA is more akin to restricting solution access to the electrode surface. Again this corrosion inhibition action is exclusive of atmospheric condition.

Finally, when CDTA is present in combination with hydrazine and nitric acid transpassive currents are lowered further than those observed independently of the addition of each agent. Thus, it would appear that both hydrazine and CDTA can act in

This project has received funding from the EURATOM research and training programme 2014-2018 under grant agreement No 755171. The content of this deliverable reflects only the author's view. The European Commission is not responsible for any use that may be made of the information it contains.

combination to inhibit transpassive corrosion if both are present in solution.

Recommendations for further work: CDTA has been shown to inhibit transpassive corrosion, i.e. corrosion under maloperations conditions, for a number of candidate process steels. Too, experiments conducted at the nitric acid concentration of 1.5 mol dm^{-3} indicate that hydrazine and CDTA exhibit a strong cooperative corrosion inhibiting effect. Thus, this cooperative effect of CDTA and hydrazine on the corrosion of all steels studied here should be investigated at the higher nitric acid concentrations that occur elsewhere in the GANEX flow sheet – specifically ~7.4 and 3.74 mol dm^{-3} HNO_3 , so far unexamined in the context of CDTA/hydrazine combination studies.

Too, studies of the effect that CDTA and CDTA/hydrazine mixes have on the general corrosion and transpassive corrosion processes observed in the presence of AHA, SO_3-Ph-BTP, SO_3-Ph-BTPhen should also be conducted in order to determine whether there is any additional protection afforded over and above that provided by the AHA hydrolysis product, hydroxylamine.

This project has received funding from the EURATOM research and training programme 2014-2018 under grant agreement No 755171. The content of this deliverable reflects only the author's view. The European Commission is not responsible for any use that may be made of the information it contains.

REFERENCES

[1] K. Bell, C. Carpentier, M. Carrott, A. Geist, C. Gregson, X. Heres, D. Magnusson, R. malmbeck, F. McLachlan, G. Modolo, U. Mullich, M. Sypula, R. Taylor, A. Wilden, *Procedia Chemistry* **7** (2012), pp392-397

[2] "Process Description of the EURO-GANEX Process" NNL 13172, R3.1.1, 05/06/2014

[3] J.W. Palmer and P.J. Boden, *British Corrosion Journal* **27**(4) (1992), pp305-309

[4] G.M. Treacy, A.L. Rudd, C.B. Breslin, *Journal of Applied Electrochemistry* **30** (2000), pp675-683

[5] ASTM International. Standard Practice for Preparing, Cleaning and Evaluating Corrosion Test Specimens. G1-03, 1-12. 2011.

[6] ASTM International. Standard Test Method for Conducting Potentiodynamic Polarization Resistance Measurements. G59 - 97, 1-4. 2014.

[7] ASTM International. Standard Practice for Calculation of Corrosion Rates and Related Information from Electrochemical Measurements. G102 - 89, 1-8. 2015.

[8] R.J. Wilbraham, C. Boxall, *Electrochemistry Communications* **62** (2016), pp52-55

[9] R. Robin, F. Miserque, V. Spagnol, *Journal of Nuclear Materials* **375** (2008) pp65-71

[10] F. Balbaud, G. Sanchez, G. Santarini, G. Picard European Journal of Inorganic Chemistry **2000** (2000) pp665-674

[11] J.M.S. Almeida, R.M. Dornellas, S. Yotsumoto-Neto, M. Ghisi, J.G.C. Furtado, E.P. Marques, R.Q. Aucelio, A.L.B. Marques, Fuel **115** (2014) pp658-665

[12] P. Fauvet, F. Balbaud, R. Robin, Q.T. Tran, A. Mugnier, D. Espinoux, *Journal of Nuclear Materials* **375** (2008) pp52-64

This project has received funding from the EURATOM research and training programme 2014-2018 under grant agreement No 755171. The content of this deliverable reflects only the author's view. The European Commission is not responsible for any use that may be made of the information it contains.

CORROSION STUDIES OF PROCESS STEELS IN THE PRESENCE OF A GAMMA FIELD

1. INTRODUCTION

CDTA is utilised at the start of the 2nd cycle in the EURO-GANEX process. CDTA is fed from a constant head feed tank into the primary separation stream to prevent extraction of FPs (particularly zirconium (IV) and palladium (II) [1]) in the next Transuranium element (TRU) extraction and scrub through the formation of Zr and Pd complexes in the aqueous phase. At the start of the 2nd cycle the nitric acid concentration is still relatively high, 7.408 mol dm^{-3}, the U-stripped aqueous input stream coming from the primary separation step after fuel dissolution. The added CDTA concentration at this stage is expected to be 0.104 mol dm^{-3}.

CDTA complexed with Zr at a lower concentration (0.033 mol dm^{-3}) will also be apparent in the resultant FP loaded (Sr and Cs) nitric acid stream generated by the TRU extraction and scrub step at the start of the 2nd cycle. Some residual hydrazine is also expected in this stream (0.023 mol dm^{-3}) having been carried through from the 1st cycle uranium scrub and the nitric acid concentration is also expected to be lower at 3.74 mol dm^{-3} [2]. Thus, with regards to process steel corrosion behaviour two different scenarios need to be assessed:

1) CDTA in nitric acid concentrations of ~7.4 mol dm^{-3} and 3.74 mol dm^{-3} HNO_3
2) CDTA and hydrazine in nitric acid concentrations of ~7.4 and 3.74 mol dm^{-3} HNO_3.

In the previous section, the first scenario was assessed and was shown to extend the region of passivity on the surface of both 304L and 316L stainless steel electrode. For CDTA, this was attributed to the formation of an adsorbed layer of CDTA at the steel surface (most likely affiliating through Fe centres) that then serves to protect the surface against oxidative attack. The second scenario was recommended for further work, although some studies conducted at the lower nitric acid concentration of 1.5 mol dm^{-3} indicated that hydrazine and CDTA exhibit a strong cooperative corrosion inhibiting effect.

All studies presented to date have focussed on the corrosion chemistry of key reagents in the GANEX flowsheet in the absence of any radiation field. However, these materials will be exposed to very significant radiation fields indeed on plant and the effects of these fields on corrosion of plant fabric materials in the presence of such fields needs to be assessed.

This project has received funding from the EURATOM research and training programme 2014-2018 under grant agreement No 755171. The content of this deliverable reflects only the author's view. The European Commission is not responsible for any use that may be made of the information it contains.

During the course of the GENIORS project, we were offered unexpected access to a gamma irradiator, thus affording the opportunity to conduct a series of preliminary studies of the behaviour of key GANEX process components under irradiated conditions. Given resource availability and that CDTA can exhibit a corrosion inhibiting effect, the decision was taken to begin these preliminary studies by examining the effect of irradiation on CDTA and to determine whether its corrosion inhibiting properties were retained in the presence of a gamma field.

Thus, this section of the deliverable report focusses on the corrosion behaviour of CDTA and nitric acid in scenario 1) above – after 96 hours of continuous gamma irradiation is presented.

Hitherto the radiolytic degradant products of CDTA have yet to be fully elucidated and it has not been established whether a threshold dose can be reached whereby the surface protection observed in the last experimental section of this report no longer applies.

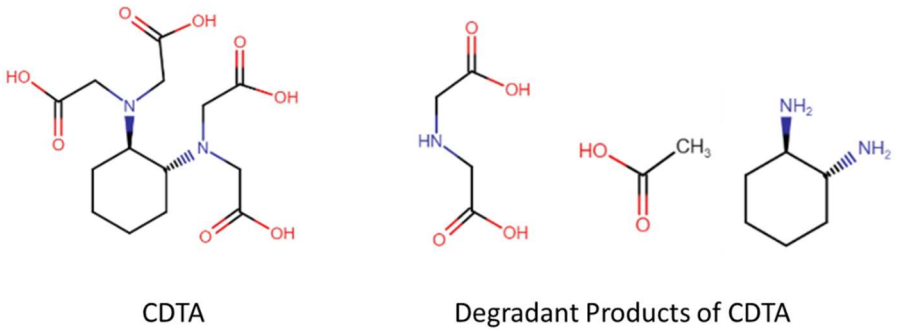

Figure 1: Chemical structures of CDTA (left) and proposed radiolytically produced degradant products of CDTA (right).

While laboratory scale experiments and potentiometric scanning can be used to simulate a range of expected solution potentials in a reprocessing stream that may occur as a result of, for example, the presence of oxidative species, temperature and acidity changes the effect of a strong radiation field, as stated above, cannot be fully accounted for easily. The reason for this is that many radicals generated in radiation fields are short lived and strongly oxidising. Furthermore, radiolysis will result in significant breakdown of the nitric acid and extraction ligands used; creating new smaller molecular weight species that may exhibit different corrosion inhibition/acceleration chemistries to that of the parent molecule. Again, such behaviour cannot easily be simulated in a standard laboratory. This is particularly of interest over longer corrosion periods, i.e. a matter of days rather than hours, one of the objectives of this work package.

This project has received funding from the EURATOM research and training programme 2014-2018 under grant agreement No 755171. The content of this deliverable reflects only the author's view. The European Commission is not responsible for any use that may be made of the information it contains.

The radiolytic decomposition of nitric acid has been well characterised with the primary long-lived species being NO_2^-, HNO_2, NO_3•, NO_2 and O_2. HNO_2 [3] as well as being electrochemically activie in driving the transpassive corrosion of the stainless steel surface (see above, *passim*), is also known to be the primary species in the nitration of organic molecules leading to denaturing of reprocessing solvents and reduction in extraction efficiency.

Turning to the effect of ionising radiation on the structure of CDTA; while few citations have studied the specific reaction, it would be reasonable to assert that subject to gamma radiation and especially in the presence of nitric acid, the CDTA molecule would decompose into its carboxylic acid and cyclohexylamine moieties, as seen in Figure 1. This would, over time, diminish the inhibiting corrosion effect observed in previous electrochemical studies. It is this latter hypothesis that is explored in this section of the report.

Based on the above, two types of preliminary experiment are described in this section:

1) *In situ* irradiation physical corrosion damage studies on SS304L flags/specimens in nitric acid with and without CDTA.
2) *Ex situ* electrochemical testing of post-irradiation aqueous phases with and without CDTA

Irradiation experiments were conducted using the Co-60 gamma irradiator at the Dalton Cumbrian Facility (DCF), University of Manchester. Post irradiation SEM and electrochemical corrosion studies were conducted in Lancaster University's UTGARD Lab (Uranium / Thorium beta-Gamma Active R&D Laboratory). Both DCF and UTGARD Lab are UK Government-funded facilities established for the study of spent nuclear fuel recycle and waste management as part of the EPSRC (Engineering and Physical Sciences Research Council) supported NNUF (National Nuclear Users Facility) initiative.

This project has received funding from the EURATOM research and training programme 2014-2018 under grant agreement No 755171. The content of this deliverable reflects only the author's view. The European Commission is not responsible for any use that may be made of the information it contains.

2. EXPERIMENTAL

Foil sheets of 304L stainless steel, 100mm x10mm x 9mm (WxLxT) with a manufactured mirror polish were purchased from Goodfellow (Huntingdon, UK). The foil was further water cut into small 5mm x 5mm flags using the water jet cutter within Lancaster University's in-house workshops. The size of the steel pieces was determined by the width of the irradiation vial neck used in these experiments; accommodating a maximum diagonal width of 7mm, Figure 2.

Figure 2: Amber glass irradiation vial used in irradiation experiments.

The water jet cutting process is quite abrasive. Most pieces had retained a mirror polish on one side but had been roughened on the reverse. The sample edges were also significantly roughened by the jet cutting. Thus, the steel pieces subsequently required re-polishing by hand using decreasing grades of SiC paper (800, 1200 and 2400 grit), followed by diamond polishing pastes (10, 6, 3 and 1 µm).

In order to prepare samples, solutions were pipetted into vials, capped and degassed via a septum needle using a continuous flow through of argon for one hour. When placing steel samples into irradiation vials an effort was made to have the polished side facing up, i.e. in contact with the solution and steel pieces were degassed with the steel piece *in-situ*. Technical grade nitric acid was used along with Puriss grade Trans-1,2-diaminocyclohexane-N,N,N',N'-tetraaceticacid (CDTA). All H_2O used was doubly distilled water from a home-made still, further purified by a deionisation system (E-pure model 04642, Barnstead/Thermodyne, Dubuque, Iowa, USA) to a resistivity of 1.8×10^5 Ωm.

Sample vials were loaded into the irradiator using a rack mount system, with vials positioned on either the top rack or bottom rack, Figure 3.

This project has received funding from the EURATOM research and training programme 2014-2018 under grant agreement No 755171. The content of this deliverable reflects only the author's view. The European Commission is not responsible for any use that may be made of the information it contains.

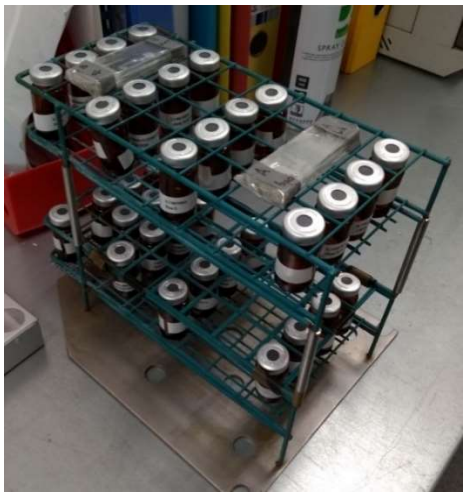

Figure 3: Two deck rack mounting system showing vial positions used in this study.

The sample racks were irradiated using the Co-60 gamma irradiator at the Dalton Cumbrian Facility (DCF), University of Manchester. The gamma irradiator at DCF is a FTS Model 812 (Foss Therapy Services, Inc., UK) which uses three rods of Co-60 contained within a lead lined steel chamber, Figure 4.

Figure 4: FTS Model 812 (Foss Therapy Services, Inc., UK) irradiator (left) and internal irradiation chamber showing dimensions (right).

The rack system allows controlled sample spacing at interval distances from the front of the irradiator chamber (closest to the Co-60 rods) to allow study of the effect of total absorbed dose. Dosimetry of the racks was determined by experimental staff at DCF and is regularly measured directly by RadCal probe (RadCal, California, USA). Emulating the range of doses available to the INL radiolysis test Loop, the four doses tested were

This project has received funding from the EURATOM research and training programme 2014-2018 under grant agreement No 755171. The content of this deliverable reflects only the author's view. The European Commission is not responsible for any use that may be made of the information it contains.

~1.6 MGy, 0.6 MGy, ~0.3 MGy and ~0.15 MGy. In order to achieve such doses, sample vials were spaced and irradiated continuously for a total of 4 days, 96 hours.

Post-irradiation, the solid stainless steel flag and solution phase were separated. The stainless steel flag was gently washed with deionised water before being allowed to dry. The aqueous phase was immediately frozen and the solution thawed prior to its use in the electrochemical tests.

For electrochemical testing, 500 µl of each irradiated solution was removed from the thawed vial after removing the septum cap. This was transferred to the small volume electrochemical cell described in previous reports in order to allow high ligand concentrations to be achieved. Working electrodes were constructed using 1 mm diameter SS304L wire in glass Pasteur pipettes, backfilled with epoxy resin and polished using decreasing SiC paper grades and 6, 3 and 1 µm diamond polishing pastes. To complete the three electrode cell, a Ag/AgCl reference electrode and coiled platinum wire counter electrode were inserted via simple PTFE manifold.

Linear sweep voltammetry (LSV) was used as the predominant experimental technique to assess *in situ* corrosion behaviour. After an open circuit potential (OCP) equilibration period of 1 hour, a large window LSV was performed from -0.3 V to +1.5V versus the reference electrode. All such electrochemical experiments described here are performed at scan rates of 0.1 mV/s with solutions purged with argon prior to use.

Scanning electron microscope images were collected at 5 spots across the surface of the irradiated 304L stainless steel flags. Imaging was carried out using a JEOL JSM-7800F Field Emission SEM within the Chemistry Department at Lancaster University. A beam energy of 5 keV was used and 5 regions across the surface of the irradiated steel pieces were imaged at 10000, 5000 and 2000 x magnification in order to understand the general surface morphology of the samples.

3. RESULTS

3.1. SCANNING ELECTRON MICROSCOPE STUDIES OF IN SITU IRRADIATION CORROSION

In order to understand changes in surface morphology of SS304L steel samples that may occur during irradiation, scanning electron microscope images have been collected of added stainless steel flags pre- and post- irradiation. A comparison of the steel surfaces irradiated in 3.7 mol dm^{-3} HNO_3 with and without CDTA is presented in Table 1. Emulating the range of does available at the INL radiolysis test loop, flags and solutions were irradiated to maximum total adsorbed does of 1.6 MGy.

This project has received funding from the EURATOM research and training programme 2014-2018 under grant agreement No 755171. The content of this deliverable reflects only the author's view. The European Commission is not responsible for any use that may be made of the information it contains.

Table 1: SEM images at 5000x magnification of steel samples in 3.7 mol dm^{-3} HNO_3 (left) with 3.7 mol dm^{-3} HNO_3 + 0.1M CDTA (right).

Total Dose (MGy)	3.7 mol dm^{-3} HNO_3 only	3.7 mol dm^{-3} HNO_3 + 0.03 mol dm^{-3} CDTA
0	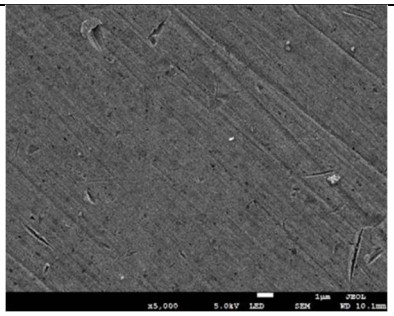	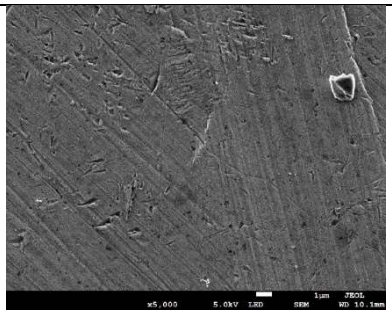
0.15	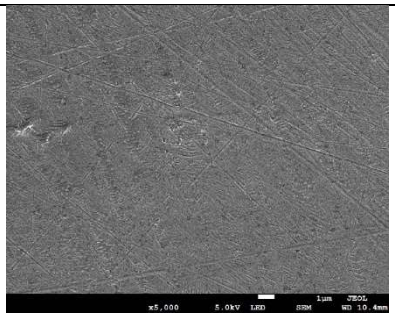	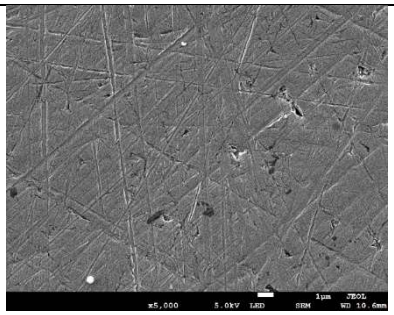
0.30	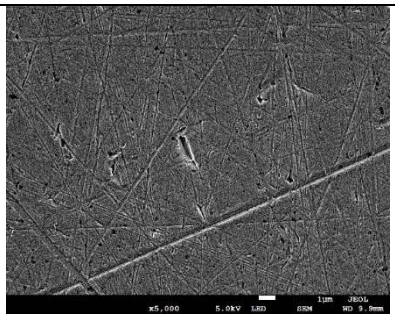	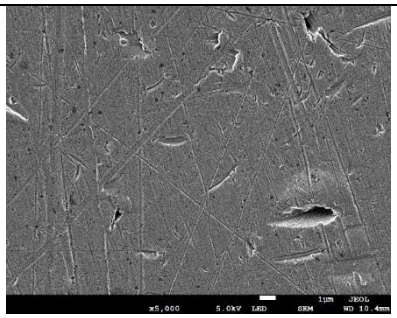
0.60	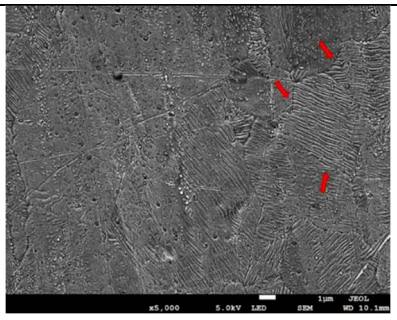	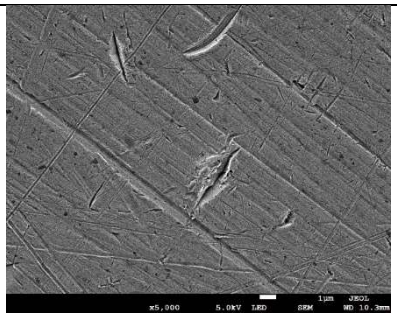
1.60	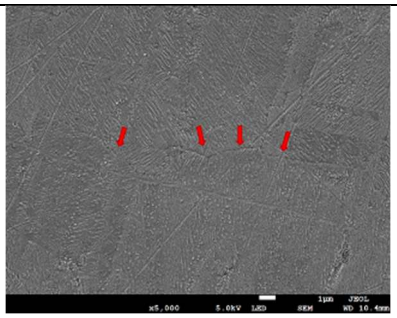	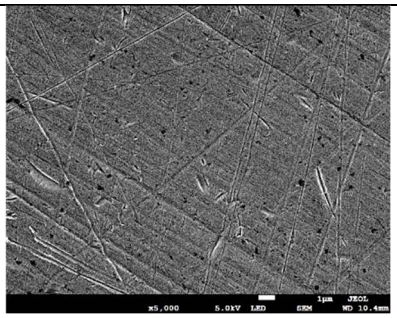

This project has received funding from the EURATOM research and training programme 2014-2018 under grant agreement No 755171. The content of this deliverable reflects only the author's view. The European Commission is not responsible for any use that may be made of the information it contains.

Despite hand polishing surfaces using diamond paste, many scratches still remain on the SEM images of Table 1. Nevertheless, in both the presence and absence of CDTA no significant changes in surface morphology are observed up to a dose of 0.6 MGy. At a dose of 0.6 MGy and the highest dose of 1.6 MGy and in the 3.74 mol dm^{-3} HNO_3 only condition some surface particulates become apparent on the steel and general roughening of the surface can be also be seen. Importantly, intergranular corrosion is also apparent at both dose levels, with particularly large ditches highlighted by red arrows in Table 1.

The causes and mechanism of intergranular corrosion in stainless steels in nitric acid are well reported [4]. The susceptibility of stainless steel to failure in boiling 8 mol dm^{-3} HNO_3 is the result of one or more of the following processes: (i) intergranular corrosion due to sensitization, (ii) intergranular corrosion due to impurity segregation at grain boundaries, (iii) transpassive dissolution of passive films, and (iv) selective corrosion of welds [5]. In the SS304L plate used here processes (ii) and (iii) are most applicable to the observed intergranular corrosion morphologies of Table 1

Interestingly, and as described in previous sections of this report on SS316L corrosion in the absence/presence of hydrazine, a significantly oxidising solution potential must be being created by the radiolysis products of nitric acid in order for the transpassive dissolution of the passivating Cr^{3+} oxide surface film to Cr^{6+} soluble species to occur, resulting in attack of the underlying Fe/Cr/Ni bulk steel matrix. This also supports our assertation in previous sections of this report that a potentiostatically applied potential scan is a suitable way of approximately simulating corrosion under a radiation field in a standard laboratory, as the same morphology transpassive attack features are observed here as those seen in SS316L bulk electrode potentiostatically scanned to +1.5V vs. SCE, an example of which is shown in Figure 5.

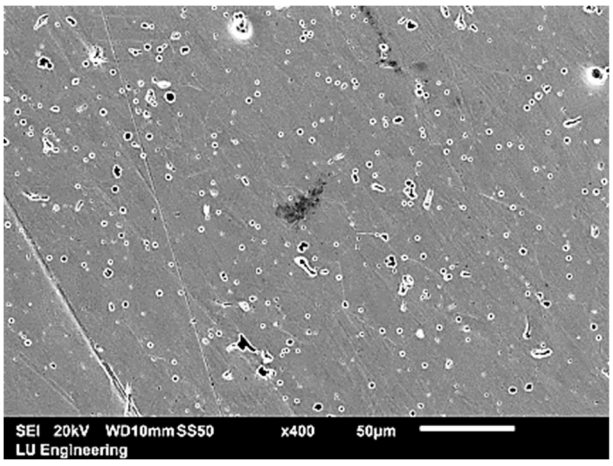

Figure 5: Example of transpassive corrosion on a SS316L electrode scanned to +1.5V vs. SCE in 0.5 mol dm^{-3} HNO_3.

This project has received funding from the EURATOM research and training programme 2014-2018 under grant agreement No 755171. The content of this deliverable reflects only the author's view. The European Commission is not responsible for any use that may be made of the information it contains.

While *in situ* electrochemical corrosion studies within the gamma irradiator would be required to ascertain the oxidative stress applied to the steel flag under irradiation, from the aforementioned electrochemical scans, a potential > 0.8 V vs. SCE would be expected.

Returning to Table 1 and turning now to the effect of the addition of CDTA on the surface of the irradiated steel flags, it can be seen that at 0.6 MGy and 1.6 MGy no surface particulates, general roughening or transpassive grain etching of the surface is apparent, with the sample surfaces looking similar to the images of the steel flag in the unirradiated condition.

As described in previous reports, corrosion inhibition action by CDTA could be explained by either one or both of the following different processes: 1) Scavenging of nitrous acid by CDTA and 2) CDTA blocking adsorption sites for NO, inhibiting the generation of the electroactive species HNO_2 at the steel surface, said generation shown in Equations (1) and (2):

$$(HNO_2)_{el.} + H^+ + e^- + s = (NO)_{ads} + H_2O \quad (1)$$

$$HNO_3 + (NO)_{ads} = (HNO_2)_{el.} + (NO_2)_{ads} \quad (2)$$

Where *s* represents a free adsorption site.

The former process is discussed in more detail in the next section. With regards to the latter process, a possible mechanism has been described in the immediately previous section of this deliverable report for the corrosion inhibition behaviour of CDTA on SS316L and SS304L steels in the absence of a radiation field. CDTA-Fe(II) complexes are known to readily occur [6,7]. Thus, it can be foreseen that a similar complex could form at the exposed iron scale on the steel flags. As a result, a layer of CDTA would already be pre-adsorbed at the steel surface before irradiation, restricting the ability of NO to surface adsorb and reducing the regeneration of HNO_3 to HNO_2 shown in equation (2). As reduction of nitrous acid is responsible for charge transfer via equation (1), the consequence of NO adsorption site blocking is a reduction in corrosion.

As noted in the introduction, CDTA is expected to radiolytically degrade under strong gamma fields to the possible products shown in Figure 1. Interestingly, and despite the increased degradation that must be occurring as a function of the increasing gamma dose, the corrosion inhibition effect of CDTA seems unaffected (e.g. surface morphologies in the SEM images of Table 1 at 0.6 and 1.6 MGy are unchanged). This would suggest that the radiolytic breakdown products may also act as corrosion inhibitors. Indeed, many simple amino acids and carboxylic acids have previously been reported as efficient iron/carbon steel corrosion inhibitors [8].

This project has received funding from the EURATOM research and training programme 2014-2018 under grant agreement No 755171. The content of this deliverable reflects only the author's view. The European Commission is not responsible for any use that may be made of the information it contains.

A comparison of the surfaces of steel irradiated in 7.4 mol dm^{-3} HNO_3 with and without CDTA are presented in Table 2.

Considering first the images taken of samples in nitric acid only, at this higher nitric acid concentration, roughening, surface participates and intergranular cracks (highlighted again with red arrows) are observed at the lowest irradiation dose of 0.15 MGy, but not in samples leached for the same time in non-irradiated nitric acid. This is not surprising, as compared to Table 1 the nitric acid concentration is almost doubled and therefore the open circuit potential of the steel would already be significantly more anodic than that exhibited in 3.74 mol dm^{-3}.

As the dose increases to 0.30 MGy, no corrosion features are observed. Further repeat studies are under way to determine exactly why this particular condition does not show any corrosion despite the higher gamma dose applied. Nevertheless, as dose further increases to 0.6 and 1.6 MGy it can be seen that roughening, surface participates and, in particular, intergranular cracks increase in size and commonality with increasing dose.

Turning now to the 7.4 mol dm^{-3} HNO_3 with CDTA condition of Table 2, immediate differences can be seen compared to the same dose exposure conditions for 7.4 mol dm^{-3} HNO_3 only. No corrosion features are observed up to a dose of 1.6 MGy, suggesting that again CDTA actively inhibits corrosion of SS304L. However, and unlike at the lower (and less aggressive) nitric acid concentration images of Table 1, at 1.6 MGy roughening, surface participates and intergranular cracks are apparent. This indicates that there is a dose threshold above which CDTA no longer provides a corrosion inhibiting effect at this nitric acid concentration. Whether this is due to the radiolytic breakdown of CDTA resulting in reduced surface protection or the excess generation of radiolytic nitrous acid/radical species is currently unclear, but considering the effectiveness of CDTA protection across the lower doses tested we suspect the latter may be the controlling factor. Indeed, comparison between the 1.6 MGy images recorded in 7.4 mol dm^{-3} nitric acid only and those recorded at the same dose in the presence of CDTA reveals that despite the presence of similar levels of surface roughening, surface participates and in particular intergranular cracks are less common and smaller in size/depth in the CDTA condition.

Having described the *in-situ* corrosion behaviour of SS304L flags in nitric acid and CDTA, we now consider, via electrochemical testing, the corrosion and electrochemical behaviour of post-irradiation solutions of nitric acid and CDTA.

This project has received funding from the EURATOM research and training programme 2014-2018 under grant agreement No 755171. The content of this deliverable reflects only the author's view. The European Commission is not responsible for any use that may be made of the information it contains.

Table 1 : SEM images at 5000x magnification of steel samples in 7.4 mol dm^{-3} HNO_3 (left) with 7.4 mol dm^{-3} HNO_3 + 0.1M CDTA (right).

Total Dose (MGy)	7.4 mol dm^{-3} HNO_3 only	7.4 mol dm^{-3} HNO_3 + 0.03 mol dm^{-3} CDTA
0	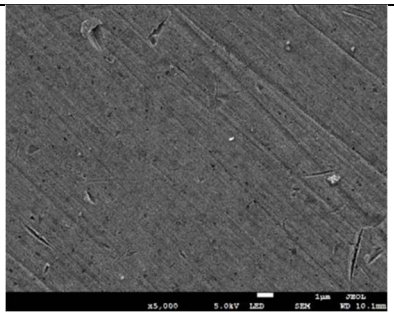	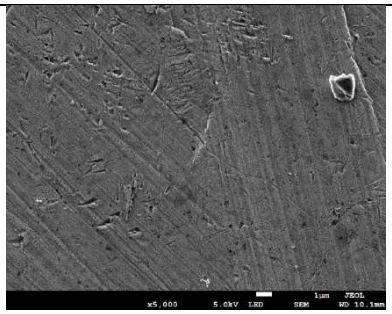
0.15	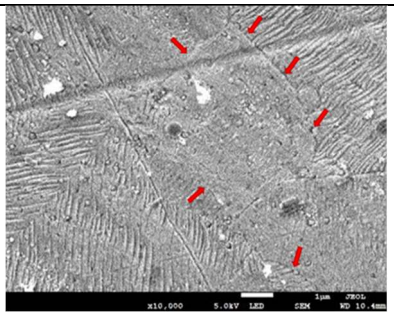	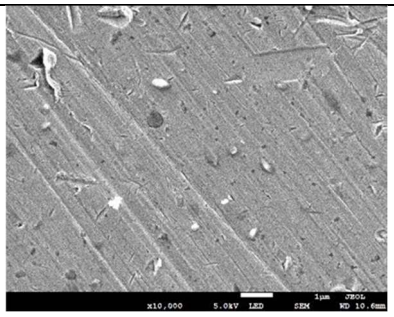
0.30	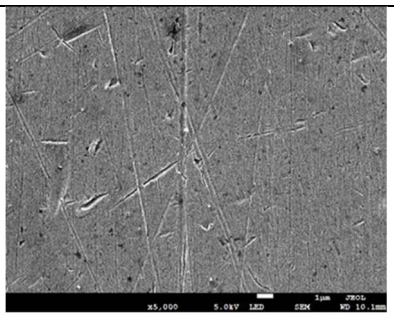	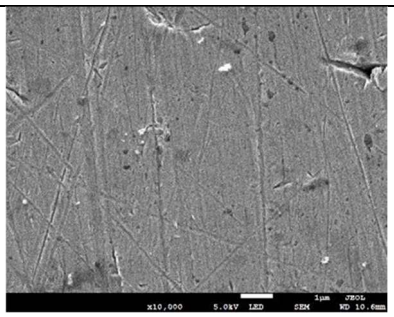
0.60	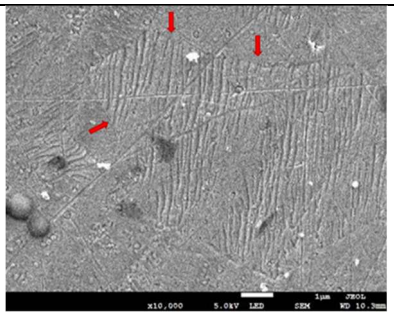	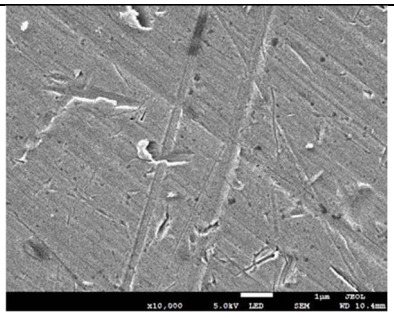
1.60	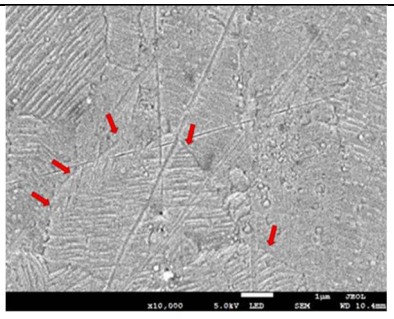	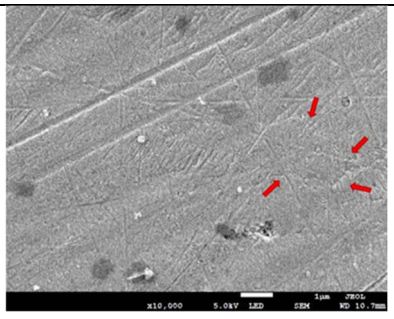

This project has received funding from the EURATOM research and training programme 2014-2018 under grant agreement No 755171. The content of this deliverable reflects only the author's view. The European Commission is not responsible for any use that may be made of the information it contains.

3.2. EX-SITU ELECTROCHEMICAL CORROSION TESTING - 3.7 mol dm^{-3} HNO_3

Before considering the effect of post-irradiated nitric solutions on the corrosion behaviour of SS304L wire electrodes, the background electrochemical response of said solutions must be understood. In order to do this cyclic voltammograms were recorded using glassy carbon electrodes between -0.3 and +1.5 vs. SCE using a scan rate off 50 mV/s for solutions of 3.7 mol dm^{-3} HNO_3 irradiated to doses of 0.15, 0.3, 0.6 and 1.6 MGy. The results of these scans, which must be considered preliminary, are shown in Figure 6.

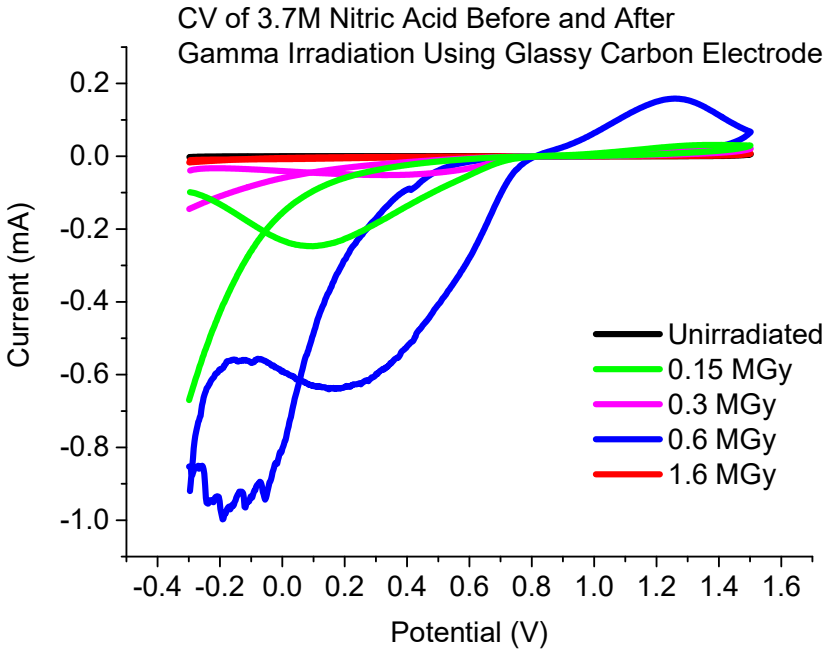

Figure 6: Cyclic Voltammograms of 3mm diameter glassy carbon electrode in a solution of 3.7 mol dm^{-3} HNO_3 before and after exposure to gamma irradiation.

Before analysing Figure 6, it is first useful to define the key features of cyclic voltammograms of nitric acid available from the extant literature.

The electrochemical reduction mechanism of nitric acid has been well described at temperatures up to 100ºC by Baulbard *et al.* [9] on platinum disk electrodes and was summarised in the previous experimental section of this deliverable report. For the convenience of the reader, this mechanism is revisited here – but in the context of the annotated example CV of Figure 7, recorded in 4 mol dm^{-3} HNO_3 solution scanned at 10 mV/s, to provide added insight.

This project has received funding from the EURATOM research and training programme 2014-2018 under grant agreement No 755171. The content of this deliverable reflects only the author's view. The European Commission is not responsible for any use that may be made of the information it contains.

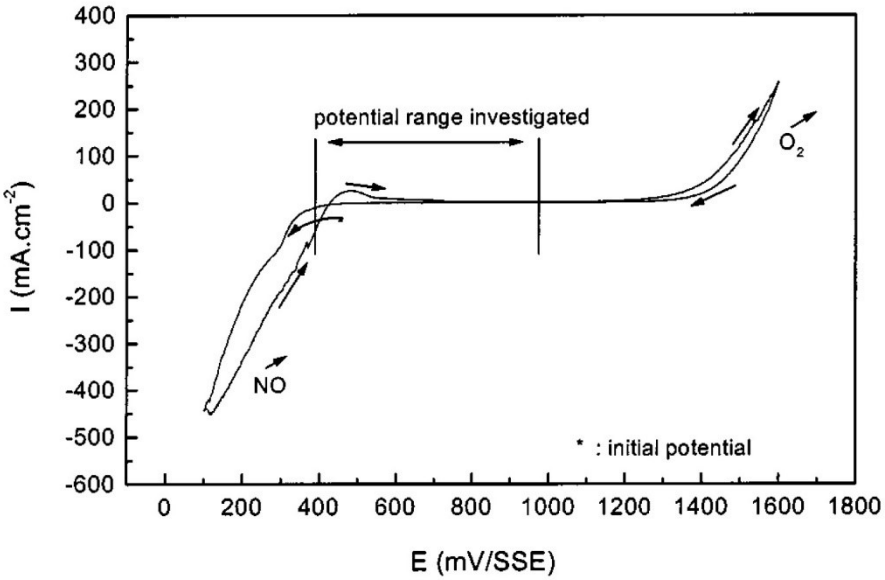

Figure 7: CV of 4 mol dm-3 HNO_3 at 100 °C at a scan rate of 10 mV/s on a platinum disk electrode [9].

Considering first the oxidative current peak at > 1.1V, this is due to oxygen evolution at the electrode surface from the high applied potential breaking down water:

$$2H_2O \rightarrow O_2 + 4H^+ + 4e^- \quad (3)$$

Turning now to the main reductive peak in the CV at < 400 mV, this is due to the primary charge transfer reduction step:

$$(HNO_2)_{el.} + H^+ + e^- + s = (NO)_{ads} + H_2O \quad (4)$$

Where *s* represents a free adsorption site.

Note in this electrochemical reduction process the nitric acid molecule is not directly reduced; it is reduced through an autocatalytic mechanism involving an electrochemical step and a chemical reaction regenerating the active species, the latter shown in Equation (5):

$$HNO_3 + (NO)_{ads} = (HNO_2)_{el.} + (NO_2)_{ads} \quad (5)$$

Finally, as the scan is reversed anodically from +100 mV a small oxidation peak is observed at ~+480 mV. This is attributed by Baulbard *et al.* to the oxidation of species formed during the reduction of nitric acid in the cathodic scan, as it does not appear in smaller window scans performed directly on this oxidation wave region.

This project has received funding from the EURATOM research and training programme 2014-2018 under grant agreement No 755171. The content of this deliverable reflects only the author's view. The European Commission is not responsible for any use that may be made of the information it contains.

Returning to Figure 6, it can be seen that there is generally an enhancement in nitrous acid reduction current and oxygen evolution as dose increases up to 0.6 MGy.

The effect of gamma dose on nitrous production from nitric acid has been previously described by Horne [3], Figure 8

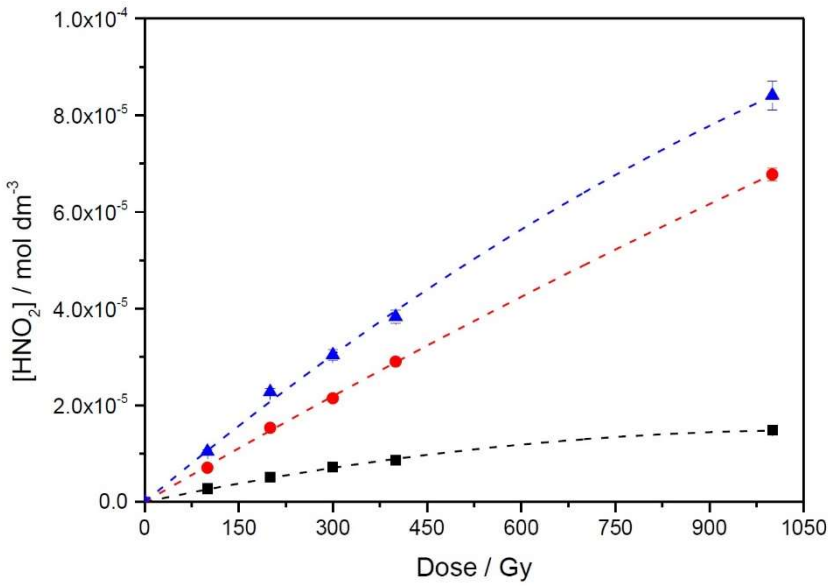

Figure 8: Concentration of HNO_2 from the gamma radiolysis of HNO_3, as a function of absorbed dose: 1 mol dm^{-3} (▪), 4 mol dm^{-3} (●), and 6 mol dm^{-3} (Δ); experimental error ≤ (±) 2.97 × 10^{-6} mol dm^{-3}; dashed lines are for visual aid only [3].

From Figure 8 it can be seen that nitrous concentration increases with dose in a similar concentration 4 mol dm^{-3} nitric acid solution. However, it should be noted that the studied dose range is only up 1 kGy in Figure 8, which is relatively low compared to the up to 1.6 MGy adsorbed dose described here. As noted by Horne, doses above 1 kGy may well result in a levelling off or even a slight decrease in nitrous concentration. This is due to the mechanism of nitric radiolysis. According to Horne, the radiolytic formation of HNO_2 can be described by the following simplified reaction scheme:

Water Radiolysis

$$H_2O \rightarrow e_{aq}^-, H_{aq}^+, H\cdot, OH\cdot, H_2, H_2O_2 \quad (6)$$

Nitrate Radiolysis

$$NO_3^- \rightarrow NO_3^{-*} \rightarrow NO_2^- + O \quad (7)$$

$$NO_3^- \rightarrow NO_3^{-*} \rightarrow NO_3\cdot + e^- \quad (8)$$

Nitric Acid Radiolysis

This project has received funding from the EURATOM research and training programme 2014-2018 under grant agreement No 755171. The content of this deliverable reflects only the author's view. The European Commission is not responsible for any use that may be made of the information it contains.

$$HNO_3 \rightarrow HNO_3^* \rightarrow HNO_2 + O \quad (9)$$

Diffusion-Reaction Chemistry of Nitrogen Species

$$NO_3^- + e_{pre}^- \rightarrow NO_3^{2-} \quad (10)$$

$$NO_3^- + e_{aq}^- \rightarrow NO_3^{2-} \quad (11)$$

$$NO_3^- + H \cdot \rightarrow HNO_3^- \quad (12)$$

$$NO_3^{2-} + H_2O \rightarrow NO_2 + 2OH^- \quad (13)$$

$$HNO_3^- \rightarrow NO_2 + OH^- \quad (14)$$

$$NO_2 + NO_2 \leftrightarrow N_2O_4 \quad (15)$$

$$N_2O_4 + H_2O \rightarrow HNO_2 + HNO_3 \quad (16)$$

$$HNO_2 \leftrightarrow NO_2^- + H_{aq}^+ \quad (17)$$

The radiolytic formation of HNO_2 is due to a combination of direct (7 and 9) and indirect (10 to 12) radiation chemical effects, the relative contributions of which are dependent upon the concentration of NO_3^-/HNO_3. As the concentration of NO_3^-/HNO_3 increases, so too does 1) its electron fraction, which leads to increased direct radiolysis of NO_3^-/HNO_3, and 2) the scavenging of e_{pre}^-, e_{aq}^-, and H●. Finally, it should be noted that the reaction scheme above is actually a simplified version of a considerably larger complex reaction scheme, comprising over a hundred reactions.

Returning again to the analysis of Figure 6, the general increase in electrochemically detected nitrous concentration (inferred by the current associated with nitrous reduction) is therefore in line with that expected to occur from radiolysis of nitric acid. Interestingly, a hysteresis phenomenon is also present in the nitrous reduction wave, being particularly clear in the 0.6 MGy dose condition. Such a feature is also observed and described by Balbaud *et al.* [9]. The previously described regeneration reaction of Equation (5) is dependent on the nitric acid concentration. Thus, the regeneration reaction is rapid for high HNO_3 concentrations (>9 mol dm^{-3}) and slow for low concentrations (4 to 9 mol dm^{-3} HNO_3). The relative slow speed of the regeneration reaction (5) vs. the charge transfer step of reaction (4) causes the appearance of this hysteresis, such a phenomenon becoming less obvious with increasing nitric concentration

Finally, it is interesting to note that currents are considerably lower as the dose increases from 0.6 MGy to 1.6 MGy in the nitrous acid reduction region of Figure 6. This is under further investigation, but as noted by Horne when describing the non-linearity

This project has received funding from the EURATOM research and training programme 2014-2018 under grant agreement No 755171. The content of this deliverable reflects only the author's view. The European Commission is not responsible for any use that may be made of the information it contains.

of Figure 8, it may be due to a proportional decrease in indirect effect contributions to the radiation chemistry of the HNO_3 system at higher doses, i.e. secondary bulk homogeneous chemistry related to the oxidising species involved in said indirect effects, i.e. O_2, OH●, H_2O_2, HO_2●, and NO_3●

Turning now to SS304L wire electrode studies, the average open circuit potentials (OCPs) recorded after one hour of immersion of a 304L stainless steel electrode in solutions of 3.7 mol dm^{-3} nitric acid in the absence/presence of gamma irradiation are shown in Figure 9.

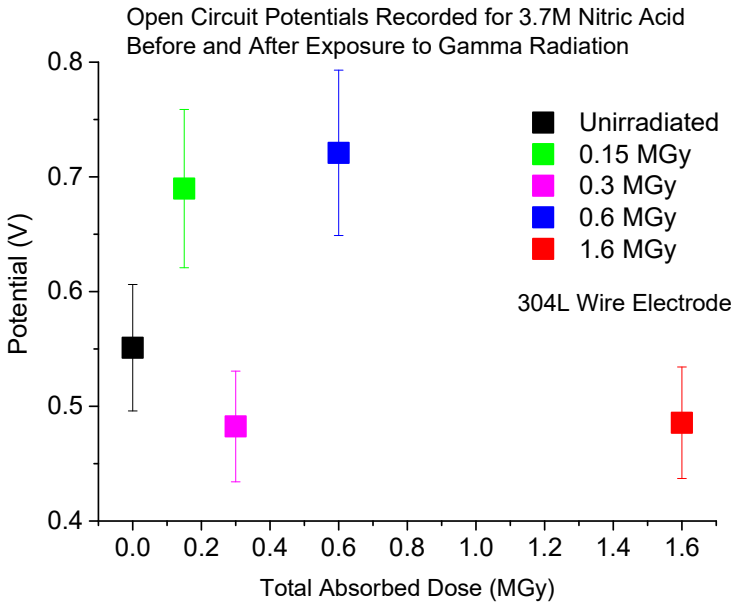

Figure 9: Open circuit potential of a 1 mm diameter 304L steel wire after one hour of immersion in a solution of 3.7 mol dm^{-3} HNO_3 after zero (■), 0.15 (■), 0.3 (■), 0.6 (■) and 1.6 MGy total absorbed gamma dose

The open circuit potentials generally follow the predicted concentration increase in nitrous acid as a function of dose shown in the glassy carbon CV's of Figure 6. As noted in the introductory section, HNO_2 is considered the electroactive species, causing reduction of nitric acid to NO_2 and H_2O, Equation (4). Importantly, the solution redox potential (and thus the potential of the stainless steel wire) is actually a result of the oxidation of NO_2 to NO_3^- and NO to NO_3^-:

$$NO_2 + H_2O \rightarrow NO_3^- + 2H^+ + e^- \quad (18)$$

$$NO + 2H_2O \rightarrow NO_3^- + 4H^+ + 3e^- \quad (19)$$

Which has a highly anodic thermodynamic potential of ~0.8V vs. SCE. As the generation of NO_2 and NO is very much dependent on the ratio of HNO_2 to HNO_3, as shown by Eq.

This project has received funding from the EURATOM research and training programme 2014-2018 under grant agreement No 755171. The content of this deliverable reflects only the author's view. The European Commission is not responsible for any use that may be made of the information it contains.

(4) to (5), excess HNO_2 will result in more anodic potentials and a decrease in HNO_2 concentration will result in more cathodic potentials being imposed on the immersed stainless steel.

It is this behaviour that is being observed in Figure 6, i.e. a more anodic open circuit potential is produced when nitrous acid concentrations are higher as a result of the higher dose (up to 0.6 MGy). Again, the counter intuitive lower concentration of nitrous acid in the 1.6 MGy dose condition is also supported in these results, the OCP being the same as that observed in unirradiated 3.7 mol dm^{-3} nitric acid solutions.

Before discussing the results of the linear sweep voltammetry (LSV) measurements it is first useful to again define the regions expected in a typical potential vs. current plot obtained using this method in the absence of irradiation.

An example annotated LSV plot of a 304L wire electrode in 3.7 mol dm^{-3} HNO_3 is shown in Figure 10.

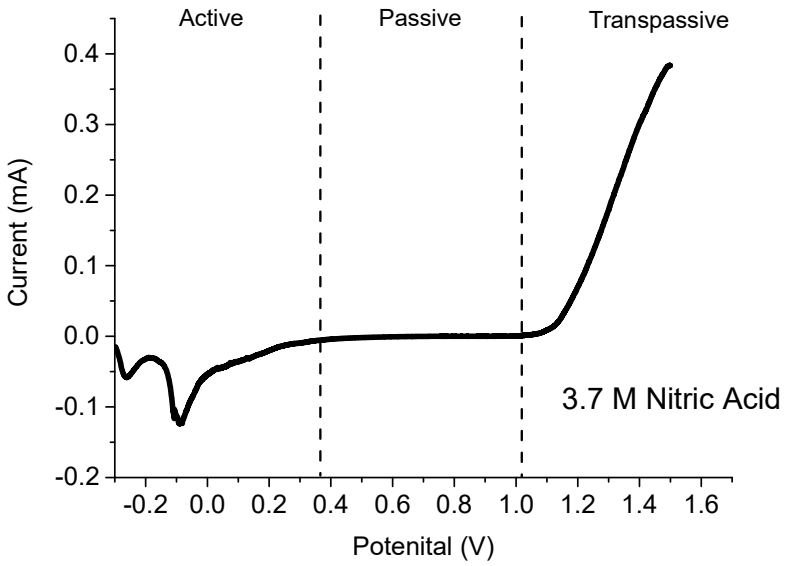

Figure 10: Annotated baseline LSV of a 304L steel wire electrode in 3.7 mol dm^{-3} HNO_3

At the most cathodic applied potentials, the electrode is said to be actively corroding and a reduction current is observed due to simultaneous hydrogen evolution.

As the potential increases anodically a point is reached at which an iron oxide and Cr_2O_3 passive film can exist. This oxide film blocks further attack of the underlying metal and the surface is said to be 'passivated', i.e. no net mass change is occurring as indicated by the extremely low currents in this region. As the potential becomes more anodic the insoluble Cr(III)oxide passive film begins to oxidise to a soluble Cr(VI) oxide and the

This project has received funding from the EURATOM research and training programme 2014-2018 under grant agreement No 755171. The content of this deliverable reflects only the author's view. The European Commission is not responsible for any use that may be made of the information it contains.

metal surface becomes 'transpassive', beginning again to corrode as indicated by the steadily increasing positive current.

At very positive overpotentials, oxygen evolution can occur through breakdown of the solvent. Alternatively, secondary passivation may occur, whereby the rate of current increase slows as the anodic potential increases. Within this region dissolution does still occur, but is partially inhibited by a porous layer of (predominantly) hematite generated at the steel surface due to the local solubility product of iron being exceeded as a considerable amount of Fe^{3+} ions are dissolved from the metal.

LSV and Tafel (log current plots) of SS304L wire electrodes in irradiated and unirradiated 3.7 mol dm^{-3} HNO_3 are shown in Figure 11 and Figure 12:

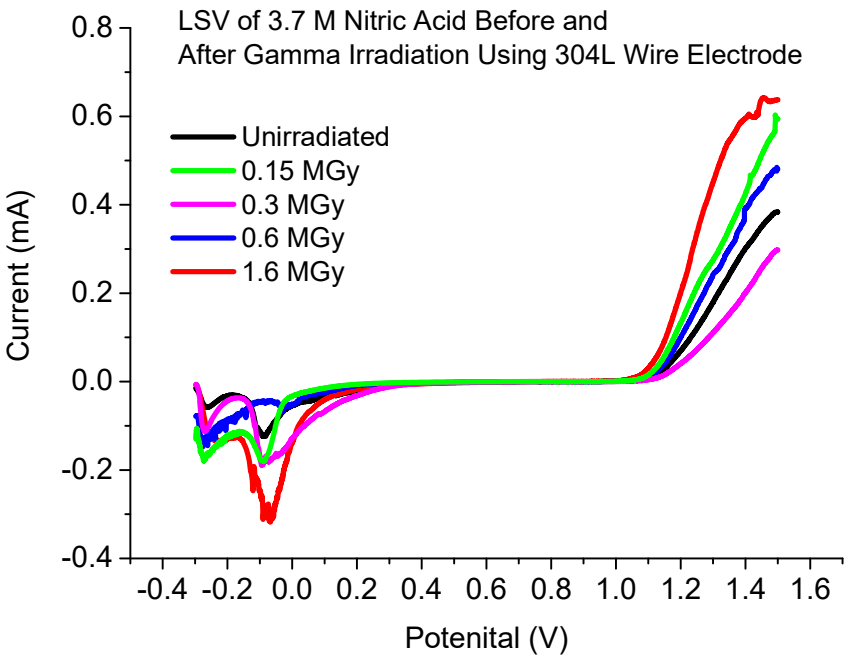

Figure 11: Linear Sweep Voltammogram of a 1 mm diameter 304L steel wire electrode in a solution of 3.7 mol dm^{-3} HNO_3 before and after exposure to gamma irradiation.

This project has received funding from the EURATOM research and training programme 2014-2018 under grant agreement No 755171. The content of this deliverable reflects only the author's view. The European Commission is not responsible for any use that may be made of the information it contains.

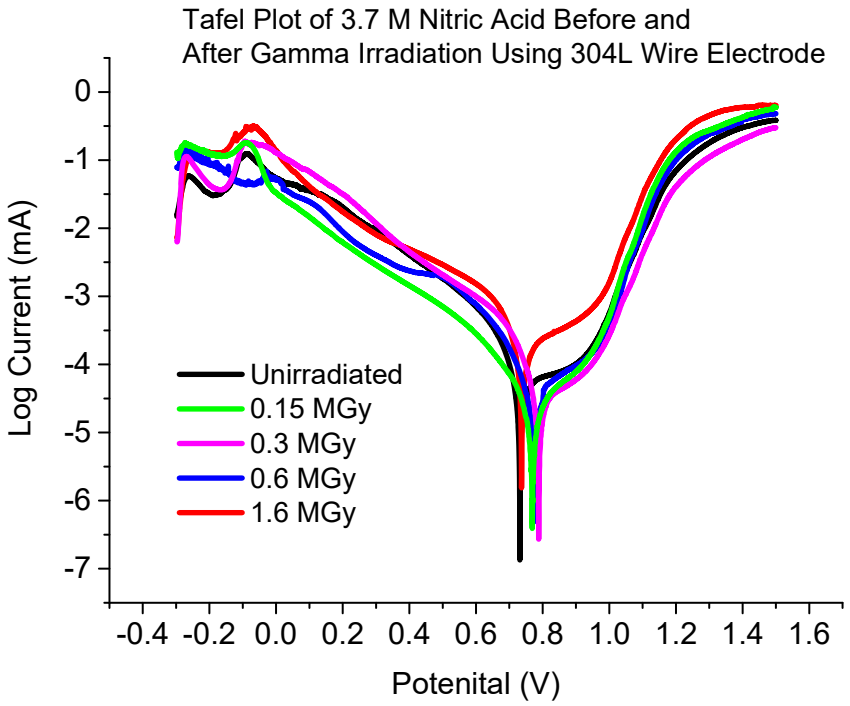

Figure 12: Tafel Plot of a 1 mm diameter 304L steel wire electrode in a solution of 3.7 mol dm^{-3} HNO_3 before and after exposure to gamma irradiation.

Considering the active corrosion region (region of hydrogen evolution) in Figure 12 first, it can be seen that the current response is very similar between all conditions regardless of dose, with the exception of the lowest dose of 0.15 MGy, which has a slightly lower cathodic tafel arm. Similarly, the corrosion potential (E_{corr}) also varies little between conditions.

This latter observation is interesting as from Eq. (18) and (19) it would be expected that an increased concentration of radiolytically generated nitrous acid should also drive the corrosion potential more positive. Clearly, other products of the radiolysis of nitric acid also have some effect on controlling the corrosion potential. A similar observation has also been reported by Nagai *et al*. [10] for *in situ* measurements of corrosion potential of SS304 ULC in boiling nitric acid solutions. They report that rather than an oxidative shift in corrosion potential occurring during gamma irradiation a reductive shift in corrosion potential is instead observed, such a shift tentatively attributed to a combination of photoconductivity changes in the gamma excited Cr_2O_3 surface film or the formation of reducing species from the radiolysis of nitric acid.

Turning now to the passive region between +0.8 and +1.0V and the transpassive region at > +1.0V, in general very little differences are observed between dose conditions. The only condition that shows a significant increase in both passive and transpassive current is the highest dose of 1.6 MGy. Again, considering the low measured reduction

This project has received funding from the EURATOM research and training programme 2014-2018 under grant agreement No 755171. The content of this deliverable reflects only the author's view. The European Commission is not responsible for any use that may be made of the information it contains.

currents in the glassy carbon electrode studies of Figure 6, i.e. the inferred concentration of nitrous acid, this is surprising. As per the analysis of E_{corr} described above, clearly other currently unknown radiolysis products are driving corrosion of the Cr_2O_3 passive film in both potential regions.

Considering now the effect irradiated CDTA has on the background behaviour of a glassy carbon electrode, cyclic voltammograms on a 3 mm glassy carbon electrode in 3.7 mol dm^{-3} with 30 mmol dm^{-3} before and after gamma irradiation at a range of doses are shown in Figure 13.

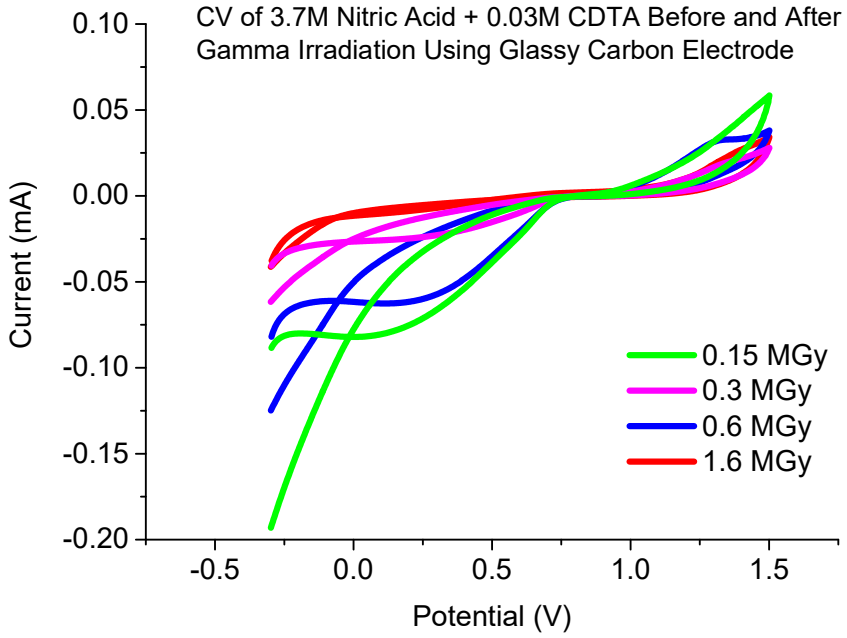

Figure 13: Cyclic Voltammograms of 3mm diameter glassy carbon electrode in a solution of 3.7 mol dm^{-3} HNO_3 and 0.03 mol dm^{-3} CDTA before and after exposure to gamma irradiation

Several observations can be made from Figure 13, which again should be considered preliminary findings.

First, and as per our analysis of nitric acid only experiments on GC electrodes (Figure 6), the nitrous acid reduction wave at < +0.75V and oxygen evolution wave at > +0.8V are both observed across all the measured gamma doses.

Second, no additional peaks are observed in the CV that could be attributed to CDTA or its radiolytic degradation products, all features instead common to the baseline electrochemical behaviour of irradiated nitric acid shown in Figure 6.

Finally, and unlike Figure 6, Figure 13 shows only minor variation in the size of the reduction wave as dose increases from 0.15 MGy to 0.6 MGy, a significant drop in

This project has received funding from the EURATOM research and training programme 2014-2018 under grant agreement No 755171. The content of this deliverable reflects only the author's view. The European Commission is not responsible for any use that may be made of the information it contains.

current only occurring at 1.6 MGy. Furthermore, the size of the observed nitrous reduction current in the dose conditions from 0.15 MGy to 0.6 MGy is reduced considerably, in particular the reduction current measured at a dose of 0.6 MGy is almost a factor of 10 smaller than that measured in the absence of CDTA.

This latter observation suggests that CDTA, or its radiolytic degradation products, must either be 1) scavenging nitrous acid, 2) interfering with nitrous acid generation through interaction with direct/indirect steps outlined in equations (6) to (17), consequently reducing the measured nitrous reduction current or 3) simply blocking nitric acid access to the electrode surface, through a surface adsorbed complex. While it is still unclear as to which mechanism or combination of mechanisms is responsible, based on unirradiated corrosion studies on bulk and wire SS316L electrodes in previous sections of this report, surface complexation with the GC electrode seems the most likely primary mechanism.

Turning now to duplicate SS304L wire electrochemical studies of those shown in Figure 9, 11 and 12, the measured open circuit potentials, LSV and Tafel plots of an SS304L wire electrode in the presence of 3.7 mol dm^{-3} HNO_3 with 0.03 mol dm^{-3} CDTA as a function of irradiation are shown in Figures 14, 15 and 16.

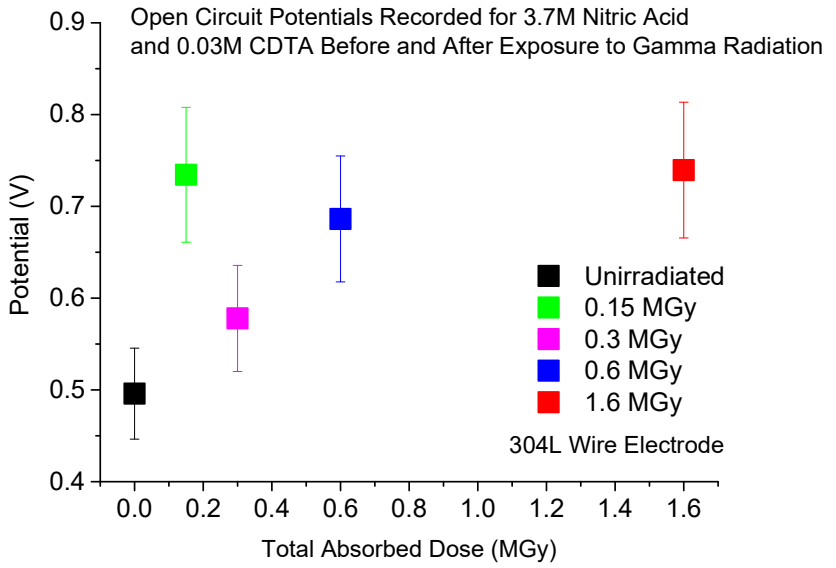

Figure 14: Open Circuit potential of a 1 mm diameter 304L steel wire after one hour of immersion in a solution of 3.7 mol dm^{-3} HNO_3 and 0.03 mol dm^{-3} CDTA after zero (■), 0.15 (■), 0.3 (■), 0.6 (■) and 1.6 MGy total absorbed gamma dose.

Considering first the OCP measured approximately 1 hour after immersion of the electrode in solutions of 3.7 mol dm^{-3} with 0.03 mol dm^{-3} CDTA, Figure 14, the results

This project has received funding from the EURATOM research and training programme 2014-2018 under grant agreement No 755171. The content of this deliverable reflects only the author's view. The European Commission is not responsible for any use that may be made of the information it contains.

are very similar to those recorded for the irradiated nitric acid only solutions of Figure 6. The only exception is the potential measurement for 1.6 MGy which increases from 0.4857 V to 0.7395 V upon addition of CDTA.

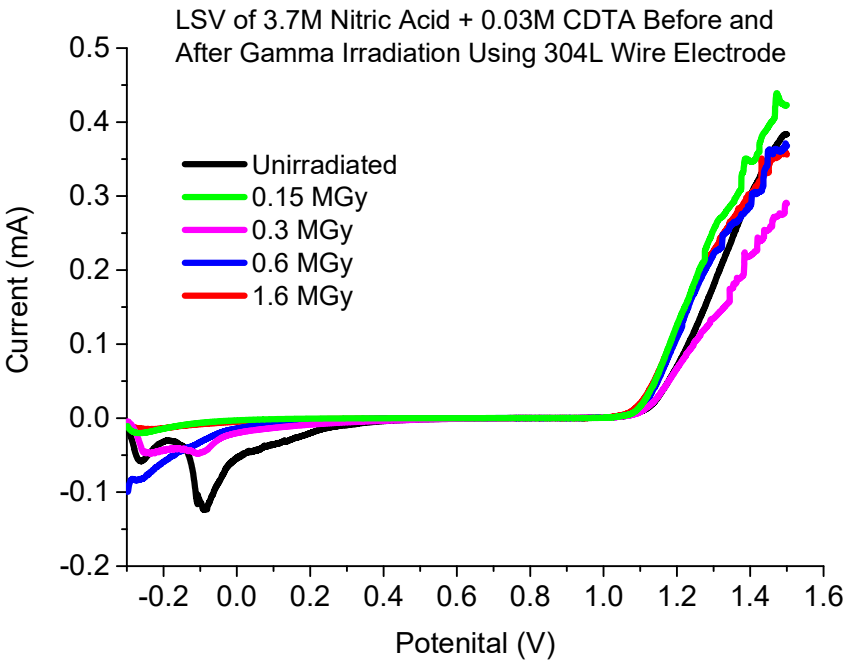

Figure 15: Linear Sweep Volatmmogram of a 1 mm diameter 304L steel wire electrode in a solution of 3.7 mol dm^{-3} HNO_3 and 0.03 mol dm^{-3} CDTA before and after exposure to gamma irradiation.

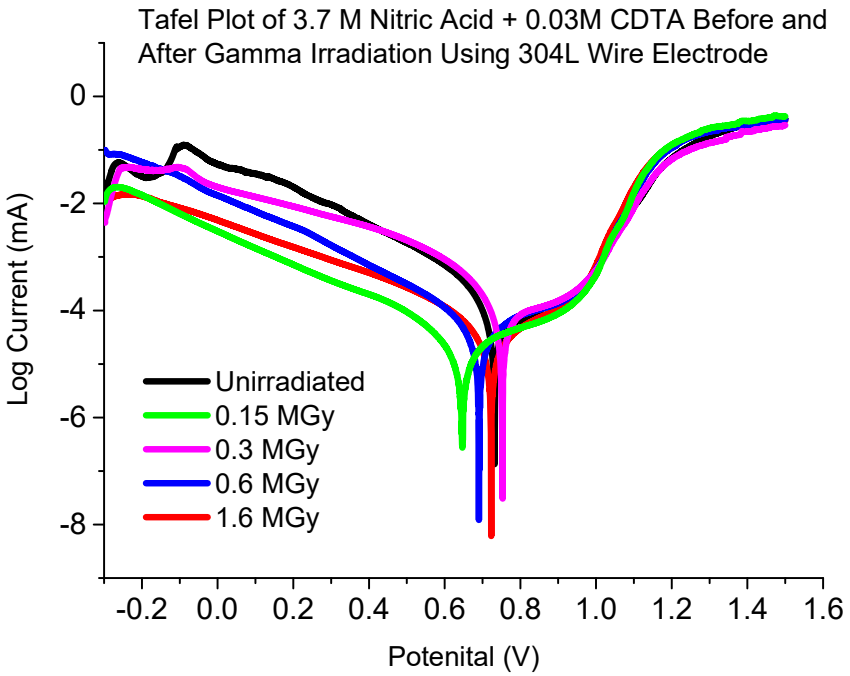

Figure 16: Tafel Plot of a 1 mm diameter 304L steel wire electrode in a solution of 3.7 mol dm^{-3} HNO_3 and 0.03 mol dm^{-3} CDTA before and after exposure to gamma irradiation.

This project has received funding from the EURATOM research and training programme 2014-2018 under grant agreement No 755171. The content of this deliverable reflects only the author's view. The European Commission is not responsible for any use that may be made of the information it contains.

Turning now to the LSV and Tafel plots recorded under the same dose conditions, Figures 15 and 16, and considering first the region of 'active' corrosion at ~< +0.7V, it can be seen that under irradiation all measured currents in this region are lower than that observed in nitric acid only, Figure 12. Considering the lower nitrous reduction currents in the GC studies of Figure 13, the lower cathodic Tafel arms may be related to the decreased concentration of nitrous present in these solutions, indicating that in the active region hydrogen evolution is also accompanied by a degree of NO evolution as well at this nitric acid concentration.

Moving now to the corrosion potential (E_{corr}), again little variation is observed as a function of dose, supporting the O.C.P. measurements of Figure 14 and our previous description that other products of the radiolysis of nitric acid must also have some effect on controlling the corrosion potential.

Finally, the most interesting regions of the LSV and Tafel plots of Figures 15 and 16 are the passive (+0.8 to +1.0V) and transpassive (> +1.0V) regions.
In the passive region, the presence of CDTA results in no effect on the recorded current across the tested gamma dose range. Similarly, in the transpassive region, currents across dose conditions are almost identical to those found with unirradiated nitric acid solutions. This can be explained by two possible scenarios:

1) CDTA and/or its degradation products either protect (through surface adsorption) or enhance the Cr_2O_3 passive film.
2) CDTA and/or it's degradation products are either scavenging nitrous acid or interfering with nitrous acid generation through interaction with direct/indirect steps outlined in equations (6) to (17), consequently reducing potential radiolysis species available for oxidative steel attack.

In-situ electrochemical experiments, along with a more thorough programme of degradant species elucidation would be warranted to be able to draw a more definitive conclusion as to the exact mechanism of protection, but it is clear from these preliminary experiments that CDTA continues to act as a corrosion inhibitor regardless of gamma radiation dose at this nitric acid concentration.

3.2. EX-SITU ELECTROCHEMICAL CORROSION TESTING – 7.4 mol dm^{-3} HNO_3

In order to ascertain the background electrochemical behaviour of irradiated 7.4 mol dm^{-3} nitric acid solutions, cyclic voltammograms between -0.3 and +1.5 vs. SCE were again taken at a scan rate off 50 mV/s for solutions irradiated to doses of 0.15, 0.3, 0.6 and 1.6 MGy. The results of these preliminary scans are shown in Figure 17:

This project has received funding from the EURATOM research and training programme 2014-2018 under grant agreement No 755171. The content of this deliverable reflects only the author's view. The European Commission is not responsible for any use that may be made of the information it contains.

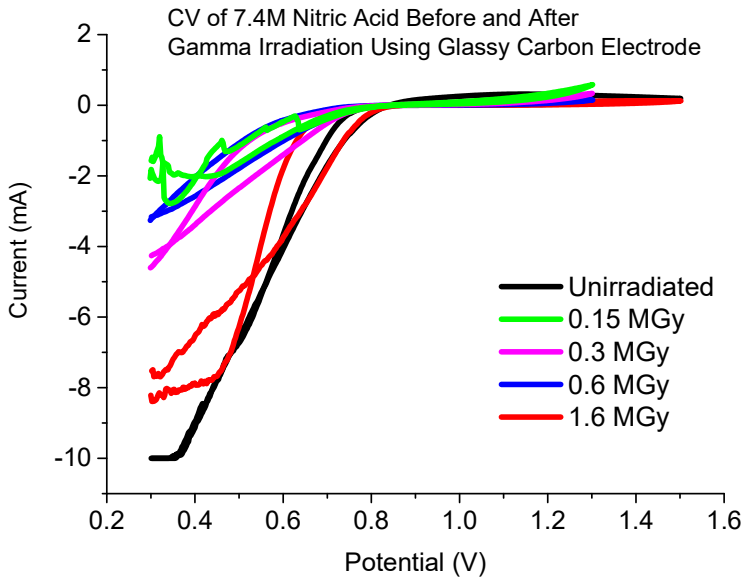

Figure 17: Cyclic Voltammograms of 3mm diameter glassy carbon electrode in a solution of 7.4 mol dm^{-3} HNO_3 before and after exposure to gamma irradiation.

Considering first the CV of unirradiated 7.4 mol dm^{-3} nitric acid in Figure 17, it can be seen that compared to the CV of unirradiated 3.7 mol dm^{-3} in the previous section (Figure 6) currents are almost a factor of 10 greater in magnitude within the region of nitrous acid reduction (< +0.8V). Such an observation suggests that a higher concentration of nitrous acid is present in this higher concentration solution. It has been reported that higher nitric acid concentrations and temperatures serve to reduce the dissociation of nitric acid [11,12].:

$$4HNO_3 \leftrightarrow H^+ + NO_3^- \quad (20)$$

As described previously, in the electrochemical reduction process the nitric acid molecule is not directly reduced; it is reduced through an autocatalytic mechanism involving an electrochemical step and a chemical reaction regenerating the active species, the latter previously shown in Equation (5). Thus, increased HNO_3 concentration through reduced dissociation at this higher nitric acid concentration will result in an increased concentration of regenerated HNO_2 at the electrode surface, subsequently increasing the nitrous reduction current through equation (4).

Turning now to the effect of irradiation, it can be seen from Figure 17 that while nitrous reduction currents are greater than those recorded in lower nitric acid concentrations at the same dose levels (Figure 6), compared to the nitrous reduction current of unirradiated solutions the reduction currents, and thus the inferred concentration, of nitrous acid are considerably lower with increasing gamma dose up to 1.6 MGy. This is

This project has received funding from the EURATOM research and training programme 2014-2018 under grant agreement No 755171. The content of this deliverable reflects only the author's view. The European Commission is not responsible for any use that may be made of the information it contains.

the reverse of Figure 6 for 3.7 mol dm^{-3} HNO_3, and is surprising as based on the mechanisms of equations of (6) to (17) increased stability of HNO_3 to dissociation should result in a greater radiolytic yield in nitrous acid concentration, via equation (9) in particular. Clearly an alternative radiolysis path must exist at this higher [HNO_3] and further investigation is required to ascertain the mechanism involved.

Finally at a dose of 1.6 MGy the reduction current of nitrous acid increases to currents similar to those found in the unirradiated condition. It is unclear as to why such a significant change should happen at this higher dose level considering the lack of change at lower doses and further experiments are required to understand this.

Turning now to studies on SS304L wire electrodes, average OCPs recorded after one hour of immersion of a 304L stainless steel electrode in a solution of 7.4 mol dm^{-3} nitric acid both in the absence and presence of gamma irradiation are shown in Figure 14.

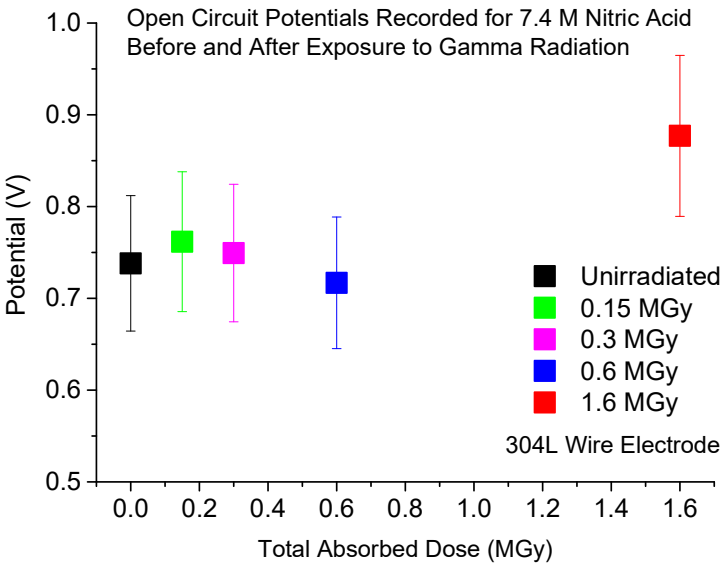

Figure 18: Open Circuit potential of a 1 mm diameter 304L steel wire after one hour of immersion in a solution of 7.4 mol dm^{-3} HNO_3 after zero (■), 0.15 (■), 0.3 (■), 0.6 (■) and 1.6 MGy total absorbed gamma dose.

Figure 18 reveals that SS304L measured open circuit potentials lie in the range 0.66V to 0.77V vs. AgCl for all irradiated and unirradiated 7.4 mol dm^{-3} nitric acid solutions tested during these preliminary experiments – except for that irradiated to a total absorbed dose of 1.6 MGy, which returns a value of 0.88V. The potential range of 0.66 to 0.77V is similar to that recorded in 3.7 mol dm^{-3} HNO_3, Figure 9, suggesting that despite the higher HNO_3 concentration tested little oxidative excursion occurs to potentials greater than ~+0.7V – at least at adsorbed doses less than 1 MGy. This is surprising, as previous studies have highlighted a considerable open circuit potential

This project has received funding from the EURATOM research and training programme 2014-2018 under grant agreement No 755171. The content of this deliverable reflects only the author's view. The European Commission is not responsible for any use that may be made of the information it contains.

difference over similar conditions, measured OCPs being +300mV and +720mV between SS304L wire electrodes in unirradiated 3 and 7 mol dm^{-3} HNO_3 respectively.

This difference in unirradiated results may be due to the difference in atmospheric conditions between experiments, the previous SS304L wire experiments having been performed under oxic conditions, compared to argon purged conditions described here. The effect of oxygen on stainless steel corrosion is highly dependent on the anions present in the solution environment. In the case of combinations of nitric acid and dissolved oxygen, the effect of dissolved oxygen on the open circuit potential and potentiodynamic polarisation behaviour of SS304L has been reported by Khobragade *et al.* [13].

While in part influenced by the solution potential of the system controlled by the NO_3^- /NO_2^- couple (see equations (18) and (19)) the OCP of SS304L is predominantly dictated by the passive film surface state. The passive film of Cr_2O_3 on a stainless steel surface can act as a p-type semiconductor and has cation vacancies as a result. Vacancy defects in most oxide surfaces display a strong interaction with molecules such as O_2 and H_2O. O_2 may be reduced to form O^{2-} ions as one of the mixed potential (measured as E_{corr}) determining half reactions at the steel surface, joining and enhancing the passive film. The coupled oxidation half reaction is most likely the oxidation of one of the alloying elements, most likely Cr, at the metal-metal oxide interface. Nitrate ions may compete with the reductively formed oxide ions for adsorption on the film surface, inhibiting film formation and driving dissolution. However, this nitrate-associated effect aside, the open circuit potentials measured on SS304L reported here is shifted towards passivity under aerated conditions as the oxygen drives Cr_2O_3 layer formation. Conversely, in the absence of oxygen, passive layer formation is inhibited in comparison to aerated solutions, causing a shift towards active dissolution, as observed here.

The exception to the above is the result recorded at a dose of 1.6 MGy where the OCP is significantly higher than that recorded over the range 0-1 MGy, measured potentials being 0.88V and in the range 0.66 to 0.77V respectively. This again suggests a higher nitrous concentration has been generated in the system that received the higher dose, a finding consistent with the voltammetry of Figure 17. We shall return to this point below.

Turning now to the effect of electrochemical scanning, LSV and Tafel plots of SS304L wire electrodes in irradiated and unirradiated 7.4 mol dm^{-3} HNO_3 are shown in Figure 19 and Figure 20 respectively. Considering the active corrosion region (region of hydrogen evolution) in Figure 20 first, it can be seen that the current response is very similar to the GC studies of Figure 17, with the unirradiated and 1.6 MGy dose conditions showing greater cathodic currents than those measured at 0.15, 0.3 and 0.6

This project has received funding from the EURATOM research and training programme 2014-2018 under grant agreement No 755171. The content of this deliverable reflects only the author's view. The European Commission is not responsible for any use that may be made of the information it contains.

MGy doses. This suggests that nitrous acid reduction at potentials < +0.8V and the resultant NO evolution has more of an effect on the cathodic tafel arm at this nitric acid molarity compared to that in 3.7 mol dm^{-3} HNO_3.

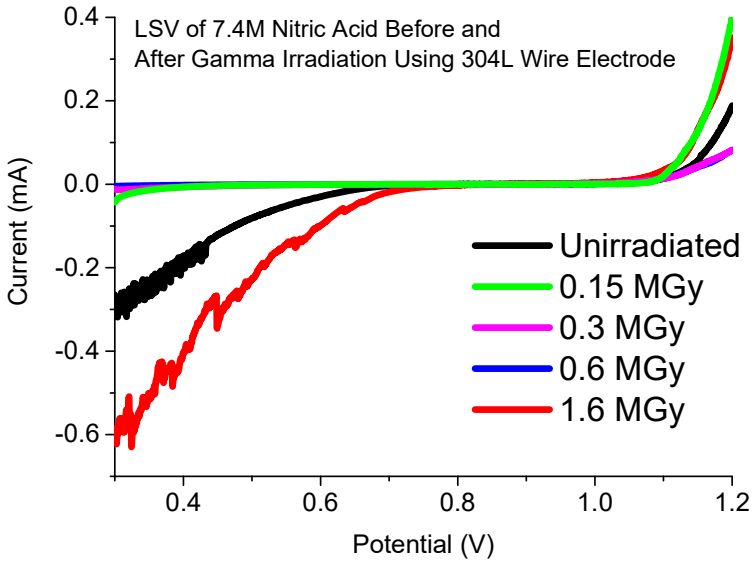

Figure 19: Linear Sweep Voltammogram of a 1 mm diameter 304L steel wire electrode in a solution of 7.4 mol dm^{-3} HNO_3 before and after exposure to gamma irradiation.

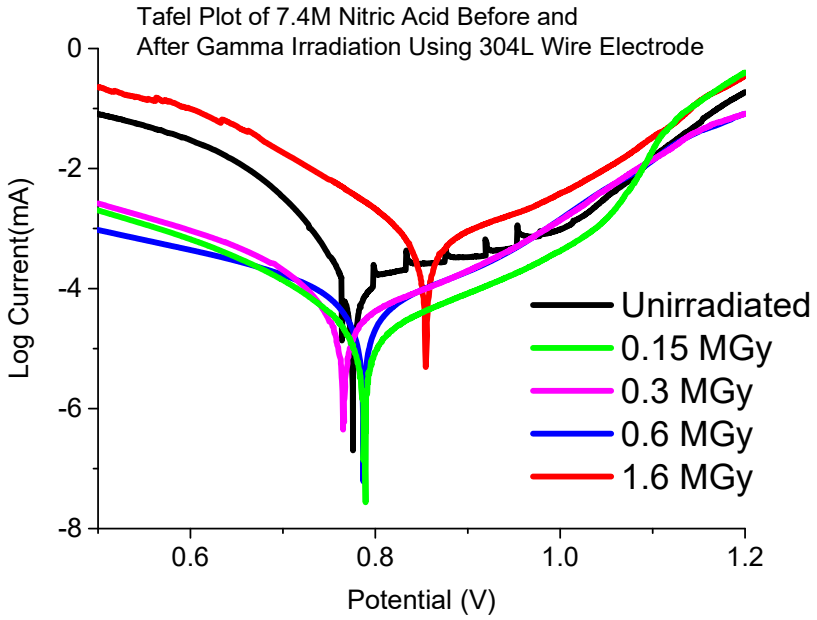

Figure 20: Tafel Plot of a 1 mm diameter 304L steel wire electrode in a solution of 7.4 mol dm^{-3} HNO_3 before and after exposure to gamma irradiation.

Considering now the corrosion potential (E_{corr}) this again varies little between conditions with the exception of 1.6 MGy, which shows a more oxidative E_{corr} of ~+0.88 V. Similarly in the subsequent passive region/anodic tafel arm currents are similar

This project has received funding from the EURATOM research and training programme 2014-2018 under grant agreement No 755171. The content of this deliverable reflects only the author's view. The European Commission is not responsible for any use that may be made of the information it contains.

across all conditions with the exception of 1.6 MGy which has a much greater measured current in this region.

Both observations suggest a greater corrosion rate at this higher, 1.6 MGy dose condition. As such behaviour is not observed in the unirradiated condition, where nitrous reduction currents/concentrations are similar (based on the analysis of the GC results of Figure 17), clearly other currently unknown radiolysis products other than HNO_2 are driving corrosion of the Cr_2O_3 passive film at this dose level.

Turning now to the transpassive region at > +1.0V, in general very little differences are observed between dose conditions. The only conditions that show an increase in transpassive current are the highest dose of 1.6 MGy and lowest dose of 0.15 MGy. It is unclear as to why both these doses should exhibit such greater transpassive currents and further experiments are ongoing to determine this effect.

Considering now the effect irradiated CDTA has on the background behaviour of a glassy carbon electrode, cyclic voltammograms on a 3 mm glassy carbon electrode in 7.4 mol dm^{-3} nitric acid with 0.1 mol dm^{-3} CDTA in the absence and presence of gamma irradiation at a range of doses are shown in Figure 21. As with the previous GC CV's at the lower 3.7 mol dm^{-3} nitric acid concentration, several observations can be made from Figure 21.

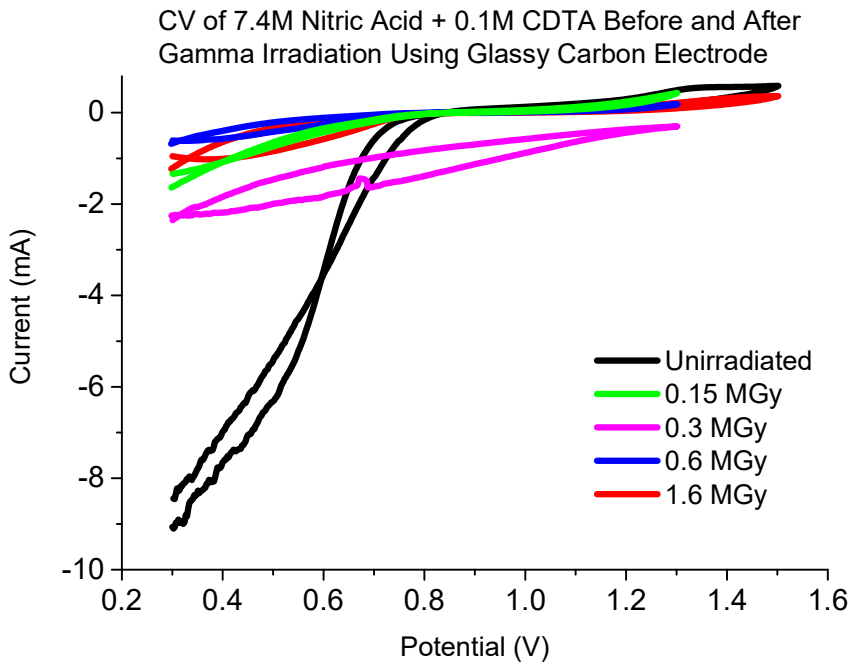

Figure 21: Cyclic Voltammograms of 3mm diameter glassy carbon electrode in a solution of 7.4 mol dm^{-3} HNO_3 and 0.10 mol dm^{-3} CDTA before and after exposure to gamma irradiation.

This project has received funding from the EURATOM research and training programme 2014-2018 under grant agreement No 755171. The content of this deliverable reflects only the author's view. The European Commission is not responsible for any use that may be made of the information it contains.

First, and as per our analysis of nitric acid only experiments on GC electrodes (Figure 17), the nitrous acid reduction wave at < +0.8V and oxygen evolution wave at > +0.8V are both observed across all the measured gamma doses.

Second, again no additional peaks are observed in the CV that could be attributed to CDTA or its radiolytic degradation products, all features instead common to the baseline electrochemical behaviour of nitric acid shown in Figure 17.

Third, measured nitrous reduction currents across all conditions are lower than those measured in the absence of CDTA, Figure 17, the same behaviour as that reported in the previous section for solutions of 3.7 mol dm^{-3} HNO_3.

As per our previous description this suggests that CDTA, or its radiolytic degradation products, must again either be 1) scavenging nitrous acid, 2) interfering with nitrous acid generation through interaction with direct/indirect steps outlined in equations (6) to (17), consequently reducing the measured nitrous reduction current or 3) simply blocking nitric acid access to the electrode surface, through a surface adsorbed complex at this higher nitric acid concentration.

Turning now to duplicate SS304L wire electrochemical studies of those shown in Figure 18, 19 and 20, the measured open circuit potentials, LSV and Tafel plots of an SS304L wire electrode in the presence of 7.4 mol dm^{-3} HNO_3 with 0.03 mol dm^{-3} CDTA as a function of irradiation are shown in Figures 22, 23 and 24.

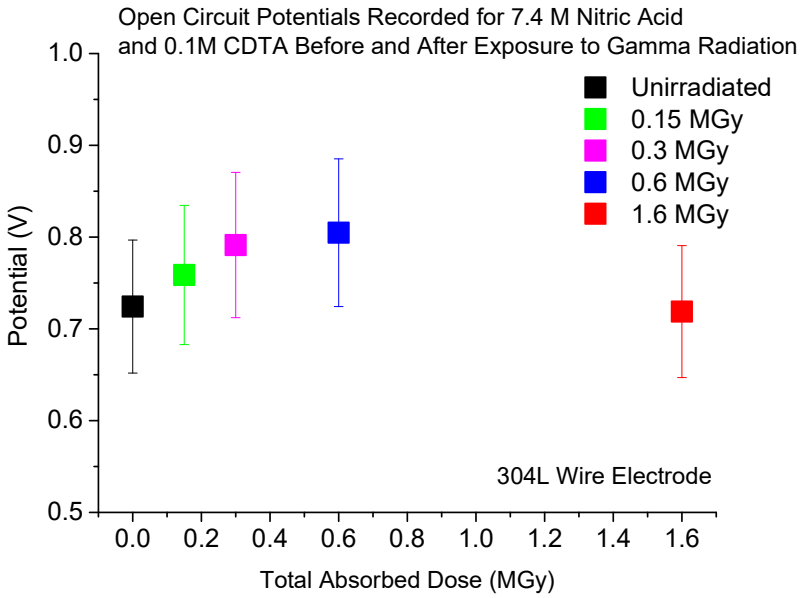

Figure 22: Open Circuit potential of a 1 mm diameter 304L steel wire after one hour of immersion in a solution of 7.4 mol dm^{-3} HNO_3 and 0.10 mol dm^{-3} CDTA after zero (■), 0.15 (■), 0.3 (■), 0.6 (■) and 1.6 MGy total absorbed gamma dose.

This project has received funding from the EURATOM research and training programme 2014-2018 under grant agreement No 755171. The content of this deliverable reflects only the author's view. The European Commission is not responsible for any use that may be made of the information it contains.

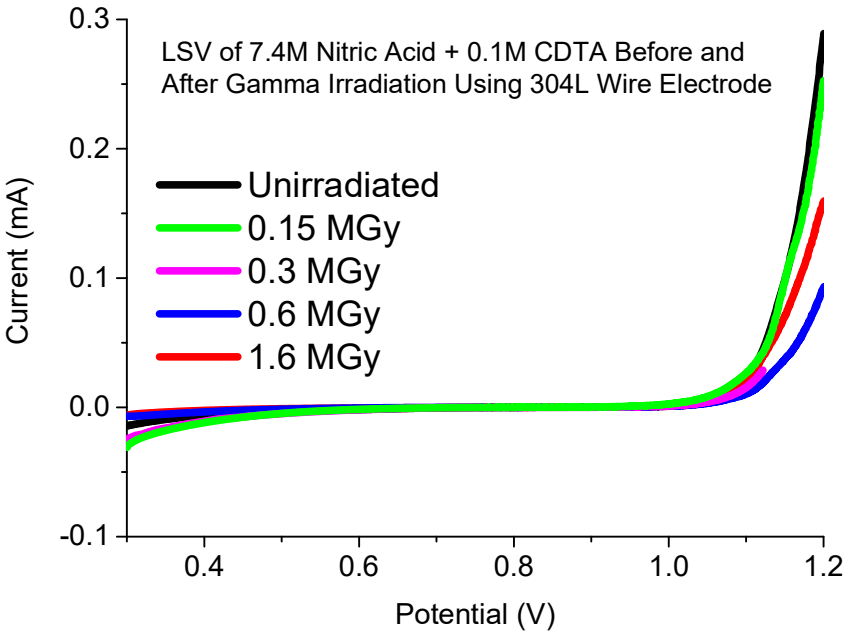

Figure 23: Linear Sweep Volatmmogram of a 1 mm diameter 304L steel wire electrode in a solution of 7.4 mol dm^{-3} HNO_3 and 0.10 mol dm^{-3} CDTA before and after exposure to gamma irradiation.

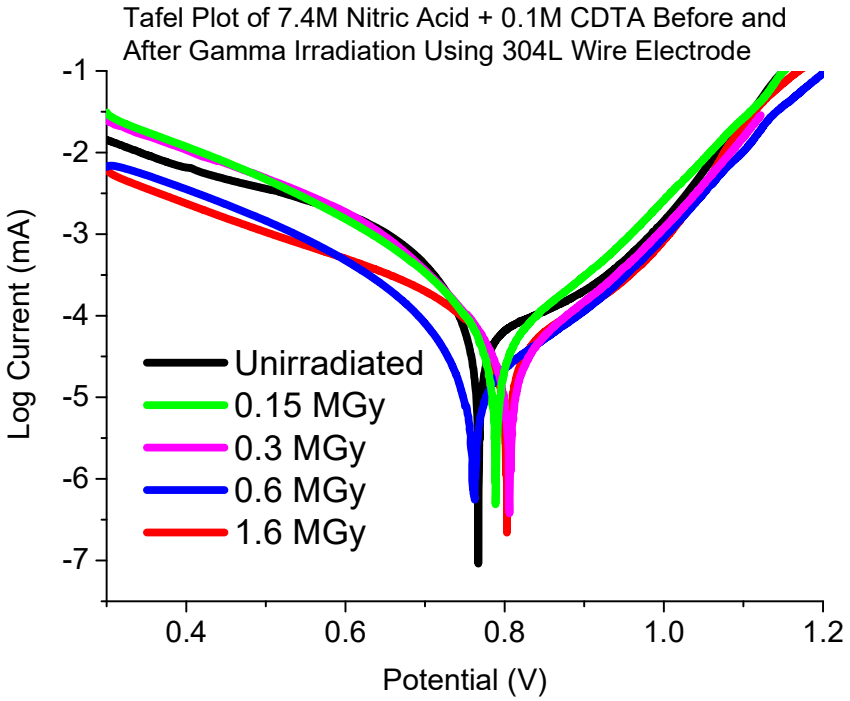

Figure 24: Tafel Plot of a 1 mm diameter 304L steel wire electrode in a solution of 7.4 mol dm^{-3} HNO_3 and 0.10 mol dm^{-3} CDTA before and after exposure to gamma irradiation.

Considering first the OCP measured approximately 1 hour after immersion of the electrode in solutions of 7.4 mol dm^{-3} with 0.1 mol dm^{-3} CDTA, Figure 22, the results are very similar to those recorded for the irradiated nitric acid only solutions of Figure 18.

This project has received funding from the EURATOM research and training programme 2014-2018 under grant agreement No 755171. The content of this deliverable reflects only the author's view. The European Commission is not responsible for any use that may be made of the information it contains.

The only exception is the potential measurement for 1.6 MGy which decreases by about 180 mV upon addition of CDTA and almost certainly reflects the role of CDTA or its radiolytic breakdown products in the scavenging of nitrous that is otherwise generated in the absence of CDTA at this higher dose rate at this higher acid concentration – see Figures 17-20.

Turning now to the LSV and Tafel plots of Figures 23 and 24 recorded under the same dose conditions and considering first the region of 'active' corrosion at ~< +0.8V, it can be seen that under irradiation all measured currents in this region are equal to or lower than that observed in unirradiated nitric acid only. Considering the lower nitrous reduction currents in the GC studies of Figure 21, the lower cathodic Tafel arms may be related to the decreased concentration of nitrous present in these solutions, again indicating that in the active region hydrogen evolution is also accompanied by a degree of NO evolution as well at this nitric acid concentration.

Moving to the corrosion potential (E_{corr}), again little variation is observed as a function of dose, supporting our previous analysis that CDTA or its breakdown products are scavenging radiolytically generated nitrous or whichever other species are generated from the radiolysis of nitric that may lead to an oxidative stress at the steel surface.

Finally, the most interesting regions of the LSV and Tafel plots of Figures 23 and 24 are the passive (+0.8 to +1.0V) and transpassive (> +1.0V) regions. In the passive region, the presence of CDTA results in little effect on the recorded passive current across the tested gamma dose range. Similarly, in the transpassive region currents across dose conditions are identical or less than those found with unirradiated nitric acid solutions.

As at the lower [HNO_3] regime, this can be explained by two possible scenarios:

1) CDTA and/or its degradation products either protect (through surface adsorption) or enhance the Cr_2O_3 passive film.
2) CDTA and/or its degradation products are either scavenging nitrous acid or interfering with nitrous acid generation through interaction with direct/indirect steps outlined in equations (6) to (17), consequently reducing potential radiolysis species available for oxidative steel attack.

Again *in-situ* electrochemical experiments, along with a more thorough programme of degradant species elucidation would be warranted to be able to draw a more definitive conclusion as to the exact mechanism of protection, but it is clear that CDTA continues to act as a corrosion inhibitor at this higher nitric acid concentration, the corrosion inhibition effect also maintaining regardless of gamma radiation dose.

This project has received funding from the EURATOM research and training programme 2014-2018 under grant agreement No 755171. The content of this deliverable reflects only the author's view. The European Commission is not responsible for any use that may be made of the information it contains.

4. CONCLUSIONS AND FURTHER WORK

Experiments to investigate the irradiation of 304L stainless steel flags in 3.7 and 7.4 mol dm^{-3} HNO_3 solutions, in both the presence and absence of CDTA, to 4 total doses; 1.59, 0.57, 0.30 and 0.15 MGy (emulating the dose range available at the INL Radiolysis Test Loop), were conducted within the gamma irradiator at the Dalton Cumbrian Facility. Results indicated that the CDTA acted to inhibit intergranular corrosion on the steel surface with greatest protection being shown at the lower acidity.

3.7 and 7.4 mol dm^{-3} HNO_3 solutions, in both the presence and absence of CDTA, were then irradiated to the same 4 total doses; 1.59, 0.57, 0.30 and 0.15 MGy, and the corrosion behaviour of unirradiated 304L stainless steel flags studied in the post-irradiation solutions. Nitrous acid was found to be generated in both 3.7 and 7.4 mol dm^{-3} HNO_3 solutions, in turn promoting transpassive corrosion at applied potentials greater than 1.1V i.e. under maloperations conditions. This corrosion was found to be inhibited in the presence of irradiated CDTA, with the range of passivity being extended and transpassive currents being suppressed.

This corrosion inhibiting effect of CDTA in radiation fields is most likely due to one or both of two effects:

a. CDTA is adsorbing at the steel surface, said adsorption providing a degree of protection to the Cr_2O_3 passivation layer, preventing oxidative attack by oxidants generated by the radiolysis of water.
b. The presence of CDTA may suppress nitrous acid production – either via providing a substrate that the nitrous may participate with in nitrating reactions or by the provision of CDTA radical species during irradiation that interrupt nitrous production

Recommendations for further work: It is important to note that this irradiation experiment was performed using an argon headspace. There is evidence in the literature that lack of O_2 will result in greater yields of highly corrosive species formed during the radiolytic breakdown of nitric acid. This is recommended for study in subsequent gamma irradiation experiments in order to assess whether the CDTA-derived corrosion inhibition holds, or is in fact enhanced under oxic conditions.

Too, the literature on nitrous generation in irradiated nitric acid solutions is restricted to total adsorbed doses at the lower end of the range studied here. Experiments need

This project has received funding from the EURATOM research and training programme 2014-2018 under grant agreement No 755171. The content of this deliverable reflects only the author's view. The European Commission is not responsible for any use that may be made of the information it contains.

to be repeated in order to better understand the effect of dose on nitrous yield at adsorbed doses up to the upper limit of 1.6 MGy employed here.

Experiments should be conducted to investigate the effect of radiation on the corrosion of steel at a range of nitric acid concentrations, ideally with the voltammetry being conducted in the presence of the gamma field in-irradiator. Parallel experiments should be conducted on unirradiated steel samples, again as at a range of nitric acid concentrations, in the presence of hydrogen peroxide as an irradiation proxy – both to obtain mechanistic insights into the corrosion processes themselves but also to assess how good a surrogate peroxide is for real irradiation experiments.

More widely, the experiments described in this section have focussed on SS304L. This generally exhibits a good resistance to intergranular corrosion, although has been shown to be vulnerable to such at the higher dose rates used here. Thus, alternative plant materials with higher resistances to intergranular corrosion, such as 18/10 NAG should be made subject to the same irradiation / corrosion experiments described here.

Given the apparent efficacy of CDTA as a corrosion inhibitor, thought should be given to its deployment throughout the GANEX 2nd cycle as a protective agent and not just as a fission product masking agent during the initial TODGA/DMDOHEMA extraction of the 2nd cycle. Its compatibility with 2nd cycle chemistry has already been demonstrated through its use as a masking agent and thus minimum disruption to the process chemistry is envisaged.

As well, given the apparent action of CDTA as a corrosion inhibitor, *in-situ* electrochemical experiments under irradiated conditions, along with a more thorough programme of degradant species elucidation would be warranted to be able to draw a more definitive conclusion as to the exact mechanism of protection

REFERENCES

[1] J.W.T Spinks, R.J. Woods, *An Introduction to radiation chemistry*, John Wiley & Sons, Chichester 1990, p269-306

[2] Katsumura, Y., *N-Centered Radicals, the Chemistry of Free Radicals*, John Wiley & Sons, Chichester, 1998.

[3] G.P Horne, *An Experimental and Computational Investigation into the Radiolysis of PUREX Solvent Systems,* Ph.D. Thesis, University of Manchester (2015).

[4] B. Raj, U.K. Mudali, *Progress in Nuclear Energy* **48** (2006), pp283-313

[5] V. Cihal, *Intergranular Corrosion of Steels and Alloys (Materials Science Monographs)*,

This project has received funding from the EURATOM research and training programme 2014-2018 under grant agreement No 755171. The content of this deliverable reflects only the author's view. The European Commission is not responsible for any use that may be made of the information it contains.

Elsevier (1984), ISBN 0444996443.
[6] G.M. Treacy, A.L. Rudd, C.B. Breslin, *Journal of Applied Electrochemistry* **30** (2000), pp675-683
[7] ASTM International. Standard Practice for Preparing, Cleaning and Evaluating Corrosion Test Specimens. G1-03, 1-12. 2011.
[8] B. El Ibrahimi, A. Jmiai, L. Bazzi, S. El Issami, *Arabian Journal of Chemistry* **13** (2020), pp740-771
[9] F. Balbaud, G. Sanchez, G. Santarini, G. Picard, *European Journal of Inorganic Chemistry* **2000** (2000), pp665-674
[10] T. Nagai, M. Takeuchi, S. Takeda, T.A. Yamamoto, S. Tsukui, S. Okamoto, Journal of Nuclear Science and Technology **35** (1998), pp502-507
[11] V.H. Veley, *Philosophical Transactions of the Royal Society* **A** (1891), pp312-313
[12] H. McKenze, J. MacDonald-Taylor, F. McLachlan, R. Orr, D. Woodhead. Procedia Chemistry **21** (2016), pp481-486
[13] N.N. Khobragade, A.V. Bansod, A.P. Patil, Materials Research Express 5 (2018), pp046526

This project has received funding from the EURATOM research and training programme 2014-2018 under grant agreement No 755171. The content of this deliverable reflects only the author's view. The European Commission is not responsible for any use that may be made of the information it contains.

GENERAL CONCLUSION

Corrosion assessment work detailed in this report has had two primary objectives:

1) To perform corrosion assessments for process plant steels in the presence of as many of the GANEX inventory permutations as resource permits.
2) To carry out long term corrosion studies in relevant inventory permutations of high risk.

With regards to the former, corrosion assessments of the following key compounds: TODGA, DEHiBA, AHA, SO_3-Ph-BTP, SO_3-Ph-BTBP, SO_3-Ph-BTPhen, hydrazine and CDTA have been carried out. Compounds have been tested in predominantly aqueous solutions, where corrosion is found to be more rapid than organic solutions and at concentrations equivalent to both normal and maloperation conditions. The results of these experiments are summarised in Table 1:

Table 1: Summary of work carried out towards objective 1).

Normal Operations

	DEHiBA	DEHiBA Degradation Products	DMODOHEMA	CDTA	Hydrazine	CDTA +Hydrazine	TODGA	TODGA +DMODOHEMA	AHA	SO_3-Ph-BTP	AHA +SO_3-Ph-BTP
Organic	GH 1	?	?	?	?	?	SH 3	?	?	?	?
Aqueous	GH 1	?	?	GH 5	GH 6	GH 6	?	?	SH 3	SH 4	SH 4

Maloperations

	DEHiBA	DEHiBA Degradation Products	DMODOHEMA	CDTA	Hydrazine	CDTA +Hydrazine	TODGA	TODGA +DMODOHEMA	AHA	SO_3-Ph-BTP	AHA +SO_3-Ph-BTP
Organic	GH 1	?	?	?	?	?	SH 3	?	?	?	?
Aqueous	GH 1	?	?	GH 5	GH 6	GH 6	?	?	SH 3 & 4	SH 4	SH3 & 4

I = Corrosion Inhibitor A = Corrosion Accelerator N/A = No Net Corrosion Effect

SH = SACSESS HYBARs GH = GENIORS HYPARS

Of these inventory permutations, AHA and SO_3-Ph-BTP have been shown to be corrosion accelerators, increasing recorded currents in the transpassive dissolution region, i.e. under high redox stresses associated with maloperation conditions. In the case of the latter, SO_3-Ph-BTPhen has been shown to have similar corrosion accelerating properties whilst SO_3-Ph-BTBP has been shown to be a suitable replacement ligand with no corrosion acceleration effect.

Complementary evidence on the corrosion protection properties of DEHiBA, CDTA and hydrazine and confidence in their long-term corrosion protection behaviour with stainless steel process pipework is also provided here, with corrosion protection maintaining even at high nitric concentrations. This also allows for other partner groups within the consortium to focus attention on diminishing the risks associated with the implementation of AHA and SO_3-Ph-BTP within the GANEX flowsheet

This project has received funding from the EURATOM research and training programme 2014-2018 under grant agreement No 755171. The content of this deliverable reflects only the author's view. The European Commission is not responsible for any use that may be made of the information it contains.

Finally, preliminary investigations into the corrosion behaviour of inventory permutations under a realistic energy gamma radiation field have been conducted . The first of these irradiation experiments has focused on the stability of CDTA. The evidence presented in here reports indicates that CDTA exhibits relatively high radiation tolerance and retains its corrosion inhibition qualities even at total absorbed doses in the Mega Gray region.

Recommendations for further work are given at the end of each section, specifically pages 27, 57, 82. 113 and 146. The most important are as follows:

Aqueous phase corrosion susceptibility studies should be conducted on candidate plant steels in the presence of DMDOHEMA. However, as alternative ligands are currently being assessed for use in GANEX-2, these too should be subject to corrosion vulnerability assessments. Thus, it is recommended that the studies described above are repeated in the presence of the new organic phase extractant, mTDDGA and the new aqueous phase extraction agent, py-tri-diol.

Those ligands that have been shown to be corrosion accelerators exhibit greatest accelerating action under maloperations conditions and especially when solution redox potentials exceed 1.1V. However, there are significant uncertainties as to the redox stresses that exist throughout the GANEX process, even under conventional operating conditions. Thus, it is recommended that a map of the solution redox potentials that obtain throughout flowsheet is compiled – both under normal and maloperation, unirradiated and irradiated conditions.

A number of the ligands investigated that have surfactant-like properties also exhibit corrosion inhibiting behaviour that is attributed to their adsorption at the steel surface, so forming a hydrophobic film that prevents corrosive agents from contacting the steel itself. However, this protection has only been observed under the stagnant conditions employed in the experiments reported here. It remains to be seen if it is retained under flow conditions and especially under the high shear flow conditions that may obtain in modern plant such as centrifugal contactors. Thus, the corrosion behaviour of ligands that exhibit this corrosion inhibition property should be studied under dynamic conditions to determine the robustness of this protection to convective flow.

Of those ligands studied AHA, SO_3-Ph-BTP and SO_3-Ph-BTPhen exhibit the strongest corrosion acceleration properties. This acceleration is restricted to maloperation conditions and predominantly involves non-localised dissolution of the passive film with only mild intergranular corrosion. However, more severe intergranular corrosion is observed when candidate steels are irradiated in the presence of high concentrations of

This project has received funding from the EURATOM research and training programme 2014-2018 under grant agreement No 755171. The content of this deliverable reflects only the author's view. The European Commission is not responsible for any use that may be made of the information it contains.

nitric acid. Thus, it is recommended that only steels designed to resist intergranular corrosion are used in plant construction (e.g. SS310, 18/10 NGA) but that those steels should also be tested in the presence of the current GANEX inventory in order to demonstrate safe levels of corrosion resistence.

CDTA has been shown to be an effect inhibitor of both non-localised passive film dissolution and intergranular corrosion. Thus, thought should be given to its deployment throughout the GANEX 2nd cycle as a protective agent and not just as a fission product masking agent during the initial TODGA/DMDOHEMA extraction of the 2nd cycle. Its compatibility with 2nd cycle chemistry has already been demonstrated through its use as a masking agent and thus minimum disruption to the process chemistry is envisaged. Too, experiments conducted at the nitric acid concentration of 1.5 mol dm^{-3} indicate that hydrazine and CDTA exhibit a strong cooperative corrosion inhibiting effect. Thus, this cooperative effect of CDTA and hydrazine on the corrosion of all steels studied here should be investigated at the higher nitric acid concentrations that occur elsewhere in the GANEX flow sheet

Experiments conducted under gamma irradiation indicate that the corrosion inhibiting properties of CDTA are retained in the presence of process-condition representative radiation fields. Thus experiments should also be conducted to investigate the effect of radiation on the corrosion of steel more generally and especially at a range of nitric acid concentrations, ideally with the voltammetry being conducted in the presence of the gamma field in-irradiator. Parallel experiments should be conducted on unirradiated steel samples, again as at a range of nitric acid concentrations, in the presence of hydrogen peroxide as an irradiation proxy – both to obtain mechanistic insights into the corrosion processes themselves but also to assess how good a surrogate peroxide is for real irradiation experiments.

With the exception of some TODGA work in Exxol-D80, this phase of the work has focussed on the aqueous phase for reasons discussed above. Thus, additional to the afore-mentioned recommendations, the vulnerability of candidate process steel to inventory permutations in the organic phase should be conducted. These should be complemented with TODGA studies in the aqueous phase, perhaps employing TEDGA as it will be the action of the diglycolamide group that will be responsible for any observed corrosion effects. Too, building on the irradiated CDTA work, additional GANEX 1st cycle work should include study of the effect of irradiation on the corrosion properties of DEHiBA, both in the aqueous and organic phase.

This project has received funding from the EURATOM research and training programme 2014-2018 under grant agreement No 755171. The content of this deliverable reflects only the author's view. The European Commission is not responsible for any use that may be made of the information it contains.